Università degli Studi di Torino
Scuola di Dottorato

Unveiling Galactic cosmic messengers: from the infinitely small to the infinitely large

Author:
Luca Orusa

Supervisor:
Prof. Fiorenza Donato

A thesis submitted in fulfillment of the requirements for the degree of Doctor of Philosophy in Physics in the
Doctoral School of Physics - XXXVI cycle

Università degli Studi di Torino
Scuola di Dottorato

Dottorato in Fisica

Unveiling Galactic cosmic messengers: from the infinitely small to the infinitely large

Author:
Luca Orusa

Supervisor:
Prof. Fiorenza Donato

A thesis submitted in fulfillment of the requirements for the degree of Doctor of Philosophy in Physics in the
Doctoral School of Physics - XXXVI cycle

Luca Orusa

Unveiling Galactic cosmic messengers:
from the infinitely small to the infinitely large

Tesi di Dottorato di Ricerca in Fisica
Defence date: December 21, 2023

Supervisor:
Prof. Fiorenza Donato

Reviewers:
Andrew Strong
Francesca Calore

Members of the PhD defence committee:
Andrew Strong
Francesca Calore
Nicolao Fornengo

Università degli Studi di Torino
Doctoral School, PhD in Physics - XXXVI cycle
Dipartimento di Fisica
Via Pietro Giuria 1
10125 Turin

Black has depth.. you can go into it..
And you start seeing what you're afraid of.
You start seeing what you love, and it becomes like a dream.

David Lynch

Acknowledgements

The PhD defence marked the end of an incredible eight-year journey that began at Via Pietro Giuria 1, a place I undoubtedly consider a second home, where I shared some of the most crucial years of my life with exceptional people. It is time to express gratitude to all those individuals without whom this journey would not have been possible, and to whom I dedicate the final chapter of this incredible experience.

To Fiorenza, after a bachelor's, master's, and a PhD thesis, I can confidently say she is the best supervisor one could imagine. Always available, ready to find time to advise, inspire, and share a laugh during our lengthy discussions. You were a role model for me, one I aim to emulate in my career as a researcher and as a person.

To Mattia, Silvia, Michael, and Sarah, for the invaluable time spent collaborating on exciting projects, for the guidance and introduction to numerous topics. The everyday work as a PhD wouldn't have been the same without the intense collaboration and exchange with all of you.

To Damiano, for guiding and introducing me to the world of plasma physics: an amazing field that I've decided will be a central part of my future research. Without the guidance of such a brilliant scientist, the decision to continue my career in the US would not have been possible.

To Nicolao, Alessandro, Carlo, Marco R., Marco T., and the rest of the astroparticle group of Torino, for enriching discussions that helped me grow during these years, and for all the lunches at Bagni Municipali. I hope to continue collaborating with you in the future.

To the referees of this manuscript, F. Calore and A. Strong, for carefully reading and commenting on the text and the results. The interactions with you were really interesting and fruitful.

To Stefano and Felix, for their collaboration and their exemplary roles as scientists.

To all the excellent researchers I had the opportunity to meet during international schools and conferences.

To my unique group of friends from Savigliano: Alex, Chiara, Elisa, Gabriele, Giacomo,

Ida, Irene C., Irene G., Lorenzo, Martina, Mattia, Mila, Sara B., Sara C., Sarah, Simone, Sofi and Stefano. To Davide, whom I would have loved to have by my side during these years.
To the fellas from Bunker, especially Alberto (a Bunker acquired son), Andrea, Francesco, Giorgio, and Gloria, for sharing the PhD experience during our daily life. To Antonio and Federica, for becoming two of my closest friends in recent years. Our personal Bunker League, in the end, was absolutely amazing.
To Giorgia, for sharing moments with me every day over the last nine years, for your constant support, and for our growth together as individuals.
To the goodfellas from Frames Cinema, especially Alberto, Alessandro, Anna, Jacopo and Rosario, with whom I shared my big passion for movies and developed a sincere friendship every day over the last few years.
To the cool kids of ISAPP, with whom I shared two amazing weeks, some of the best PhD fellows one can imagine.
To the Chicago crew, for welcoming me to the Windy City and making me feel at home. A special thank and a big hug to Emily: I look forward to our reunions in the years to come.
A special gratitude to my family for their constant support, for accepting my career and decisions without hesitation, allowing me to chase my dreams.

Research & publications

The research domain of this thesis is Theoretical Astroparticle Physics. The results presented in this thesis have been published on the following journals during time of the PhD:

- [1] L. Orusa, S. Manconi, F. Donato and M. Di Mauro, *Constraining positron emission from pulsar populations with AMS-02 data*, Journal of Cosmology and Astroparticle Physics 12, 014 (2021).
- [2] S. Recchia, M. Di Mauro, F. A. Aharonian, L. Orusa, F. Donato, S. Gabici, and S. Manconi, *Does the Geminga, Monogem and PSR J0622+3749 γ-ray halos imply slow diffusion around pulsars?*, Physical Review D 104, 123017 (2021).
- [3] L. Orusa, M. Di Mauro, F. Donato and M. Korsmeier, *New determination of the production cross section for secondary positrons and electrons in the Galaxy*, Physical Review D 105, 123021 (2022).
- [4] L. Orusa, M. Di Mauro, F. Donato and M. Korsmeier, *New determination of the production cross section for γ rays in the Galaxy*, Physical Review D 107, 083031 (2023).
- [5] M. Di Mauro, F. Donato, M. Korsmeier, S. Manconi, and L. Orusa, *A novel prediction for secondary positrons and electrons in the Galaxy*, Physical Review D 108, 063024 (2023).
- [6] L. Orusa, D. Caprioli, *Fast particle acceleration in 3D hybrid simulations of quasi-perpendicular shocks*, Physical Review Letters 131, 095201 (2023).

This research has been accomplished at the University and INFN of Turin from October 2020 to October 2023, and at the Department of Astronomy & Astrophysics of the University of Chicago, where I worked as a Visiting Researcher from September to December 2022. I acknowledge support by the University and INFN of Turin, by the Italian Space Agency and by the Cultural Association of Italians at Fermilab.

Keywords & acronyms

Few acronyms will be extensively used in this thesis, the first list reflecting true keywords of the research discussed.

AMS-02	Alpha Magnetic Spectrometer
CM	Center-Of-Mass
CMB	Cosmic Microwave Backgroung
CR	Cosmic Ray or Cosmic-Ray
DM	Dark Matter
d.o.f	degrees of freedom
DSA	Diffuse shock acceleration
Fermi-LAT	*Fermi* Large Area Telescope
HAWC	High Altitude Water Cherenkov Experiment
ICS	Inverse Compton Scattering
IS	InterStellar
ISM	InterStellar Medium
ISRF	InterStellar Radiation Field
LHAASO	Large High Altitude Air Shower Observatory
LHC	Large Hadron Collider
LHCf	Large Hadron Collider forward
l.o.s.	line of sight
PAMELA	Payload for Antimatter Matter Exploration and Light-nuclei Astrophysics
PIC	Particle-in-cell
PWN	Pulsar Wind Nebula
S. C.	Subdominant channels
SDA	Shock drift acceleration
SNR	Supernova Remnant
TOA	Top Of the Atmosphere

Abstract

In the last decade, space-based experiments like AMS-02, DAMPE, CALET and *Fermi*-LAT, and ground-based experiments like HAWC, H.E.S.S., and LHAASO have turned astroparticle physics of Galactic cosmic rays and gamma rays into a precision discipline, making our research work particularly timely. We can use the newly available data to learn more about our Universe, and in this thesis, we will use the cosmic radiation we measure at the Earth as messengers to unveil the properties of the Galactic environment. An outstanding effort is currently ongoing to characterize the properties of cosmic messengers, which raise compelling questions about the origin of cosmic radiations, the mechanisms responsible for particle acceleration, and their propagation in the Galaxy and beyond.

The research presented in this thesis contributes to unveil the origin of two types of Galactic radiation: charged cosmic rays, with a particular focus on positrons, and gamma rays. Often, our approach effectively combines these two cosmic radiations in a multi-wavelength and multi-messenger modeling of cosmic sources.

In the first Part of this thesis, we present an overview of the charged cosmic radiation detected at Earth, from the production in astrophysical sources to propagation in the Galaxy, and of the cosmic gamma-ray radiation.

Part II is dedicated to the interpretation of Galactic cosmic rays and gamma rays from a multi-messenger point of view, with the combination and interaction between extremely different physics regimes, from the infinitely small scales of fundamental particle physics, to particle propagation in the infinitely large Galactic environment. We start our journey from the infinitely small scales, using data from accelerator and collider experiments to provide a new parametrization for the production cross sections of electrons, positrons, and gamma rays in hadronic interactions. Cross sections enter in the computation of secondary fluxes and the Galactic diffuse emission, contributions generated by the interaction of cosmic rays with the interstellar medium.

We then focus on the computation of a new estimate of the secondary electrons and positrons fluxes. In particular, for positrons, the knowledge of the secondary compo-

nent is crucial for understanding this antimatter channel. To achieve this, we combine the information from cross sections with new state-of-the-art models for particle propagation in the Galaxy, fitting the measured cosmic nuclei fluxes.
After the focus on secondary fluxes, we shift our attention to the total positron flux, investigating the contribution coming from pulsars and relative pulsar wind nebulae. The high-precision AMS-02 data are used to constrain the main properties of the Galactic pulsar population needed to explain the observed flux.
In line with the multi-messenger approach of this thesis, we then focus on pulsar gamma-ray halos detected by experiments like HAWC and LHAASO. These halos are a direct product of electrons and positrons accelerated and emitted in a region around the source, and they can provide complementary information with respect to the measurements of AMS-02, that refer to particles detected after a long journey before reaching the Earth, allowing us to test different propagation models around these sources.
We complete the picture showing how kinetic plasma simulations are necessary for the modelling and understanding of the phenomenology of particle acceleration at astrophysical shocks. In line with the spirit of this thesis, which is based on the interaction between effects at different physics scales, we demonstrate that it is necessary to consider the turbulence generated at scales of hundreds of kilometers for the understanding of particle injection and acceleration in these environments that cover parsec scales.

Italian abstract

Nell'ultimo decennio, esperimenti nello spazio come AMS-02, DAMPE, CALET e *Fermi*-LAT, ed esperimenti a Terra come HAWC, H.E.S.S. e LHAASO hanno trasformato la fisica astroparticellare dei raggi cosmici Galattici e dei raggi gamma in una disciplina di precisione. Possiamo utilizzare i nuovi dati disponibili per raggiungere una conoscenza dettagliata del nostro Universo e, in questa tesi, useremo la radiazione cosmica che misuriamo sulla Terra come messaggero per svelare e comprendere le proprietà della nostra Galassia. Uno sforzo eccezionale è attualmente in corso da parte della comunità scientifica per comprendere le proprietà di tali messaggeri, che sollevano domande fondamentali sull'origine delle radiazioni cosmiche, i meccanismi responsabili dell'accelerazione delle particelle e la loro propagazione nella Galassia e oltre.

La ricerca presentata in questa tesi contribuisce a svelare l'origine di due tipi di radiazione Galattica: i raggi cosmici carichi, con particolare attenzione ai positroni, e i raggi gamma. Spesso, la nostra metodologia combina efficacemente queste due componenti attraverso un approccio multimessaggero nella modellizzazione delle sorgenti cosmiche.

Nella prima parte di questa tesi, presentiamo una panoramica sulla radiazione cosmica carica rilevata sulla Terra, dalla sua produzione in sorgenti astrofisiche alla propagazione nella Galassia, e sui raggi gamma.

La Parte II è dedicata all'interpretazione dei raggi cosmici Galattici e dei raggi gamma da un punto di vista multi-messaggero, con la combinazione e l'interazione tra regimi fisici estremamente diversi, dalle scale infinitamente piccole della fisica fondamentale, alla propagazione delle particelle nell'ambiente Galattico infinitamente grande. Iniziamo il nostro viaggio dalle scale infinitamente piccole, usando i dati degli acceleratori e dei collider per fornire una nuova parametrizzazione per le sezioni d'urto di produzione di elettroni, positroni e raggi gamma nelle interazioni adroniche. Le sezioni d'urto entrano nel calcolo dei flussi secondari e dell'emissione diffusa Galattica, contributi generati dall'interazione dei raggi cosmici con il mezzo interstellare.

Ci focalizziamo successivamente sul calcolo di una nuova stima del flusso di elettroni

e positroni secondari. In particolare per i positroni, la conoscenza dettagliata della componente secondaria è fondamentale per l'interpretazione di questo canale di antimateria. Per ottenere tale predizione, combiniamo la parametrizzazione per le sezioni d'urto precedentemente ottenuta con nuovi modelli per la propagazione delle particelle nella Galassia, calibrati sui flussi dei nuclei cosmici misurati.
Dopo il focus sui flussi secondari, spostiamo la nostra attenzione sul flusso totale di positroni, studiando il contributo proveniente dalle pulsar wind nebulae. I dati di AMS-02 sono utilizzati per comprendere le principali caratteristiche della popolazione Galattica di pulsar necessarie per spiegare il flusso osservato.
In linea con l'approccio multimessaggero di questa tesi, ci concentriamo quindi sugli aloni di raggi gamma rilevati attorno alle pulsar da esperimenti come HAWC e LHAASO. Questi aloni sono un prodotto diretto delle particelle accelerate ed emesse in una regione estremamente vicina alla sorgente e possono fornire informazioni complementari rispetto alle misurazioni di AMS-02, che riguardano particelle rilevate dopo un lungo viaggio prima di raggiungere la Terra, permettendoci di testare diversi modelli di propagazione intorno a tali sorgenti.
Completiamo il quadro della tesi dimostrando come le simulazioni cinetiche del plasma siano necessarie per la modellizzazione e la comprensione dell'accelerazione delle particelle agli shock astrofisici. In linea con lo spirito di questa tesi, basato sull'interazione tra effetti a diverse scale fisiche, mostriamo come sia fondamentale considerare la turbolenza generata a scale di centinaia di chilometri per la comprensione del processo di iniezione e accelerazione delle particelle in ambienti astrofisici che coprono scale delle dimensioni del parsec.

Contents

Part I

Introduction

Chapter 1

Charged cosmic rays

Cosmic-ray (CR) radiation commonly refers to charged particles hitting the top of Earth's atmosphere with energies ranging from a few hundred MeV to 10^{11} GeV. In this Chapter, we provide an overview of Galactic CR radiation.

1.1 The discovery of cosmic rays

The history leading to the discovery of CR radiation began in the 18th century with the invention of electroscopes by W. Gilbert, and the observation that they spontaneously discharge over time. In 1785, Coulomb [7] verified that this discharge was induced by the air, then confirmed around 1900 by Wilson, Elster, and Geitel. The discovery of radioactivity in 1896 by Becquerel [8], along with subsequent studies on radioactive materials by P. and M. Curie [9], connected the discharge rate of electroscopes to the emission of charged particles from radioactive decays. This simple hypothesis was initially attributed to radioactivity from the Earth's crust or the atmosphere. However, in 1909, Wilson, Kurtz, and Cline [10] visionary proposed an extraterrestrial origin.
After some measurements at the top of the Eiffel Tower in 1909 by T. Wulf [11], trying to prove a terrestrial origin, the first evidence that the observed radiation did not originate from the Earth's crust came in 1911 from experiments conducted by D. Pacini. He compared the discharge rate of electroscopes on mountains, over a lake, and over the sea [12, 13, 14], founding a significant decrease of approximately 20% in the discharge rate when the electroscope was placed three meters underwater, consistent with radiation absorption by water.
The conclusive answer came from balloon experiments, which demonstrated that the penetrating radiation was of cosmic origin. The first flight specifically designed to study penetrating radiation was conducted in 1909 by A. Gockel, ascending up to

4500 meters above sea level. V. F. Hess continued the campaign in 1912, making seven flights using different instruments. He measured the penetrating radiation to be almost constant with altitude within errors below 3000 meters. Furthermore, he observed an increase of 50% from 3000 to 4000 meters, and values exceeding 100% from 4000 to 5200 meters, compared to ground-level observations [15]. The discovery of CRs is generally associated with V. F. Hess's most successful flight on August 7, 1912. Thanks to his discoveries he won the Noble Prize in 1936 together with C. D. Anderson, who discovered the positron (e^+).

The investigations carried out by J. Clay in 1927 [16] resulted in the discovery that the intensity of penetrating cosmic radiation is dependent on geomagnetic latitude, indicating the presence of charged particles. The regions that CRs can access are determined by the spatial distribution of the geomagnetic field, which deflects low-energy ($E \lesssim 10$ GeV) charged particles, known as the geomagnetic cut-off.

In 1932, a global survey conducted by Compton [17] confirmed that cosmic radiation primarily consists of charged particles, while in 1933, parallel and independent studies conducted by Alvarez and Compton [18], Johnson [19] and Rossi [20] demonstrated that CRs are predominantly composed of positively charged particles. Schein in 1941 [21] outlined that CRs are primarily composed of protons (p), while in 1950-1951 Critchfield [22] determined that electrons and positrons ($e^{\pm}$) accounted for a small fraction of the total particle count. In 1948, the presence of various elements, including iron, was detected using photographic emulsions in the stratosphere. The discovery of electrons (e^-) in cosmic radiation dates back to 1961 with the findings of J.A. Earl [23].

Currently, we know that p constitute approximately 90% of cosmic radiation, helium (He) and nuclei up roughly 10%, and all other components a small percentage [24].

1.2 The cosmic-ray flux

Since V. F. Hess's pioneering balloon flight in 1912 [15], significant advancements in experimental techniques have driven the field forward, leading to modern balloon flights and the development of detectors on satellites, on the International Space Station, and terrestrial installations. CR experiments can measure incoming fluxes with a precision of a few percent. The total CR flux is reported in Figure 1.1, taken from Ref. [25]. The figure illustrates the flux of CR particles multiplied by the energy squared ($E^2\phi$) in units of GeV/m^2/s/sr as a function of energy (E) in GeV. The CR flux in first approximation can be described as power-laws with different slopes, depending on the energy range. In particular four key features are observed: below approximately 30 GeV, the flux

bends downwards due to modulation caused by the presence of a magnetized solar wind, preventing very low-energy particles from reaching the inner solar system. The steepening of the flux at around 10^6 GeV, known as the knee, signifies a change in the slope of the observed flux from about -2.7 to about -3.1. The ankle at approximately 10^{10} GeV marks the transition to a slope of -2.7 again. Finally, the flux exhibits a cut-off above approximately 3×10^{19} eV, known as the GZK cut-off, which arises from the interaction of CRs with the photons of the Cosmic Microwave Background (CMB) [26].
The data points represent the fluxes measured by:

- AMS-02: all particle flux [27, 28], antiprotons ($\bar{p}$) [29] and leptons data [30, 31].
- Auger: all particle flux [32].
- BESS-TeV: all particle flux [33].
- CALET: lepton flux [34].
- CREAM: all particle flux [35, 36].
- DAMPE: lepton flux [37].
- FERMI: the γ-ray diffuse flux [38] and the isotropic diffuse γ-ray emission [39].
- HAWC: all particle flux [40].
- H.E.S.S.: lepton flux [41].
- IceCube: neutrino fluxes of astrophysical origin [42].
- IceTop: all particle flux [43].
- KASKADE-Grande: all particle flux [44].
- PAMELA: all particle flux [45], $\bar{p}$ [46] and leptons data [47].
- Tibet-III: all particle flux [48].

This thesis will focus on the study of CR nuclei and γ rays, with a large space dedicated to $e^{\pm}$ observed in the GeV$-$TeV energy range. In fact, although they constitute only about 1% of the overall CR flux, these particles carry valuable information about the sources of CRs and their propagation through the Galactic magnetic field. In this thesis we will focus on Galactic CRs, more specifically, on CRs in the range between the GeV level and a few hundred TeV.

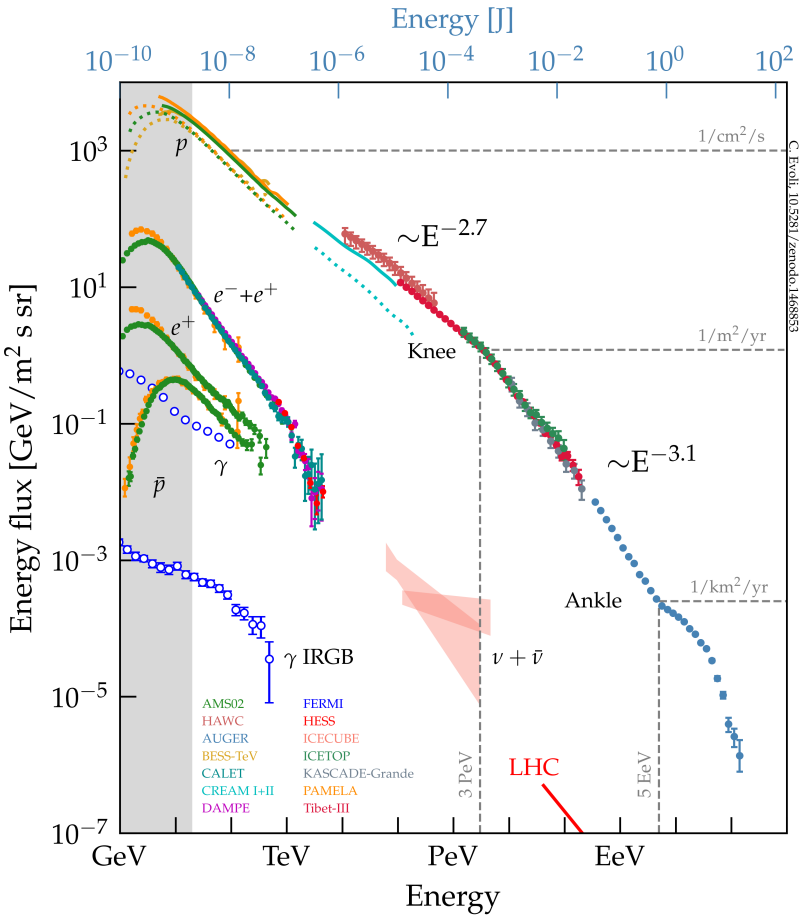

Figure 1.1: The data points illustrate the energies and rates of Galactic CR particle species as recently measured from AMS-02 [27, 28, 29, 30, 31], Auger [32], BESS-TeV [33], CALET [49], CREAM [35, 36], DAMPE [37], FERMI [38, 39], HAWC [40], H.E.S.S. [41], IceCube [42], IceTop [43], KASKADE-Grande [44], PAMELA [45, 46, 47], and Tibet-III [48]. Figure taken from Ref. [25].

1.3 Sources of Galactic cosmic rays

In this Section, we investigate the origins and mechanisms responsible for the production of Galactic CRs. CRs can be broadly categorized into two main groups: primaries and secondaries. Primary CRs are directly produced within the sources and undergo acceleration within the same environment. Conversely, secondary CRs are the result of interactions between CRs and the Galactic material. Two primary source classes are primarily considered for CRs, up to several hundred TeV: Supernova Remnants (SNRs) and Pulsar Wind Nebulae (PWNe) [50]. These Galactic objects represent the advanced stages of massive star evolution and are estimated to occur at a rate from one to four per century within our own Galaxy [51, 52, 53]. In this Section we will describe both point sources of primary CRs and the secondary production mechanism.

1.3.1 Supernova Remnants

The origin of CRs has remained an outstanding question in astrophysics ever since their groundbreaking discovery by V. H. Hess in 1912. For energies below the knee, SNRs have been considered as the most promising candidates for the source of CRs [54].

In 1934, Baade and Zwicky proposed that supernova (SN) explosions occur due to the release of an enormous amount of gravitational binding energy during the transition from an ordinary star to a different final stage. A SN of type II arises from the violent explosion of a star with a mass approximately 8 times that of the Sun ($M_\odot$) [55] toward the end of its lifespan. Following the explosion, a compact object such as a neutron star or a black hole is formed. Turbulent shells of gas, known as SNRs, are produced around these objects by the outer layers of the SN. These shells then expand into the interstellar medium (ISM) at highly supersonic speeds, persisting for millions of years. A SN explosion results in the injection of a total mass M_{ej} moving with a velocity V_{ej} in the ISM.

The total energy output, in the form of kinetic energy, for the ejected mass is approximately $E_{SN} \sim 10^{51}$ erg [56]. The velocity of the ejecta can be expressed as $V_{ej} = 10^4 E_{SN}^{1/2} M_{ej,\odot}^{-1/2}$ km/s, where $M_{ej,\odot}$ denotes the mass of the ejecta in solar masses. The sound speed in the ISM can be estimated as c_s given by $c_s = \sqrt{\gamma k_b T/m}$, where k_B denotes the Boltzmann constant, γ is the adiabatic index, T is the temperature in the ISM and m is the proton mass [56]. The motion of the ejecta is highly supersonic ($M_s = V_{ej}/c_s \gg 1$), resulting in the formation of a shock front characterized by abrupt changes in density, temperature, and pressure within the interstellar gas. In the SN environment, the shock is collisionless, meaning that the transfer of energy and momentum between particles occurs through interactions with collective plasma processes, rather than direct collisions. The expansion of a SNR into the surrounding medium is a complex process that can be divided into three main stages [57, 58]. In each stage, the radius of the remnant (r_R) exhibits different scaling with time from the explosion (t_R).

- Free expansion: $r_R \propto t_R$. In the initial phase, the shell expands at a constant speed due to the dominance of kinetic energy over gravitational energy. The velocity of the ejected material is much higher than the sound speed of the surrounding gas, resulting in the formation of a high Mach number blast shock wave. This phase typically lasts for $10 - 100$ years.

- Adiabatic expansion (Sedov-Taylor): $r_R \propto t_R^{2/5}$. This phase begins when the

mass of the ISM swept by the shock wave becomes comparable to the mass of the original stellar ejecta. The evolution of the shock front follows the self-similar blast wave model known as the Sedov-Taylor model [59]. Gas cooling is solely due to expansion, making it adiabatic. Typically, this stage begins around 100 years after the SN explosion. During the Sedov-Taylor phase, the shock front is strong, and particles in the surrounding medium can potentially undergo acceleration through diffusive shock acceleration (see the next Section).

- Late evolution: the velocity of the shock front decreases linearly with time as the SNR ages, eventually reaching a velocity of approximately 100 km/s after an average time of 10^5 years. At this stage, energy dissipation causes the dispersal of the remnants, and the expanding shell slows down to subsonic speeds of $1-10$ km/s. Advanced magnetohydrodynamical (MHD) simulations, as demonstrated in studies like Ref. [60, 61], are required to investigate the evolution of SN shells in the ISM.

Diffusive shock acceleration

In this Section we describe the standard particle acceleration mechanism that has been deeply investigated over the past century. Baade and Zwicky [54] not only introduced the groundbreaking concept of SN formation but also put forth the idea that CRs are accelerated by SNRs. Their proposal was based on an energetic analysis, estimating that a significant portion $(20-30\%)$ of the kinetic energy of SN ejecta is converted into relativistic particles, accounting for the energetics of CRs. While Baade and Zwicky primarily focused on extragalactic supernovae, the notion that Galactic CRs are accelerated in Galactic SNRs has gained widespread acceptance, commonly known as the SNR paradigm [62].

After attending a lecture by H. Alfvén at the University of Chicago, where magnetic irregularities in the ISM were discussed, E. Fermi recognized the potential of particle energization through the scattering with Alfvén waves [63, 64]. In astrophysical contexts, collisions between particles and magnetic irregularities or Alfvén waves are typically elastic. However, when these irregularities are in motion, collisions can result in either energy gain in head-on collisions or energy loss in tail-on collisions. In scenarios involving Alfvén waves or magnetized clouds as magnetic irregularities, the higher frequency of head-on collisions compared to tail-on collisions statistically accelerates

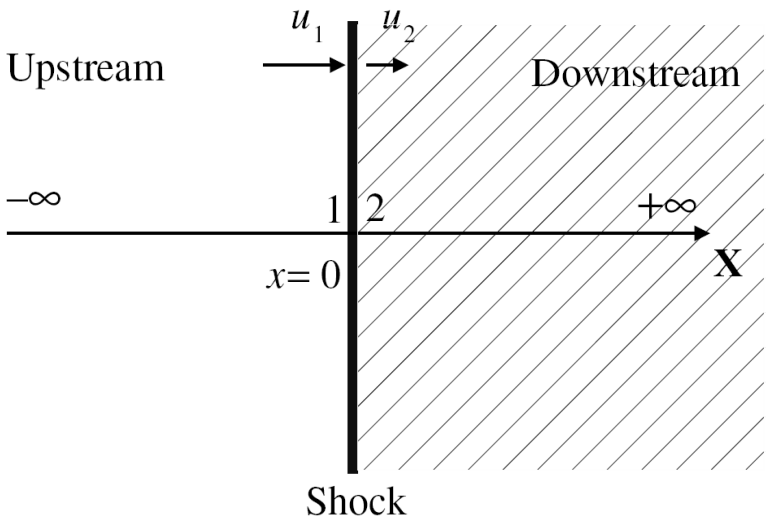

Figure 1.2: Schematic structure of a shock, in a frame centered on the discontinuity: the upstream medium is un-shocked and moves towards the shock with velocity $u_1 = v_{\rm sh}$.

particles. The average energy gain per cycle of this process is:

$$\left\langle \frac{\Delta E}{E} \right\rangle = \frac{8}{3}\frac{V^2}{c^2}, \tag{1.1}$$

where V is the velocity of the magnetic field irregularities. Since the gain is proportional to $(V/c)^2$, this process is often referred to as the second-order Fermi mechanism. However, it may not be very efficient due to the typically low values of V compared to c. For example, for interstellar magnetic fluctuations, V is approximately $1 - 10$ km/s. If all collisions are head-on, each of them results in an energy gain. From this principle, in the late '70s, various authors independently realized that when the Fermi mechanism is applied to shocks, it can lead to highly efficient acceleration of CRs [65, 66, 67, 68, 69]. This process, known as Diffusive Shock Acceleration (DSA), relies on the repeated scattering of particles back and forth across the shock, allowing for multiple head-on collisions and efficient energy gain. For a non-relativistic shock with velocity between the upstream and downstream fluids given by $V = u_1 - u_2$ (see Figure 1.2), the energy gain for one DSA cycle is:

$$\left\langle \frac{\Delta E}{E} \right\rangle \simeq \frac{4}{3}\frac{u_1 - u_2}{c}. \tag{1.2}$$

The presence of a tangled magnetic field and/or a diffusion process is crucial to allow for multiple occurrences of this process. It is important to note that DSA is not guaranteed to occur at every shock. In the case of relativistic shocks, where $u_2 = c/3$,

it can be challenging for particles to travel back upstream after crossing the shock [70]. As shown by Ref. [68], combining Equation 1.2, with the probability for a particle to escape the system, it is possible to obtain the differential spectrum of accelerated particles:

$$\frac{dN(E)}{dE} = f(E) \propto E^{-\gamma_e} \quad \text{with} \quad \gamma_e = \frac{R+2}{R-1}. \tag{1.3}$$

The spectral index γ_e depends solely on the compression ratio $R = u_1/u_2$. This means that for any strong shock, where R tends to the asymptotic value of $R = 4$, the value of γ_e is always 2. This is valid for relativistic particles at non-relativistic shocks. If we relax the assumption that particles are relativistic, the universal spectrum is a power-law in momentum:

$$\frac{dN(p)}{dp} = 4\pi p^2 f(p) \propto p^{-\gamma_p} \quad \text{with} \quad \gamma_p = \frac{3R}{R-1}. \tag{1.4}$$

The conversion between energy and momentum must be taken into account, recalling that $4\pi p^2 f(p)dp = f(E)dE \rightarrow f(E) = 4\pi p^2 f(p)(dp/dE)$. Therefore, for $R = 4$, in the non-relativistic regime where $E = p^2/2m$, we have $\gamma_e = 1.5$, while in the relativistic limit where $E \propto p$, we have $\gamma_e = 2$. Thus the basic prediction for DSA is a power-law momentum spectra with index $\gamma_p = 4$, and not a energy spectra with $\gamma_e = 2$ as usually reported in literature, which is valid only for relativistic particles.
This basic picture is complicated by different non-linear effects, such as dynamical reaction and plasma instabilities generated by the accelerated particles, and amplification of magnetic fields [71, 72]. Recent advancements in numerical methods and the availability of modern supercomputers have enabled *ab initio* simulations of astrophysical plasmas, allowing us to model the intricate, non-linear interplay between particles and electromagnetic waves. These simulations are unveiling the underlying processes responsible for the energization of the highest-energy particles in the Universe and will be the main topic of Chapter 7.

1.3.2 Pulsar Wind Nebulae

Neutron stars are compact, rapidly spinning, and highly magnetized stars that exhaust their nuclear fuel and collapse under their own gravity. The outer layers of the star rebound and explode, giving rise to a SN event. Due to conservation of angular momentum, the collapsed neutron star ends up rotating at a rate of tens of revolutions per second, with densities reaching several solar masses compressed within a radius of $10 - 14$ km.

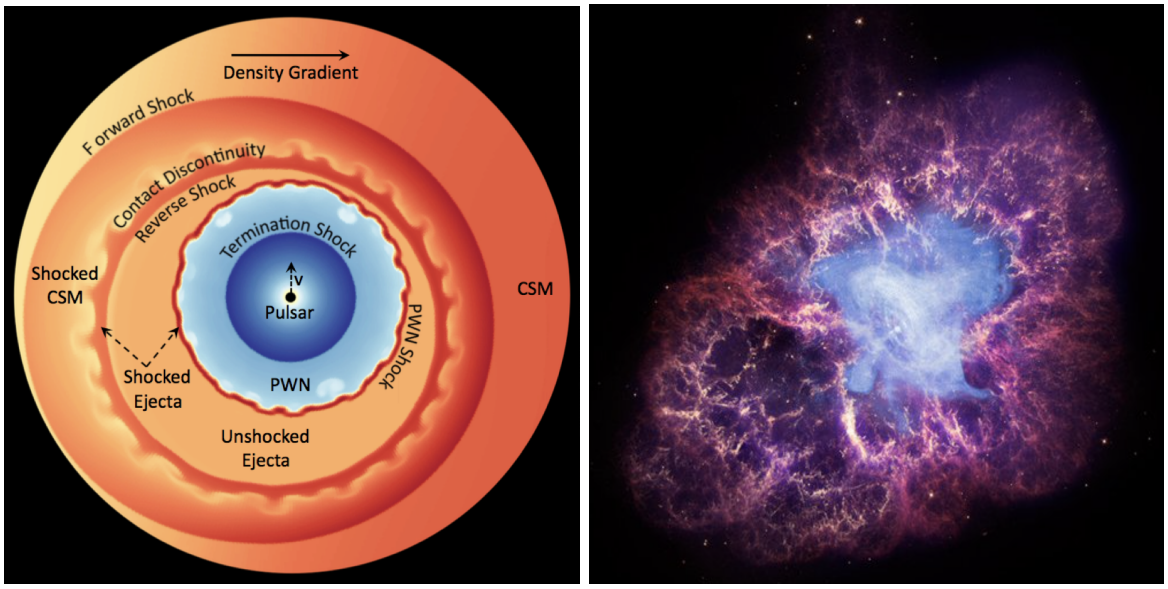

Figure 1.3: Left panel: a PWN expanding into a SNR that is evolving within a medium with a density gradient of the surrounding ISM increasing towards the right, as viewed from a hydrodynamical simulation. Figure taken from [74]. Right panel: the Crab Nebula captured in different wavelengths. The Chandra X-ray image (NASA/CXC/SAO/F.Seward) is shown in blue, the Hubble Space Telescope optical images (NASA/ESA/ASU/J.Hester & A.Loll) are in yellow and red, and the Spitzer Space Telescope's infrared image (NASA/JPL-Caltech/Univ) is in purple.

Neutron stars emitting pulses of radiation in various wavelengths such as radio, optical, X-rays, and γ rays, are referred to as pulsars. These highly spinning and magnetized neutron stars release energy through a relativistic wind composed of $e^{\pm}$ pairs. This wind is confined by the surrounding material ejected during the SN explosion and gives rise to a PWN that emits radiation across the entire electromagnetic spectrum.

The Crab Nebula serves as a well-studied example of a young PWN, observed across various wavelengths from radio to the TeV band (see [73] for a review). Observations indicate that the Lorentz factor of accelerated particles within the Crab Nebula reaches values of $10^8 - 10^9$. For a comprehensive analysis of the observational properties and evolution of PWNe, we refer to [74, 75]. The idea that pulsars could be sources of CR $e^{\pm}$ in our Galaxy dates back $30 - 40$ years [76, 77]. In the following paragraphs, we provide a brief description of the model concerning the production of $e^{\pm}$ in PWNe.

The rapid rotation and strong magnetization of pulsars induce an electric field that extracts e^- from the star's surface. As these extracted e^- propagate along the magnetic field lines, they lose energy through curvature radiation. Given the intense magnetic field strength ($10^{11} - 10^{13}$ Gauss), the emitted high-energy photons can produce $e^{\pm}$ pairs. This process initiates an electromagnetic cascade, populating the pulsar mag-

netosphere with pairs. The number of generated pairs, referred to as multiplicity, depends on the structure of the magnetospheric gaps [78], and it is expected to be in the range of $10^4 - 10^5$. The relativistic magnetized wind of pairs evolves within a complex environment.

Figure 1.3 (left panel) provides a schematic representation of a PWN expanding into the surrounding ISM as depicted in a hydrodynamical simulation [74], during the stage 1 described below. The PWN region is indicated by blue colors, while the shock system and the ISM are depicted in orange and red, respectively. The region enclosed by the ejecta from the massive star progenitor is further encompassed by the SN blast wave propagating in the ISM (orange area). When the magnetized wind encounters the sub-relativistic expansion of the ejecta, a system of shock waves is generated. An outer shock propagates within the ejecta, while a reverse shock, known as the termination shock (blue area), moves back towards the star. At the termination shock, a significant portion of the wind's bulk energy is converted into accelerated $e^{\pm}$ pairs, which emit radiation across a wide range of photon energies through synchrotron radiation and inverse Compton processes. The accelerated pairs are confined by the magnetic field and lose energy until they are eventually released into the ISM, through a mechanism still under investigation and of great interest in determining the potential contribution of PWNe to the CR $e^{\pm}$ detected on Earth. The typical value for the total energy lost by the star is approximately $E_{tot} \sim 10^{49}$ erg over a characteristic timescale of $\tau_0 \sim 10$ kyr. The right panel of Figure 1.3 displays a false-color image of the Crab Nebula, which is located at a distance of 2 kpc. The Crab Nebula is the most extensively studied PWN, with observations spanning from radio to γ-ray wavelengths [73].

The environment of pulsars changes dramatically over time, firstly as contained within an evolving SNR, and finally within the general ISM when the kick velocity received by the pulsar at birth moves it beyond the decelerated shell of the host SNR. A sketch of the main evolutionary stages of a PWN taken from Ref. [79] is reported in Figure 1.4. There are three stages considered:

- Stage 1, $t < 10$ kyr: at early times the pulsar is still relatively close to its birthplace. The high-energy leptons accelerated at the PWN are thought to remain confined inside at this stage. The Larmor radius in the nebular magnetic field (B $\sim 100\mu$G) is extremely small, making diffusive escape inefficient.

- Stage 2, $t \sim 10 - 50$ kyr: at intermediate times, the morphology of a PWN-SNR system is often highly irregular. It depends both on the properties of the material in the surrounding ISM, and on the direction and velocity of the pulsar. The nebula is disrupted and the pulsar can be strongly off-centre with respect

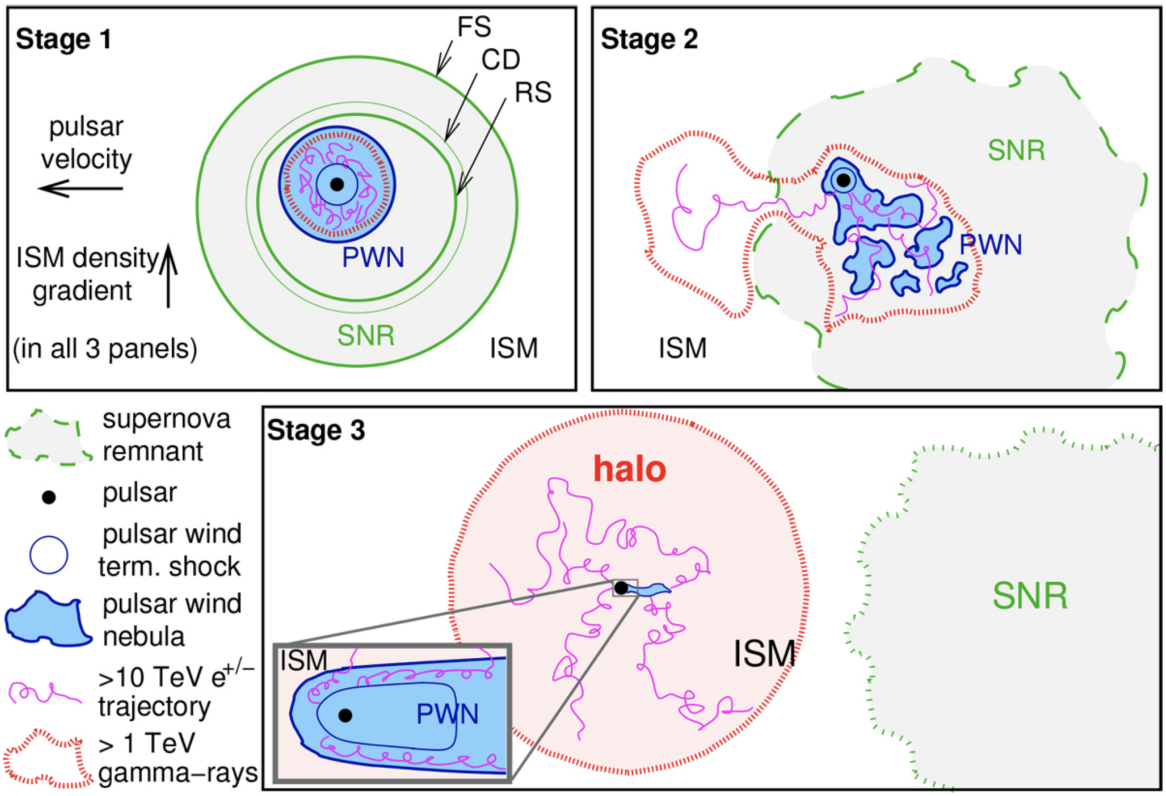

Figure 1.4: Sketch of the main evolutionary stages of a PWN. See the text for details. Figure taken from Ref. [79].

to the PWN. At this stage, high-energy $e^{\pm}$ start to escape from the PWN, and propagate in the surrounding SNR and eventually are able to leave it.

- Stage 3, $t \gtrsim 50$ kyr: at late times, the pulsar has finally escaped from its parent SNR, thanks to its kick velocity. The SNR is expanding very slowly and fading away. The supersonic motion of the pulsar through the ISM transforms the PWN into a bow-shock PWN [80], and particles are free to leave the system, contributing to the CR population.

Particle Acceleration in Pulsar Wind Nebulae

The acceleration of particles in PWNe to TeV energies and beyond is generally thought to happen at the wind termination shock and is still an open problem. Among the various proposed mechanisms, the two most extensively studied are DSA and driven magnetic reconnection.

- DSA at relativistic shock: the performance of this mechanism is poor at relativistic magnetized shocks [81], that is the scenario that characterizes the termination

shock. Unless the shock normal and magnetic field direction are aligned within an angle of $1/\Gamma$, where Γ is the wind Lorentz factor, the shock is effectively superluminal, and particles struggle to return from downstream. A high level of turbulence with $\delta B/B \gg 1$ is required to counteract advection and to allow particles to diffuse back to the shock. This condition is only easily met if the magnetization σ is very low, where σ is defined as the ratio between the wind Poynting flux and particle kinetic energy:

$$\sigma = \frac{B^2}{4\pi n_e m_e \Gamma^2 c^2}, \tag{1.5}$$

with B the magnetic field and n_e the comoving $e^{\pm}$ number density. In such cases, the growth of the Weibel instability [82] ensures sufficient turbulence and efficient particle acceleration. The condition for this mechanism to work, in terms of wind magnetization, is $\sigma \lesssim 10^{-3}$. In principle, the shock can accelerate particles with a nearly universal spectrum of $\sim E^{-2.3}$, similar to what is inferred from X-ray observations of PWNe. However, even when this condition is met, the turbulence develops typically at small-scales, causing the acceleration time to increase with E^2, preventing particles from reaching very high energies. This is a general challenge when invoking Fermi acceleration at relativistic shocks (e.g., [81]). One possible solution is the existence of large-scale turbulence of external origin in the shock vicinity (see e.g., [83]).

- Driven magnetic reconnection: magnetic reconnection is a physical process occurring in electrically conducting plasmas, in which the magnetic topology is rearranged and magnetic energy is converted to kinetic energy, thermal energy, and particle acceleration. The sector of the wind close to the equator of the pulsar characterized by alternating magnetic field lines is likely to undergo magnetic reconnection when compressed at the shock. In addition to creating a low magnetization region where the Fermi mechanism could potentially operate, reconnection itself can lead to highly efficient particle acceleration. If conditions are suitable, all the dissipated magnetic energy can be converted into particle acceleration, resulting in hard ($E^{-\gamma_e}$ with $1 < \gamma_e < 2$) and extended power-law spectra. The flat spectral indices observed in radio emission from PWNe are consistent with this process. Moreover, this mechanism can completely remove the Maxwellian component of the particle distribution, which is always present in Fermi acceleration but never observed in PWNe. However, the outcome of the process in terms of spectral slope and energy range extension depends on

the initial magnetization and pair loading of the flow. Detailed particle-in-cell (PIC) simulations (see Section 7.1) have shown that to account for the observed 3 decades in particle energy spanned by radio emission, considering a particle spectrum with $\gamma_e \sim 1.5$, one would require pair multiplicities of approximately 10^8 [84], which is much larger than what current pulsar theories can explain [85], and also larger than what is inferred from observations.

1.3.3 Spallations of cosmic rays on the interstellar medium

The so-called secondary CRs are generated through the interaction of CRs with atoms in the ISM. Flux computations of CRs are inherently linked to the production and fragmentation cross sections of particles resulting from nuclear interactions. Cross sections are not solely relevant for secondary CRs; they also significantly impact primary CRs. Primary CRs can originate from the fragmentation of higher-mass nuclei or can be disrupted during their interaction with the ISM. The field of high-energy particle physics is of fundamental importance for understanding CRs. The state-of-the-art models of production and fragmentation cross sections are constructed using a phenomenological approach, as attempts to compute them from first principles through perturbative calculations fall short in this particular regime. Below, we present examples that underscore the significance of cross sections in astroparticle physics.

In the diffusion model that will be presented in Section 1.4, that is the state-of-the-art method of treating particle propagation in the Galaxy, it is assumed that particles travel in a diffusive halo with height L, escaping from the Galaxy once they reach the boundaries. One of the main uncertainties in these models that will be further discussed in Chapter 4, is the estimation of the halo size L. Historically, propagation of CR has mainly been investigated using boron (B) and the boron-to-carbon (B/C) ratio, since B is almost completely absent in the sources and is instead produced from the fragmentation of heavier nuclei during propagation, i.e., it is a secondary CR nucleus. In the context of the standard diffusion model, these ratios typically are sensitive to $L/D(E)$ at high energies, where $D(E)$ is the energy dependent diffusion coefficient that describes the scattering of particles off the irregularities of the Galactic magnetic field. Precious information about CR transport can then be gathered through their measurement. The B/C ratio strongly depends on the fragmentation cross sections of heavier nuclei than B, pointing out the crucial role played by these quantity.

Radioactive secondary species, whose lifetime is shorter than escape time, decay before reaching the boundary of the Galaxy. These species are only sensitive to the diffusion coefficient $D(E)$, whereas stable secondary species can escape and are sensitive to

$L/D(E)$. Any fit combining the information of a stable and radioactive secondary species breaks the $L/D(E)$ degeneracy, allowing for the determination of L [86]. As outlined in Ref. [87, 88], the impact of production cross sections for the determination of L is significant, as has been already argued by different teams from beryllium over boron (Be/B) analyses [87, 89, 90]. As demonstrated in Ref. [88], the ^{10}Be/^{9}Be ratio, being ^{10}Be radioactive, is directly related to the value of the production cross sections of these isotopes, that are crucial for a good determination of L. This topic will be further discussed in Chapter 4.

A major contribution to antimatter fluxes arise as a secondary product of primary CRs with the ISM, outlining the importance of production cross section of these particles in hadronic interactions, that will be the main topic of Chapter 3, focusing on $e^{\pm}$. To accurately assess the potential contributions of primary sources to the e^{+} flux, a precise understanding of secondary production is crucial. The primary source of secondary flux arises from proton-proton ($p+p$) interactions, specifically the interaction between CR protons and ISM hydrogen atoms. Other significant contributions involve CRs colliding with various ISM atoms, including He (He+p, p+He, and He+He). Channels involving heavier CR species and atoms can contribute at a few percent level to the production of secondary $e^{\pm}$. Spallation processes resulting in the production of pions ($\pi^{\pm}$) and kaons ($K^{\pm}$), which subsequently decay into $e^{\pm}$ particles, are the primary mechanisms responsible for the production of secondary $e^{\pm}$. Therefore, accurate cross section measurements for $\pi^{\pm}$ and $K^{\pm}$ production are essential for calculating secondary $e^{\pm}$ production. Similar considerations apply to $\bar{p}$ [91], $\bar{d}$ and $\overline{\mathrm{He}}$ [92].

1.3.4 Other sources

In this thesis we will consider only the sources described thus far for the interpretation of the CRs fluxes measured at the Earth. For completeness we report here other potential sources or production mechanism of CRs.

- Dark matter (DM): anomalous components and spectral features observed in CR fluxes may serve as signatures of exotic sources, including DM. In particular, the study of antimatter in CRs, like cosmic e^{+}, $\bar{p}$, $\bar{d}$ and $\overline{\mathrm{He}}$, is of particular interest due to their rarity compared to cosmic matter (see Figure 1.1). The self-annihilation or decay of DM particles into Standard Model (SM) particles can contribute to the CR yield (see e.g. e^{+} [93], $\bar{p}$ [94], $\bar{d}$ [92], $\overline{\mathrm{He}}$ [95]).

- Secondary contribution from SNRs: in the conventional CR paradigm, only matter particles (p, e^{-}, nuclei) are accelerated at the collisionless shocks of SNRs.

However, also secondary particles can be generated within these sources and subsequently undergo acceleration similar to the primary particles typically considered [96, 97, 98, 99]. Primary CRs accelerated by a SNR can produce secondary particles via hadronic interactions in the same vicinity of the SNR shock, that can be accelerated as well in the same environment. Hence, although secondary particles may be sub-dominant in terms of their total number, they can have observable consequences at high energies in the $e^{\pm}$, $\bar{p}$ and antinuclei spectra [96]. This effect should also manifest in other observable phenomena, such as an increase in secondary-to-primary CR ratios [100]. Recently, in Ref. [99], the authors found that assuming the same SNR population accelerates both light nuclei (p, He) and heavier CR species, this mechanism can account for all the antimatter fluxes. However, this analysis involved an extensive number of free parameters with a scan of their values on large intervals, which can significantly influence the final results.

- Star clusters: winds of massive stars could serve as suitable sites for CR acceleration (see e.g., [101, 102]). Recent measurements of γ-ray emission (see Sections 2.1.1 and 2.1.2) from regions surrounding compact star clusters, such as Cygnus cocoon [103, 104, 105] and 30 Doradus in the Large Magellanic Cloud [106], support the notion that a significant fraction of the wind kinetic energy is converted into non-thermal particles, reaching maximum energies above 100 TeV. These findings imply that stellar clusters may contribute significantly to the flux of Galactic CRs. Further support for this conclusion comes from the analysis of the $^{22}\mathrm{Ne}/^{20}\mathrm{Ne}$ abundance in CRs, which is approximately five times greater than in the solar wind [107]. This result is challenging to explain solely within the framework of particle acceleration at SNR shocks [108], but can be more readily accommodated if CRs are partially accelerated from material contained in the winds of massive stars [109]. The theoretical description of the particle energization and transport process within the cavity created by the wind launched by a star cluster was recently outlined by Ref. [110].

1.4 Propagation of cosmic rays in the Galaxy

Throughout their journey, the characteristics of CRs are altered from their initial values. All the phenomena that impact on the life of CRs between their origin and detection are collectively referred to as propagation, which is the central topic of this Section. In the remainder of this Chapter we will focus on Galactic CRs, more specifically, on

CRs in the range between the GeV level and a few hundred TeV. The propagation of charged CRs within our Galaxy, regardless of the mechanism responsible for their production and acceleration, is influenced by interactions with the Galactic magnetic field, ISM, and radiation fields. Examining CR propagation offers an indirect means of investigating the characteristics of our Galaxy.

1.4.1 The diffusion model

The initial approach to modeling Galactic CR propagation was presented by Parker with the leaky-box model [111]. This model portrays the Galaxy as a finite volume for propagation, with homogeneous source densities and interstellar matter. Modern treatments of CR propagation are based on diffusion models, originally proposed and developed by Ginzburg and Syrovatskii [112]. These models incorporate a more detailed treatment of source and interstellar matter distributions. The central concept in diffusion models is that random scattering in the irregularities of the Galactic magnetic field results in spatial diffusion. The idea of diffusion can be traced back to the pioneering works of Chandrasekhar [113] and Fermi [63], who respectively demonstrated that diffusion can be described as a random walk and provided the initial statistical description of particle scattering and acceleration in random magnetic irregularities. For a comprehensive discussion of diffusion models for CR propagation, we refer to [112, 114, 115, 116, 117, 118, 119].

The first evidence for cosmic-ray diffusion in galactic magnetic fields came in 1977 from cosmic-ray e^-, with the observation of non-thermal radio emission in the spiral galaxy NGC 4631 [120]. An extended radio halo exceeding the spatial extension of the galaxy by a few kpc was observed. This was interpreted as synchrotron emission from e^- interacting with magnetic fields, revealing thus the presence of cosmic-ray e^- trapped in a magnetic halo exceeding the optical extension of the galaxy.

The present understanding of the Galactic magnetic field encompasses two coexisting components: a regular component aligned parallel to the Galactic plane with an average strength of a few μG, and a stochastic component of similar strength. The ISM can be regarded as a weakly turbulent magnetoactive plasma, containing turbulence and inhomogeneities on the pc scale. CRs interact and scatter off plasma oscillations and waves, which in turn modify their energy and cause spatial diffusion. Due to the impracticality of measuring the microscopic properties of magnetic fields throughout the entire Galaxy, a phenomenological and macroscopic description of the propagation process is constructed.

CRs propagate within the diffusion halo, which corresponds to the Galactic magnetic

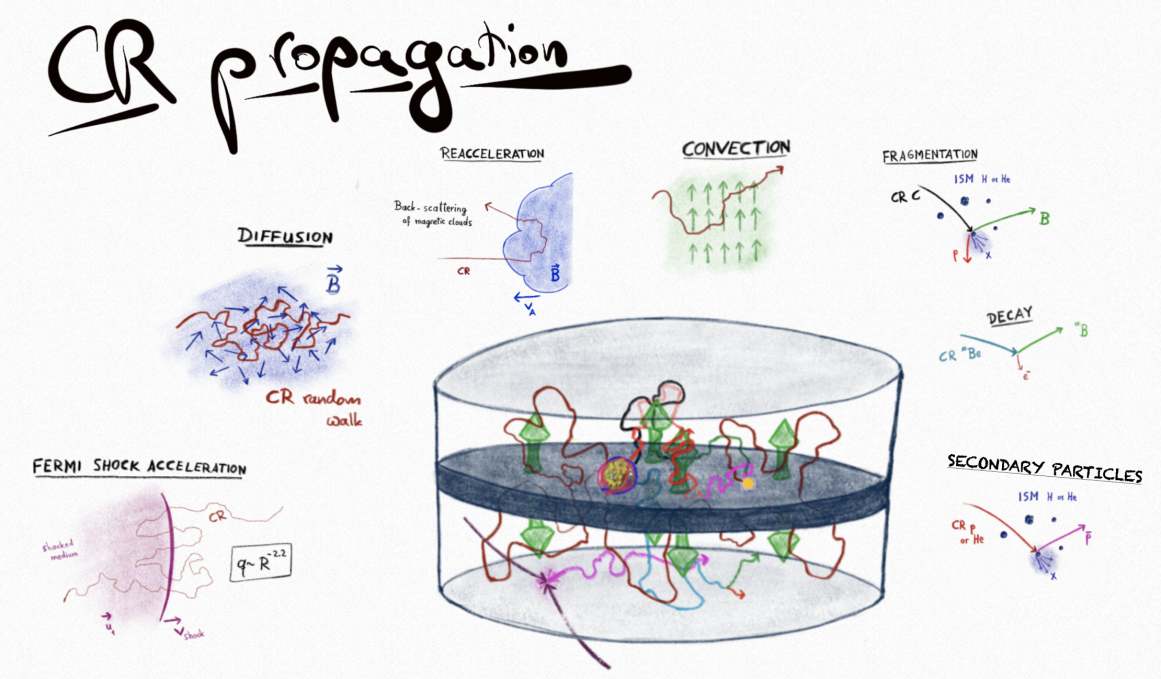

Figure 1.5: Schematic view of the Milky Way diffusive halo. The stellar and gaseos disc has two confinment thick layers which contain turbulent magnetic fields. After having been accelerated by the sources, particles diffuse on magnetic irregularities and can be affected by convection, reacceleration, fragmentation and decay. Figure taken from http://www.astroparticle.to.infn.it/?nav=Home. Courtesy of M. Korsmeier.

halo. This region is typically represented as a cylindrical volume with a radius of 20 kpc and a half-thickness ranging from 2 to 10 kpc [87, 88, 89, 5]. The sources of CRs and interstellar material are confined to a thin disk with a half-height of $h = 0.1$ kpc. The diffusion zone sets the boundaries where the diffusion process occurs. The diffusion coefficient, named D_{xx}, quantifies the transport of CRs through the turbulent Galactic magnetic field. In a more general treatment, the diffusion coefficient should be represented by a tensor with parallel and transverse components, as the distribution of magnetic field inhomogeneities varies throughout the Galactic halo. We adopt the assumption of isotropic diffusion in this context. The values and properties of the diffusion coefficient D_{xx} are determined by observational constraints obtained from CR measurements and in the basic diffusion models it is assumed to be a power-law in rigidity R. In recent years also more complicated formulas have been employed, as we will see in Chapter 4.

1.4.2 Additional propagation effects

In the diffusion model, the propagation of CRs within the Galaxy is described by a transport equation [115], in which enters the D_{xx} term. The charged particles injected into the ISM by their sources undergo various processes as a result of interactions with Galactic magnetic fields, atoms or photons in the ISM, and Galactic winds. These processes can be modeled using a system of coupled propagation equations for the densities ψ_i of different CR species i. In general, ψ_i depends on position within the Galaxy ($\boldsymbol{x}$), momentum magnitude (p), and time (t) (see, e.g., [117]):

$$\begin{aligned} \frac{\partial \psi_i(\boldsymbol{x}, p, t)}{\partial t} &= q_i(\boldsymbol{x}, p, t) + \boldsymbol{\nabla} \cdot (D_{xx} \boldsymbol{\nabla} \psi_i - \boldsymbol{V} \psi_i) \\ &+ \frac{\partial}{\partial p} p^2 D_{pp} \frac{\partial}{\partial p} \frac{1}{p^2} \psi_i - \frac{\partial}{\partial p} \left(\frac{\mathrm{d}p}{\mathrm{d}t} \psi_i - \frac{p}{3} (\boldsymbol{\nabla} \cdot \boldsymbol{V}) \psi_i \right) - \frac{1}{\tau_{f,i}} \psi_i - \frac{1}{\tau_{r,i}} \psi_i. \end{aligned} \tag{1.6}$$

Equation 1.6 can be numerically solved using codes such as GALPROP and DRAGON [114, 121, 122, 123], or solved semi-analytically using for example the USINE code [124]. In this thesis we will adopt semi-analytical solutions for $e^{\pm}$ as described in detail in Chapter 5 and the GALPROP code in Chapter 4. See Figure 1.5 for a schematic representation of the CR propagation. The source term $q_i(\boldsymbol{x}, p, t)$ specifies the location and energy spectrum of CRs injected in our Galaxy. This includes the astrophysical sources of primary CRs, and the injection of secondary CRs which are produced by the interaction of primary CRs with the ISM. We briefly comment each term of Equation 1.6 in what follows.

- Time dependence: the transport equation's first term describes the time evolution of CR number density. In cases of continuous CR injection, a steady-state approximation ($\frac{\partial \psi_i(\boldsymbol{x}, p, t)}{\partial t} \approx 0$) suffices. However, for transient sources like individual SN explosions or emission from PWNe, a time-dependent approach is necessary for an accurate description of CR propagation.

- Convection: the $\boldsymbol{\nabla}(\boldsymbol{V} \psi_i)$ term accounts for convection, which occurs when a moving medium carries CRs away from the Galactic disk, resulting in a wind-like flow. Convection leads to the removal of CRs from the disk and is also responsible for adiabatic energy losses, caused by a non-zero divergence of $\boldsymbol{V}$, where $\boldsymbol{V}$ is the convection velocity vector. Here, we will assume that the convection velocity is orthogonal to the Galactic plane, $\boldsymbol{V}(\boldsymbol{x}) = \mathrm{sign}(z) v_c(z) \boldsymbol{e}_z$, with v_c typically ranging from 5 to 15 km s^{-1} [5]. The sign function sign(z) ensures that the convection is directed away from the Galactic plane, irrespective of the specific z value.

- Energy losses: the term dp/dt represents the rate of momentum loss. The dominant processes of energy losses depend on the CR energy and the species. In particular, energy losses are very different for nuclei and leptons. For $e^{\pm}$ with energies greater than 10 GeV, the most prominent energy losses occur due to synchrotron radiation in the Galactic magnetic field and inverse Compton scattering (ICS) with the CMB and star-light photons. At lower energies bremsstrahlung, ionization of interstellar neutral matter and Coulomb interactions with ISM become important. For further details about energy losses for $e^{\pm}$ see Section A.1 of the Appendix. For nuclei the dominant contributions are ionization and Coulomb interactions.

- Reacceleration: CRs can undergo reacceleration due to the motion of turbulent magnetic fields relative to the Galactic frame. This process, known as diffusive reacceleration, involves diffusion in momentum space, with a diffusion coefficient D_{pp} approximately given by $D_{pp} \sim v_{\mathrm{A}}^2/D_{xx}$, where v_{A} represents the speed of Alfvénic magnetic waves.

- Fragmentation and decay: nuclear CRs can also encounter fragmentation due to the interaction with ISM atoms or decay. These processes are taken into account by the respective fragementation and decay times $\tau_{f,i}$ and $\tau_{r,i}$.

Another effect mentioned before that has to be properly treated is the Solar modulation. The Sun emits a stream of low-energy particles known as the solar wind, consisting of fully ionized plasma traveling at a velocity of approximately 400 km/s. This solar wind acts as a barrier, preventing the penetration of low-energy CRs into the solar neighborhood. The name modulation derives from the activity of the Sun which undergoes a 22-year cycle: after 11 years of the solar cycle, the magnetic field of the Sun reverses its direction. For CRs with R at Earth greater than $10-20$ GV, the effect of solar modulation becomes negligible, and the detected flux primarily represents the interstellar flux. Solar modulation can be described by a Fokker-Planck equation which is adjusted to the solar environment and solar magnetic field. This equation can be numerically solved [125, 126]. A common approach when studying Galactic CRs is to use the so-called force-field approximation [127, 128]. In this approximation, one assumes that the propagation of CRs in the heliosphere is dominated by diffusion and solar winds. Under the further assumption of spherical symmetry and neglecting adiabatic energy losses, one obtains the steady state solution of the Fokker-Planck equation. The modulated CR density at the top of Earth's atmosphere (ψ_{TOA}) is derived from the interstellar flux (ψ_{IS}) using an effective potential (φ, also called Fisk potential) measured

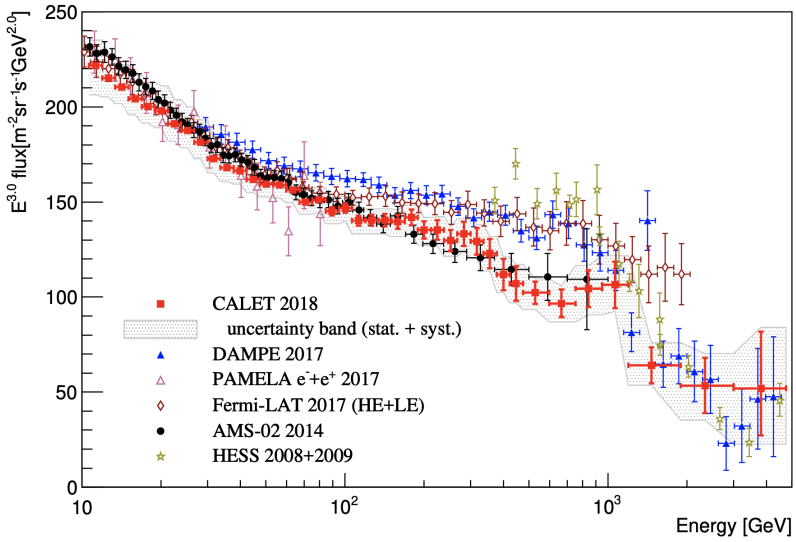

Figure 1.6: CR all-electron flux measured by CALET, AMS-02, Fermi-LAT, H.E.S.S. and DAMPE. Figure taken from Ref. [34].

in gigavolts (GV). It can be expressed as:

$$\psi_{\mathrm{TOA}}(R_{\mathrm{TOA}}) = \left(\frac{R_{\mathrm{TOA}}}{R_{\mathrm{IS}}}\right)^2 \psi_{\mathrm{IS}}(R_{\mathrm{IS}}) \tag{1.7}$$

Here, $R_{\mathrm{TOA}} = R_{\mathrm{IS}} - \varphi$, where R_{IS} is the interstellar rigidity. The force-field approximation describes solar modulation by a single effective parameter φ.

1.5 Experiments for electrons and positrons detection

Since a large part of the discussion will be focused on $e^{\pm}$, we here list the detectors that are currently measuring these particles, from ground-based experiments to balloon and space-born detectors. The most precise data comes from space-born experiments such as AMS-02, which is described below. One significant advantage of these detectors is that they avoid the systematic uncertainties associated with modeling CR interactions with the atmosphere, which affect balloon experiments flying at altitudes of a few tens of kilometers from the ground, and ground-based experiments. Furthermore, space-born experiments have large data-taking period (years) with respect to balloon flights (weeks).

One of the pioneristic space-born experiment was PAMELA (Payload for Antimatter Exploration and Light-nuclei Astrophysics) [129], launched in June 2006 and terminated in 2016. Employing a calorimeter and a magnetic spectrometer, it enabled the identification of the charge of detected CRs and the measurement of various particles,

including p, $\bar{p}$, $e^{\pm}$, light nuclei, and light isotopes, spanning from a few MeV to hundreds of GeV [129]. Notable discoveries from the PAMELA experiment include the observation of an increasing e^{+} fraction for $E > 10$ GeV [130], and precise measurements of $\bar{p}$ fluxes [46], as well as He and p fluxes [45] up to energies of hundreds of GeV/n.

- The Alpha Magnetic Spectrometer (AMS-02) experiment, deployed on the International Space Station in 2011, represents the cutting-edge technology in CR detection [131, 132, 133]. It comprises a highly precise particle spectrometer equipped with an electromagnetic calorimeter, time-of-flight counters, a silicon tracker, transition radiation detectors, and ring-imaging Cherenkov detectors. AMS-02 employs independent strategies to measure the mass, energy, and arrival direction of CRs, spanning from a few GeV up to TeV energies. The unprecedented precision and statistics of AMS-02 data offer a unique tool for testing models of CR propagation and production in our Galaxy.

- The *Fermi* Large Area Telescope (*Fermi*-LAT) is the primary instrument aboard the *Fermi* Gamma-ray Space mission [134]. It serves as a high-energy γ-ray telescope with a wide field of view, covering the energy range from tens of MeV to over 300 GeV. In its 15 years of operation, the *Fermi*-LAT has played a crucial role in studying γ rays reaching Earth. Although its primary purpose is γ-ray observation, the *Fermi*-LAT also acts as a detector for $e^{\pm}$ pairs. However, due to the absence of a magnet for charge separation, the *Fermi*-LAT can only measure the combined flux of incoming $e^{\pm}$ [135]. Attempts to measure separate $e^{\pm}$ fluxes using methods such as the shadow of the Earth and the offset direction caused by the geomagnetic field have resulted in large errors [38].

- The CALorimetric Electron Telescope (CALET) [34] is a space-based instrument installed on the International Space Station. It is optimized for measuring the flux of $e^{\pm}$ in the energy range from a few GeV up to around 20 TeV. Additionally, CALET is capable of measuring the spectra of other CR particles, including p (ranging from 50 GeV to 100 TeV), nuclei such as carbon and iron (ranging from 300 GeV to 100 TeV), and γ rays up to approximately 20 TeV energy.

- The DArk Matter Particle Explorer (DAMPE) [37] is a particle detector designed for studying CRs (p, He and nuclei up to oxygen) and γ rays. DAMPE is specifically optimized for detecting particles with energies ranging from a few GeV up to tens of TeV, with energy resolution of 1.5% at 800 GeV.

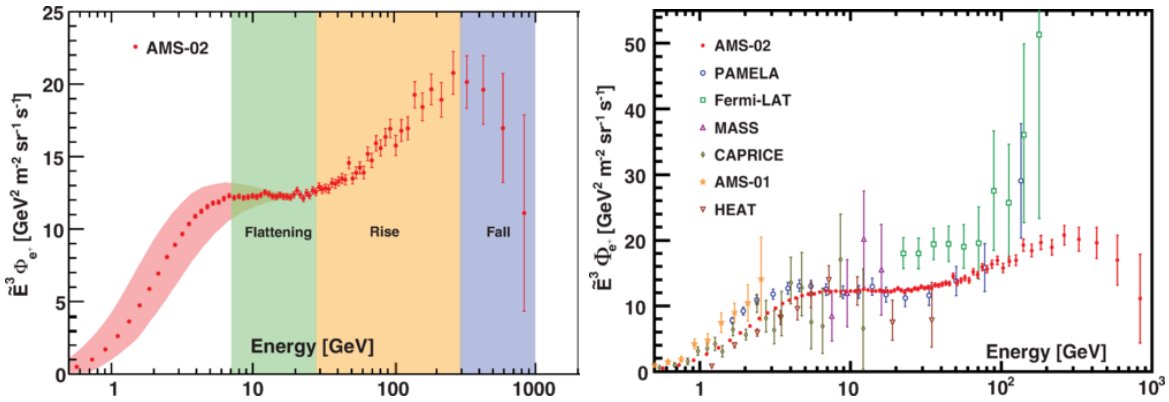

Figure 1.7: Left panel: the AMS-02 e^+ flux scaled by E^3. Right panel: the AMS-02 e^+ flux together with earlier measurements from PAMELA [47], *Fermi*-LAT [38], MASS [139], CAPRICE [140], AMS-01 [141], and HEAT [142]. Figures taken from Ref. [131].

- Ground-based detectors: Imaging Atmospheric Cherenkov Telescopes (IACTs) in the last few years were able to measure the CR $e^{\pm}$ flux indirectly, despite the significant difficulties due to the background from hadronic CRs. The High Energy Stereoscopic System (H.E.S.S.), that consists of IACTs located in Namibia, improved the ability to reject hadrons, providing data on the total $e^+ + e^-$ flux, although with significant systematic uncertainties [136]. Similarly to H.E.S.S. , also the Major Atmospheric Gamma-ray Imaging Cherenkov Telescopes (MAGIC) recently presented preliminary results on the $e^+ + e^-$ flux [137]. MAGIC is a stereoscopic system located in La Palma, Spain, consisting of two IACTs. In the end, Large High-Altitude Air Shower (LHAASO) experiment was able to provide preliminary upper limits on the $e^+ + e^-$ flux up to $E \sim 5 \times 10^5$ GeV [138]. The LHAASO experiment is a ground-based extended air shower observatory with a hybrid technique. With its wide aperture and its almost 100% duty cycle, LHAASO may be able to extend the $e^+ + e^-$ spectrum further in energy.

In Figure 1.6 are reported the measurements of the $e^+ + e^-$ flux of various experiments. It can be noticed that CALET and AMS-02, employing different detection principles (calorimeter versus magnetic spectrometer), exhibit agreement in identifying $e^{\pm}$ up to 1 TeV. However, in the energy range of 300 GeV to 1 TeV, the fluxes of AMS-02 and CALET display softer behavior and lower values compared to the measurements from DAMPE and *Fermi*-LAT. Nevertheless, all measurements between different experiments are compatible at 1σ for energies below 70 GeV. These observed discrepancies between the different experiments suggest the presence of unidentified systematic effects. Another interesting topic whose interpretation is still debated today is the so-called e^+ excess (see Figure 1.7). Hinted by the rise of the e^+ fraction detected by

PAMELA for $E > 10$ GeV [130], then confirmed by the AMS-02 data [131], the e^+ excess is the result of the discrepancy between the measurements of the e^+ flux and the predictions for the secondary production of e^+. In the GeV energy range, the flux of cosmic e^+ particles is primarily dominated by secondaries (see Chapter 4). However, above a few GeV, the data (see, e.g., [131]) exceed the predictions for secondary production. The intepretation of this excess will be one of the main focus of this thesis.

Chapter 2

Cosmic gamma-ray radiation

The γ-ray radiation is commonly referred to as electromagnetic radiation with energy above approximately 100 keV. The observation of γ rays is of fundamental importance in understanding the origin of CRs (see Chapters 6 and 7). Additionally, the joint observation of astrophysical phenomena using different cosmic messengers, including CRs, neutrinos, gravitational waves, and γ rays, plays a crucial role in enhancing our knowledge about CR sources and their environments, thereby enabling multi-messenger approaches in CR physics. In this Chapter, we provide an overview of γ-ray radiation of cosmic origin observed on Earth in the high-energy range, spanning from a few MeV to TeV energies.

2.1 Production mechanism of gamma rays in astrophysical environments

Since photons cannot be directly accelerated, to produce γ rays of pure astrophysical origin it is necessary a population of accelerated charged particles, that then produce γ rays through different mechanisms. This highlights the intrinsic link between the study of γ rays and the origin and acceleration of CRs in our Galaxy. The emission of γ rays is classified as either leptonic or hadronic, depending on whether the parent CR population consists of leptons or hadrons, respectively. Leptonic γ rays provide information about the cosmic e^- density and the radiation fields, while hadronic γ rays trace the CR hadrons and the densities of target gases.

2.1.1 Leptonic gamma rays

In various astrophysical sources within our Galaxy, such as pulsars, PWNe, SNRs, and active galactic nuclei (AGN) in other galaxies, ultra-relativistic e^- can be accelerated to high Lorentz factors of approximately 10^{8-9}. These accelerated e^- produce photons through processes like ICS, synchrotron emission, and synchrotron self-Compton processes.

- ICS occurs when energetic $e^{\pm}$ interact with low-energy ambient photons:

$$e^{\pm}\gamma \rightarrow e^{\pm}\gamma'. \tag{2.1}$$

  The behavior of this process depends on the energy of the photon, and it can be accurately described by the Thompson regime ($E_\gamma \ll m_e c^2$) or the Klein-Nishina regime ($E_\gamma \gg m_e c^2$) (see [143, 144] and the Appendix A.1). Details regarding our modeling of ICS emission from a CR $e^{\pm}$ distribution can be found in Chapter 6.

- Synchrotron photons are emitted by relativistic charged particles undergoing acceleration in magnetic fields. The power loss due to synchrotron radiation is more significant for e^- than for hadrons, since it is proportional to $\propto (Zme/M)^4$ [143]. Therefore, this process is typically associated with lepton acceleration. The typical energy of synchrotron photons produced by a population of e^- at TeV energies, for typical values of the ambient magnetic field B of a few μG, is a fraction of eV, which is not within the γ-ray energy range. However, the synchrotron self-Compton process is important for γ-ray emission: in this process, photons produced through synchrotron emission by relativistic leptons can interact with the parent leptons, resulting in their up-scattering through ICS. This can energize the synchrotron photons to the γ-ray regime. The parameterization of synchrotron emission from a distribution of relativistic e^- is described in detail in Chapter 6.

- Bremsstrahlung emission occurs when e^- are accelerated in the electrostatic fields of ions and atoms, such as in the interstellar gas [143], producing photons in the γ-ray energy range:

$$e^{\pm} + \mathrm{H(He)}_{\mathrm{ISM}} \rightarrow e^{\pm} + \mathrm{H(He)}_{\mathrm{ISM}}\gamma'. \tag{2.2}$$

2.1.2 Hadronic gamma rays

γ rays can also be generated through interactions involving p and/or heavier nuclei, with the main processes being hadro-production and photo-production.

- Hadron-nucleon collisions involve the collision of a p/nuclei with a nucleon target, resulting in a cascade of hadronic particles. In this cascade, π^0 mesons are produced, that decay into γ rays carrying approximately half of the π^0 energy [144]:

$$p(\mathrm{He})_{CR} + \mathrm{H(He)}_{\mathrm{ISM}} \rightarrow X + \gamma. \tag{2.3}$$

  This type of emission will be the primary focus of Section 3.3.

- Photo-production of γ rays occurs in interactions between protons and a sea of photons. It happens in environments where there is a high density of target photons [145]. The main process involves the production of a Δ^+ resonance, with the produced π^0 mesons that decay into γ rays:

$$p + \gamma \rightarrow \Delta^+ \rightarrow \pi^0 + p. \tag{2.4}$$

Hadronic production of γ rays is always accompanied by the production of neutrinos in the subsequent decay of charged pions and muons. Therefore, the simultaneous detection of γ rays and neutrinos from a particular source is considered a signature of hadro-production [146], indicating the acceleration of hadrons. Recently, this correlation has been observed for the first time, with the detection of γ rays and neutrinos at PeV energies originating from the active nuclei of a galaxy [147]. Additionally, evidence of an excess of neutrinos associated with the nearby active galaxy NGC 1068 [148] and with the Galactic plane [149] have been reported.

2.2 Cosmic gamma rays: current detectors

The field of γ-ray astronomy began through space-based experiments, as Earth's atmosphere is opaque to high-energy photons. The γ-ray spectrum spans 7 decades in energy and approximately 14 decades in flux, exhibiting a rapid decrease towards higher energies [39]. Consequently, the effective area of the detector needs to increase as the energy of the γ rays increases. Direct detection of γ rays exceeding the TeV becomes impractical for space-based detectors, necessitating the use of indirect ground-based methods, that observe the electromagnetic cascades generated by γ rays interacting with Earth's atmosphere.

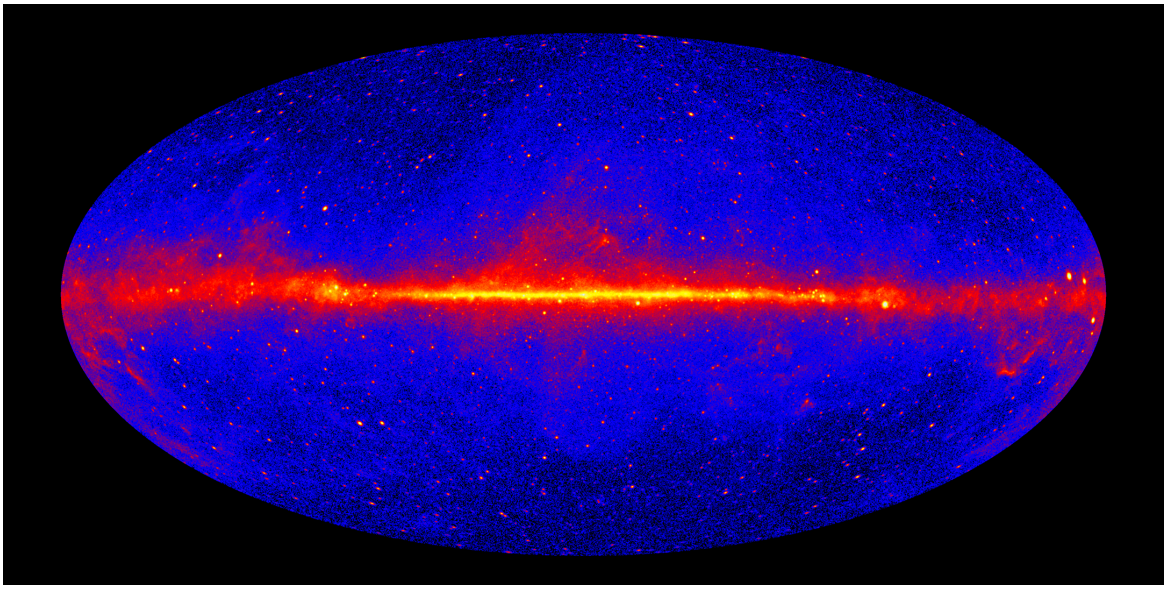

Figure 2.1: This image shows the entire sky as seen by *Fermi*'s Large Area Telescope. The most prominent feature is the bright, diffuse glow running along the middle of the map, which marks the central plane of our Milky Way Galaxy. The γ rays there are mostly produced by the interaction of CRs with interstellar gas and radiation fields. Many of the bright features above and below the Milky Way plane are distant galaxies, while the ones along the plane are pulsars. The image was constructed from 12 years of observations of γ rays with energies greater than 1 GeV. The figure is taken from https://svs.gsfc.nasa.gov/14090.

Space-based detectors are now able to measure γ rays within the energy range of approximately 300 keV to several hundred GeV [150, 151]. The *Fermi*-LAT represents the state of the art in satellite-based γ-ray experiments [134], as introduced in the previous Chapter. Over the past 15 years, the *Fermi*-LAT experiment has revolutionized γ-ray astronomy by providing data of unprecedented precision, detecting approximately 6500 γ-ray sources across the entire sky, covering an energy range from 100 MeV to around 1 TeV [152, 153, 154]. In Figure 2.1 it is shown the entire sky as seen by *Fermi*-LAT. The image was constructed from 12 years of observations of γ rays with energies larger than 1 GeV. The figure is taken from https://svs.gsfc.nasa.gov/14090.

The CALET mission, presented in Section 1.2, recently reported the observation of γ rays spanning from 1 GeV to 10 TeV and so overlapping with the *Fermi*-LAT energy range. The collaboration provided an analysis of the properties of Galactic diffuse γ rays as well as the spectra of 23 prominent Galactic point sources [155]. Similarly to CALET, the DAMPE experiment has also recently released new results concerning γ rays, reporting the detection of over 300,000 photons ranging from 2 GeV up to 10 TeV. Leveraging this dataset, DAMPE has successfully detected and analyzed a total of 248

γ-ray sources [156]. Over the next few years, both CALET and DAMPE will provide measurements within the same energy range as *Fermi*-LAT and beyond, allowing a direct comparisons between different experiments.
The detection of cosmic γ-ray sources using ground-based experiments is relatively recent, beginning in 1989 with the first observation of the Crab Nebula by the Whipple telescope [157]. Ground-based experiments use their larger collective area to extend the energy range up to the PeV scale. These experiments utilize the Earth's atmosphere as a calorimeter and employ different techniques to distinguish between air showers produced by CRs and very-high-energy γ rays [151]. Two detection techniques of air showers are adopted to observe energetic γ rays: IACTs, which detect the optical Cherenkov light produced by shower particles in the atmosphere, and Water Cherenkov Detectors, which directly detect the shower particles using the Cherenkov light produced in water detectors on the ground. The current IACTs include MAGIC [158], Very Energetic Radiation Imaging Telescope Array System (VERITAS) [159], H.E.S.S. [160], and the upcoming Cerenkov Telescope Array (CTA) [161]. The water Cherenkov technique is currently employed by the High Altitude Water Cherenkov Experiment (HAWC) γ-ray observatory [162] and LHAASO [163, 164], and previously by the Milagro Gamma-ray Observatory [165].

2.3 The gamma-ray sky

γ rays are generated by a wide variety of astrophysical sources, unveiling non-thermal processes and cosmic particle accelerators. The observed γ-ray sources that have been cataloged and detected thus far are referred to as resolved sources, while faint sources that cannot be individually identified are unresolved sources. The all-sky γ-ray emission, such as the *Fermi*-LAT counts map shown in Figure 2.1, is typically divided into three main components:

- Resolved sources: these are individual sources of γ rays, both from our Galaxy and of extragalactic origin, such as SNRs, blazars, and others (see 2.3.1).
- Galactic diffuse emission: the bright emission observed along the Galactic plane corresponds to the Galactic diffuse emission or background. It originates from the interaction of CRs with interstellar gas and radiation fields within our own Galaxy, as described in Section 2.3.2. This component is the primary contributor to the observed γ-ray emission above 100 MeV [166].
- Isotropic γ-ray background (IGRB): the IGRB represents the remaining measured

γ-ray emission after subtracting the contributions from the Galactic diffuse emission and resolved sources [167]. On large angular scales, this component appears approximately isotropic and is usually attributed to the collective contribution from unresolved sources, including extragalactic ones. Interestingly, more exotic processes like dark matter annihilation/decay, originating from both Galactic and cosmological distances, can also be embedded within the IGRB, see Section 2.3.3 and [168, 169, 170, 171].

The Extragalactic γ-ray background (EGB) includes the total emission from resolved sources combined with the IGRB, representing the superposition of all γ-ray sources (both individual and diffuse) spanning from the edge of the Milky Way to the edge of the observable universe. The EGB has been observed by the LAT in the energy range of 100 MeV to 820 GeV with unprecedented precision [39].

2.3.1 Resolved sources of gamma rays

The *Fermi*-LAT Fourth Source Catalog (4FGL) [152, 153, 154], compiled by the *Fermi*-LAT collaboration, presents information on characteristics, including sky positions, energy spectra, and integral γ-ray fluxes, of resolved steady sources in the γ-ray sky. Figure 2.2 displays a sky map with the positions of all 5064 4FGL sources as reported in Ref. [152], which has been extended to 6658 sources in Ref. [154]. The sources are categorized based on their class and further distinguished as associated or identified. Associations are primarily determined by close positional correspondence with known sources, while identifications require the detection of correlated emissions at other wavelengths [152]. Galactic γ-ray sources, such as pulsars, PWNe, and SNRs, are predominantly concentrated within the Galactic plane, with a few exceptions, while the majority of high-latitude sources originate from extragalactic origins.

Galactic gamma-ray sources: Pulsars, PWNe, SNRs, Star clusters

Pulsars were observed to emit γ-ray pulses in the early 1970s [172]. The observed pulses with short durations and stable frequencies are explained as rotating beams of light that point towards the Earth with a frequency of $f = 1/P$, where P is the star's rotation period [173]. Only dense stars like neutron stars can rotate fast enough to match the observed frequencies. The third *Fermi*-LAT pulsar catalog contains 294 pulsar found in GeV energy range of 12 years of LAT data [174]. PWNe have been discussed in Section 1.3.2. The PWN emits radiation via ICS of $e^{\pm}$ on the local radiation fields.

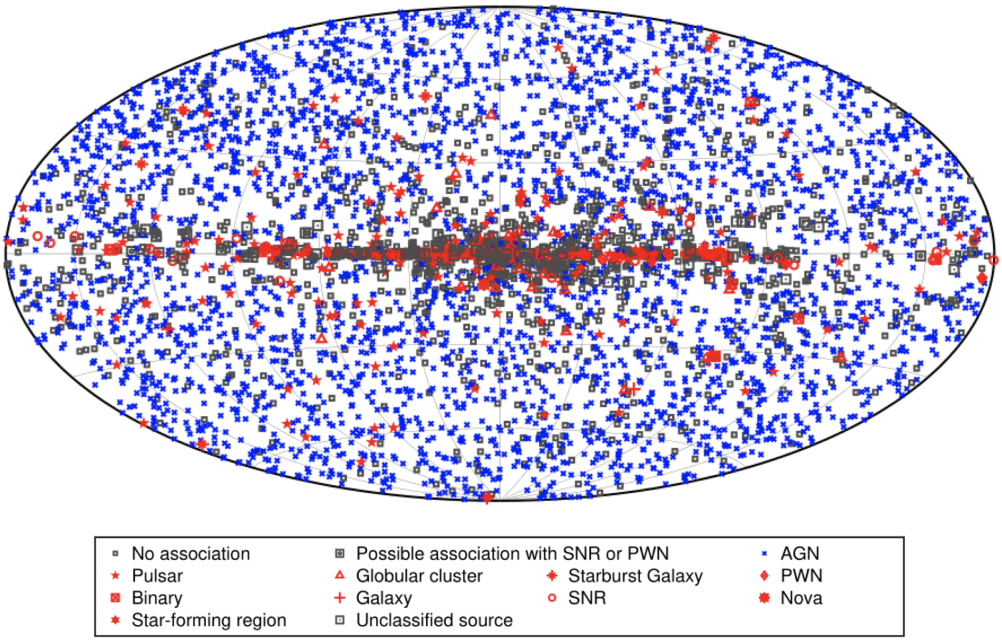

Figure 2.2: *Fermi*-LAT full sky map showing sources by source class. All AGN classes are plotted with the same blue symbol for simplicity. Other associations to a well-defined class are plotted in red. Unassociated sources and sources associated to counterparts of unknown nature are plotted in black. Figure taken from [152].

Another type of steady sources recently discovered and connected to pulsars are pulsar halos. Section 2.4 is focused on the presentation of these objects.

SNRs have been discussed in Section 1.3.1. SNRs are the most numerous detected Galactic γ-ray sources [175]. The origin of γ rays in SNRs can be attributed to either leptonic or hadronic processes, and in some cases, a combination of both, to explain the observed spectra [150, 176, 177, 178]. Determining which scenario dominates in a given case is often challenging and inconclusive. An example highlighting this ambiguity is the source RX J1713.7-3946, initially identified as a high-energy γ-ray emitter when detected in the TeV energy range by the H.E.S.S. collaboration [179]. As demonstrated in Ref. [180], both hadronic and leptonic scenarios could explain the observed H.E.S.S. data. Subsequent data from *Fermi*-LAT, however, favored leptonic models, suggesting that RX J1713.7-3946, RCW 86,Vela Jr. and SN 1006 are not efficient hadron accelerators [181, 182, 183, 184, 185]. Conversely, Ref. [186] later identified Tycho's SNR as a strong candidate for hadronic γ-ray emission based on VERITAS and *Fermi*-LAT data. Also IC443 and W44 confirmed the hadronic nature of γ-ray emissions from these SNRs interacting with molecular clouds [187]. These findings raise questions about the prevalence of hadronic emission from SNRs as the primary accelerators of Galactic CRs. Ideally, to determine the hadronic/leptonic nature of a

source, multi-wavelength measurements would be necessary for all γ-ray bright SNRs under consideration. However, this approach is time-consuming and often inconclusive due to limited constraints on the age and distance of these sources.
Recent measurements of γ-ray emission from regions surrounding compact star clusters, such as Cygnus cocoon [103, 104, 105] and 30 Doradus in the Large Magellanic Cloud [106], support the notion that a significant fraction of the wind kinetic energy is converted into non-thermal particles, reaching maximum energies above 100 TeV. The recent measurement of the spectrum and spatial distribution of γ-ray emission from the Cygnus cocoon [105] provides a unique opportunity to test our understanding of particle acceleration in the vicinity of star clusters.

Extragalactic gamma-ray sources: active galactic nuclei and star forming galaxies

AGN [188] in external galaxies are considered the most powerful sources of non-thermal radiation known in astrophysics and exhibit the highest levels of electromagnetic luminosity, reaching approximately 10^{48} erg/s. The emitting region of AGN, in most electromagnetic bands, is relatively small, spanning a mpc scale [189]. As mass accretes onto the supermassive black hole, an accretion disk forms, converting a portion of the gravitational energy into electromagnetic emission. Magnetic fields near the black hole launch collimated jets of relativistic particles, extracting energy from either the spinning black hole or the accretion disk. The resulting electromagnetic emission arises from various processes, covering a wide range from radio to high-energy γ-ray photons.
The same mechanism that causes diffuse emission in the Milky Way is expected to generate γ rays in other star-forming galaxies. These galaxies, though intrinsically faint, are abundant and expected to contribute significantly to the observed γ-ray flux [190]. To date, only a few galaxies of this nature have been detected in γ rays, including M31 and M33 [191].

2.3.2 Gamma-ray emission from Galactic cosmic rays

The γ-ray emission coming from our Galaxy is peaked around the GeV range where, for the model adopted by *Fermi*-LAT collaboration, constitutes 80% of the total observed γ rays [192]. In order to properly model the spectrum and morphology of the Galactic diffuse γ-ray emission, all these key ingridients are necessary: models for CR sources, their injection spectra, and CR propagation; a good knowledge of the Galactic magnetic field, of the production cross section of γ rays in hadronic interactions, of the interstellar

gas distribution (important for the hadronic emission and bremsstrahlung) and the structure of radiation fields in our Galaxy (for the leptonic emission). In the next two Sections we will focus on these last two components.

Galactic interstellar medium

The ISM constitutes approximately $10-15\%$ of the total mass of the Galactic disk and consists of gas and a small fraction $(0.5-1\%)$ of dust [193]. Hydrogen dominates the gas component, and depending on its temperature, three forms are recognized: atomic (HI), molecular (H_2), and ionized (HII) hydrogen [194]. Overall, HI accounts for the majority of mass, constituting approximately 60%, while H2 and HII contribute 25% and 15% of the interstellar gas mass, respectively. The interstellar gas also includes He, with a number density ratio of around $\sim 1/10$ with respect to hydrogen, although He remains primarily neutral due to its higher ionization potential. Heavier elements make up a negligible fraction of the total gas mass.
The distribution of gas in the Milky Way aligns with its complex structure. Being a spiral galaxy, the Milky Way likely possesses a bar-like central structure [195]. Observations of line emission and absorption data [196, 197, 198] reveal that atomic gas extends up to $20-30$ kpc from the Galactic center. When considering a 2D distribution with cylindrical symmetry, the gas surface density increases with distance from the Galactic center, ranging from $1.9\,M_\odot\mathrm{pc}^{-2}$ within 6 kpc to approximately $\sim 4\,M_\odot$ pc^{-2} at $7-12$ kpc, and then decreasing to $\sim 1\,M_\odot\mathrm{pc}^{-2}$ at 17 kpc [194]. Simplified parameterizations of hydrogen distributions can be found in [199] (H2), [200] (HI), and [201] (HII). Actually, the distribution of interstellar gas is related to the complex 3D spatial structure of the Milky Way's spiral arms. A model for the 3D gas distribution in the Milky Way has been recently developed in Ref. [202].

Galactic interstellar radiation fields

The interstellar radiation fields (ISRF) originates from the emission of stars and subsequent scattering, absorption, and re-emission of the absorbed light by dust in the ISM [194]. Interstellar dust absorbs and scatters starlight in the UV and optical bands, re-emitting the absorbed photons in the infrared. Additionally, the CMB contributes to the ISRF with a black body energy distribution characterized by its temperature T_{CMB}. γ rays are produced through ICS by Galactic $e^{\pm}$ interacting with the ISRF. To accurately describe the γ-ray emission resulting from this process, models for the ISRF in our Galaxy are necessary. The spectral and spatial distribution of the ISRF is inferred from models that account for the distribution of stars, absorption, dust emission

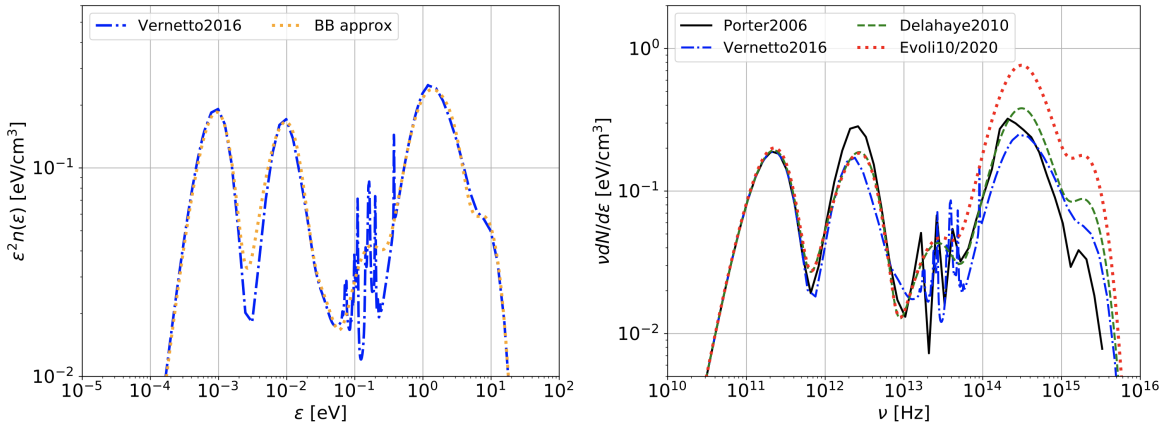

Figure 2.3: Left panel: comparison between the spectrum of the ISRF density $n(\epsilon)$ published in Vernetto2016 [204] (blue dot-dashed line) with the black body approximation (dotted orange line, see the text for the details). Right panel: comparison among the ISRF models Porter2006 [205] (solid black line), Vernetto2016 [204] (blue dot-dashed line), Delahaye2010 [206], (dashed green line) and Evoli10/2020 [207] (dotted red line). Figures taken from [208].

spectra, and emissivities [194]. The GALPROP code represents the state of the art in this field, with numerical models developed to incorporate all these elements [203]. Simpler models, such as Vernetto2016 [204], Porter2006 [205], Delahaye2010 [206], and Evoli10/2020 [207], are also available, providing reasonably accurate ISRF calculations while requiring less computational time compared to numerical models.

In a given region of the Galaxy, the ISRF can be effectively approximated as a superposition of rescaled black body distributions for each component i, as shown in Figure 2.3 (left panel) with dotted orange line. The distribution is given by the equation:

$$n(\epsilon) = N_a \frac{\epsilon^2}{\pi^2} \frac{1}{\exp(\epsilon/T_i) - 1} \tag{2.5}$$

where ϵ represents the energy, N_a is the normalization of the black body spectra, and T_i correspond to the peak temperatures of the CMB, dust component, and stellar light, respectively. The spectral energy distribution of the ISRF as a function of energy is illustrated in the left panel of Figure 2.3, with dashed lines taken from Ref. [204]. The CMB occupies the microwave energy range, while the starlight spans from the infrared and visible light to the high-energy ultraviolet tail above 3 eV. The black-body approximation provides an excellent representation of the ISRF at the different peaks, as well as during the transitions between the three components. The only part of the ISRF spectrum where the black-body approximation falls short is between $0.06 - 0.6$ eV, where the full model includes lines associated with the absorption of starlight

by dust. The right panel of the Figure compares different ISRF models: Porter2006 [205] (solid black line), Vernetto2016 [204] (blue dot-dashed line), Delahaye2010 [206] (dashed green line), and Evoli10/2020 [207] (dotted red line). It is worth noting that all the models are quite similar across the entire frequency range, except for Evoli10/2020 around $10^{14} - 10^{16}$ Hz. This discrepancy is due to the choice made in Ref. [207] to multiply the model initially used in Delahaye2010 by a factor of approximately 2 in this frequency range. This factor was determined by computing the ratio of starlight to dust emission over a scale of about 5 kpc around the Sun. However, the mere doubling of the local density of starlight does not guarantee that multiplying the former photon field's density by a factor of two is sufficient to obtain the correct ISRF.

2.3.3 Isotropic gamma-ray background

The origin of this γ-ray residual represents one of the most mysterious open problems in astrophysics. The IGRB is usually associated to the γ-ray emission from unresolved blazars, misaligned AGN and star forming galaxies [209, 210, 211]. Truly diffuse processes, like ultra-high energy cosmic-ray interactions with the extragalactic background light or intergalactic shocks, are other possible γ-ray emission mechanisms [212].
More exotic processes like DM annihilation/decay, originating from both Galactic and cosmological distances, can also be embedded within the IGRB [168, 169, 170, 171]. The self-annihilation or decay of DM into SM particles, can give rise to γ-ray photons through processes like hadronization, π^0-meson decay, and internal bremsstrahlung. These mechanisms generate a continuous γ-ray spectrum across multiple energy decades, commonly termed as prompt emission. Additionally, highly energetic photons can emerge as secondary γ-ray emissions, resulting from the radiative energy losses of cosmic particles originating from DM annihilations. Furthermore, the possibility of direct annihilation exists, potentially yielding distinct line-like features.
Dwarf spheroidal galaxies within the Milky Way are considered optimal targets for DM Galactic searches due to their dominance by DM and minimal backgrounds arising from CR interactions [213, 214]. Exploration of signals emanating from extragalactic DM structures involves cumulative assessments from galaxy groups [215], anisotropies in the IGRB [216], and cross-correlations of γ-ray signals with various DM tracers, e.g. [217]. Around 12 years ago, an excess of GeV-scale γ rays in the vicinity of the Galactic Center was detected using data from the *Fermi*-LAT [218, 219, 220, 221]. These studies established that the spectrum, angular distribution, and overall intensity of the signal are consistent with the predictions associated with annihilating DM in the form of a thermal relic with a mass of approximately $m_\chi \sim 50$ GeV. Subsequently several groups

reported the evidence that the photons constituting this excess can be explained by a population of astrophysical point sources (such as millisecond pulsars), rather than from annihilating DM [222, 223, 224]. The origin of the Galactic Center excess it still a matter of debate today.
For an extensive overview of indirect dark matter signals in γ-rays, we refer to Ref. [225].

2.3.4 Other gamma-ray emissions

The interaction between ultra high-energy CRs (with energies exceeding 3×10^{19} eV) and CMB leads to the GZK cutoff in the CR spectrum observed on Earth, as shown in Figure 1.1. Subsequent electromagnetic cascades generate observable diffuse γ-ray emissions through processes like pion production and ICS of charged particles in the surrounding photons.
The Sun is a source of γ rays with energies ranging from approximately 100 MeV to 100 GeV, as reported in [226]. These γ rays originate from the interactions of CRs with the outer solar atmosphere and from ICS of CR e^- by solar photons within the heliosphere.
Gamma-ray bursts (GRBs) are brief and intense bursts of γ rays. They come in two varieties: short GRBs, which last a fraction of a second, and long GRBs, which can persist for several seconds or longer. These bursts have energy spectra that are typically centered around a few hundred keV and can extend up to several GeV [227].
In addition to the discussed diffuse emission, there are two expansive, bubble-like structures known as the *Fermi Bubbles*. These structures extend roughly 50 degrees above and below the Galactic center and were discovered emitting γ rays in the range from a few GeV up to several hundred GeV, as documented in Ref. [228]. While these bubbles are believed to have formed due to the injection of high-energy CRs near the Galactic center, there is ongoing debate, particularly regarding whether their origin is leptonic or hadronic, as discussed in Ref. [229].

2.4 Pulsar gamma-ray halos

Another type of steady source discovered in recent years are the so-called pulsar γ-ray halos, which are opening a new window in the study of CRs and will be the main topic of Chapter 6.
In 2007, the Milagro Gamma-ray Observatory published the detection of an extended TeV γ-ray source surrounding the Geminga pulsar [230]. Initially, the source was

interpreted as a TeV PWN associated with Geminga [231]. However, the puzzling $\sim 3^{\circ}$ extension of the source was significantly larger than the bow-shock of the Geminga PWN observed at X-ray wavelengths [232]. A decade later, the HAWC improved the measurements of this γ-ray source always in the TeV, providing greater sensitivity and angular resolution [233]. The detection was reported recently also in the same energy range by H.E.S.S. [234]. These structures in γ-ray emission are commonly referred to as γ-ray pulsar halos, TeV halos, or ICS halos. Throughout this thesis we will use the term pulsar halos to describe them.

Pulsar halos are more likely generated by $e^{\pm}$ that have escaped from the central PWN and are freely diffusing in the ISM, performing ICS with the background photons [235, 236, 237, 238, 239, 240]. Pulsar halos serve as unique probes for investigating CR propagation in specific regions of the Galaxy and can provide indirect information about the progenitor $e^{\pm}$ from a region that is close to the source. In fact, the energy spectrum of the $e^{\pm}$ injected from PWNe into the ISM (referred to as the injection spectrum) should be deduced from the halo spectrum rather than the spectra of PWNe themselves. The injection spectrum can be used to estimate the acceleration limit of PWNe [241].

2.4.1 Observed pulsar halos

Currently, approximately ten γ-ray sources are suggested to be pulsar halos or potential candidates for pulsar halos [242]. Among these sources, three have been extensively studied as pulsar halos: the Geminga halo, the Monogem halo and LHAASO J0621+3755.

- The Geminga halo: considered the prototypical example of this class, it is the brightest pulsar halo. Geminga is a highly luminous γ-ray pulsar [243] located in close proximity to Earth. It has garnered significant attention from the CR community, as it is a likely contributor to the cosmic e^{+} excess [244].

- The Monogem halo: it is associated with PSR B0656+14, also known as the Monogem pulsar. The Monogem halo was initially reported by HAWC alongside the Geminga halo [233] and is another nearby source. However, it is notably fainter than the Geminga halo.

- LHAASO J0621+3755: it corresponds to the pulsar halo of PSR J0622+3749 and represents the first halo reported by LHAASO [242]. Interestingly, this source may be situated far above the Galactic plane (approximately 300 pc), distinguishing it from other known pulsar halos.

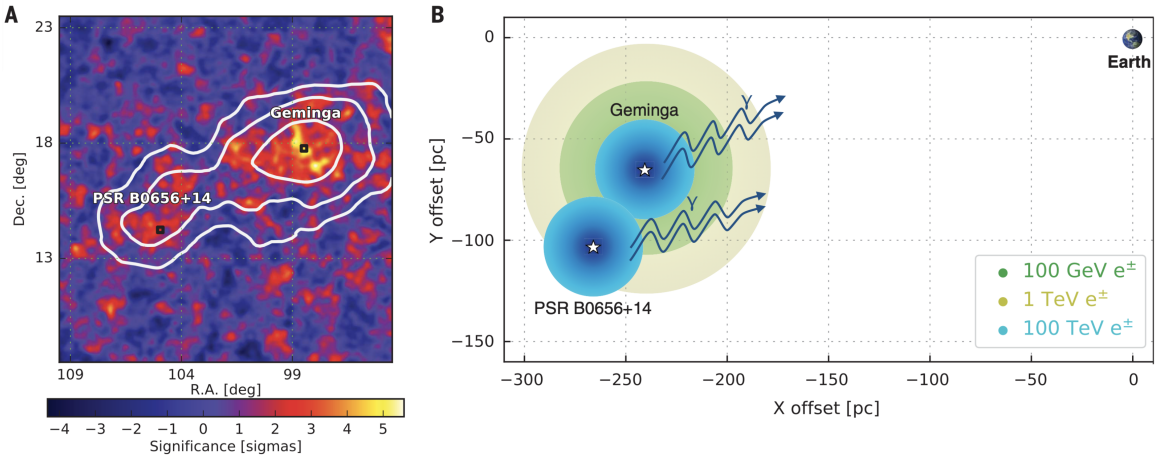

Figure 2.4: Left panel: HAWC significance map (between 1 and 50 TeV) for the region around Geminga and Monogem, convolved with the HAWC point spread function and with contours of 5σ, 7σ, and 10σ for a fit to the diffusion model. Right panel: schematic illustration of the observed region and Earth, shown projected onto the Galactic plane. The colored circles correspond to the diffusion distance of leptons with three different energies from Geminga; for clarity, only the highest energy (blue) is shown for Monogem. Figure taken from Ref. [233].

Additionally, J1831-098 potentially constitutes the pulsar halo of PSR J1831+952. Initially discovered by H.E.S.S and originally considered an old PWN [245], recent findings by Ref. [246] suggest that it could be classified as a pulsar halo. In Figure 2.4, taken from Ref. [233] it is reported the spatial morphology of Geminga and Monogem halos.

2.4.2 Multiwavelength observations

Pulsar halos are spatially extended without clear boundaries. In the following we list other energies apart from TeV in which pulsar halos have been detected or were studied:

- GeV γ-ray observation: pulsar halos are good candidates for *Fermi*-LAT which operates primarily in an all-sky survey mode and scans the entire sky every three hours. Authors of [238] have analysed the *Fermi*-LAT data around Geminga and Monogem, claiming significant detection from Geminga. The proper motion of the pulsar was considered when making the template, and it was pointed out that the interstellar emission may affect the conclusion of detection significantly. On the other hand, no significant GeV emission is found around Monogem. Null detection of a GeV halo around PSR J0622+3749 has also been reported [242].

- X-ray Observation: $e^{\pm}$ pairs that are responsible for 10 TeV γ-ray emission via the

ICS off ISRF will inevitably radiate X-ray photons via the synchrotron radiation in the interstellar magnetic field. Therefore, the pulsar halo's fluxes at 10 TeV and 1 keV are supposed to be comparable. Authors of [247] analysed the data of X-ray satellites Chandra and XMM-Newton on Geminga, without putting constraints on the nature of the pulsar halo. These two X-ray instruments have fields of view quite limited (order of 10' × 10') and when they point to Geminga, they can only observe the very central region of the pulsar halo, without being able to separate the emission of the pulsar halo from the background. Authors of [248] analysed the data on Geminga and other potential pulsar halos of the X-ray satellite eROSITA [249], characterized by a wider field of view with respect to Chandra and XMM-Newton. Also in this case, no degree-wide diffuse halo-like emission was detected around the pulsars.

Authors of [250] demonstrated that AMEGO (All-sky Medium Energy Gamma-ray Observatory) [251] and AdEPT (The Advanced Energetic Pair Telescope) [252], that are Astrophysics Probe mission concepts designed to explore the sky in the energy range between $0.2 - 1000$ MeV and $5 - 200$ MeV, respectively, would be ideal for detecting synchrotron halos from middle-age pulsars.

2.4.3 Possible origins of pulsar halos

Among the hypothesis tested to explain the morphology of TeV halos, one of the most popular suggests that the inferred diffusion coefficient in the halos is suppressed with respect to the average CR diffusion coefficient in the Galaxy D_{xx} [235, 236, 237, 238, 239, 240, 233]. D_{xx} should be at least two orders of magnitude smaller than the standard value used in conventional models of Galactic CR propagation [233].
A pulsar halo, because of the enhanced flux and extension, is not expected to form under the average D_{xx} in the Galaxy due to the rapid spread of escaping $e^{\pm}$ from the PWN [235], while a small D_{xx} can accurately fit the γ-ray profile of the Geminga halo. This aspect led to the acceptance in the community of the slow-diffusion scenario, despite ongoing investigations into alternative interpretations. In the following we list several possible theoretical explanations for the suppression of the diffusion, that is still a matter of debate [253, 254]:

- Resonant streaming instability (RSI): one possible interpretation is the self-generated scenario, which has been used to explain the slow-diffusion environment around SNRs [255, 256] and the spatially dependent diffusion of CRs at the Galactic scale [257]. In this scenario, a large density gradient of CRs near the

sources can trigger the RSI [258] leading to the growth of MHD turbulence in the background plasma, on scales spatially resonant with the CR Larmor radius. The enhanced MHD turbulence suppress the diffusion coefficient. Numerical calculations considering one-dimensional (1D) diffusion without accounting for the pulsar motion indicate that D_{xx} can be suppressed to the required level through RSI, in particular for Geminga [259, 260, 261]. However, measurements of the proper motion of Geminga suggest that the pulsar has traveled a significant distance from its birthplace, implying that the contribution of early released $e^{\pm}$ pairs to the formation of the slow-diffusion zone at Geminga's current position is negligible [262, 260]. Moreover, the 1D diffusion model may transition to a 3D mode, as implied by the symmetry of the Geminga halo [263]. Recent studies by [263] and [261] have highlighted the limitations of RSI growth in the 3D mode, where the injected $e^{\pm}$ are diluted compared to the 1D case.

- Non-resonant streaming instability (NRSI): another proposal of the self-generated scenario involves turbulent growth through the NRSI [264]. The instability is dubbed non-resonant because the wavelength of the fastest growing mode is shorter than the CR gyroradius. While the growth rate of NRSI may be higher than RSI [263], it is proportional to the total CR current, which is typically zero for symmetric production of $e^{\pm}$ pairs. Nonetheless, there are indications from PIC simulations that e^{+} and e^{-} may exhibit asymmetries during acceleration or escape processes, potentially generating a net current that excites the lepton NRSI [265, 266]. Quantitative calculations are still necessary to further test this interpretation.

- External turbulence: stellar feedback, such as SN explosions or stellar winds, is considered a significant source of turbulence in the ISM [267]. For pulsars, their parent SNRs could be direct sources of turbulence. When the plasma streams through the shock front of an SNR, part of its kinetic energy is converted into turbulence and thermal energy behind the shock [68, 69], producing a highly turbulent region in the downstream [268]. The diffusion coefficient downstream of the SNR shock could be significantly suppressed if a small fraction $(1 - 10\%)$ [260] of the initial SNR energy is converted into MHD turbulence. Therefore, if pulsars remain within their associated SNRs, a slow-diffusion environment can be explained. For Geminga, its parent SNR has not been detected, possibly due to its old age. The proper motion measurements indicate that Geminga is approximately 70 pc away from the SNR center, suggesting that the pulsar might still be downstream of the SNR shock [260]. As for other known pulsar

halos, Monogem is likely located within its parent SNR, observable in X-rays [269], while the SNR associated with PSR J0622+3749 has not been detected. Searching for evidence of these associated SNRs is an important aspect of this interpretation. Alternatively, a slow-diffusion environment could exist also in the turbulent medium upstream of the SNR shock [256]. Unlike $e^{\pm}$ pairs discussed in the previous point, CR nuclei could effectively induce the NRSI, and the resulting slow-diffusion zone may persist for a long time due to the large growth rate of NRSI [263].

In general the suppression of the diffusion coefficient in the source region may pose challenges for the detection of multi-TeV e^{-}, which have been observed up to 20 TeV (see Figure 1.6). If such a strong suppression is a common characteristic of CR sources, not only pulsars but also SNRs, the ability of multi-TeV e^{-} to escape the small-diffusion region becomes questionable. It raises concerns about whether these e^{-} can retain any energy or if they lose it entirely within that region. This depends on the size of the area with reduced diffusion compared to the diffusion length of multi-TeV particles (see Section A.1 of the Appendix).

Other possible interpretations of pulsar halos without assuming anomalously slow diffusion are still investigated. One of these is the so-called anisotropic diffusion. In the case of Alfvénic turbulence, CRs are expected to mainly propagate along the mean magnetic field lines, while diffusing perpendicularly to the field with a significantly smaller diffusion coefficient [270]. The propagation of CRs in this scenario is anisotropic, which may appear inconsistent with the observed symmetry of pulsar halos. However, authors of [254] pointed out that if the local interstellar magnetic field near the Geminga pulsar is aligned with our line of sight, the morphology of the pulsar halo can be explained by inefficient perpendicular diffusion. This model does not require strong MHD turbulence sources as discussed in previous points, but relies on stringent requirements for the inclination angle (ϕ_{incl}) between the line of sight and the magnetic field direction within the pulsar's environment. Calculations by [271] indicate that to consistently reproduce the symmetry and extension of the Geminga halo, the allowed range for ϕ_{incl} is extremely small. Consequently, the likelihood of finding multiple Geminga-type halos is extremely low, a scenario that can be tested by future experiments.

In Chapter 6 we will propose another mechanism that could explain pulsar halos without relying on a suppressed diffusion coefficient.

Part II

Results

Chapter 3

Production cross sections of electrons, positrons and gamma rays for astroparticle physics

To understand the processes responsible for the production of CRs, their propagation, and the data we measure, it is necessary to combine physics at extremely different scales, ranging from interactions ruled by fundamental particle physics to propagation on Galactic scales. In this Chapter we discuss the production cross sections of $e^{\pm}$ and γ rays in hadronic collisions, that enter in the computation of the secondary $e^{\pm}$ fluxes and of the Galactic diffuse emission respectively. Our results dramatically reduce the uncertainties on these quantities, pointing out which measurements are further required to improve the models here presented. With these results, we emphasize the importance of measurements provided by collider experiments and accelerators in understanding the origin of CRs in our Galaxy. This Chapter is based on Refs. [3, 4].

3.1 From cross sections to the source term

The secondary source term of a CR species a that enters in the propagation Equation 1.6, is the sum of all the possible combinations of the i-th CR species that interacts with the j-th ISM components as:

$$q(\vec{x}, T_a) \;=\; \sum_{i,j} 4\pi\, n_{\mathrm{ISM},j}(\vec{x}) \int dT_i\, \phi_i(\vec{x}, T_i) \frac{d\sigma_{ij}}{dT_a}(T_i, T_a)\,, \tag{3.1}$$

where T_a is the kinetic energy of the particle a, ϕ_i is the CR flux of the species i at the

kinetic energy T_i, $n_{\mathrm{ISM},j}$ is the number density of the ISM j-th atom, and $d\sigma_{ij}/dT_a$ is the energy-differential production cross section for the reaction $i + j \to a + X$. The factor 4π corresponds to the angular integration of the isotropic CR flux. In general, the source term depends on the position in the Galaxy because both the CR gas density and the CR flux are a function of the position $\vec{x}$. Solving the propagation equation the CRs flux of a given species is obtained.

On the other hand for γ rays, the flux detected at Earth ϕ_γ is given by the line of sight (l.o.s.) integral of the γ-ray emissivity $\epsilon^{i,j}$, summed over all interactions of CR species i and ISM components j:

$$\frac{d^2\phi_\gamma}{d\Omega dE_\gamma}(E_\gamma, l, b) = \sum_{ij} \int_{\text{l.o.s.}} ds \;\; \epsilon^{ij}\Big(\vec{x}(s, l, b), E_\gamma\Big) \,. \tag{3.2}$$

Here s is the distance along the l.o.s. while l and b are the Galactic longitude and latitude. The γ-ray flux is differential in γ-ray energy, E_γ, and solid angle, Ω. The emissivity at each location in the Galaxy $\epsilon^{ij}(\vec{x}, E_\gamma)$ for the reaction $i + j \to \gamma + X$ is the equivalent of the i, j term of the sum in Equation 3.1, divided by 4π and applied to γ rays instead of the particle a.

The dominant production of secondary $e^\pm$ and γ rays, main focus of this Chapter, comes from the proton-proton $(p + p)$ channel, namely CR p interacting on ISM hydrogen atoms. Other relevant contributions involve He projectile or ISM target atoms (He+p, p+He, and He+He). Following the analysis performed for secondary $\bar{p}$ in Ref. [91], for which the calculation involves the same CRs and ISM atoms, channels involving heavier CR species and atoms can contribute at the few percent level to secondary $e^\pm$ and γ rays.

Secondary $e^\pm$ and γ rays are not produced directly in the $p + p$ (or nuclei) collisions but rather by the decay of intermediate mesons and hadrons. Focusing on e^+, but it applies similarly to other cases, we provide now the calculations to find the source term starting from the production cross sections of π^+, since it gives a contribution of about $80 - 90\%$ to the final e^+ yield. After production, π^+ first decay into muons with a branching ratio of 99.99%, and then the muons decay into e^+. The e^+ production cross section is calculated from the π^+ production cross section as follow:

$$\frac{d\sigma_{ij}}{dT_{e^+}}(T_i, T_{e^+}) = \int dT_{\pi^+} \, \frac{d\sigma_{ij}}{dT_{\pi^+}}(T_i, T_{\pi^+}) \; P(T_{\pi^+}, T_{e^+}) \,, \tag{3.3}$$

where T_{π^+} is the kinetic energy of the π^+ that decays into a e^+ with kinetic energy T_{e^+}. $P(T_{\pi^+}, T_{e^+})$ is the probability density function of the process. The π^+ production

cross section cannot be derived directly from quantum field theory. It rather has to be modeled and fitted to experimental data. High-energy experiments provide measurements of the fully differential production cross section usually stated in the Lorentz invariant form:

$$\sigma_{\text{inv}}^{(ij)} = E_{\pi^+} \frac{d^3\sigma_{ij}}{dp_{\pi^+}^3}. \tag{3.4}$$

Here E_{π^+} is the total π^+ energy and p_{π^+} its momentum. The fully differential cross section is a function of three kinematic variables. We choose them to be the center-of-mass (CM) energy $\sqrt{s}$, the π^+ transverse momentum p_T, and the radial scaling x_R. The latter is defined as the π^+ energy divided by the maximal π^+ energy in the CM frame, $x_R = E^*_{\pi^+}/E^{\text{max}\,*}_{\pi^+}$, where the asterisk denotes the CM reference frame.
The energy-differential cross section for π^+ production as required in Equation 3.3 is obtained from σ_{inv} by first transforming the kinetic variables into the fix-target frame, *i.e.* the frame where the ISM target atom is at rest, and then by integrating over the solid angle Ω:

$$\begin{aligned} \frac{d\sigma_{ij}}{dT_{\pi^+}}(T_i, T_{\pi^+}) &= p_{\pi^+} \int d\Omega\, \sigma_{\text{inv}}^{(ij)}(T_i, T_{\pi^+}, \theta) \\ &= 2\pi p_{\pi^+} \int_{-1}^{+1} d\cos\theta\, \sigma_{\text{inv}}^{(ij)}(T_i, T_{\pi^+}, \theta), \end{aligned} \tag{3.5}$$

where θ is the angle between the incident projectile and the produced π^+ in the LAB frame. The derivation of the other channels works in analogy to the π^+ channel.

3.2 Electron and positron cross sections

There are two different strategies to parametrize the $e^\pm$ production cross sections. The first possibility is to find an analytic description of σ_{inv} for the production of intermediate mesons and hadrons that decay into $e^\pm$ performing a fit to cross section data. This strategy was first pursued by Ref. [272] and then repeated with new data by Ref. [273]. The other option is to use predictions from Monte Carlo event generators [274, 275, 276, 277].
Both methods have advantages and drawbacks. Analytic functions permit to calibrate cross sections very precisely on existing data, but they imply large extrapolations in the parameter space where measurements are not available. Moreover, it is hard to use this method on production channels for which data are scarce or not available, as for p+He. Monte Carlo generators can be used to derive the cross sections for all the possible channels of production, but they typically do not fully reproduce the available

measurements which are relevant for CRs at low energies (see, e.g., [278, 279, 280] for $\bar{p}$). In fact, codes like Pythia or QGSJET are mainly tuned to high-energy data, with CM energy of the order of TeV. As outlined in Ref. [281], the adoption of different cross section models [282, 272, 274] produces a variation in the normalization of the secondary $e^{\pm}$ flux up to a factor of 2. Instead, in Ref. [277] the authors have shown that the differences in the source term obtained by using the results in Ref. [274] and different event generators can reach 30% in the relevant energies for $e^{\pm}$ CR physics. However, Ref. [277] does not consider the models from Refs. [282, 272], so the reported uncertainty could be underestimated.

The production cross section of $e^{\pm}$ from Kamae *et al.* [274] are largely used by the community, despite being tuned on at least 20-year old data. The analysis by Ref. [274] carefully checks the total $p+p$ cross sections, but this does not guarantee that their model catches the correct dependence of cross sections from the relevant kinematic variables (e.g. in the transverse momentum and rapidity). The reason is that, until recently, the available dataset was limited to data collected from the sixties to the eighties. In the last decades, however, new experimental datasets have been provided. For example, the NA49 and NA61/SHINE collaborations at the CERN Super Proton Synchrotron (SPS) [283, 284] reported important information for the energies of interest for AMS-02 and covered the interesting kinematic space for astroparticle physics. Moreover, high-energy data at CM-energy $\sqrt{s} > 200$ GeV have been collected from different experiments [285, 286, 287, 288]. These data permit to calibrate precisely the dependence with the $\sqrt{s}$. Given the importance of these data in astroparticle physics, a reevaluation of the leptonic production cross sections is mandatory for $p+p$, He+p, p+He, and He+He collisions.

In Figure 3.1, we show a sketch of all the production channels for e^+ that are considered in our analysis. The channels that produce e^- are the same as in Figure 3.1, but all particles have to be replaced by their antiparticles (e.g. $\pi^+ \to \pi^-$ and $\mu^+ \to \mu^-$). We neglect production or decay channels that contribute less than 0.5% to the total e^+ production. One example is the production of e^+ from the decay of antineutrons ($\bar{n}$), and the same for e^- from neutron (n). This channel is suppressed because in the decay almost all of the energy is carried away by the $\bar{p}$ (p for e^-) and e^+ (e^-) are only produced at very small energies [274].

We first concentrate on the e^+ production cross sections, then we provide parallel results for secondary e^-. The channels and cross sections are very similar, but not identical. In fact, charge conservation implies that the production of e^+ is enhanced with respect to e^- since both the target and the projectiles involved in the production process are positively charged particles.

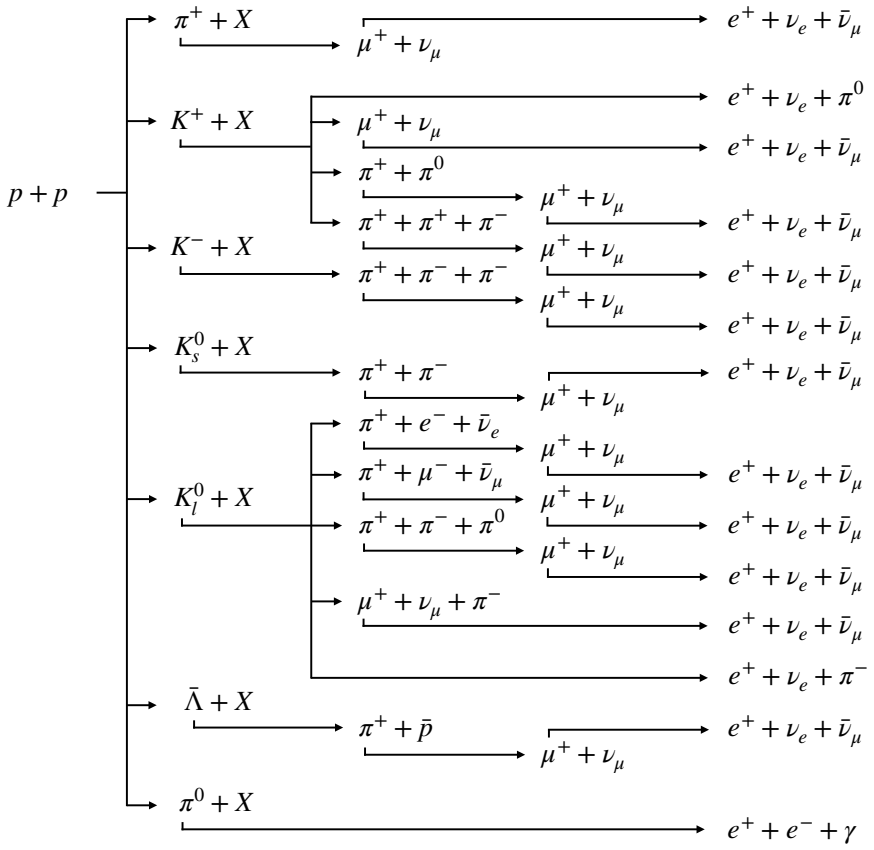

Figure 3.1: This diagram represents the e^+ production channels from a $p + p$ collision considered in our analysis. The same scheme holds for e^- production under charge conjugation (except for the initial $p + p$ state). We report here only the channels that produce at least 0.5% of the total yield (see the main text for further details).

The probability density functions of the decays shown in Figure 3.1 can be computed analitically. In particular, the $\pi^\pm$ decay is entirely modelled from kinematics, namely, in the $\pi^\pm$ rest frame, the energy of the $\mu^\pm$ is determined by energy and momentum conservation. In contrast, the $\mu^\pm$ decay goes into three final states and has to be computed in Fermi theory. The $\mu^\pm$ are fully polarized into their direction of motion after the $\pi^\pm$ decays. We implement the polarized $\mu^\pm$ decay rate including the next to leading order (NLO) corrections [289] for the first time in this field. Please refer to Section IIA of Ref. [3] for the details about how we obtain $P(E_{\pi^\pm}, E_{e^\pm})$.

Table 3.1: Summary of all $p+p$ datasets used for $\pi^{\pm}$ and/or $K^{\pm}$ fits, their CM energies, and references. σ_{inv} is the fully differential production cross section usually stated in the Lorentz invariant form and n is the total multiplicity of a particle. With $\surd$ we indicate when the quantity is considered in the analysis.

Experiment	$\sqrt{s}$ [GeV]		σ_{inv}	n	Ref.
NA49	17.3	$(\pi^{\pm}, K^{\pm})$	$\surd$	-	[283, 292]
ALICE	900	$(\pi^{+}, K^{\pm})$	$\surd$	-	[291]
CMS	900, 2760, 7000, 13000	$(\pi^{\pm}, K^{\pm})$	$\surd$	-	[290, 288]
Antinucci	3.0, 3.5, 4.9, 5.0, 6.1, 6.8	$(\pi^{\pm})$	-	$\surd$	[293]
	2.8, 3.0,3.2, 5.3, 6.1, 6.8	(K^{+})	-	$\surd$	[293]
	4.9, 5.0, 6.1, 6.8	(K^{-})	-	$\surd$	[293]
NA61/SHINE	6.3, 7.7, 8.8, 12.3, 17.3	$(\pi^{\pm}, K^{\pm})$	-	$\surd$	[284]

3.2.1 Positrons from $p + p \to \pi^{+} + X$ collisions

In this Section, we focus on the π^{+} production channel. Many concepts from this Section will be applied analogously to the other channels discussed in Section 3.2.2. The secondary production gives most of its contribution to AMS-02 e^{+} data in the range between 0.5 and 10 GeV. In this energy interval e^{+} are mostly produced from CR p with energies between 5 GeV and 200 GeV, which corresponds to CM energies between 3.6 and 20 GeV. The measurement of π^{+} production in this energy range and with the widest coverage of the kinetic parameter space is provided by the NA49 experiment [283] at $\sqrt{s} = 17.3$ GeV. Therefore, we decided to gauge our modeling of the e^{+} invariant cross section on NA49. To good approximation σ_{inv} is scaling invariant:

$$\sigma_{\text{inv}}(s, x_R, p_T) \approx \sigma_{\text{inv}}(s_0, x_R, p_T). \tag{3.6}$$

However, two ingredients are violating this approximate invariance: first, the rise of the inelastic cross section for $p + p$ collisions and, second, the softening of the p_T shape at large CM energies. Guided by the above considerations, our strategy is as follows: in the first step, we fix the kinematic shape of the π^{+} production cross section using only the NA49 data. In the second step, we combine measurements of the multiplicity at different $\sqrt{s}$ down to 3 GeV, and measurements of the multiplicity and the p_T shape by CMS [290, 288] and ALICE [291] to calibrate our model over a large range of energies. A summary of the included datasets is provided in Table 3.1.

Model for the invariant production cross section

In this Section, we specify the analytical model of the invariant cross section for the inclusive production of π^+ in $p+p$ collisions. We propose a new parametrization of $\sigma_{\rm inv}$ which can fit a large number of datasets of the inclusive production of π^+ in $p+p$ collisions, with $\sqrt{s}$ ranging from few GeV up to LHC energies. As outlined in Ref. [283], the π^+ are produced by a combination of prompt emission, emerging from the hadronization chains, and the decay of hadronic resonances, in particular from ρ and Δ. Inspired by this idea, we write $\sigma_{\rm inv}$ as the sum of two terms, called F_p and F_r, which should roughly follow the prompt and resonance components. The Lorenz invariant cross section is given by:

$$\sigma_{\rm inv} = \sigma_0(s)\, c_1 \left[F_p(s, p_T, x_R) + F_r(p_T, x_R) \right] A(s), \tag{3.7}$$

where $\sigma_0(s)$ is the total inelastic $p+p$ cross section. The derivation of $\sigma_0(s)$ along with its uncertainty is discussed in the Appendix of [3]. The functional form of $F_p(p_T, x_R)$ is partially inspired by the parametrizations from Ref. [294] (and Refs. therein). Specifically, we use:

$$\begin{aligned} F_p(s, p_T, x_R) &= (1-x_R)^{c_2} \exp(-c_3\, x_R)\, p_T^{c_4} \\ &\times \exp\left[-c_5 \sqrt{s/s_0}^{\,c_6} \left(\sqrt{p_T^2 + m_\pi^2} - m_\pi \right)^{c_7 \sqrt{s/s_0}^{\,c_6}} \right], \end{aligned} \tag{3.8}$$

where $\sqrt{s_0} = 17.3$ GeV is the energy of NA49 beam. The model parameters c_i are fitted to the available cross section data, as explained in the following of this Section. On the other hand, the empirical expression for F_r is motivated by the contributions from resonances, as simulated in Ref. [283] (see their Figure 54). The functional form of $F_r(p_T, x_R)$ reads:

$$\begin{aligned} F_r(p_T, x_R) &= (1-x_R)^{c_8} \times \exp\left[-c_9\, p_T - \left(\tfrac{|p_T - c_{10}|}{c_{11}} \right)^{c_{12}} \right] \\ &\times \left[c_{13} \exp(-c_{14}\, p_T^{c_{15}} x_R) + c_{16} \exp\left(- \left(\tfrac{|x_R - c_{17}|}{c_{18}} \right)^{c_{19}} \right) \right]. \end{aligned} \tag{3.9}$$

Finally, we allow for an additional scaling with $\sqrt{s}$, which is required to obtain the correct π^+ multiplicity at different energies. The functional form is given by:

$$A(s) \;=\; \frac{1 + \left(\sqrt{s/c_{20}} \right)^{c_{21}-c_{22}}}{1 + \left(\sqrt{s_0/c_{20}} \right)^{c_{21}-c_{22}}} \left(\sqrt{\frac{s}{s_0}} \right)^{c_{22}}, \tag{3.10}$$

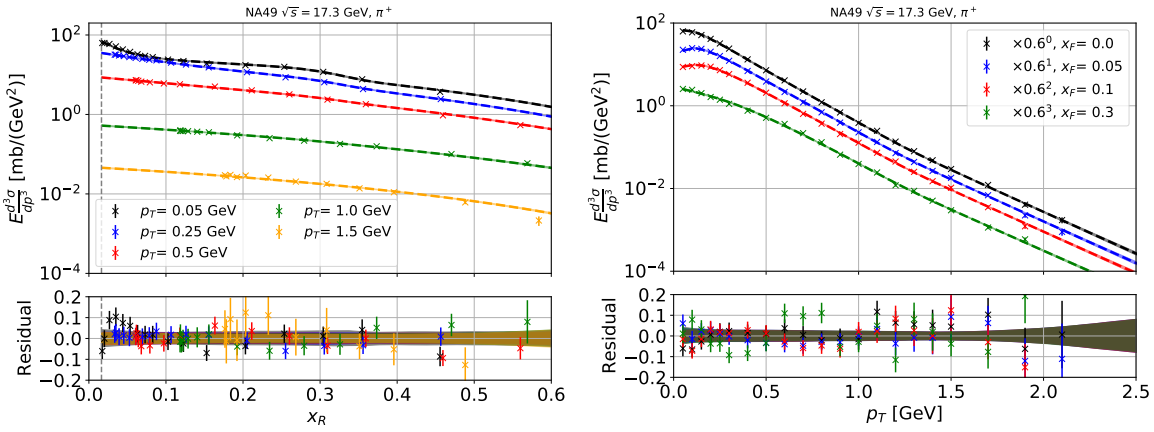

Figure 3.2: Results of the fit on the NA49 data [283] invariant cross section for the inclusive π^+ production in $p+p$ collisions. The left (right) panel shows the NA49 data along with our fit results for representative p_T (x_F) values, as a function of x_R (p_T). Each curve is plotted along with its 1σ uncertainty band. In the bottom part of each panel we plot the residuals, which are defined as (data-model)/model, and the width of the 1σ uncertainty band on the model.

which represents a smoothly broken power law as function of $\sqrt{s}$ with slopes c_{21} and c_{22} above and below the break position at $\sqrt{s} = c_{20}$, respectively. In all the formulas reported in the Section, $p_T, \sqrt{s}$, the mass of the particles, $\sqrt{s_0}$ and energies are intrinsically normalized to 1 GeV, in order to have dimensionless parameters.

Fit of the π^+ production to NA49 data

The NA49 experiment at the CERN SPS performed precise measurements of π^+ inclusive cross sections of $p+p$ interaction. Data are collected at $\sqrt{s} = 17.3$ GeV and over a large range of x_F and p_T, where $x_F = 2p_L/\sqrt{s}$ is the reduced longitudinal momentum. In the first step, we fix the shape of the Lorenz invariant cross section as a function of x_R and p_T at the NA49 CM energy. The parametrizations of Equations 3.8-3.10 contain a few parameters, c_6, c_{20}, c_{21} and c_{22}, that change the behavior of the invariant cross section as function of $\sqrt{s}$. However, the parametrization is chosen such that the cross section at the CM energy of NA49 is independent of those parameters. Hence we can use the NA49 data to fix all the other parameters of our model that do not depend on $\sqrt{s}$. We perform a chi-square (χ^2) fit using the MultiNest package [295], that will be adopted for all other fit of this Chapter, to minimize the χ^2, with statistical and systematic uncertainties added in quadrature. We note that there is also a normalization uncertainty of 1.5%. This normalization uncertainty is not included in the fit but taken into account separately (see below). We use MultiNest with 1000 live points, an enlargement factor of `eft`= 0.7 and a stopping parameter of `tol`= 0.1.

Our results are summarized in Figure 3.2, where we plot the invariant cross section for the inclusive π^+ production in $p+p$ collisions as a function of x_R (left) and p_T (right). The data are displayed along with our best-fit results and the 1σ uncertainty for a few representative values at fixed p_T and x_F, respectively. The residuals of the data and the width of the theoretical uncertainty band are displayed in the bottom panels. The fit converges to a total χ^2_{NA49}=338 with 263 degrees of freedom (d.o.f.). The data are well described at all p_T and x_F values. The structures in the low p_T data are very well followed by our parametric formulae, Equations 3.8 and 3.9.

Finally, we derive the uncertainties on our cross section fit, a major goal of this research. To this end, we extract the covariance matrix and the mean parameter values from the MultiNest fit. The covariance matrix C contains the uncertainties and correlations of all the fit parameters. At this point, we account for the previously neglected normalization uncertainty of the NA49 data. The overall normalization of the cross section is dictated by the c_1 parameter. So, an additional 1.5% uncertainty on the normalization can be accounted by resetting the corresponding diagonal entry of the covariance matrix: $C_{1,1} \to C_{1,1} + 0.015^2\, c_1^2$. Then, we sample 500 parameter realizations using a multivariate Gaussian distribution. Figure 3.2 shows the uncertainty band at the 68% confidence level, which spans about 5% over all the kinematic range explored by the data. For $p_T > 2$ GeV it increases to almost 10%. However, we note that high p_T values are suppressed after the angular integration (see Equation 3.3).

Fit to different center of mass energies data

The general kinematic shape of the invariant π^+ production cross section has been fixed in the previous Section. Here we focus on the scaling of the cross section at different $\sqrt{s}$. The parameter c_6 in Equation 3.8 allows a softening of the p_T shape as observed at high energies, while on the other hand the factor $A(s)$ and the parameters c_{20} to c_{22} introduce an overall renormalization. In this Section, we proceed with the determination of the parameters c_6, c_{20}, c_{21}, and c_{22}. All the other parameters are fixed to the values of the fit to the NA49 data, as described above in Section 3.2.1.

To extend to $\sqrt{s}$ below NA49 measurement we use the multiplicity measurements of NA61/SHINE [284] as well as a collection of data points provided in Ref. [293] (in the following also called Antinucci). At larger $\sqrt{s}$ we use the p_T dependent data provided by CMS [290, 288] and ALICE [291] at central rapidity. All datasets and their $\sqrt{s}$ are summarized in Table 3.1.

Typically, each cross section measurement contains a statistical, a systematic, and a scale uncertainty. In the last Section, we only used the single NA49 dataset, which

allowed us to use a simplified treatment where we ignore the scale uncertainty of 1.5% at first and then added it in a post-procedure. Here we combine datasets from different experiments and, thus, the scaling uncertainty has to be included from the beginning. For datasets with only a single data point, NA61/SHINE and Antinucci, this is straightforward and we can simply add all the individual uncertainties in quadrature. On the other hand, at higher energies, we use the measurements of the invariant cross section by ALICE and CMS at central rapidity. The cross section is provided for values of p_T between 0.1 and 2.5 GeV. For those data points the scaling uncertainty is fully correlated so we cannot simply add them in quadrature in the definition of the total χ^2. Instead, we follow Ref. [91] and introduce nuisance parameters allowing for an overall renormalization of each dataset from ALICE and CMS. Then, the total χ^2 is defined as the sum of two parts:

$$\chi^2 = \chi^2_{\text{stat}} + \chi^2_{\text{scale}}. \tag{3.11}$$

Here the first term accounts for the statistical and systematic uncertainty, while the second term constrains the nuisance parameters according to the scale uncertainties. Explicitly, χ^2_{stat} is given by the sum over all data points i_k and all datasets k:

$$\chi^2_{\text{stat}} = \sum_k \sum_{i_k} \frac{\left(\omega_k \sigma_{\text{inv}i_k} - \sigma_{\text{inv}}(\sqrt{s}_{i_k}, x_{Ri_k}, p_{Ti_k})\right)^2}{\omega_k^2 \sigma^2_{i_k}}, \tag{3.12}$$

where $\sigma_{\text{inv}i_k}$ is the measured cross sections and $\sigma_{\text{inv}}(\sqrt{s}_{i_k}, x_{Ri_k}, p_{Ti_k})$ is the evaluation of our cross section parametrization at the corresponding kinematic variables. The nuisance parameters ω_k rescale both the cross section measurement and the uncertainties $\sigma^2_{i_k}$. Then, the second term of the Equation 3.11 is given by

$$\chi^2_{\text{scale}}(\omega) = \sum_k \frac{(\omega_k - 1)^2}{\sigma^2_{\text{scale},k}}, \tag{3.13}$$

where $\sigma_{\text{scale},k}$ is the scale uncertainty for each dataset. We stress that the sum in Equation 3.12 runs over every single data point, while the sum in Equation 3.13 only runs over datasets. So, moving up or down all the data points of a dataset by the same factor is only penalized once and not for each data point.

Finally, we address two more subtleties. First, the ALICE and CMS experiments provide data averaged in relatively large rapidity bins of $|y| < 0.5$ and $|y| < 1$, respectively. In order to take this into account, we also average our model evaluation over those rapidity ranges. Second, the recent experiments (NA49, NA61/SHINE, ALICE,

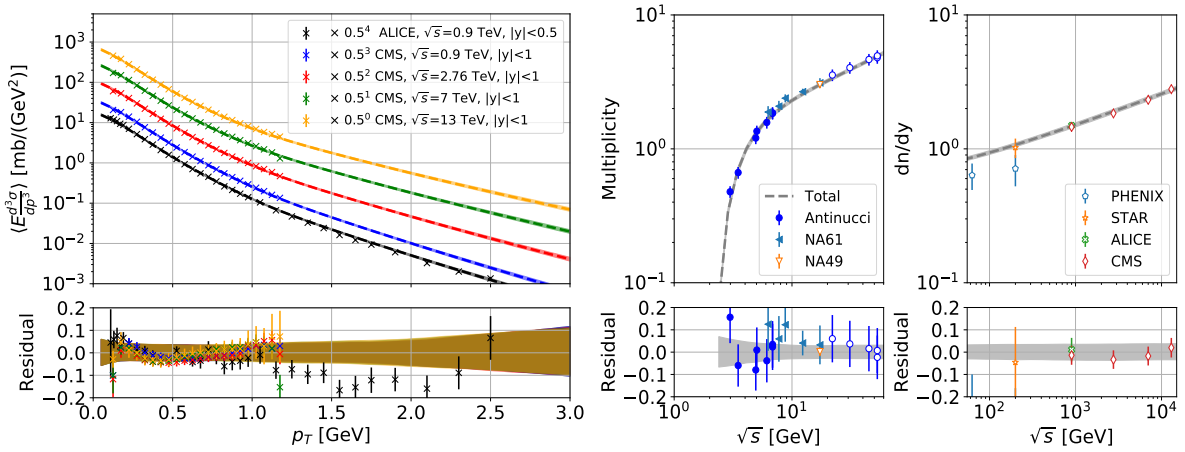

Figure 3.3: Left panel: invariant cross section of inclusive π^+ production in $p+p$ collisions at large $\sqrt{s}$ as measured by ALICE and CMS. The dashed lines represent the best-fit parametrization and the shaded bands show the uncertainty at the 1σ level. Right panel: multiplicity (left sub-panel) and dn/dy (right sub-panel) of π^+ production in $p+p$ collisions measured at different $\sqrt{s}$. The solid lines represent the best-fit parametrization and the grey shaded bands show the uncertainty of our fit at the 1σ level. Filled data points are included in the fit while open data points are only plotted for comparison. The bottom panels shows the residuals defined as (data-model)/model.

and CMS) perform feed-down corrections, namely they subtract the π^+ production from the weak decay of strange particles which are mainly K_0^S, but also $\bar{\Lambda}$ and Σ^+. In contrast, the collection of multiplicity measurements from Antinucci is not corrected for this feed-down. So, we correct those data points by subtracting the contributions of these particles using our estimation from Section 3.2.2. This contributions to the total multiplicity vary from 0.4% for $\sqrt{s}$=3 GeV to 1.7% for $\sqrt{s}$=6.8 GeV. To be conservative we add this correction at each data point to the measurement uncertainty in quadrature.

Figure 3.3 shows the results of the fit at high energies. The invariant cross section is plotted as a function of p_T and at different energies of the corresponding ALICE and CMS data. The fitted function provides a good agreement with the data. The uncertainty on σ_{inv} is about 5% at the lowest p_T values and increases to 10% for $p_T > 2$ GeV.

In Figure 3.3 (right panel), we compare the multiplicity from our parametrization with the available data as a function of $\sqrt{s}$. The plot is divided into two energy regimes: at lower energies, experiments determine the total multiplicity which is integrated over the whole kinematic parameter space, while the collider experiments only determine the multiplicity at central rapidity, often expressed as an average dn/dy. The fit includes

the data points with the filled symbols from Antinucci and NA61/SHINE, while the open data points are only plotted for comparison. At high energies, we show next to the ALICE and CMS data also data from PHENIX [286] and STAR [296]. At high energy our model is plotted for $|y| < 0.5$. However, dn/dy is fairly flat at high energies and midrapidity such that the impact on the model (grey line) is negligible. ALICE and CMS provide measurements which are feed-down corrected, while we perform the feed-down correction for PHENIX and STAR ourselves.

In general, both the fitted data and the ones plotted for comparison are in good agreement with our best-fit parametrization. For the data points from NA49, ALICE, and CMS this is expected, since their data in the $x_R - p_T$ plane have been included in the fits to Equations 3.8-3.10. Instead, the comparison of the data from STAR and PHENIX provides an independent cross-check. The STAR is in very good agreement with our model, while the PHENIX data lie systematically below our multiplicity line. We note that something similar was also observed for $\bar{p}$ [297], potentially pointing to a more general unaccounted systematic.

Overall, our parametrization provides a good fit to the datasets at different $\sqrt{s}$, with a χ^2_n/d.o.f. =189/129, and the parameters c_6, c_{21}, c_{22}, and c_{23} are well contrained. Within our model, the multiplicity is determined with a precision of about 3% above $\sqrt{s}$ of 10 GeV, increasing to 5% at the lowest $\sqrt{s}$.

NA61/SHINE also provided data in the $x_R - p_T$ plane which are however not included in our fit to Equations 3.8-3.10. As discussed above we use a phenomenologically motivated function and fix the kinematic shape of the cross section with the most reliable data from NA49 assuming radial scaling invariance. An additional dataset would require a more careful assessment of systematics errors to avoid over-constraining the fit parameters, and thus underestimating uncertainties. Moreover, we observed some inconsistencies in the tables provided by Ref. [284]. We decided therefore not to include this data in the fit, checking however that the NA61/SHINE data are generally consistent with our parametrization also in the $x_R - p_T$ plane. Please refer to the Appendix of [3] for more details.

In our parametrization, we assume scaling invariance in x_R. While the bulk of π^+ (and thus finally also e^+) are produced at midrapidity, the steeply falling CR projectile flux in the source term enhances π^+ produced in forward direction [298]. The enhancement is supposed to become less important at very high energies, but it might be important at intermediate energies, *i.e.* between NA49 and ALICE/CMS. In the future, more experimental data might help to solve the issue.

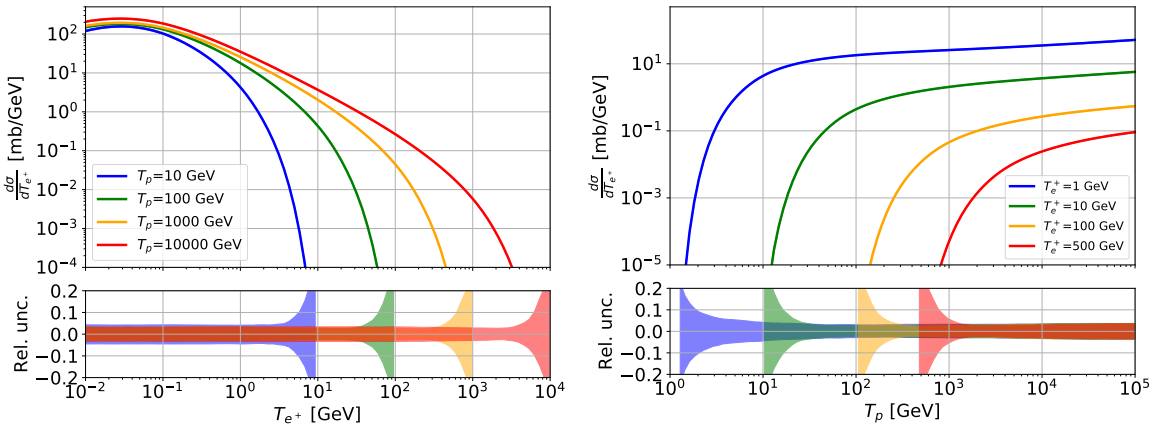

Figure 3.4: Differential cross section for the production of e^+ from π^+ in p+p collisions, computed for different incident kinetic p energies as a function of e^+ kinetic energy (left) and different e^+ kinetic energies as a function of p kinetic energy (right).

Results on the positron production cross section

Now we have all the ingredients to compute the differential cross section for the production of e^+ as a function of the incident p kinetic energy, T_p, and the e^+ energy, T_{e^+}, using Equation 3.3 and Equation 3.6. In Figure 3.4, we present the result for the cross section $d\sigma_{pp\to\pi^+ + X}/dT_{e^+}$ as function of T_{e^+} (left panel) and T_p (right panel) for a few representative values of T_p and T_{e^+}, respectively. The cross section peaks at e^+ energies below 100 MeV almost independently of T_p, and decreases rapidly to zero for $T_{e^+} \sim T_p$. The uncertainties are about 5% for almost all T_{e^+}, which is in agreement with the results in previous Sections. Since the π^+ channel is the dominant one, the final uncertainties on $d\sigma/dT_{e^+}$ will reflect this results, and the small values found is the major result of this work. The relative uncertainty increases above 20% when approaching the threshold. We note, however, that this kinematic range is suppressed in the e^+ source term and has a negligible impact on the final uncertainty.
The projection of the cross section on T_p for fixed values of T_{e^+} shows a rapid increase above the threshold which continues for about one order of magnitude in T_p. Afterward the cross section keeps rising very slowly with energy. As before, the relative uncertainty is large close to the threshold.

3.2.2 Contribution from other channels

Contribution from K^+

About 10% of the e^+ produced in $p + p$ collisions come from the decays of K^+. As sketched in Figure 3.1, the main decay channels considered in this work (branching

fraction in brackets) are:

- $K^+ \to \mu^+\nu_\mu$ (63.6%),
- $K^+ \to \pi^+\pi^0$ (20.7%),
- $K^+ \to \pi^+\pi^+\pi^-$ (5.6%),
- $K^+ \to \pi^0 e^+\nu_e$ (5.1%).

To obtain the decay spectrum from K^+ we proceed in this way: for the $K^+ \to \mu^+\nu_\mu$ channel we follow the same method reported in Section 3.1, but adapted to K^+; for $K^+ \to \pi^+\pi^0$ we have to add one step to the π^+ decay, considering all the possible energies of the π^+ produced from this process; for the last two and less important three-body decay channels we adopt a simplified treatment, assuming that the three particles take 1/3 of the K^+ energy. To obtain the total e^+ yield we closely follow the steps from π^+ as detailed in Section 3.2.1, fitting an analytical formula for the Lorentz invariant cross section of the inclusive K^+ production in $p+p$ collisions. In contrast to π^+, K^+ do not contain strong resonant production. So, we can use a simplified version of Equation 3.7 and Equation 3.8 and define the Lorenz invariant cross section by:

$$\sigma_{\text{inv}} = \sigma_0(s)\, d_1\, F_K(s, p_T, x_R)\, A_K(s) \tag{3.14}$$

with

$$\begin{aligned} F_K(s, p_T, x_R) &= (1 - x_R)^{d_2} \exp(-d_3\, p_T^{d_4} x_R)\, p_T^{d_5} \\ &\times \exp\left[-d_6 \sqrt{s/s_0}^{\,d_7} \left(\sqrt{p_T^2 + m_K^2} - m_K \right)^{d_8 \sqrt{s/s_0}^{\,d_7}} \right], \end{aligned} \tag{3.15}$$

where m_K is the mass of the kaon, d_i are the fit parameters and $\sqrt{s_0}$ is set to 17.3 GeV. The energy dependent normalization $A_K(s)$ is taken to be:

$$A_K(s) \;=\; A_K^0 \left(1 - \frac{\sqrt{s_{\text{th}}}}{\sqrt{s}}\right) \left(1 + \sqrt{\frac{s}{d_9}}^{\,d_{10} - d_{11}}\right) \sqrt{s}^{\,d_{11}} \tag{3.16}$$

where s_{th} is the threshold energy for K^+ production and A_K^0 is determined by the condition $A_K(s_0) = 1$. We follow the two-step procedure previous used for π^+ (see Section 3.2.1), fixing first the $x_R - p_T$ shape with NA49 data [292], and then adjusting the $\sqrt{s}$ behavior with the multiplicity measurements from Antinucci, NA61/SHINE,

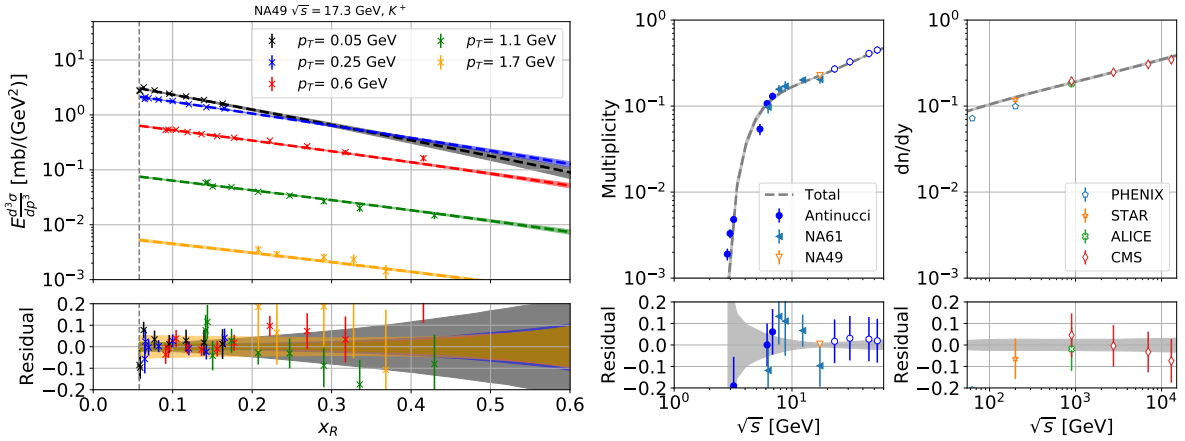

Figure 3.5: Comparison of the best-fit cross section parametrization for the inclusive K^+ production in $p+p$ collisions with NA49 data (left panel) and multiplicity measurements at different CM energies by various experiments (right panel). Right panel: filled data points are included in the fit while open data points are only plotted for comparison. The plots are similar to Figures 3.2 and 3.3(right).

ALICE and CMS [293, 284, 291, 290, 288]. For ALICE and CMS we use the p_T-dependent multiplicity measurements at midrapidity. A summary of the datasets is provided in Table 3.1.

The χ^2/d.o.f. converges to 306/253. In Figure 3.5, we compare our best-fit parametrization with the experimental measurement. In the left panel, the NA49 data of the invariant cross section is shown as a function of x_R and for a few representative values of p_T, while the right panel shows the comparison with various multiplicity measurements as a function of $\sqrt{s}$. All in all, our parametrization provides a very good description of the available data. The shaded bands mark the 1σ uncertainty at fixed p_T, which is below 5% at smallest x_R and increases to 15% at $x_R = 0.45$ for the smallest p_T. Finally, we also compute the e^+ cross section from the decay of K^- into $\pi^+\pi^-\pi^-$ and the subsequent decay of the π^+ into e^+. For this, we use the fit of the inclusive K^- production in $p+p$ collisions, which is performed in analogy to the fit of K^+.

Contribution from K^0_S, K^0_L, Λ and other subdominant channels

K^0_S meson. We start from discussing K^0_S, that generate $e^\pm$ producing $\pi^\pm$ via $K^0_S \to \pi^+\pi^-$ ($B_r = 69.2\%$), thus contributing to the final $e^\pm$ cross sections with the same amount. The NA61/SHINE experiment recently measured the spectra for the production of K^0_S from $p+p$ collisions at $\sqrt{s} = 17.3$ GeV [299].

Following a similar strategy as for π^+ and K^+, we first fix the p_T and x_F dependence of the cross section by fitting the data of NA61/SHINE, while the variation with $\sqrt{s}$ is

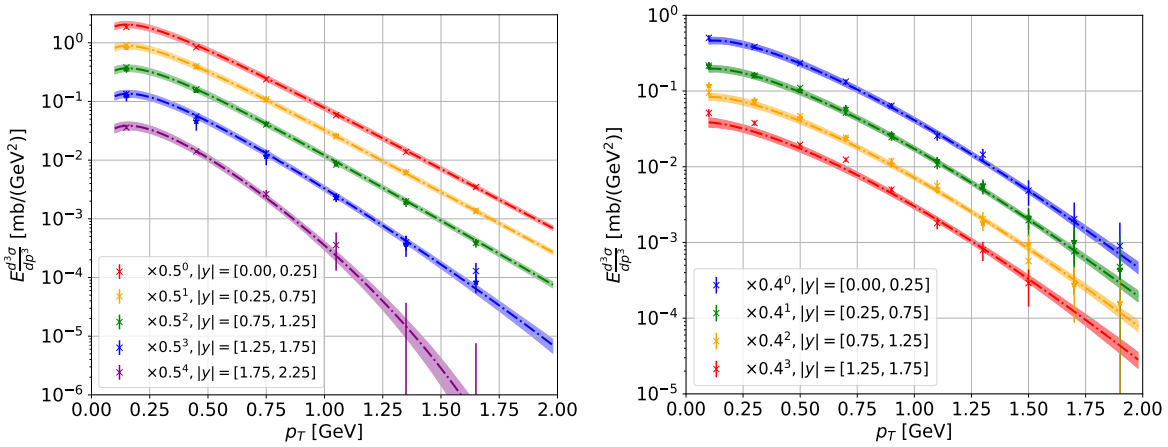

Figure 3.6: Left (right) panel: comparison of the K^0_S (Λ) production cross section measured by the NA61/SHINE experiment and our best-fit.

determined by a second fit to the multiplicities data from Ref. [292], using the model reported in Equations 17-19 of [3]. Figure 3.6 (left panel) shows that our parametrization provides a good description of the NA61/SHINE data.

K^0_L meson. The decay time of the K^0_L meson is 5.1×10^{-8} s which is a factor of about 600 larger than the one of K^0_S, making it very difficult to detect K^0_L particles at accelerator experiments. The lack of experimental data makes it impossible to determine an independent parametrization of the production cross section. Therefore, we checked with the Pythia event generator (we employ the Pythia version 8.3 [300]) that the p_T and x_F shapes for the production of e^+ is very similar for K^0_L and K^0_S in $p+p$ collisions. The difference is simply a normalization factor. The K^0_L meson produces about a factor of 1.16 more e^+ than K^0_S which can be explained by different decay modes of the two kaons. In the following we assume that the production cross section of e^+ from K^0_L can be obtained from K^0_S by rescaling with a factor 1.16. Because of charge symmetry, we apply the same results for e^- production.

Λ baryon. The Λ hyperon contributes only to the e^- through the channel $\Lambda \to p\pi^-$ ($B_r = 63.9\%$). The NA61/SHINE experiment recently measured the spectra for the production of Λ from $p+p$ collisions at $\sqrt{s} = 17.3$ GeV [301]. Following a similar strategy as for K^0_S, we first fix the p_T and x_F dependence of the cross section by fitting the data of NA61/SHINE, while the $\sqrt{s}$ dependence is determined by a second fit to the multiplicities at different $\sqrt{s}$ taken from [301]. See details in Section IV.D of [3]. Figure 3.6 (right panel) shows that our parametrization provides a good description of the data.

Other channels. Other channels contribute with a subdominant amount to the e^+ and

e^- yield, in particular the $\bar{\Lambda}$, the charged Σ and Ξ hyperons, for which no data are available at the energies of interest for the secondary source term. We thus estimate the contribution of the $\bar{\Lambda}$, Σ and Ξ baryons using Pythia [300], running simulations of $p+p$ collisions for $\sqrt{s}$ ranging from a few GeV to 100 TeV. We calculate the multiplicities of these particles (and their antiparticles), n_i, and the ratio n_i/n_Λ, both derived with Pythia for consistency. In fact, for Λ we have a model for the invariant cross section and its mass is similar or equal to the $\bar{\Lambda}$, Σ and Ξ, so we expect the dependence of the cross section with the kinematic parameters to be alike. To add each subdominant channel i to the total yield of $e^\pm$ we rescale the Λ cross sections into $e^\pm$ with the correction factor $\mathcal{F}^i(T_p)$:

$$\frac{d\sigma}{dT_e}(T_p, T_e) = \frac{d\sigma}{dT_e}(T_p, T_e)_\Lambda \times \sum_i \mathcal{F}^i(T_p). \tag{3.17}$$

For example, for charged Σ particles can be written as $\mathcal{F}^\Sigma(T_p) = \frac{n_\Sigma(T_p)\cdot B_r{}^{\pi^+}_\Sigma}{n_\Lambda(T_p)\cdot B_r{}^{\pi^-}_\Lambda}$, where $B_r{}^{\pi^\pm}_\Sigma$ is the branching ratio for the decay of the Σ into $\pi^\pm$.

π^0 mesons. In the end π^0 are expected to be produced in $p+p$ collisions with a similar rate as charged $\pi^\pm$, but decaying only with a branching ratio of 1.17% into $e^+e^-\gamma$. Therefore, the contribution of the π^0 to the $e^\pm$ production is expected to be at the 1% level. Since no data are available for the $e^\pm$ from π^0 at the energy of interest, we use Pythia to derive the p_T and x_F dependence of $e^\pm$ produced from $\pi^\pm$ and π^0, finding that dn/dx_F and dn/dp_T are very similar in shape for the production of $e^\pm$ from π^0 and from $\pi^\pm$. The difference is just a normalization factor that depends on the different multiplicity of π^0 and $\pi^\pm$ from $p+p$ collisions. We add the contribution from π^0 to the $e^\pm$ yield by multiplying the $\pi^\pm$ cross sections by a factor $(1 + n_{\pi^0} \cdot B_r^{\pi^0}/n_{\pi^\pm})$, where $B_r^{\pi^0} = 0.0117$.

3.2.3 Contribution from nuclei collisions

Nuclei interactions (p+A, A+p, and A+A) in the Galaxy give a significant contribution to the production of secondary particles. Many former analyses relied on a simple, overall rescaling of the $p+p$ cross section by a geometric factor or mass number [281, 302, 303]. Here we go beyond this approximations by using the data of NA49 for the production of π^+ in p+C collisions at $p_p = 158$ GeV [304]. While $\pi^\pm$ production in $p+p$ collisions is by definition symmetric under a reflection along the beam axis in the CM frame, this is not necessarily the case in $p+A$ collisions (in the nucleon-nucleon CM frame). Actually, the NA49 p+C data reveals an asymmetry in the cross section

between forward and backward production [305], which is plausible, because the carbon target contains not only p but also n and the binding force of the nucleons could play a role. The asymmetry makes inconsistent a description of the cross section in terms of x_R, an intrinsically symmetric variable. Thus, we use x_F instead of x_R to parametrize $p + A$ collisions.

In principle, it would be useful to determine a standalone parametrization for the $\pi^{\pm}$ production of each $p+A$ initial state, especially for p+He, which is most relevant in the context of CRs. However, the currently available data on π^+ production measurements in $p + A$ collisions are not sufficient to obtain independent descriptions. Especially for p+He collisions the available data is very scarce, with a few measurements in the 1980s [306] of $\pi^{\pm}$ production in kinematic regions that are not interesting for astroparticle physics. Inspired by the treatment for $\bar{p}$ in Ref. [91] we exploit a rescaling of $p+p$ cross section in terms of overlap functions. The idea is to split the π^+ production into two components produced by either the projectile or the target, where the π^+ from each component are mainly produced in forward direction. Adjusting the normalization of the overlap functions separately allows accommodating an asymmetry.

We model the inclusive Lorentz invariant cross section of the $A_1 + A_2 \rightarrow \pi^+ + X$ scattering by:

$$\sigma_{\text{inv}}^{A_1A_2}(\sqrt{s}, x_R, p_T) = f^{A_1A_2}(A_1, A_2, x_F, D_1, D_2, D_3)\ \sigma_{\text{inv}}^{pp}(\sqrt{s}, x_R, p_T), \tag{3.18}$$

where A_1 and A_2 are the mass numbers of the projectile and target nucleus, respectively, and D_1, D_2, and D_3 are three fit parameters. Explicitly, the factor $f^{A_1A_2}$ is defined by:

$$f^{A_1A_2}(x_F) = A_1^{D_1} A_2^{D_1} \left[A_1^{D_2} F_{\text{pro}}(x_F) + A_2^{D_2} F_{\text{tar}}(x_F)\right], \tag{3.19}$$

with $F_{\text{pro}}(x_F)$ and $F_{\text{tar}}(x_F)$ given by:

$$F_{\text{pro/tar}}(x_F) = \frac{1 \pm \tanh(D_3 x_F)}{2}. \tag{3.20}$$

In the above equations, the kinetic variables x_F and $\sqrt{s}$ refer to the nucleon-nucleon CM frame. We do not claim that $F_{\text{pro}}(x_F)$ and $F_{\text{tar}}(x_F)$ are the actual projectile and target overlap functions. They are rather an effective treatment that we have introduced to describe the NA49 data.

To determine σ_{inv}^{pA}, we fit the x_F-dependent rescaling factor $f^{A_1A_2}(x_F)$ of Equation 3.19, while $\sigma_{\text{inv}}^{pp}(\sqrt{s}, x_R, p_T)$ is fixed to the best-fit values of Section 3.2.1. In other words, we obtain the three free parameters that are D_1 to D_3 fitting the NA49 data on σ_{inv} for the inclusive π^+ production in p+C collisions at $\sqrt{s} = 17.3$ GeV [304]. We obtain a

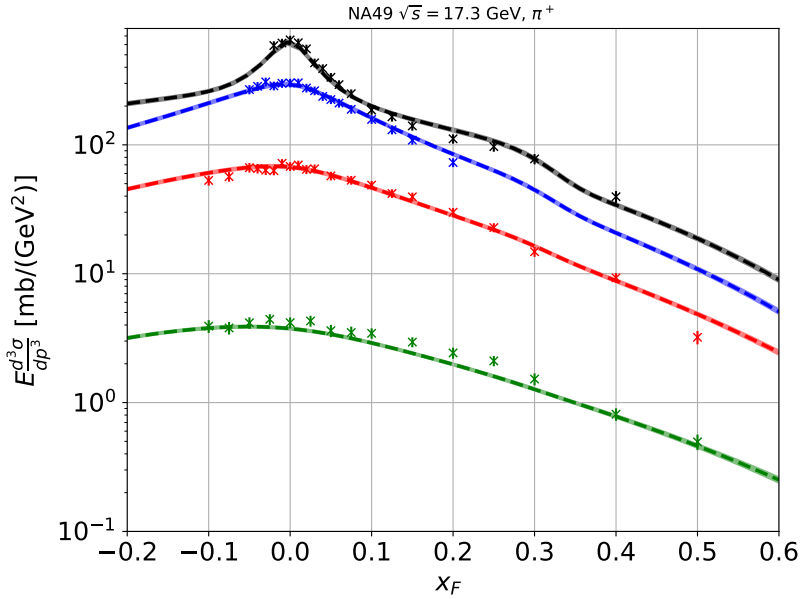

Figure 3.7: Results of the fit on the NA49 data [304] invariant cross section for the inclusive π^+ production in p+C collisions. We show the NA49 data together with our fit results as a function of x_F for some representative values of p_T. Shaded bands show the 1σ uncertainty band.

good fit with a χ^2/d.o.f. of 400/265. Our model is compared to the NA49 data of σ_{inv} in Figure 3.7. The cross section is plotted as a function of x_F for a few representative values of p_T. We observe a good agreement of the data with the parametrization, especially at low values of p_T, which are the most important for e^+ production in the Galaxy. The uncertainties on the model turn out to be about 5%, which mostly comes from the uncertainty in the $p+p$ collisions. Finally, we also check, a posteriori (as for $p+p$ collisions), that our parametrization is qualitatively in good agreement with NA61/SHINE data [307] of p+C scattering provided at $\sqrt{s} = 7.7$ GeV. Using the rescaling relation of Equation 3.18 we obtain the cross sections for p+He and all other nuclei collisions.

While we are improving the state of the art [281, 302, 308], which is based on a rescaling of the normalization of $p+p$ cross section by a simple geometrical factor, our result points to the need of collecting data of the $p + \text{He} \to \pi^+ + X$ cross section. This might allow disentangling $p+p$ and $p+A$ fits in the future by performing separate fits of the parametrizations for each p+He and $p+A$, in order to avoid a rescaling from $p+p$. Actually, one reason for the small uncertainty bands in Figure 3.7 can be related to the fact that the kinematic shape of our parametrization for $p+A$ is already partly fixed by $p+p$, see Equation 3.18. In this sense, more data in the p+He (and more

general $p + A$) collisions might allow a more correct estimation of uncertainties. We also note the absence of data for $x_F < -0.1$ in Figure 3.7, a kinematic regime which is important for the production of $\pi^{\pm}$ in $A + p$ collision in CRs. Here we rely on an extrapolation of our parametrization.

For the K^+ production channel, we refer to NA61/SHINE [307] data at $\sqrt{s} = 7.7$ GeV. We found that a simple rescaling from the $p+p$ case ($f^{pA} = A^{D_1}$) is sufficient. For the remaining subdominant production channels discussed in Section 3.2.2 we adopt the same rescaling as for K^+.

3.2.4 Results on the positron production cross section and source spectrum

We now have all the elements to compute the total differential cross section $d\sigma/dT_{e^+}$, displayed in Figure 3.8, for the inclusive production of e^+ in $p+p$ inelastic collisions. The result is obtained by summing all the contributions of π^+, K^+ and K^-, K_0^S, K_0^L, and subdominant channels (S. C.) discussed in Section 3.2.1 and 3.2.2. We plot $d\sigma/dT_{e^+}$ for the separate production channels, and their sum, along with the relevant 1σ uncertainty band. At the bottom of each panel we display the 1σ uncertainty band around the best fit for the total $d\sigma/dT_{e^+}$. The four plots are for incident p energies T_p of 10, 100, 1000, and 10000 GeV. The π^+ channel dominates the total cross section, being about 10 times higher than the K^+ channel. The e^+ production from K_0^S, K_0^L, and S. C. results to be at a few % level, slightly depending on T_{e^+} and T_p. The main comment to these results is the smallness of the uncertainty with which we determine $d\sigma/dT_{e^+}$. At 1σ the uncertainty band around the best fit is 4% to 7% at all T_p energies. For T_{e^+} values close to T_p, the error band spreads up since data for this limit (which corresponds to $x_R = 1$) are not available. We conclude that the e^+ production cross section from $p + p$ collisions is determined with very high precision. This result is mainly due to the precision of the data at our disposal, and also to the appropriate empirical description provided by our algebraic model.

In Figure 3.9, we present the computation of the source spectrum of e^+ in the Galaxy as a function of T_{e^+}, implementing Equation 3.1. We fix $n_{\rm H} = 0.9\,{\rm cm}^{-3}$ and $n_{\rm He} = 0.1\,{\rm cm}^{-3}$. The CR fluxes ϕ_i for a nucleus i are taken from Ref. [309]. We plot separate results for the collision of $p + p$, p+He, He+p, He+He and C, N and O scattering off H, with their uncertainty due the production cross sections computed in this Chapter. The $q(E)$ is predicted with a remarkably small uncertainty, ranging from 5% to 8% depending on the energy. We nevertheless remind that the different estimations and parametrizations used in the literature pointed out differences by a factor of two. Our

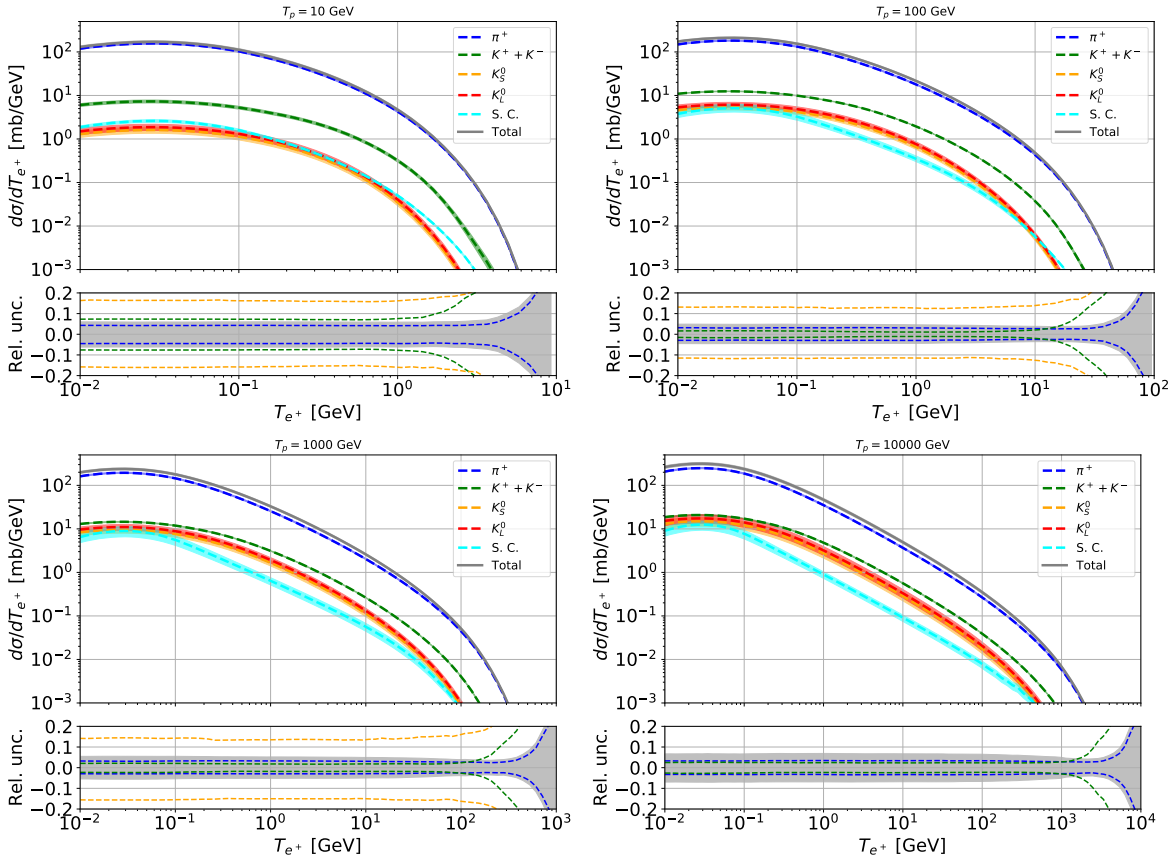

Figure 3.8: Differential cross section for the inclusive production of e^+ in p+p collisions, derived from fits to the data as described in Section 3.2.1 and 3.2.2. We plot separate production of π^+, K^+ and K^-, K_0^S, K_0^L and subdominant channels (S. C.), and their sum. Each plot is computed for incident p energies T_p, of 10, 100, 1000, and 10000 GeV. The curves are displayed along with their 1σ error band. At the bottom of each panel the 1σ uncertainty band is displayed around the best fit individually for each contribution.

results definitively exclude that e^+ cross sections can gauge the source spectrum, and consequently the flux at Earth, by more than a factor of few %. We compare our results for the p+p channel with [274] (labeled Kamae) and [277] (labeled AAfrag). The Kamae cross section predicts an about 20% smaller source term above 5 GeV, while it predicts a significantly larger source term below 1 GeV. In contrast, for AAfrag, we only report results for T_{e^+} above 1 GeV, since they provide cross sections only for $T_p \geq 3.1$ GeV meaning that the source term cannot be predicted accurately at lower energies. The differences are within 10% for most of the energy range between 1 and 100 GeV. We also checked the predictions for p+He, He+p, and He+He, finding differences at a similar level.

After this analysis, authors of [280] compared the cross sections of different models,

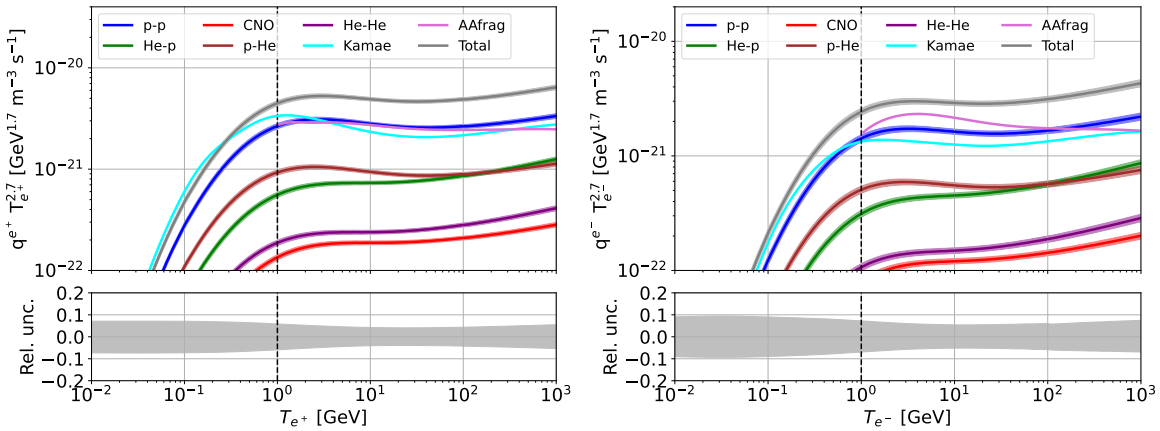

Figure 3.9: Source terms of CR e^+ (left panel) and e^- (right panel). Next to the total source term we show the separate CR-ISM contributions. In the bottom panels, we display the relative uncertainty of the total source term. We note, however, that for $T_{e^+} \lesssim 1$ GeV (black dashed line) the source term is not constrained by cross section data but rather an extrapolation of our parametrization which could possibly be affected by systematics.

including our results, and the predictions obtained with the FLUKA code [310]. For the $p+p$ channel, the inclusive cross sections of e^+ production from our model and FLUKA differ by no more than $5-10\%$ in the $5-100$ GeV region, exhibiting a very similar energy dependence. In general the predicted FLUKA source spectrum is compatible with our model within a 10% factor from 1 GeV to a few hundred GeV.
Finally, we note that the available cross section data (especially for π^+ production) constrain the e^+ source term down to about 1 GeV. Below this energy, the prediction of the source term relies on an extrapolation from our parametrization and could be affected by larger systematics.

3.2.5 Results on the electron production cross section and source spectrum

Secondary e^- are produced in the Galaxy from the same $p+p$ collisions as e^+. We also provide new results for the e^- production cross section. We mirror the same analysis performed for e^+ and described in the previous Sections. In particular, for the $\sigma_{\rm inv}$ for π^- production we adopt the parametrizations reported in Equations 3.7, 3.8, 3.9 and 3.10. The data employed in the fits are taken from NA49 [283], NA61/SHINE [284], Antinucci [293], ALICE [291] and CMS [290, 288], as reported in Table 3.1.
The results of the fit to the NA49 production cross section π^- data are displayed in Figure 3.10 (left panel), as a function of x_R and for a few representative values of p_T.

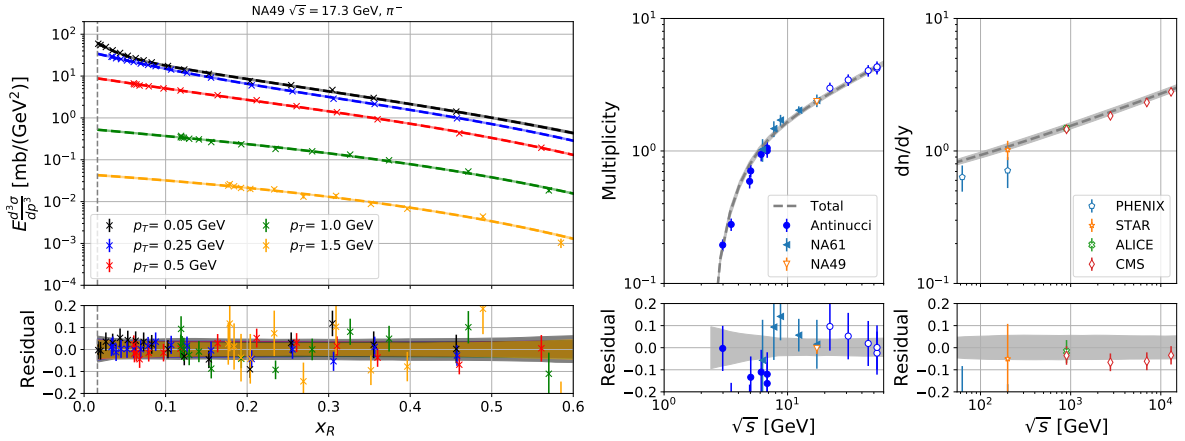

Figure 3.10: Left panel: same as Figure 3.2 (left panel) but for π^- production in $p+p$ collisions. Right panel: same as Figure 3.3 (right panel) but for π^- production in $p+p$ collisions at various $\sqrt{s}$ (see text for details).

The fit is globally very good, and the resulting uncertainties are about $5-6\%$. The energy dependence of the cross section has been fixed as for π^+, see Section 3.2.1. The only difference is that the ALICE data points have not been considered in the final fit, because they show some tension with CMS data at $\sqrt{s} = 0.9$ TeV. The results on the multiplicity are shown in Figure 3.10 (right panel). Again, the fit is good, and the uncertainty is below 10%.

The contribution from K^- is computed following the same procedure as for the e^+ from K^+, see Section 3.2.2, fitting the data from the same experiments (and same references). The contributions from K^0_S, K^0_L and π^0 decays are symmetric for both e^+ and e^-. In addition, we consider also the contribution from the Λ baryon and from the other S. C., as reported in Section 3.2.2.

In Figure 3.9 (right panel) we present the computation of the source spectrum of e^- in the Galaxy as a function of T_{e^-}, as discussed for e^+ in Section 3.2.4. It is predicted with a remarkably small uncertainty, ranging from 6% to 10% depending on the energy. With respect to [274], we obtain for the $p+p$ channel a higher prediction of $20-30\%$ between 1 GeV to 1 TeV. Instead, at lower energies our cross sections are lower. However, at such low energies our results, in particular below 1 GeV, are driven by extrapolation. In contrast, the AAfrag cross sections predict a $30-40\%$ larger source term compared to our cross section between 1 GeV and 100 GeV. The large difference for e^- between the AAfrag model and Kamae was already observed in Ref. [277]. In the end our results are similar to the ones obtained in [280] with the FLUKA code.

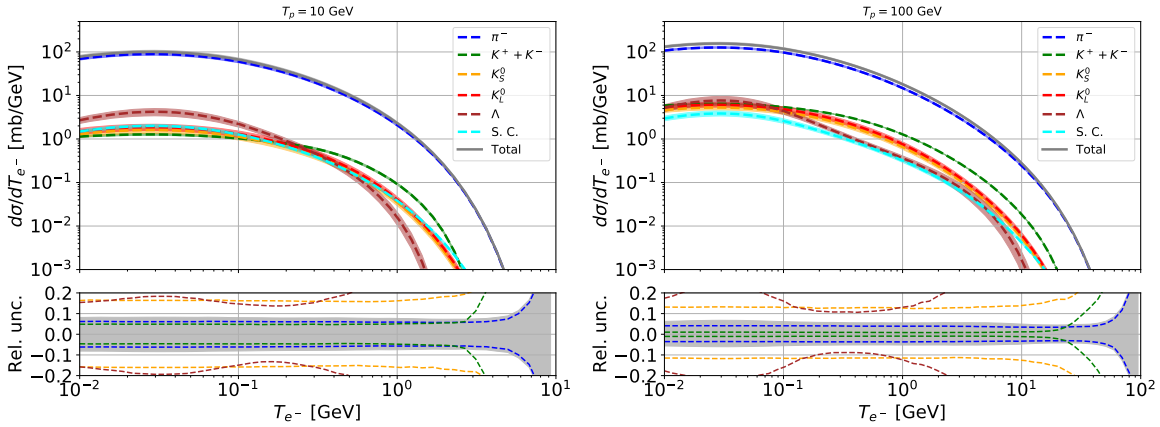

Figure 3.11: Differential cross section for the inclusive production of e^- in $p+p$ collisions, derived from fits to the data as described in Section 3.2.5. We plot separately the contribution from π^-, K^+ and K^-, K_0^S, K_0^L, Λ, subdominat channels (S. C.), and their sum. We provide the result for incident p energy T_p of 10 and 100 GeV. The curves are displayed along with their 1σ uncertainty band. At the bottom of each panel it is displayed the 1σ uncertainty band around the best fit for the total $d\sigma/dT_{e^-}$.

3.2.6 Discussion and summary

The secondary production of $e^\pm$ in our Galaxy presents a significant contribution to the $e^\pm$ fluxes measured at the Earth. In particular, the e^+ flux is dominated by secondaries below few GeV. The correct interpretation of any primary contributions depends on the accurate description of the secondary production. Most of the secondary $e^\pm$ are produced in $p+p$ collisions and by channels involving He, both as a target and as a projectile. The main production channels of the secondary $e^\pm$ involve the intermediate production and decay of $\pi^\pm$ and $K^\pm$, while some additional channels can contribute to the source term at the percent level each.

Here, we have determined a new analytical description of the Lorentz invariant cross section for the production of $\pi^\pm$ and $K^\pm$, especially focusing on $p+p$ collisions, and we have evaluated, either by exploiting further data or by referring to Monte Carlo generators, the inclusive cross section into K_0^S, K_0^L, Λ and S. C. The differential cross section $d\sigma/dT_{e^\pm}(p+p \to e^\pm + X)$, which enters in the computation of the $e^\pm$ source term, is predicted from 10 MeV up to tens of TeV of $e^\pm$ energy, with an uncertainty of about $5-10\%$, directly inferred from data. This is a major improvement with respect to the state of the art, where previous uncertainties in the normalization of the secondary $e^\pm$ flux due to cross section were large up to a factor of 2 among different models. Our results definitively exclude that e^+ cross sections can gauge the source spectrum, and consequently the flux at Earth, by more than a factor of few %.

The cross section for scattering of nuclei heavier than p is obtained by fitting the

NA49 data for the production of $\pi^{\pm}$ on p+C collisions. Future measurements of $\pi^{\pm}$ production in the p+He could help to improve our model. Our results, especially in the e^{+} sector, eventually open the door to interpretations of CR data, especially from the AMS-02 experiment, in which the calculation of secondary component is no longer limited by the $e^{\pm}$ production cross sections.

3.3 Gamma-ray cross sections

In this Section, we investigate the hadronic production cross section of γ rays. As explained in Chapter 2, most of the γ rays detected by *Fermi*-LAT are produced by the Galactic insterstellar emission [39]. The dominant processes, especially at low latitudes, are the hadronic interactions of CR nuclei with the gas of the Galactic disk [192, 203, 311, 202, 312, 313, 314], whose modelling is described by $\sigma(i + j \rightarrow \gamma + X)$. Any uncertainty in these cross sections comparable or greater than the *Fermi*-LAT statistical errors undermine the study of the Galactic interstellar emission of the observed γ-ray sky. Since data are very limited for these cross sections, the standard approach is to employ Monte Carlo event generators [274, 279, 315, 316]. As for $e^{\pm}$, the most commonly used cross section is the Kamae [274] model, and more recent result has been provided by AAfrag [279]. As shown in Ref. [277] the differences in the production cross sections of γ rays obtained with different Monte Carlo generators can be larger than 30%. This demonstrates the necessity of improving the parametrization of these cross sections.

We present here a new and more precise model relying mostly on an analytic prescription as done in Section 3.2 for $e^{\pm}$. The main production mechanism of γ rays is the decay of π^{0} mesons. However, data for the π^{0} production are extremely scarce. There are measurements of the multiplicity, but data on the Lorentz-invariant differential cross section are either not given or affected by large systematics or do not cover the kinematic region relevant for Astroparticle physics. Therefore, we decide to fit the multiplicity of π^{0} and extrapolate the kinematics from the production cross section of π^{+} and π^{-} by taking a combination of the parametrizations obtained in Section 3.2.1. Then, we carefully model also the production cross sections of η and K mesons and Λ baryons. This strategy closely follows the one explained in the previous Section where we derived cross sections for $e^{\pm}$. We note that the most obvious application of the results here presented is the computation of the diffuse γ-ray background. Thus, in the following, we use it as a benchmark to exemplary show the implications of our work. However, we note that cross sections are actually important also in a much larger con-

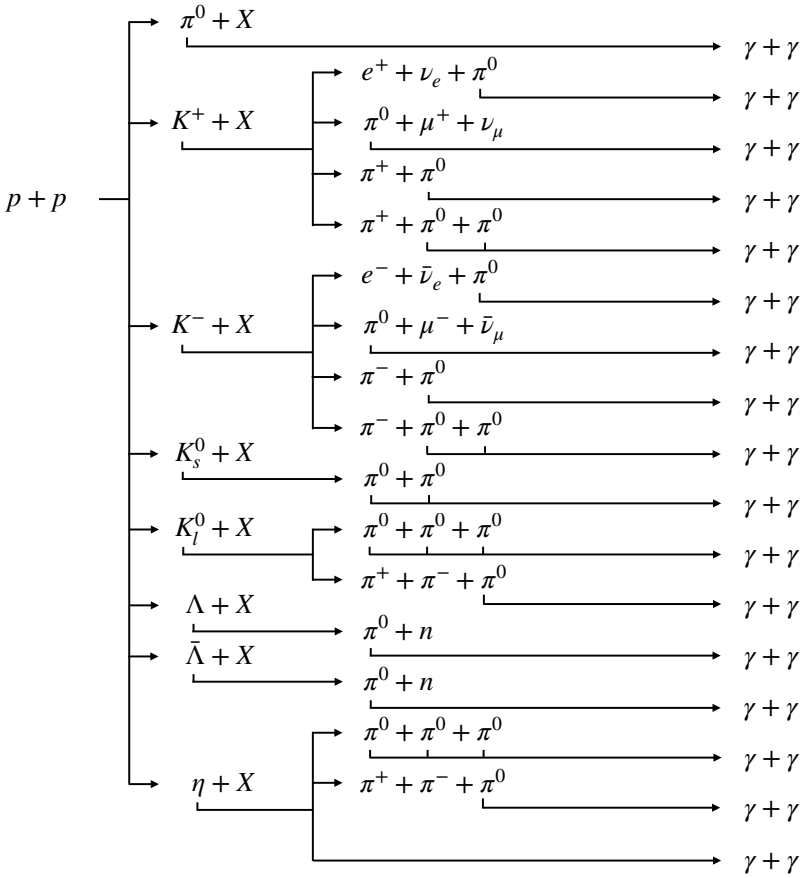

Figure 3.12: This diagram shows the γ-ray production channels from $p + p$ collisions considered in our analysis. We report here only the channels that produce at least 0.5% of the total yield (see the main text for further details).

text. They are required as input for modeling most of the point sources mentioned in Chapter 2 and in this sense, almost every γ-ray analysis relies either directly or indirectly on the cross sections we investigate in the following.

In Figure 3.12, we show a sketch of all the production channels considered in this analysis. Channels that contribute less than 0.5% to the total γ production are not shown and neglected. The γ-ray production cross section is derived from the π^0 production cross section as in Equation 3.3, with π^0 and $P(T_{\pi^0}, E_\gamma)$ instead of $\pi^\pm$ and $P(T_{\pi^\pm}, E_{e^\pm})$. $P(T_{\pi^0}, E_\gamma)$ of the process can be computed analytically. Similarly, the fully differential production cross section is defined as in Equation 3.4, with π^0 instead of $\pi^\pm$. We now discuss the γ-ray production cross sections from π^0, benefiting from the results obtained in Section 3.2.1 for the $\pi^\pm$.

3.3.1 Gamma rays from $p + p \to \pi^0 + X$ collisions

Given the relevance of the π^0 channel for the γ-ray production, it would be important to have precise data on a wide coverage of the kinematic phase space for the reaction $p + p \to \pi^0 + X$. Unfortunately, the available data are either not given for the double differential cross sections or affected by large systematics or do not cover the kinematic region relevant for Astroparticle physics. Instead, for the process $p + p \to \pi^{\pm} + X$ data for σ_{inv} that satisfy all these requirments are available (see Section 3.2). Therefore, we decide to model σ_{inv} for the production of π^0 using the results of $\pi^{\pm}$ cross sections that we derived in Section 3.2.1. More specifically, we assume that the shape of the π^0 cross section lies in between the π^+ and π^- shape. Then, we use the difference between the π^+ and the π^- cross section to bracket the uncertainty as further detailed below.

Model for the invariant production cross section

We assume that σ_{inv} depends on kinematic variables by a relation between the shapes of the production cross sections of π^+ and π^- in Equations 3.7, 3.8 and 3.9. Thus, for $p + p$ scattering we define σ_{inv} as:

$$\sigma_{\text{inv}} = \sigma_0(s)\, c_{20} \left[G_{\pi^+}(s, p_T, x_R) + G_{\pi^-}(s, p_T, x_R) \right] A_{\pi^0}(s), \tag{3.21}$$

where $\sigma_0(s)$ is the total inelastic $p+p$ cross section, the function G_{π^+} (G_{π^-}) represents the kinematic shapes of the invariant π^+ (π^-) cross section, and c_{20} is an overall factor that adjusts the total normalization of the cross section. The functions $G_{\pi^{\pm}}(s, p_T, x_R)$ are defined as:

$$G_{\pi^{\pm}}(s, p_T, x_R) = c_{1,\pi^{\pm}} \left[F_{p,\pi^{\pm}}(s, p_T, x_R) + F_{r,\pi^{\pm}}(p_T, x_R) \right] \tag{3.22}$$

with c_1, F_p, and F_r specified in Equations 3.8 and 3.9. Finally, the factor $A_{\pi^0}(s)$ allows adjusting the cross section to the measured π^0 multiplicities at different incident energies:

$$\begin{aligned} A_{\pi^0}(s) \;=\; & \left(1 + \left(\sqrt{s}/c_{21}\right)^{c_{22}-c_{23}}\right) \left(1 + \left(\sqrt{s}/c_{24}\right)^{c_{23}-c_{25}}\right) \\ & \left(1 + \left(\sqrt{s}/c_{26}\right)^{c_{25}-c_{27}}\right) \left(\sqrt{s}\right)^{c_{27}} \Big/ A(\sqrt{s_0}), \end{aligned} \tag{3.23}$$

where $\sqrt{s_0}$ is fixed to 17.27 GeV, while the parameters from c_{20} to c_{27} are derived in this work.

Fit to total cross section at different $\sqrt{s}$

The kinematic shape of the invariant π^0 production cross section with respect to p_T and x_R has been fixed in the previous Section. Here we focus on the scaling of the cross section at different $\sqrt{s}$, introduced in our parametrization through the function $A_{\pi^0}(s)$ that acts as an overall renormalization. Here we proceed with the determination of the parameters from c_{20} to c_{27}. To obtain a complete dependence from $\sqrt{s}$ we use the collection of total π^0 cross section measurements provided in Ref. [302] (in the following also called Dermer86).

At larger $\sqrt{s}$ we fit the $x_F dn/dx_F$ data provided by LHCf experiment [317] in the forward-rapidity region integrated for $p_T < 0.4$ at $\sqrt{s} = 2.76$ and 7 TeV. In particular we consider only the data provided for $x_F < 0.7$, since the x_F shape of our $\sigma_{\rm inv}$ model determined in Section 3.2.1 is tuned on data of Ref. [283], which cover $x_F < 0.7$ in the low p_T region. We have verified a posteriori that the kinematic space of $x_F > 0.7$ contributes less than 2% of the final emissivity ϵ described in Section 3.1. The highest $\sqrt{s}$ of LHCf is 7 TeV, namely $T_p = 2.61 \times 10^7$ GeV in the LAB frame for a fixed target collision. Beyond this incident p energy our parametrization must be considered as an extrapolation. In the same $\sqrt{s}$ range, data from the ALICE experiment [318] are available for the dn/dy at mid-rapidity, and $x_F \sim 0$. Since LHCf provides a larger coverage of the kinematic space, we tune our analysis on this dataset, checking a posteriori that the total multiplicity measured by ALICE is compatible with our result. The inclusion of the ALICE data in the fit would not produce significant differences, being the fit dominated by the LHCf measurements. We perform a χ^2 fit and use the MultiNest [295] package to scan over the parameter space.

As explained in Section 3.2.1, for datasets with only a single data point, we can simply add all the individual uncertainties in quadrature. In practice, those are the Dermer86 measurements, which are a collection from different experiments and therefore have independent uncertainties. On the other hand for the measurements of $x_F dn/dx_F$ provided by LHCf [317], the scaling uncertainty is fully correlated and we cannot simply add them in quadrature in the definition of the total χ^2. Instead, we introduce nuisance parameters allowing for an overall renormalization of each LHCf dataset as done in Section 3.2.1.

Finally, there is one subtlety about the datasets. While the LHCf experiment can distinguish if photons are produced by the π^0 or an intermediate η, the collection of measurements in Dermer86 ascribe all photons to the π^0 decay, namely, they are not corrected for the η contribution. Therefore, we correct those data points by subtracting the contributions of η using our estimation from Section 3.3.2. The contribution to the

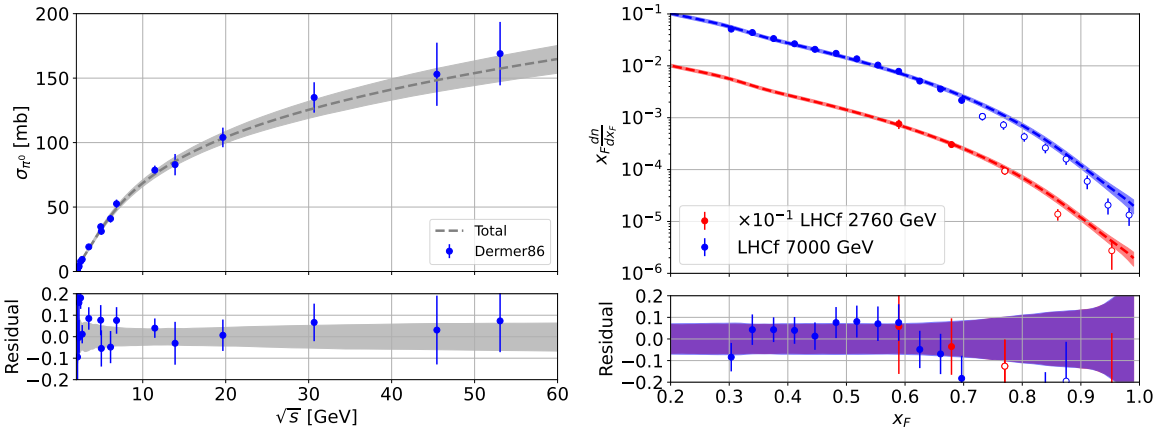

Figure 3.13: Total cross section (left panel) and $x_F dn/dx_F$ (right panel) of π^0 production in $p+p$ collisions measured at different $\sqrt{s}$. The solid lines represent the best-fit parametrization and the shaded bands show the uncertainty of our fit at the 1σ level. The bottom panels shows the residuals defined as (data-model)/model.

total multiplicity varies from <0.001% at $\sqrt{s} = 2.2$ GeV to 3% at $\sqrt{s} = 53$ GeV. To be conservative, we increase the uncertainty by adding this correction to the total error in quadrature at each data point.

Overall, our parametrization provides a good fit to the datasets at different $\sqrt{s}$. The χ^2/d.o.f. of the best fit converges to 26/24. The parameters from c_{20} to c_{27} are all well constrained by the fit and their values are reported in Table I of Ref. [4]. The results are displayed in Figure 3.3. In the left panel, we report the fit to the low-energy data on the total cross section, while the right panel reports the fit to LHCf data. Within our parametrization, the π^0 total cross section is determined with a precision between 5% and 10% below $\sqrt{s}$ of 60 GeV (left panel). At LHCf energies the uncertainty varies between 5% and 10% below 0.7 with x_F, and increase to more than 10% for higher x_F values (right panel). There is a reasonable agreement between our predictions and the data also in the x_F range not considered in the fit. Moreover our model is compatible within 2σ with the dn/dy measured by ALICE, confirming the goodness of our model.

Results on the gamma-ray production cross section

The differential cross section $d\sigma/dE_\gamma$, for the production of γ rays from $p+p \to \pi^0 + X$ scattering, is obtained from Equation 3.3, once $\sigma_{\rm inv}$ is fully determined. There are mainly three contributions to the uncertainty band:

- We have fitted the overall normalization of the π^0 multiplicity to the Dermer86 and LHCf data using Equation 3.21. From the MultiNest scan we obtained the best-fit value and the covariance matrix with correlated uncertainties of the

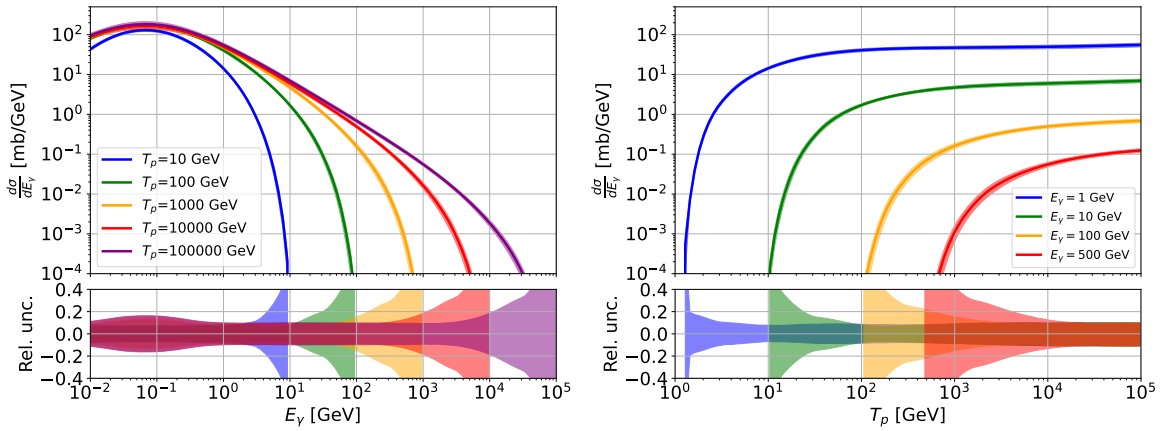

Figure 3.14: Differential cross section for the production of γ-rays from π^0 in $p+p$ collisions, computed for different incident kinetic p energies as a function of γ energy (left) and different γ energies as a function of p kinetic energy (right).

parameters c_{20} to c_{27}. We numerically propagate this uncertainty by sampling the cross section parametrization for 500 realizations using the covariance matrix and assuming Gaussian statistics.

- The G_{π^+} and G_{π^-} functions both come with statistical uncertainties. In Section 3.2.1, we derived the covariance matrices for the parameters c_{1,π^+} to c_{19,π^+}, and equivalently for π^-. This is the statistical uncertainty on the kinematic shape of the cross section. We propagated the uncertainty individually for π^+ and π^-, i.e. we assume that the shapes are uncorrelated. Also the uncertainty of $A_{\pi^0}(s)$ is assumed to be uncorrelated from the kinematic shapes.

- Finally, we consider a systematic uncertainty for the kinematic shape. For this, we evaluated the difference of the cross section by assuming either a pure π^+ or a pure π^- kinetic shape. It means that in Equation 3.22 we replace $G_{\pi^+} + G_{\pi^+}$ by $2G_{\pi^+}$ or $2G_{\pi^-}$, respectively. Then, we derived the energy differential cross section, Equation 3.3, from these two cases. We compared the two results and use the maximal deviation as a function of energy as an additional contribution to the total uncertainty, which is obtained by adding all contributions in quadrature.

In Figure 3.14, the differential cross section is reported for the production of γ from π^0 in $p+p$ collisions. It is provided for different T_p as a function of E_γ (left) and different E_γ as a function of T_p (right). Uncertainties are between 6% and 20% for most of the energy range, except for E_γ close to T_p, where both statistical and systematic errors increase. For most combinations of E_γ and T_p the statistical uncertainty dominates, while the systematic uncertainty due to the kinematic shape is at most at the same

level as the statistical error. Only for E_γ close to T_p, which is suppressed in the total emissivity, the systematic uncertainty dominates. We obtain the most precise prediction for T_p of about 100 GeV, which corresponds to the NA49 and NA61 data for $\pi^\pm$ production.

3.3.2 Contribution from other production channels and from nuclei

In this Section we present our model for the photon production from further intermediate mesons and hyperons, and for scatterings involving nuclei heavier than hydrogen. The decay channels relevant for photon production for which we have available data are:

- $K^+ \to \pi^+\pi^0$ (20.7%) and $K^+ \to \pi^0 e^+ \nu_e$ (5.1%),
- $K^- \to \pi^-\pi^0$ (20.7%) and $K^- \to \pi^0 e^- \bar{\nu_e}$ (5.1%),
- $K^0_S \to \pi^0\pi^0$ ($B_r = 30.7\%$),
- $\Lambda \to n\pi^0$ ($B_r = 35.8\%$),

where the relevant branching ratio is reported in parenthesis. We include their contribution by using the production cross sections derived in Section 3.2.2. We calculate the spectra of photons assuming that π^0 are produced from a two or three body decay. In particular, for three body decays we consider, as in Section 3.2.2, that each of the three particles takes 1/3 of the parent's energy.
The K^0_L meson is expected to give a contribution similar to the K^0_S meson. Due to the lack of experimental data we employ Pythia [300] as in Section 3.2.2 finding that the p_T and x_F shapes for the production of photons is very similar for K^0_L and K^0_S. The difference is approximately a normalization factor of 1.16 connected to the branching ratio of K^0_L and K^0_S into π^0.
The hyperons $\bar{\Lambda}$, Σ and Ξ give a subdominant contribution to the total photon yield. For all these particles their π^0 contributions are usually removed in the data by feed-down corrections. We thus have to add it into our calculations. Since no data are available at the energies of interest, we follow Section 3.2.2 and estimate the contribution of these particles using Pythia, running the Monte Carlo event generator for $p+p$ collisions from a few GeV to 10^4 TeV and computing the multiplicities n_i of each particle i. We adopt Equation 3.17 considering this time the branching ratios of the decay channels that produce γ rays.

Another relevant channel for the production of photons is the η meson, which decays into:

- $\eta \to \gamma\gamma$ ($B_r = 39.41\%$),
- $\eta \to \pi^0\pi^0\pi^0$ ($B_r = 32.68\%$),
- $\eta \to \pi^+\pi^-\pi^0$ ($B_r = 22.92\%$),
- $\eta \to \pi^+\pi^-\gamma$ ($B_r = 4.22\%$).

Cross section data for the production of η mesons have been measured by several experiments at different $\sqrt{s}$ [319, 318, 320, 321]. These data are typically collected at mid-rapidity and the double differential cross section is not available. The π^0 produced in the second and third decay channels are not distinguished experimentally from the prompt ones because the decay time of η is much smaller than the one of π^0. Therefore, the π^0 production from η decay is already included in the total one as described in the previous Section. We include the photons from the direct η decay by using the measured ratio between its multiplicity with respect to the π^0 one, as a function of p_T. At low p_T the ratio between the η and π^0 multiplicites n_η/n_{π^0} is of the order of $0.05 - 0.15$ while at high p_T reaches a plateau at the level of 0.4. Since most of the contribution to the γ-ray source term is at low p_T we expect the contribution of η to be at the level of $5 - 15\% \times Br(\eta \to \gamma\gamma) = 2 - 6\%$. The contribution from the fourth channel only contributes less then 0.5% and thus it is neglected.
As for the inclusion of scatterings including nuclei, in either the CRs or in the ISM, we closely follow the prescriptions derived in Section 3.2.3 for $\pi^\pm$, given the lack of any dedicated data. Specifically, if a π^0 is produced in collisions between projectile and target nuclei with A_1 and A_2 mass numbers, the G functions in Equation 3.21 are corrected as in Equations 3.19, 3.18 and 3.20. The $K^\pm$ channel is modified analogously. For all the other channels, we assume a correction function which is the average from the K^+ and K^- ones.

3.3.3 Results on the gamma-ray production cross section and emissivity

We now can compute the total differential cross section $d\sigma/dE_\gamma$ for the inclusive production of γ rays in $p+p$ inelastic collisions, shown in Figure 3.15 for four representative incident p energies. The result is obtained by summing all the contributions from π^0 and the other channels, as discussed in Sections 3.3.1 and 3.3.2. The contribution of $\pi^0 \to 2\gamma$ is dominant at all p and photon energies.

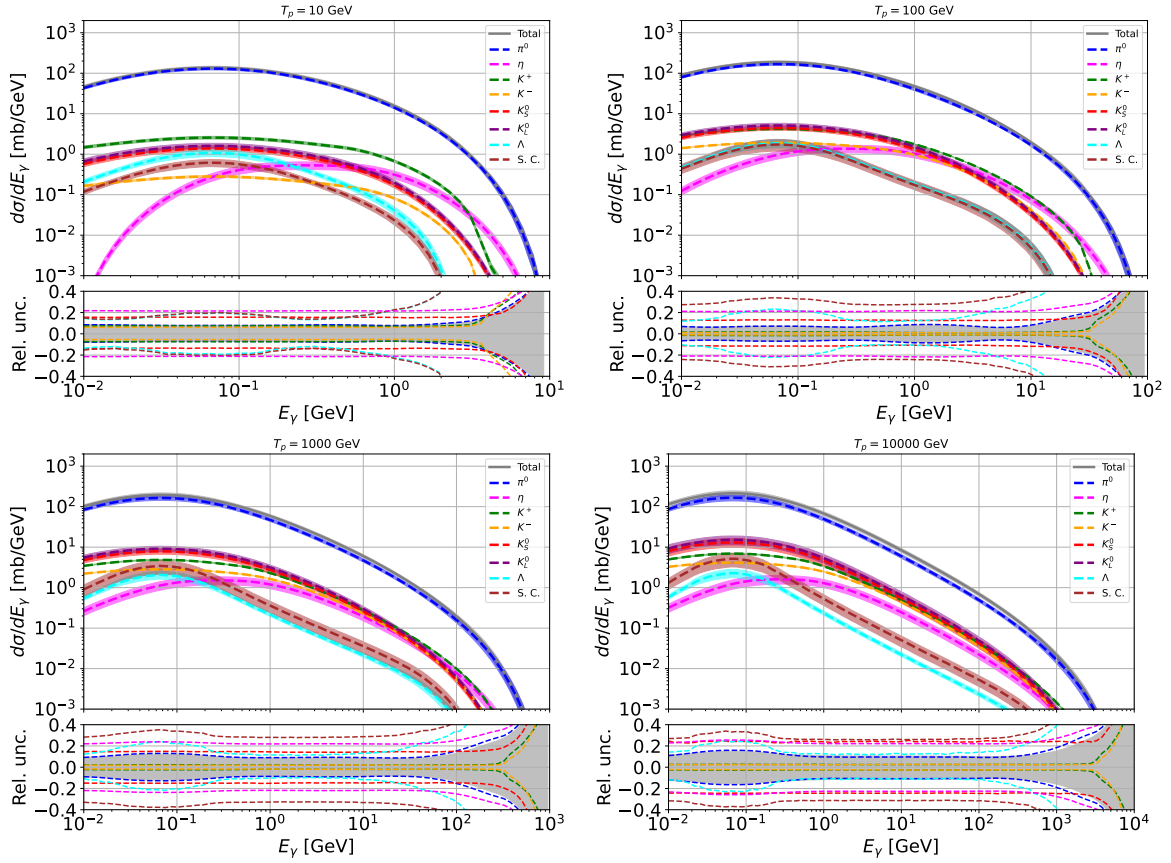

Figure 3.15: Differential cross section for the inclusive production of γ rays in $p + p$ collisions, derived from fits to the data as described in Sections 3.3.1 and 3.3.2. We plot separate production of π^0, η, K^+, K^-, K_0^S, K_0^L, Λ and S. C., and their sum. Each plot is computed for incident p energies T_p of 10, 100, 1000 and 10000 GeV. The curves are displayed along with their 1σ error band. At the bottom of each panel the 1σ uncertainty band is displayed around the best fit individually for each contribution.

For the decays of η, K^+, K^-, K_0^S, K_0^L, and Λ we also show the individual contributions, while all the S. C. are combined into a single curve. All these channels contribute at most few percent of the total cross section. However, their shapes, as a function of T_p and E_γ, slightly differ from the dominant π^0 channel. The grey curve and shaded band display the total $d\sigma/dE_\gamma$ and the 1σ uncertainty band, respectively. The final uncertainty spans from 6% to 20% at different T_p and E_γ, and is driven by the modeling of the π^0 cross section.

For illustration, we compute the emissivity ϵ described in Section 3.1 assuming a constant $n_{\rm ISM}$ and incident CR spectra independent of Galactic position. In Figure 3.16 (left panel) we show $\epsilon(E_\gamma)$ as a function of E_γ for $p + p$, He+p, p+He, He+He and CNO+p scatterings, and their sum. We assume $n_{\rm H} = 0.9\,{\rm cm}^{-3}$ and $n_{\rm He} = 0.1\,{\rm cm}^{-3}$. Each prediction is plotted with the relevant uncertainty from the production cross sec-

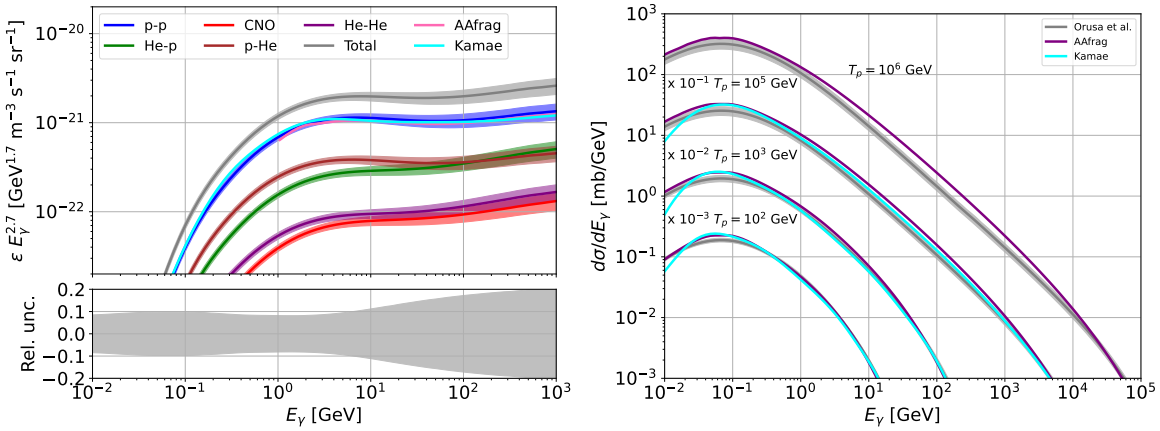

Figure 3.16: Left panel: the γ-ray emissivity is computed for $p+p$, He+p, p+He, He+He and CNO+p scatterings. The grey line is the sum of all contributions (see text for details). Each prediction is plotted with the relevant uncertainty due to the production cross section derived in this Chapter. In the bottom panel, the relative uncertainty to the total $\epsilon(E_\gamma)$ is reported. For comparison, we show the results by Kamae [274] and AAfrag [277] in the $p+p$ channel. Right panel: comparison among our differential cross section and Kamae [274] and AAfrag [277], for incident p energy $T_p = 10^6, 10^5, 10^3$ and 10^2 GeV. The three lower curves have been rescaled by the factor indicated in the figure for the sake of visibility.

tion derived in this Chapter. The relative uncertainty to the total $\epsilon(E_\gamma)$ is reported in the bottom panel. As expected, the most relevant contribution comes for $p+p$ reactions. Nevertheless, the contributions from scatterings involving He globally produce a comparable source spectrum. The uncertainty on $\epsilon(E_\gamma)$ due to hadronic production cross sections is about 10% for $E_\gamma \leq 10$ GeV, and increases to 20% at TeV energies. In order to estimate the impact of our results on the diffuse Galactic emission at *Fermi*-LAT energies, we report the results by Kamae [274], that is used in the *Fermi*-LAT official Galactic interstellar emission model [192], and AAfrag [277] for the $p+p$ channel. The latter is plotted for $E_\gamma > 1$ GeV since their results start from $T_p > 4$ GeV. The emissivity shown in Figure 3.16 (left panel) is comparable or slightly higher with respect to the Kamae and AAfrag ones.

We also show in Figure 3.16 (right panel) the direct comparison between our cross section and the one derived by Kamae and AAfrag. Our cross section is larger than Kamae at *Fermi*-LAT energies by a rough $5-10$%, depending on the energies. Also, the high energy trend of our cross section is slightly harder than Kamae and AAfrag. Figure 3.16 (right panel) shows how our model predicts similar or slightly higher values of the cross section for those E_γ produced in the forward direction, that are the relevant ones for the emissivity in the plotted energy range. In the relevant energies for *Fermi*-LAT, the results obtained in this Chapter are however compatible with Kamae and

AAfrag at 1σ of the estimated uncertainty bands.

3.3.4 Discussion and summary

The secondary production of γ rays from hadronic collisions is a major source of energetic photons in the Galaxy. The diffuse Galactic emission is dominated by the decay of π^0, in turns produced by the inelastic scattering of nuclei CRs with the ISM. A precise modeling of the production cross section of γ rays of hadronic origin is crucial for the interpretation of data coming from the *Fermi*-LAT, for which the diffuse emission is an unavoidable foreground to any source or diffuse data analysis. In the near future, the full exploitation of the data from CTA is subject to a deep understanding of the diffuse emission.

We propose a new evaluation for the production cross section of γ rays from $p + p$ collisions, based on existing data on the total cross sections rather than Monte Carlo predictions, and relying on previous analysis for $e^{\pm}$ reported in Section 3.2. The cross section for scattering off nuclei heavier than p is also derived. Our results are supplied by a realistic and conservative estimation of the uncertainties affecting the differential cross section $d\sigma/dE_\gamma$, intended as the sum of all the production channels. This cross section is estimated here with an error of 10% for $E_\gamma \leq 10$ GeV, increasing to 20% at 1 TeV. The uncertainty obtained is for the first time directly tuned on existing data, rather than from the discrepancy among different Monte Carlo event generators, that were estimated to reach the 30% level [277].

In order to improve the accuracy of the present result, new data from colliders are needed. Specifically, data is required on the Lorentz invariant cross section, and not only on the total cross section, for π^0 productions. The most important kinetic parameter space is $p_T \lesssim 1$ GeV, a large coverage in x_R and beam energies in the LAB frame covering from a few tens of GeV to at least a few TeV. It would be important to get the same measurements also on a He target.

Chapter 4

Novel predictions for secondary positrons and electrons in the Galaxy

In the previous Chapter 3, we highlighted the significance of fundamental interactions in the physics of CRs. Now, we proceed by integrating this information with the propagation of CRs on kpc and so macroscopic scales. In this Chapter we discuss the computation of the secondary production of $e^{\pm}$, obtained using the results from Section 3.2.1 on the cross sections and after a new analysis on CR propagation. This Chapter is based on Ref. [5].

4.1 Introduction

The measured e^+ flux and e^+ fraction clearly indicate that a secondary component alone cannot explain the data (see Section 1.5 and [322, 281, 131, 323]). Secondary e^+ contribute mostly at energies below a few GeV while at higher energies this process contributes to the data very likely less than a few tens of %. This is even more pronounced in the e^- flux data, which are mainly explained by the cumulative flux of e^- accelerated by Galactic SNRs [324, 132, 208, 207].

The room left to primary e^+ is gauged by the exact amount of secondary e^+ predicted in the whole energy range in which data are available. The e^+ flux measured by AMS-02 have an uncertainty smaller than 5% for almost the whole energy range [131]. Even though it is currently not achievable, significant effort should be devoted to produce a prediction of secondary production with a theoretical uncertainty that converges to the level of the AMS-02 data points. This is essential for investigating potential primary sources of e^+.

The flux of secondary $e^{\pm}$ is mainly determined by the physics of CR transport in the

Galaxy and by the spallation and fragmentation cross sections of CRs scattering off the atoms of the ISM. A remarkable progress has been made on the propagation side, thanks to high quality data from AMS-02 nuclei and on parallel theoretical efforts to explain them [123, 87, 325, 309, 326, 88, 327]. Nevertheless, the exact size of the Milky Way diffusive halo L is still not known. This has important consequences for the predictions of the flux of secondary particles (see, e.g., [87]). As pointed out in Section 3.2, the theoretical uncertainties on the parameterization of cross sections for the production of $e^{\pm}$ have been remarkably reduced. Here we provide a new evaluation of the CR flux of secondary e^+ and e^- at the Earth by implementing these new results. In order to estimate the uncertainties coming from the propagation model, we perform a new fit to the 7 years fluxes of primary and secondary CRs measured by AMS-02 [328], by using different assumptions for the physical processes that characterize the propagation of particles in the Galaxy and the diffusive halo size L.

4.2 Models for cosmic-ray production and propagation

The propagation setup is explained in details in Section 1.4. We employ here the GALPROP code [329, 330] to solve the CR propagation equation numerically. As in [309], KoCu22 in the following, we model the diffusion coefficient (see Equation 1.6) by a double broken power law in rigidity, R, with the functional form:

$$D_{xx}(R) \propto \beta R^{\delta_l} \cdot \left(1 + \left(\frac{R}{R_{D,0}}\right)^{\frac{1}{s_{D,0}}}\right)^{s_{D,0}\,(\delta-\delta_l)} \cdot \left(1 + \left(\frac{R}{R_{D,1}}\right)^{\frac{1}{s_{D,1}}}\right)^{s_{D,1}\,(\delta_h-\delta)} . \tag{4.1}$$

Here β is the CR velocity in units of speed of light, $R_{D,0}$ and $R_{D,1}$ are the rigidities of the two breaks, δ_l, δ, and δ_h are the power-law index below, between, and above the breaks, respectively. We also allow a smoothing of the breaks through the parameters $s_{D,0}$ and $s_{D,1}$. The diffusion coefficient is normalized to a value D_0 at a reference rigidity of 4 GV so that $D_{xx}(R = 4\,\mathrm{GV}) = \mathrm{D}_0$. The first break, if included in the model, is typically in the range of $1 - 10$ GV while the second break, whose existence is suggested by the flux data for secondary CRs, is at about $200 - 400$ GV (see, e.g., [331, 309, 326, 332]).

The source term for each primary CR species accelerated by astrophysical sources can

be factorized as $q(\boldsymbol{x}, p) = Q(R)\rho(\boldsymbol{x})$. The energy spectrum $Q(R)$ is parametrized as a smoothly broken power-law in rigidity:

$$Q(R) = Q_0 R^{\gamma_1} \left(1 + \left(\frac{R}{R_{\rm inj}}\right)^{1/s_{\rm inj}}\right)^{s_{\rm inj}\,(\gamma_2-\gamma_1)}, \tag{4.2}$$

where $R_{\rm inj}$ is the break rigidity, and γ_1 and γ_2 are the two spectral indices above and below the break. The smoothing of the break is parameterized by $s_{\rm inj}$. For the spatial distribution of SNRs sources of CRs $\rho(\boldsymbol{x})$, we assume the one reported in Ref. [333]. Finally, we include the solar modulation using the force-field approximation [127], which is fully determined by the Fisk potential φ (see Section 1.4.2). For CRs with rigidities above 1 GV the force-field approximation reproduces with a good precision the solar modulation of e^+ and e^-, as demonstrated in Ref. [334]. A similar conclusion is obtained by using SOLARPROP [335], a code that numerically solves the transport of CRs in the heliosphere. By using input parameters similar to the standard ones suggested within SOLARPROP, we obtained results that closely aligned with the force-field approximation, for both e^+ and p. In particular, for p with a rigidity above $1-2$ GV and e^+ with an energy above $0.5-1$ GeV, the differences between the SOLARPROP models and the force-field approximation are within the uncertainty range of the AMS-02 data.

We test the following models for the propagation of CRs (see Section 1.4 for the different effects considered):

- `Conv` $v_{0,c}$: it contains convection with a fixed velocity $v_{0,c}$ orthogonal with respect to the Galactic plane: $v_c(z) = v_{0,c}$. The CR injection spectra from SNRs are taken as simple power laws ($\gamma_1 = \gamma_2$ in Equation 4.2) with separate spectral indexes for p ($\gamma_{\rm p}$), He ($\gamma_{\rm He}$) and CNO ($\gamma_{\rm CNO}$). The fact that these CR species require different injection spectra has been inferred from data and extensively demonstrated, e.g., in Refs. [309, 326, 336, 327]. The observed low and high-rigidity breaks in CR fluxes are reproduced by a double smooth broken power-law shape for the diffusion coefficient as reported in Equation 4.1. The free propagation parameters are thus the following: γ_p, $\gamma_{\rm He} - \gamma_p$, $\gamma_{\rm CNO} - \gamma_p$, the diffusion coefficient parameters D_0, δ_l, δ, δ_h, $R_{D,0}$, $R_{D,1}$, $s_{D,0}$ and $s_{D,1}$, $v_{0,c}$ and the same solar modulation potential φ for all the CR species.

- `Conv` dv_c/dz: this model is very similar to `Conv` $v_{0,c}$, but instead of using a constant convection velocity $v_{0,c}$, here $v_c(z)$ increases linearly as function of z. The exact functional form is $v_c(z) = dv_c/dz \cdot |z|$, where dv_c/dz replaces $v_{0,c}$ as

the free parameter in the fit.

- `Reacc`$_0$: this model has no convection while the reacceleration is turned on and modulated through the Alfvèn velocity v_a, which is a free parameter in the fit. The diffusion coefficient and the injection spectra are modeled as in `Conv` $v_{0,c}$. As we will see in Section 4.5 the best-fit value for v_a is around 0 km/s, this is why the label of the model reports 0 as subscript.

- `Reacc`$_{10}$: this model is the same as the previous one except that the Alfvèn velocity is fixed to 10 km/s.

- `Reacc`$_{30}$ `Inj`: in this model we replace the low-rigidity break in the diffusion coefficient with a low-rigidity break in the injection CR spectra. Therefore, we model the injection spectra of CRs with separate spectral indexes for p ($\gamma_{1,p}$ and $\gamma_{2,p}$), He ($\gamma_{1,\mathrm{He}}$ and $\gamma_{2,\mathrm{He}}$) and CNO ($\gamma_{1,\mathrm{CNO}}$ and $\gamma_{2,\mathrm{CNO}}$), which have a common rigidity break R_{inj} and smoothing s_{inj}. The diffusion coefficient is modeled with a single smooth broken power-law with free parameters: D_0, δ, δ_h, $R_{D,1}$ and $s_{D,1}$, and we leave free v_a. This model has 30 as a subscript because the best-fit value for v_a is found at 30 km/s.

For all the above mentioned models we also leave free the abundance of primary CRs. Specifically, we leave free the abundance of p and He using a renormalization factor with respect to the reference values used in GALPROP. For this, we iteratively adjust the reference isotopic abundances in GALPROP to ensure that the renormalizations converge to values close to 1[1]. We call these parameters $\mathrm{Ren\,Abd_p}$ and $\mathrm{Ren\,Abd_{He}}$ for p and He, respectively. This procedure is equivalent of having as free parameters the normalization factors Q_0 of the source terms in Equation 4.2 and allows a fast profiling over the parameters (see Section 4.3.2). For the heavier nuclei, we leave free to vary the isotopic abundance of carbon ^{12}C, nitrogen ^{14}N and oxygen ^{16}O, which are all of primary origin, through the parameters: $\mathrm{Abd_{^{12}C}}$, $\mathrm{Abd_{^{14}N}}$ and $\mathrm{Abd_{^{16}O}}$. We do not use renormalizations as for p and He here because the isotopic abundances also affect the fluxes of the secondaries Li, Be, and B.
The source term of secondary CRs is reported in Equation 3.1. The uncertainty of fragmentation cross sections severely affects the production of secondary nuclei. The level of precision of fragmentation cross sections is for many channels significantly worse

[1]Technically, in GALPROP the isotopic abundance of p is not fixed by the Q_0 of the source terms in Equation 4.2 but rather indirectly by aposteriori choosing a normalization of the p flux. In our case, we use 4.3×10^{-9} cm^{-2} sr^{-1} s^{-1} MeV^{-1} at 100 GeV. For all other primary CRs, the isotopic abundance is then provided as the ratio with respect to p (in units of 1.06×10^6). We fix the ^{4}He abundance to 9.65×10^4.

compared to the AMS-02 CR flux measurements (see, e.g., [337]). Uncertainties are very often at the level of $20-30\%$, or even more for those cases with very poor data, and they represent the main limiting factor for the interpretation of the AMS-02 data. In our analysis we allow some flexibility in the fragmentation cross sections in order to take into account the related uncertainties. This is the same procedure used in several other papers (see, e.g., [94, 87, 309, 326, 327]).

We include CR nuclei up to silicon in the calculation of secondary leptons. Particularly relevant ingredients for the prediction of the secondary $e^{\pm}$ are the ISM gas density and the treatment of the energy losses. For the gas, we use the 2D default models implemented in GALPROP [121]. The numerical solution of the transport equation permits to include all relevant energy losses for $e^{\pm}$, additionally modeling its spatial dependence. We include synchrotron losses on the Galactic magnetic field and inverse Compton losses on the ISRF, as well as adiabatic, bremsstrahlung and ionisation losses, which affect the prediction at few GeV (see Section A.1 of the Appendix). The ISRF model is the default GALPROP model, which is consistent with more recent estimates in the few kpc around the Earth [204], where most of the secondary leptons are produced. The synchrotron energy losses are computed by assuming a simple exponential magnetic field. Specifically, we include a regular magnetic field in the Galactic disk and a random component modeled as exponential functions as $B_{\rm reg,ran} = B_{0,\rm reg,ran} \cdot \exp\left(-(r-r_{\odot})/r_{0,\rm reg,ran}\right) \cdot \exp(-z/z_{0,\rm reg,ran})$, with $B_{0,\rm reg,ran} = 4$ μG, $z_{0,\rm reg} = 4$ kpc, $z_{0,\rm ran} = 2$ kpc, $r_{0,\rm reg} = 13$ kpc and an infinite $r_{0,\rm ran}$. This gives a local total magnetic field of $B_{\rm tot} = \sqrt{B_{reg}^2 + B_{ran}^2} = 5.65$ μG, which is compatible with what found with state-of-the-art magnetic field spatial models fitted to CR and multiwavelength emissions [338].

4.3 Methods for the determination of the propagation parameters

In this Section we discuss the numerical solution of the transport equation, and the statistical methods for the determination of the propagation parameters and injection spectrum of primary CRs, obtained by fitting AMS-02 nuclei data.

4.3.1 Modeling cosmic-ray propagation with GALPROP

GALPROP divides the Galaxy, which is assumed to be a cylinder, in a spatial grid with respect to Galactocentric coordinates. We use the 2D grid where r is the dis-

tance from the Galactic center and z is the distance from the plane. We assume the Galactic plane to be extended 20 kpc, while for the half-height of the diffusion halo L we test values from 0.5 to 8 kpc. The new version of GALPROP v.57 [121] includes new solvers for the propagation equation, the possibility of using non-uniform grids, improved implementation of the convection velocity, new source distributions and improved parameterisations for calculations of the cross sections.

4.3.2 Fit to nuclei cosmic ray data

We fit the latest data measured by the AMS-02 experiment after 7 years of data taking, from 2011 to 2018 [328]. In particular we fit the absolute fluxes of p, He, C, O, N, B/C, Be/C and Li/C. The ratio of secondaries over primaries (B/C, Be/C and Li/C) are particularly relevant for fixing the propagation parameters, while the one of He, C, O, N to derive the injection spectra. Moreover, in the ratio some systematic uncertainties cancel out with respect to the absolute flux of secondary CRs. Since all the AMS-02 measurements considered have been measured for the same data-taking period, we adopt one unique Fisk potential for the all the species.
The AMS-02 data for the fluxes available for $R > 1$ GV are complemented with the p and He data from Voyager [339] above 0.1 GeV/nuc. The addition of Voyager data helps to calibrate the interstellar injection spectrum. We use Voyager data only above 0.1 GeV/nuc to avoid further complications which might arise at very low energies, like stochasticity effects due to local sources or the possible presence of a further low energy break in the spectra [340, 341].

Fitting procedure

The main goal of the analysis is to find the parameters of the model by fitting CR absolute flux data or flux ratios between secondary and primary CRs. To optimize the computation time, we rely on a hybrid strategy to explore the wide parameter space, comprising of up to about 30 free parameters, as done in Refs. [309, 326]. We use the MULTINEST [295] algorithm to sample all parameters that depend on the evaluation of GALPROP[2]. As a result, we obtain the posterior distributions and the Bayesian evidence. For the other parameters which do not need a new evaluation of GALPROP (for example, parameters equivalent to a linear rescaling), we profile over those parameters on-the-fly with respect to the likelihood of Equation 4.4 and directly pass the maximum value to MULTINEST. The profiling is performed using

[2]We use a MULTINEST setting with 400 live points, an enlargement factor of EFR=0.7, and a stopping criterion of TOL=0.1.

MINUIT [342]. The best-fit and errors as well as the uncertainty bands for the fluxes and parameters correlations will be given in the Bayesian framework. We will use the Bayesian evidence and Bayes factors to compare the different propagation models. In contrast, to quantify the goodness of fit for each model we employ the reduced χ^2 statistics.

The posterior probability for the parameter θ_i is given by

$$p(\theta_i|D) = \int d\theta_1 ... d\theta_{i-1} d\theta_{i+1} ... d\theta_n \, \frac{p(D|\boldsymbol{\theta})p(\boldsymbol{\theta})}{Z} \,, \tag{4.3}$$

where $p(D|\boldsymbol{\theta}) = \mathcal{L}(\boldsymbol{\theta})$ is the likelihood given the data D, $p(\boldsymbol{\theta})$ is the prior, and $Z = \int d\boldsymbol{\theta} p(D|\boldsymbol{\theta})p(\boldsymbol{\theta})$ is the evidence. We also use a χ^2 function to compare our CR model with the available data:

$$\begin{aligned} \log\left(\mathcal{L}(\boldsymbol{\theta}_{\rm CR}, \boldsymbol{\theta}_{\rm XS})\right) &= -\frac{1}{2}\chi^2(\boldsymbol{\theta}_{\rm CR}, \boldsymbol{\theta}_{\rm XS}) = \\ &= -\frac{1}{2}\sum_{s,i}\left(\frac{\phi_{s,i} - \phi^{(\rm m)}_{s,i}(\boldsymbol{\theta}_{\rm CR}, \boldsymbol{\theta}_{\rm XS})}{\sigma_{s,i}}\right)^2 . \end{aligned} \tag{4.4}$$

Here the sum is performed over the CR datasets s and the rigidity or energy bins i, and $\phi_{s,i}$ and $\phi^{(\rm m)}_{s,i}$ are the measured and modeled CR flux of species s at the rigidity R_i, respectively. The errors of the fluxes, labeled as $\sigma_{s,i}$, include both statistical and systematic uncertainties added in quadrature. We note that systematic uncertainties of the AMS-02 flux data are expected to exhibit correlation in R. Such correlations play only a marginal role on the inferred propagation parameters [326], while they can have an important impact for dark matter searches with CR $\bar{p}$, as pointed out in [343, 344, 94].

When fitting the model to AMS-02 data, we distinguish between two type of free parameters. The parameters $\boldsymbol{\theta}_{\rm CR}$ in Equation 4.4 are connected to the physics of CR propagation as introduced in Section 4.2. Instead, the $\boldsymbol{\theta}_{\rm XS}$ are related to uncertainties in the nuclear fragmentation cross sections which are considered in the fit as nuisance parameters. This strategy permits marginalizing over the uncertainties in the fragmentation and production cross sections, as introduced in Refs. [309, 326]. In particular, we parametrize the cross sections for the production of secondaries CRs with a re-normalization factor, which for B production is labeled as $A_{\rm XS} \rightarrow$ Be, and a change of slope, which for B is $\delta_{\rm XS} \rightarrow$Be. In particular, we use priors for the re-normalization and change of slope of the nuclear cross sections values of $0.8, 1.2$ for the former, which means a variation of 20%, and $-0.1, 0.1$ for the latter, similarly to Ref. [331]. A summary of the fit parameters and priors for each model tested is reported in the Appendix

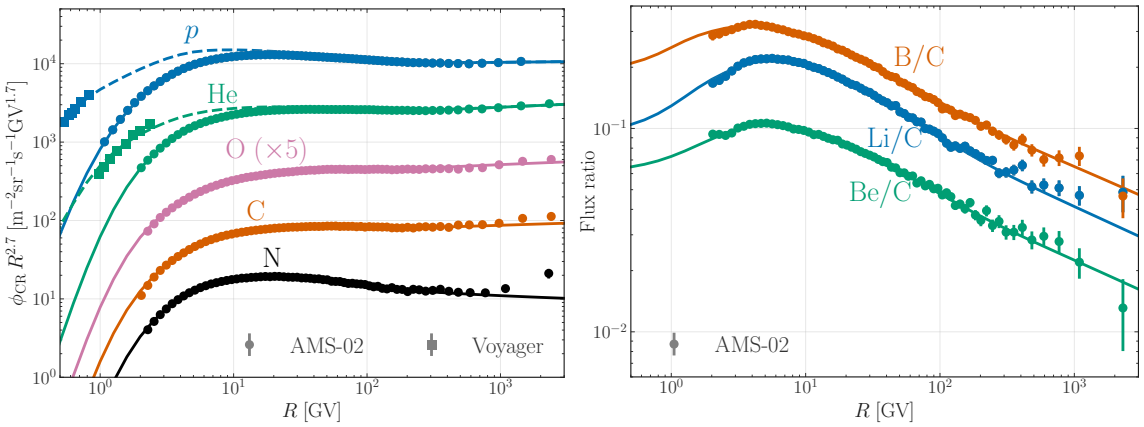

Figure 4.1: Left: fluxes of p, He, O, C and N nuclei as predicted by the parameters fitted on the data by AMS-02 and Voyager (for p and He). Right: secondary-to-primary flux ration for B/C, Li/C and Be/C along with AMS-02 data.

of Ref. [5]. We assume linear priors for all the parameters. Some first attempts to provide new data on fragmentation cross sections of nuclei are currently performed and will definitely help to reduce the uncertainties in the near future, as reported in Ref. [345], with the pilot study on the measurement of the production of B isotopes in C+p reactions at a beam momentum of 13.5A GeV/c by NA61/SHINE collaboration.

4.4 Primary and secondary nuclei

We show here the results for the fit to the primary and secondary CR nuclei. Figure 4.1 summarizes the results of the fit for `Conv` $v_{0,c}$ along with the AMS-02 data for primaries and secondaries species as a function of rigidity. In the left panel we report the results for the primary p, He, O and C nuclei, and the half-primary N flux. On the right panel we show the secondary-to-primary flux ratios for B/C, Li/C and Be/C. In the Appendix of Ref. [5] are reported the best-fit values for the propagation parameters, while in Figures A.2 and A.3 of the Appendix the residual plots for different cases.

We obtain reduced χ^2 ($\tilde{\chi}$) smaller than 1 within each of the tested models. The lowest $\tilde{\chi}$ of 0.50 is provided by the $\texttt{Reacc}_{30}$ `Inj` model, pointing out a statistically preference for this scenario. However, this is the only model for which we allow larger priors of the nuclear cross section uncertainties and with the highest number of free propagation parameters. Namely, instead of only 3 free slopes in the `Conv` $v_{0,c}$, this model has 6 free slopes as well as a free position and smoothing of the break, that cause the improvement of $\tilde{\chi}$.

The fact that all our models converge to a best-fit with of $\tilde{\chi}$ smaller than one is ex-

pected and in agreement with previous studies. The reason for the small $\tilde{\chi}$ is that the systematic uncertainties of the CR data points of AMS-02 are correlated. The correlations typically slightly reduce the uncertainty on the propagation parameters and increase the $\tilde{\chi}$. In the absence of correlations provided by the AMS-02 collaboration we follow a conservative approach and assume uncorrelated uncertainties, adding statistical and systematic contributions in quadrature for each data point as explained above. In contrast, the quality of the fit to p and He Voyager data is slightly worse with a $\tilde{\chi} = 2 - 3$. However, the Voyager data are at very low energy, below the main focus of this work. A better fit of those data typically would require an additional low-energy break in the injection spectra [341]. In the end our models, except for $\texttt{Reacc}_{30}$ `Inj`, does not perfectly fit the highest energy data points, especially the N spectra.

4.5 Propagation and cross section parameters

In this Section we report the results on the propagation parameters as derived from the fits to the nuclear data. We start discussing the results of the `Conv` $v_{0,c}$ model for different values of L. The injection spectra of primaries are well constrained. For $L \geq 2$ kpc, γ_p is very similar and converges to values between 2.36 and 2.37, while for smaller L is softens up to 2.40. We find that the injection slope for He and CNO are significantly different from p by about 0.055 and 0.02, respectively.

In contrast, the diffusion coefficient changes significantly as function of L, with a major impact on its normalization D_0. This is due to the well-known degeneracy between L and D_0 [116] as already discussed in Section 1.3.3. By fitting a power law to the fit results for $L \in [0.5, 6]$ kpc we obtain the empirical relation:

$$D_0(L) = 4.70 \cdot 10^{27}\,\mathrm{cm}^2/\mathrm{s} \left(\frac{\mathrm{L}}{\mathrm{kpc}}\right)^{1.08\pm0.01} . \tag{4.5}$$

The slope of 1.08 ± 0.01 is close to 1 indicating that a L and D_0 are almost direct proportional to each other. We note that for large L the relation breaks down because the height of the Galactic halo starts to be comparable to the radial size of the Galaxy. We see that already at $L = 8$ kpc this relation starts to break, explaining why we did not include it in the fit of Equation 4.5. Next to the strong correlation of D_0 and L there is a smaller correlation between $v_{0,c}$ and L. The best-fit values of $v_{0,c}$ increase as a function of L, namely, we find 9 km/s for $L = 0.5$ kpc and 14 km/s for $L = 8$ kpc. Moreover, for fixed L there is a small anticorrelation between D_0 and $v_{0,c}$ meaning that for smaller values of v_c it is possible to have larger values of D_0.

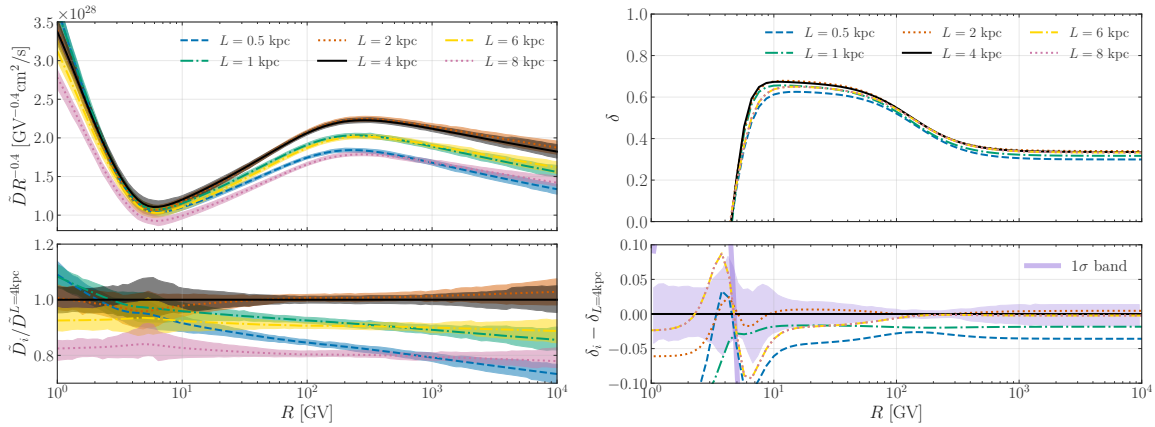

Figure 4.2: Left Panel: shape of the diffusion coefficient rescaled as $\tilde{D}(R)R^{-0.4}$ as a function of R found from the fit to the nuclei data for different values of L. The value of D_0 is rescaled at $L = 4$ kpc (see the text for details). The bottom part of the plot shows the ratio between the value obtained in the different cases with respect to the one obtained in the case where $L = 4$ kpc. The bands represent the 1σ C.L. band obtained from the fit to CR data in each case. Right panel: slope of the diffusion coefficient $\delta(R)$ as a function of rigidity, as selected by the fit to the nuclei data. The bottom part of the plot shows the difference between the value of δ obtained in the different cases with respect to the one where $L = 4$ kpc. The purple band represents the 1σ C.L. band obtained from the fit to CR data.

The shape of the diffusion coefficient as a function of rigidity is very similar for all L, as we show in Figure 4.2. In order to focus on the shape rather than the normalization, we use Equation 4.5 to rescale all the diffusion coefficients to $L = 4$ kpc, more specifically, we define the rescaled diffusion coefficient: $\tilde{D} = (4\,\text{kpc}/L)^{1.08}D$. All the curves in the left panel of Figure 4.2, except the case with $L = 8$ kpc, which is not fitted, have the same normalization within the 1σ error band at 4 GV, where the value of D_0 is fixed. The differences at lower and higher rigidities are due to small differences in the best-fit values of the slope parameters. The case for $L = 8$ kpc has a 20% normalization shift with respect to the other cases because, as explained before, the correlation between D_0 and L breaks for large values of L. In order to compare the shape of $D(R)$ we plot in the right panel of Figure 4.2 the slope of the function defined as $\delta(R) = dD/dR$. As clearly shown in the Figure, the slope of the diffusion coefficient is very similar in all the tested cases and also with respect to the results in Refs. [331, 88].

In Figure 4.3 we show the interplay between the value of L and the normalization of the Be cross section. We do this exercise for the `Conv` $v_{0,c}$ model. In the upper panel the points show the evidences obtained from CR fits with L as a fixed parameter. Instead, for the cases with fixed Be cross section normalization we allow L as a free parameter. The connection between the evidence with free and fixed L can be derived as follows.

Let us denote with $\boldsymbol{\theta}$ all fit parameters except L. If L is a fixed parameter the evidence is given by:

$$Z_L = \int d\boldsymbol{\theta}\; p(D|\boldsymbol{\theta}, L)p(\boldsymbol{\theta})\,. \tag{4.6}$$

On the other hand, if L is a free parameter in the fit, the posterior probability for L is defined by

$$\begin{aligned} p(L|D) &= \frac{\int d\boldsymbol{\theta}\; p(D|\boldsymbol{\theta}, L)p(\boldsymbol{\theta})p(L)}{\int d\boldsymbol{\theta} dL\; p(D|\boldsymbol{\theta}, L)p(\boldsymbol{\theta})p(L)} \\ &= \frac{p(L)}{Z}\int d\boldsymbol{\theta}\; p(D|\boldsymbol{\theta}, L)p(\boldsymbol{\theta})\,, \end{aligned} \tag{4.7}$$

assuming that the prior of L factorizes (i.e. is uncorrelated) from $\boldsymbol{\theta}$. It is thus possible to extract the equivalent of the evidence with fixed L:

$$Z_L = \frac{p(L|D)Z}{p(L)}\,, \tag{4.8}$$

where Z is the evidence of the fits with free L.

Among the tested cases for L the best propagation model is the one for $L = 8$ kpc. In fact, we can see from the top panel of Figure 4.3 that the smaller is L and the worse is the fit. We expect however that the Bayesian evidence Z_L has a plateau for $L > 8$ kpc. Taking the statistical results for L at face value, our findings can be used to put a frequentist lower limit for L which is at the level of 4 kpc at 5σ C.L. The ratio of the Bayesian evidence between the case with $L = 4$ kpc and 8 kpc is about 2.6×10^4, similarly to the result obtained in the frequentist statistical framework on the lower limit for L. This result is qualitatively compatible with the one shown in Ref. [326].

The results for L are affected by the uncertainties on the nuclear cross sections, in particular the ones for the Be production. The β-decay of ^{10}Be to ^{10}B in a $\tau_{1/2} = 1.37$ Myr alters both the Be and the B fluxes [86, 346, 88, 89]. Given their short lifetime, the radioactive clocks such as ^{10}Be can be used to set bounds of the thickness of the diffusive halo [86]. The impact of ^{10}Be is maximal in the ^{10}Be/^{9}Be ratio, but can be sizeable also in the Be/B ratio.

In the bottom panel of Figure 4.3 we report the best-fit value for the parameter $A_{\rm XS} \to$ Be and $A_{\rm XS} \to$ B that we obtain when we perform the fit fixing L, testing different values. We remind that the parameters $A_{\rm XS} \to$ Be and $A_{\rm XS} \to$ B remormalize the nuclear cross sections implemented in GALPROP for the Be and B production. We can see that $A_{\rm XS} \to$ Be takes values of the order of 0.95 when $L = 0.5$ kpc and increases

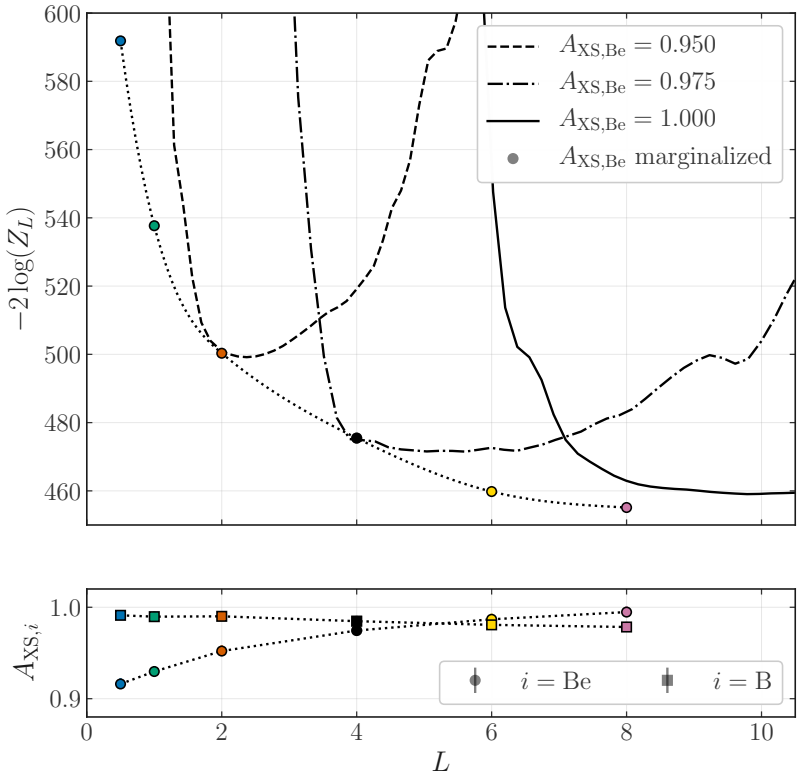

Figure 4.3: Evidence as function of L. The dots combine the results of the six fits of the `Conv` $v_{0,c}$ model to construct the posterior. Additionally, we show the evidences of L for different fixed values of the Be cross section renormalization (this is rescaled from the posteriors, see text for details). In the bottom panel, we display the renormalization factors for Be and B production cross sections within the `Conv` $v_{0,c}$ model for different L, i.e. in correspondence of the dots in the upper panel.

with L reaching a plateau at 1 for $L > 6$ kpc. This is expected because ^{10}Be is the only isotope with a decay time comparable to the size of the diffusive halo. Therefore, the exact value of $A_{\rm XS} \to$ Be can affect the best-fit value of L in our results.

Due to the scarce knowledge of the cross sections for the production of Be, B and Li, we marginalize over the cross section parameters assuming them as nuisance parameters. In particular, values of these renormalizations of the order of 10%, which are reasonable given the current collider data, bring very different best-fit values of the diffusive halo. In order to demonstrate this, we perform a fit to the data by fixing the cross sections for the production of B, Be and Li, and leaving free the value of L. We work with the model `Conv` $v_{0,c}$ and we fix $A_{\rm XS} \to$ B, $A_{\rm XS} \to$ Li, and $\delta_{\rm XS} \to$ B, Be, Li to the best-fit values reported in Table I of Ref. [5]. For $A_{\rm XS} \to$ Be we test three different values of 0.95, 0.975 and 1.00. We find that for this three possibilities the best-fit values of L are: $2.4^{+0.2}_{-0.3}$ kpc, $5.4^{+1.0}_{-0.7}$ and $10.8^{+1.3}_{-1.9}$ kpc, respectively. The Bayesian log-evidences we obtain

for each of the three tested cases are -247.9, -232.7 and -225.6 respectively, showing that the models with large L are statistically favoured. The propagation parameters are in good agreement with the values obtained for fixed L at 2, 4 and 8 kpc.

We note that a purely statistical interpretation of the L dependence might not cover the whole story. The CR propagation model is phenomenological and not completely derived from first principles. Therefore, some level of discrepancy between model and data is expected. This might lead to some bias which is compensated by the cross section nuisance parameters. A robust conclusion will rely on a better determination of the cross section. For example, if the Be cross sections turn out to be five percent smaller than the default assumed in this thesis, L will be constrained to smaller values around 2 kpc (see Figure 4.3). In terms of the absolute χ^2 also $L \in [2, 4]$ kpc provides a good fit to the data. So, all in all we find a statistical preference for large values of L while noting that because of systematic effects also smaller values around 2 kpc should not be completely discarded.

4.6 Secondary lepton predictions

We here detail how we evaluate the uncertainties in the secondary e^+ and e^- prediction coming from the new propagation models and from the production cross sections. We take the local CR flux found by fitting the data and then we compute, within the same propagation setup, the secondary $e^\pm$ fluxes due to the collision of CRs with the atoms of the ISM as in Equation 3.1. For each propagation model, the mean and the 1σ Bayesian uncertainty are computed. This represents the statistical uncertainty connected to the fit to the CR propagation parameters only. This procedure is repeated for each propagation model tested. Additional uncertainty coming from the $e^\pm$ production cross section is considered separately as obtained in Section 3.2 and summed in quadrature to build the final uncertainty bands for the predictions. We believe this choice to be conservative enough, since the propagation and cross section uncertainties can be considered independent and Gaussian to a good approximation. Additional systematic uncertainties connected for example to the size of the diffusion halo or to the choice of the propagation model are discussed separately, and are found to be the dominant ones.

In Figure 4.4 (left panel) we display the predictions for the secondary e^+ flux obtained with all the different models introduced in Section 4.2 for L fixed to 4 kpc. We show the best-fit and 1σ uncertainty band found in the Bayesian framework. The models `Conv` $v_{0,c}$, $\texttt{Reacc}_0$ and $\texttt{Reacc}_{10}$ predict a similar flux in the entire energy range. In

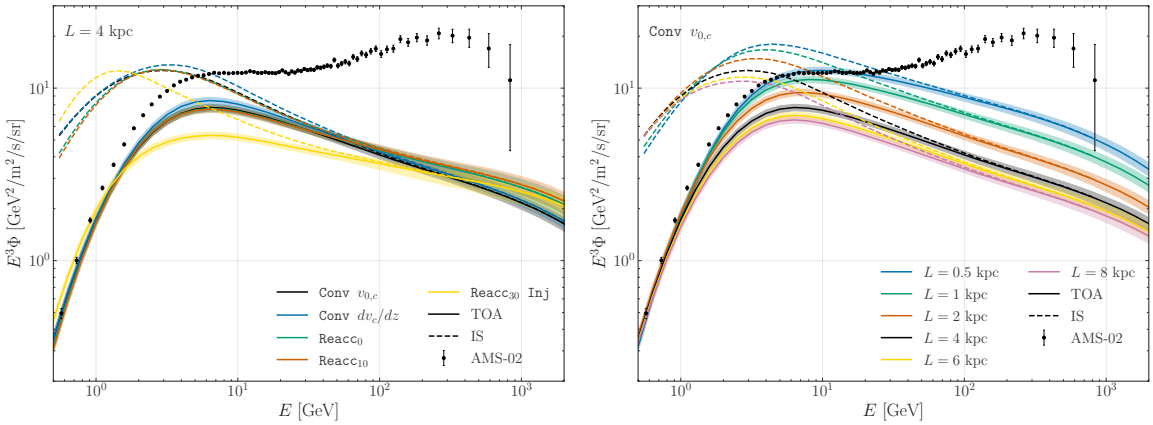

Figure 4.4: Left panel: prediction for the secondary e^+ flux at Earth as obtained for all the propagation model tested in this work (see Section 4.2) when fixing $L = 4$ kpc. For each case, we show the IS (dashed lines) and modulated TOA flux (solid lines). We display the best-fit and 1σ Bayesian uncertainty band. AMS-02 data are included for comparison. Right panel: prediction for the e^+ flux at Earth within the model `Conv` $v_{0,c}$ when varying the size of diffusive halo from $L = 0.5$ to 8 kpc.

particular, at the lowest measured energies the secondary fluxes are comparable to the e^+ data, while they are increasingly smaller with respect to the AMS-02 measurements at larger energies. At 5 GeV the secondary e^+ can account for about $50 - 70\%$ of the data while at the highest energy they are about $20 - 30\%$ of the measured e^+ flux.

The `Reacc`$_{30}$ `Inj` provides a smaller flux by a factor of about 1.6 between 2 and 100 GeV with respect to the other cases, related to the fact the model converges to a larger value for the diffusion coefficient. The larger diffusion coefficient in turn is partly obtained because we allow for larger uncertainties in the nuisance parameters of the nuclei fragmentation cross sections. Moreover, this model is the only one that slightly overshoots the lowest AMS-02 data point at about 500 and 700 MeV. This result is expected because strong reacceleration significantly increases the lepton fluxes at low energies; similar results have been obtained by Ref. [87] in the QUAINT model. All models predict a similar flux of secondary e^+ at energies larger than 100 GeV, which is about a factor of five below the data. The variation at 1 TeV is about a factor of two from the minimum to the maximum contribution.

In Figure 4.4 (right panel) we show the e^+ flux predicted for different values of the diffusive halo size between 0.5 and 8 kpc within the `Conv` $v_{0,c}$ model. Above about 5 GeV, the secondary e^+ $E^3\,\Phi$ flux decreases systematically with L. This can be understood from the well-known degeneracy between L and the normalization of the diffusion coefficient [116]. To a first approximation, CR nuclei data only constrain the ratio L/D_0. In contrast, $e^\pm$ suffer from stronger energy losses which restrict them more

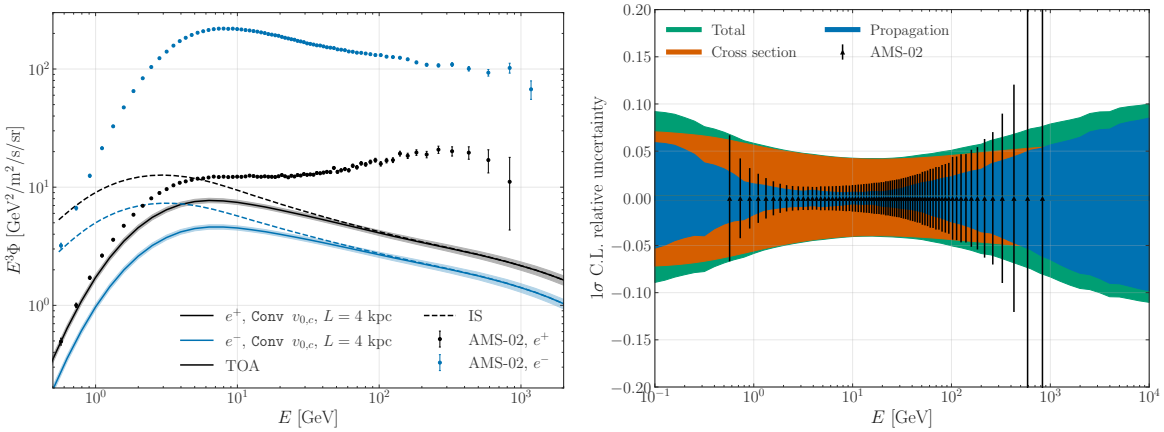

Figure 4.5: Left panel: flux of e^+ (black line and band) and e^- (blue line and band) obtained for the model `Conv` $v_{0,c}$ with $L = 4$ kpc. We show the AMS-02 data for e^+ (black data) and e^- (blue data). Right panel: uncertainty for e^+ flux due to the propagation parameters and $e^\pm$ production cross sections for the case `Conv` $v_{0,c}$ with $L = 4$ kpc. We also show the total uncertainty obtained with the sum in quadrature of the two uncertainties. For comparison, we show the errors of the e^+ AMS-02 data.

locally than nuclei, such that they do not perceive the same effect of the boundary at L as nuclei. For them the degeneracy between L and D_0 is broken and they only sense the effect of decreasing D_0, which increases the secondary flux. For $L = 0.5$ kpc the e^+ flux is at the level of the data between 0.5 to 20 GeV, while the flux for $L = 2$ kpc (4 kpc) decreases of 20% (40%) at 5 GeV. For 8 kpc, the predicted secondary flux is about 50% of the data at 5 GeV. The contribution of secondary e^+ to the highest AMS-02 energy at $E \sim$ TeV spans from few percent to 50% of the data, mostly depending on the value of L.

In Figure 4.5 (left panel) we show the flux for secondary $e^\pm$ compared to the AMS-02 data. As expected, secondary e^- have a smaller flux with respect to e^+, reflecting the charge asymmetry in the colliding CR and ISM particles. We verified that the variation of the secondary e^- with the size of the diffusive halo and propagation model follows the e^+ trends, as shown in Figure 4.4 (left panel).

In all the predictions shown in Figures 4.4 and 4.5 (left panel) we report the uncertainty band related to the fit to the CR propagation parameters and on the $e^\pm$ cross sections. We detail in Figure 4.5 (right panel) the uncertainties related to both contributions for the case `Conv` $v_{0,c}$ with $L = 4$ kpc. The propagation parameters' uncertainties are in general smaller than the cross section ones up to 1 TeV, above which they both reach 10%, and they are at the level of few % between 1 and 100 GeV, always comparable or smaller than the size of experimental errors. The latter are shown as the sum in quadrature of the AMS-02 statistical and systematic errors on the e^+ flux. Instead, the

uncertainties related to the $e^{\pm}$ production cross sections are almost energy independent and at the level of $5-7\%$.

Further uncertainties may derive from leptonic energy losses. Updated estimates of the ISRF model in the solar neighborhood [204], which well agree with the default GALPROP model, reduce significantly the uncertainties in the ISRF provided by star and dust, as compared e.g. with the uncertainties parametrized in the M1-M3 models of [206]. In addition, we have verified that accounting for the 3D structure of the ISRF as recently modeled within GALPROP [203] by using the two benchmarks named F98 and R12, provides consistent results. This is due to the fact that the local photon densities are well constrained. Finally, a consistent estimate of the uncertainties in the synchrotron losses coming from the Galactic magnetic field model and its local value should proceed through a combined fit of the CR propagation models and of multi-wavelength data, such as radio, microwave and γ-ray emissions [338].

The ISM target gas density is another crucial ingredient for the computation of the secondary e^+ in Equation 4.2. The impact of updated models for the 3D ISM structure on CR was recently studied in Ref. [202], finding variations up to a factor of two for the column density of the local gas. In the analysis of CR nuclei data, we expect that the ISM density is effectively degenerate with the value of the diffusion coefficient. As a confirmation of this hint, we have verified that varying the ISM gas model among the ones available within GALPROP [121] in 2D and 3D, secondary CRs such as e^+ are affected in the same way, and the ratio of secondary e^+ to B remains constant to a good approximation. These results suggest that the impact on the $e^{\pm}$ flux by varying the ISM as well as changing from a 2D to a 3D modeling would be very moderate.

4.7 Discussion and summary

In this Section we discuss our results in the context of recent literature on secondary CR e^+, and we outline their broader implications. We also assess possible further uncertainties on our predictions.

A first comparison can be made with what obtained with GALPROP in Ref. [347], and specifically with their model named B', which includes reacceleration and high rigidity break in the diffusion coefficient with $L = 3.61$ kpc. Our results within $\texttt{Reacc}_{30}$ `Inj` model are lower by a factor of about 1.5 at 10 GeV and of about a factor of two at few GeV. As for the `Conv` $v_{0,c}$ model, we obtain similar results at tens of GeV. At lower energies, their model, including a reacceleration velocity of about 20 km/s, drives higher fluxes of secondary IS e^+, larger by a factor up to 1.5 at 2 GeV, and indeed

overshooting the AMS-02 data.

Predictions obtained with the semi analytical propagation models SLIM, BIG and QUAINT as defined in Ref. [87] compare to our results as follows. The case `Conv` $v_{0,c}$ with $L = 4$ kpc is a factor of two larger at about 5 GeV with respect to their BIG-MED, which has zero reacceleration and a best-fit convection velocity around zero. Similar differences are found with respect to the SLIM model. When comparing the QUAINT model results with our $\texttt{Reacc}_{30}$ `Inj`, which both include significant reacceleration velocities, we consistently find lower e^+ fluxes. We note that these semi-analytical propagation models assume different shapes for the diffusion coefficients as a function of rigidity, for the source terms, as well as of course the production cross sections, which can be the reasons of the discrepancies. Further predictions for the secondary e^+ at Earth, obtained with semi-analytic models in Ref. [207], using primary CR fluxes from Ref. [348], and Ref. [325], derived from a fit to the AMS-02 data for the B/C, $\bar{p}$ and p, are very similar to our predictions within the $\texttt{Reacc}_{30}$ `Inj` propagation model.

Authors of [280] also provided a new evaluation of secondary e^+ using the DRAGON code, finding similar results with our $\texttt{Reacc}_{30}$ `Inj` model. However, the main focus of the paper was to test different e^+ cross-section models, gas distribution, halo size, and solar modulation, rather than different propagation models.

Our results indicate that, within the propagation model explored here, an excess of e^+ is present at energies larger than a few GeV, where the secondary flux starts to be less than 50% than the data, consistently with a number of previous works [349, 331, 350]. We proved that for fixed values of $L \sim 4$ kpc, e^+ cross sections uncertainties, presented in Section 3.2, are too small to explain the mismatch at low energies. Uncertainties in the flux due to cross sections amount to $5 - 7\%$, reflecting directly the results on the hadronic cross sections. For a fixed value of L, our results reduce significantly all the other class of uncertainties with respect to the state of the art, in particular regarding $e^\pm$ cross sections, and is a major finding of our work. However, we should notice that a larger secondary production is still not firmly excluded for smaller values of L, even if they correspond to worse fits to current nuclei CR data. From a study of the nuclear fragmentation cross section, we can conclude that measurements for the Be (and its isotopes) nuclear cross sections are needed with a precision below 5% in order to estimate the size of the diffusive halo with a precision better than 50%. In this way we would be able to break the degeneracy between L and D.

Chapter 5

Contributions of pulsars to the positron flux

In the previous Chapter 4, we combined the physics of fundamental interactions with the propagation of CRs on kpc and so macroscopic scales, obtaining new predictions on the secondary e^+ flux. By combining secondary e^+ and the flux coming from primary sources it is possible to constrain the characteristics required for these sources in orther to explain the e^+ AMS-02 data. In particular in this Chapter we discuss how the e^+ excess can be explained considering the contribution from pulsars. This Chapter is based on Ref. [1].

5.1 Introduction

Among the investigated explanations for the e^+ excess [351, 352, 322, 353, 354, 355, 356, 357, 324, 358, 359, 360, 361, 93, 99], pulsars have been consolidating as significant factories of high-energy CR $e^\pm$ in the Galaxy (see Section 1.3.2).
The $e^\pm$ fluxes from Galactic pulsars are expected to contribute to the e^+ data and to the $e^+ + e^-$ spectrum as well. Many authors in recent years (e.g. [362, 207]) included the contribution from catalog pulsar or simulations to model the $e^+ + e^-$ measurements of *Fermi*-LAT [135], AMS-02 [131, 132], DAMPE [37] and CALET [34]. However, the AMS-02 e^+ data up to 1 TeV are currently the most precise observable to constrain the characteristics of Galactic pulsar populations.
Several independent works have demonstrated that pulsar models can provide a good description of AMS-02 e^+ data. This result has been obtained both by considering the contribution of few nearby sources, as well as the cumulative emission from pulsars observed in existing catalogs [351, 358, 324, 363, 350, 208] or in simulations [361,

207, 364]. While energy losses limit the distance traveled by high-energy $e^{\pm}$ to few hundreds of pc (see Section A.1 of the Appendix), where we expect few Galactic sources contributing significantly, current source catalogs might be not complete. Previous computations, such as Ref. [324], calculating the contribution of e^{+} from the ATNF catalog sources could therefore suffer for underestimation due to the incompleteness of the catalog. Simulations of the Galactic source population of pulsars are needed to extensively test the pulsar interpretation of the observed e^{+} flux in order to overcome the limitations of previous studies.

The details of the $e^{\pm}$ production, acceleration and release from pulsars and their PWN are yet not fully understood (see Section 1.3.2), as well as the spatial and energetic distribution of pulsar [365, 366]. High-precision e^{+} data can now be used to constrain the main properties of the Galactic pulsar population and of PWN acceleration. We simulate a large number of realizations for the Galactic pulsar population, implementing different updated models for the source distribution, particle injection and propagation which reproduce ATNF catalog observations, instead of *ad-hoc* realizations of pulsar properties. For each mock galaxy, we compute the CR e^{+} flux at the Earth from the resulting PWNe population. We then fit our predictions to the AMS-02 data in order to determine the physical parameters of these populations. We also inspect the properties of individual sources which are able to explain the observed e^{+} flux, and we measure the average number of pulsars necessary to fill the gap between the e^{+} secondary flux and AMS-02 data.

5.2 Positrons from Galactic pulsars

In this Section we illustrate our model for the $e^{\pm}$ production from PWNe, and we also briefly remind here the basics of $e^{\pm}$ propagation in our Galaxy.

5.2.1 Injection of electrons and positrons from pulsars

Magnetic dipole radiation is believed to provide a good description for the pulsar observed loss of rotational energy (see Section 1.3.2) that powers the emission of $e^{\pm}$. We consider a model in which $e^{\pm}$ are continuously injected at a rate that follows the pulsar spin-down energy. While 'pulsar' and 'PWN' have both been used in literature to indicate the $e^{\pm}$ source, we here use 'pulsar' when referring to the simulated properties of pulsar at birth, while PWN is used when referring to the $e^{\pm}$ primary source.

The injection spectrum $Q(E,t)$ of $e^{\pm}$ at energy E and time t is described as:

$$Q(E,t) = L(t)\left(\frac{E}{E_0}\right)^{-\gamma_e}\exp\left(-\frac{E}{E_c}\right) \tag{5.1}$$

where the cut-off energy E_c is fixed at 10^3 TeV, $E_0 = 1$ GeV and γ_e is the $e^{\pm}$ spectral index. The magnetic dipole braking $L(t)$ is described by the function:

$$L(t) = \frac{L_0}{\left(1+\frac{t}{\tau_0}\right)^{\frac{n+1}{n-1}}} \tag{5.2}$$

where τ_0 is the characteristic time scale and n defines the magnetic braking index. Alternatively the injection spectrum can be parametrized with a broken power-law [233, 238], with a break at energies of the order of tens to hundreds GeV, a slope below the break ≈ 1.4 and above the break ≈ 2.2, which is compatible with multiwavelenght observations of PWNe, but with large uncertainties on the parameters [367]. Here we adopt an effective approach using Equation 5.1, avoiding the increasing of the number of degrees of freedom. The possible effects of this assumption will be discussed in Section 5.4.3. The total energy emitted by the source only into e^+ is given by:

$$E_{tot} = \eta W_0 = \int_0^T dt \int_{E_1}^{\infty} dE E Q(E,t) \tag{5.3}$$

through which we obtain the value of L_0, fixing E_1=0.1 GeV [368, 369]. The parameter η encodes the efficiency of conversion of the spin-down energy into e^+ (which is half of the efficiency of conversion into $e^{\pm}$). W_0 is the initial rotational energy of a pulsar with a moment of inertia I (typically assumed to be 10^{45} g cm^2, as obtained from canonical neutron star values) and rotational frequency $\Omega_0 = 2\pi/P_0$:

$$W_0 = E_{\mathrm{rot},0} = \frac{1}{2} I {\Omega_0}^2 \,. \tag{5.4}$$

The spin-down luminosity $\dot{E} = dE_{\mathrm{rot}}/dt$ of a pulsar is the rate at which the rotational kinetic energy is dissipated:

$$\dot{E} = \frac{dE_{\mathrm{rot}}}{dt} = I\Omega\dot{\Omega} = -4\pi^2 I \frac{\dot{P}}{P^3} \,. \tag{5.5}$$

Assuming a small deviation from the dipole nature of the magnetic field B of the pulsar,

the evolution of the star may be parameterized as [370]:

$$P^{n-2}\dot{P} = ak(B\sin\alpha)^2 \tag{5.6}$$

where the angle $\alpha > 0$ describes the inclination of the magnetic dipole with respect to the rotation axis, a is a constant of unit s^{n-3} and k takes the value of 9.76×10^{-40} $\mathrm{s\,G^{-2}}$ for canonical characteristics of neutron stars. The spin-down luminosity evolves with time t as in Equation 5.2:

$$\dot{E}(t) = \dot{E}_0 \left(1 + \frac{t}{\tau_0}\right)^{-\frac{n+1}{n-1}}. \tag{5.7}$$

From this equation, one can notice that the pulsar has roughly a constant energy output from its birth till $t = \tau_0$, when the energy output starts to decrease as $\dot{E} \sim t^{-(n+1)/(n-1)}$. Finally, the prediction on τ_0 is derived to be:

$$\tau_0 = \frac{P_0}{(n-1)\dot{P}_0}. \tag{5.8}$$

In our benchmark model we consider only sources with ages above 20 kyr, since $e^{\pm}$ accelerated to TeV energies in the termination shock are believed to be confined in the nebula or in the SNR until the merge of this system with the ISM, estimated to occur some kyr after the pulsar formation (see Section 1.3.2). We thus leave out sources for which the $e^{\pm}$ pairs might be still confined in the parent remnant. However, this effective treatment does not account for possible spectral or time-dependent modifications of the released particles. To understand the consequences of this assumption on the interpretation of the AMS-02 e^+ flux, we also test the hypothesis that only the $e^{\pm}$ produced after the escaping of the pulsar from the SNR contribute to the flux at the Earth. Following Ref. [207], we define t_{BS} as the time at which the source leaves the parent SNR due to its proper motion and eventually forms a bow-shock nebula. The escape time of the pulsar from the remnant is described by:

$$t_{BS} \simeq 56 \left(\frac{E_{SN}}{10^{51}\mathrm{erg}}\right)^{\frac{1}{3}} \left(\frac{n_0}{3\ \mathrm{cm^{-3}}}\right)^{-\frac{1}{3}} \left(\frac{v_k}{280\ \mathrm{km/s}}\right)^{-\frac{5}{3}} \mathrm{kyr} \tag{5.9}$$

where n_0 is the ISM density taken to be 3 or 1 $\mathrm{cm^{-3}}$, $E_{SN} = 10^{51}$ erg is the energy emitted by the SN explosion and v_k is the birth velocity of the pulsar. The formalism is reported in Ref. [371], to which we refer for further details.

5.2.2 Propagation of electrons and positrons to the Earth

Once charged particles are injected in the Galaxy, they can propagate and eventually reach the Earth. The diffusion equation we consider is adapted from Equation 1.6, which reduces, for $e^{\pm}$ above a few GeV, ignoring convection and reacceleration and transforming from momentum to energy dependence, to:

$$\frac{\partial \psi(\mathbf{r}, E, t)}{\partial t} - (D(E)\boldsymbol{\nabla}\psi_i) + \frac{\partial}{\partial E}\left(\frac{\mathrm{d}E}{\mathrm{d}t}\psi_i\right) = Q(\mathbf{r}, E, t) \tag{5.10}$$

We solve the transport equation following semi-analytical methods based on the Green function approach introduced in Refs. [372, 373] and then developed in Refs. [206, 116, 363, 207]. Within this approach, the solution is found by computing the Green function of Equation 5.10 which describes the probability for a cosmic-ray $e^{\pm}$ produced at a location $\mathbf{r_s}$ in the Galaxy, and with an energy E_0, to be detected at $\mathbf{r}$ with energy E. A numerical solution is required only for diffusion in energy space. Also Bessel expansion methods [116] permit a 2D analytical model, and are based on the cylindrical symmetry of the diffusive halo. The semi-analytical model is simplified compared to numerical codes like GALPROP and DRAGON. We expect that more complex features of the Galactic environment and its geometry, like small scale inhomogeneities in the propagation that you can implement in numerical solutions, have at most a mild impact on the problem. In fact, due to energy losses, $e^{\pm}$ that reach the Earth are produced predominantly within a few kpc from the Sun (see Section A.1 of the Appendix). In this small region of the Galaxy, the effects that control the transport of CR are unlikely to have a strong spatial dependence, and therefore our semi-analytical approach is a fair approximation. In addition, with respect to fully numerical methods, the semi-analytical model has faster execution times and allows for larger parameter-space scans.

The number density per unit time, volume $\psi_e(\mathbf{r}, E, t)$ of $e^{\pm}$ at a position $\mathbf{r}$ in the Galaxy, observed energy E and time t, which is the solution to the reduced propagation equation Equation 5.10, is given by [238]:

$$\psi(\mathbf{r}, E, t) = \int_0^t dt' \frac{b(E_0)}{b(E)} \frac{1}{(\pi\lambda^2(t', t, E))^{\frac{3}{2}}} \exp\left(-\frac{|\mathbf{r} - \mathbf{r_s}|^2}{\lambda^2(t', t, E)}\right) Q(E_0, t') \tag{5.11}$$

where the integration over t' accounts for the PWN releasing $e^{\pm}$ continuously in time. The energy E_0 is the initial energy of $e^{\pm}$ that cool down to E in a loss time $\Delta\tau$:

$$\Delta\tau \equiv \int_E^{E_0} \frac{dE'}{b(E')} = t - t_{obs}. \tag{5.12}$$

The $b(E) = -dE/dt$ term is the energy loss rate, $\mathbf{r_s}$ indicates the source position, and λ is the typical propagation length defined in Section A.1 of the Appendix. The $e^{\pm}$ energy losses include ICS off the ISRF and the synchrotron emission on the Galactic magnetic field. The flux of $e^{\pm}$ at the Earth for a source of age T and distance $d = |\mathbf{r}_{\odot} - \mathbf{r_s}|$ is given by:

$$\Phi_{e^{\pm}}(E) = \frac{c}{4\pi}\psi_e(E, \mathbf{r} = \mathbf{r}_{\odot}, t = T). \tag{5.13}$$

Most of the analysis here reported was performed before the new results on secondary e^+ and on propagation in the Galaxy outlined in Chapter 4. The benchmark case considered in the analysis is based on the propagation parameters derived in Ref. [325] from a fit to the latest AMS-02 data for the B/C, $\bar{p}$ and p data. Here the diffusion coefficient is taken as a simple power-law in energy $D(E) = D_0 E^{\delta}$. We label this model as *Benchmark-prop*, where $D_0 = 0.042$ kpc^2/Myr and $\delta = 0.459$. The value of L is fixed to 4 kpc, which is compatible with what found in Chapter 4. Energy losses are computed on the interstellar photon populations at different wavelengths following Ref. [204], by taking into account the Klein-Nishina formula for ICS, and on the Galactic magnetic field with intensity $B = 3$ μG.

In the previous Chapter we considered more refined models for the diffusion term. In the energy range here considered (10 GeV$-$1 TeV), a different diffusion model does not have a large impact on the final analysis. We also tested the *SLIM-MED* model derived in Ref. [327], characherized by a low and high energy break, with the ISRF taken from Ref. [206] and $B = 1$ μG, in order to test the dependence of our results on the different propagation setup adopted. We will discuss preliminary results obtained with the diffusion coefficient found for the propagation model named `Conv` $v_{0,c}$ described in Chapter 4. We implement solutions without boundaries both in the radial and the vertical directions. In fact, the infinite halo approximation has been widely used to compute the flux from single sources located in the Galactic plane in Refs. [350, 374, 364]. As we will show in the results, the most important sources are encompassed within a few kpc from the Earth, due to the small distance travelled by $e^{\pm}$ caused by energy losses, justifying the use of the infinite halo approximation. Therefore, the parameter L is not relevant for the computation of the e^+ flux from pulsars. For completeness, for the benchmark case, we checked that our results does not change considering vertical boundaries at $L = 4$ kpc.

Pulsar property	**Simulated quantity**	**Benchmark**	**Variations**
Age	T	Uniform [0, t_{max}]	-
Spin-down		`CB20`[366]	`FK06`[53]
	P_0	Gaussian [0.3s; 0.15s]	-
	$\log_{10}(B)$	Gaussian [12.85G; 0.55G]	Gaussian [12.65G; 0.55G]
	n	Uniform [2.5-3]	Constant [3]
	$\cos\alpha$	Uniform [0-1]	Constant [0]
$e^{\pm}$ injection	γ_e	Uniform [1.4-2.2]	-
	η	Uniform [0.01-0.1]	-
Radial distribution	$\mathbf{r}$	$\rho_L(r)$ [365]	$\rho_F(r)$[53]
Kick velocity	v_k	-	`FK06VB` [53]

Table 5.1: Summary of the parameters from which we build the mock pulsar catalogs. We report the pulsar simulated quantities (first two columns), the distributions adopted in their simulation, with the boundary of their validity range, for our benchmark case (`[ModA]`, third column), as well as the tested variations (last column). See Section 5.3 for details.

5.3 Simulations of Galactic pulsar populations

We simulate Galactic pulsars following the injection and propagation model described in Section 5.2. For each realization we compute the e^+ flux from every PWN. In each simulation, the total number of sources is fixed at $N_{\rm PSR} = t_{max}\dot{N}_{PSR}$, where t_{max} is the maximum simulated age and $\dot{N}_{PSR}$ is the pulsar birth rate. Different estimates for the Galactic $\dot{N}_{PSR}$ range from one to four per century [51, 52, 53]. We here assume the maximum age of the sources to be $t_{max} = 10^8$ yr, and $\dot{N}_{PSR} = 0.01$ yr^{-1}. However, we have checked that $t_{max} = 10^9$ yr does not change the conclusions of this Chapter.

In order to compute the e^+ flux at the Earth for each mock source, we need to specify its position in the Galaxy, its age and the source term $Q(E, t)$ (see Equation 5.1). Specifically, the fundamental parameters of each simulation are: T, P_0, B, n, α, γ_e, η and the position $\mathbf{r}$ in Galactocentric coordinates. For a specific set of simulations, we also simulate the birth-kick velocity v_k. A summary of the simulated quantities is illustrated in Table 5.1 and outlined in what follows.

First of all, the simulation assigns to each mock pulsar an age T extracted uniformly between $t = 0$ and t_{max}. Then, by extending the functions implemented in the Python module `gammapy.astro.population` [375, 376], we sample the values of P_0, B, n and α from the distributions provided in Ref. [366] (`CB20`), which is our benchmark model. Specifically, P_0 is simulated according to a Gaussian distribution with $P_{0,mean} = 0.3$ s

and $P_{0,std} = 0.15$ s. We also impose a lower bound on $P_0 = 0.83$ ms, as physically motivated in Ref. [377]. The magnetic field is simulated following a Gaussian distribution for $\log_{10}(B)$, with $\log_{10}(B)_{mean} = 12.85$ G and $\log_{10}(B)_{std} = 0.55$ G. The values of n and $\cos\alpha$ are taken from uniform distributions, respectively in the range [2.5-3] and [0-1] according to Ref. [366]. We note that from the simulated values of P_0, B, n, α we derive for each pulsar W_0 and τ_0 through Equations 5.4 and 5.8. The spectral index γ_e of accelerated particles is uncertain, and may vary significantly for each PWN [75, 351]. Since the spirit of this work is to be as agnostic as possible in constraining the properties of Galactic pulsars population using directly the AMS-02 data, the spectral index has been simulated from a broad, uniform distribution. Specifically, the lower and upper values of the uniform distribution are [1.4-2.2], and have been chosen as in Ref. [364] to approximately bracket the range inferred from multi-wavelenght observations of PWN, as well as to test the range of values considered in previous works (see e.g. [361]). We also note that since PWN observations suggest source-by-source variations, it is difficult to strictly fix an interval for the spectral index. Finally, the value of η for each source is sampled from a uniform distribution in the range [0.01-0.1].

In order to assess the effect of different distributions for P_0, B, n and α, we consider the model in Ref. [53] (`FK06` hereafter). While P_0 follows the same distribution of `CB20`, $\log_{10}(B)$ is taken from a Gaussian distribution with $\log_{10}(B)_{0,mean} = 12.65$ G and $\log_{10}(B)_{0,std} = 0.55$ G, while n=3 and $\sin\alpha$=1 for each source. We note that both `CB20` and `FK06` models have been calibrated to reproduce the characteristics of the sources detected in the ATNF catalog [378], like the P, $\dot{P}$, B, flux densities at 1.4 GHz, Galactic longitudes and Galactic latitudes distributions. `CB20` is the most updated model and considers the variation of more parameters with respect to `FK06`.

To test the scenario described by Equation 5.9, we additionally simulate for each source its birth-kick velocity, adopting its distribution as reported in [53] (`FK06VB`) and implemented in `gammapy.astro.population` [375, 376], which is the sum of two Gaussians (see their Equation 7) for each of the 3 velocity components.

5.3.1 Spatial distribution of pulsars in the Galaxy

To complete the construction of the mock catalogs of Galactic sources, the position $\mathbf{r}$ of each pulsar has to be determined. Using `gammapy.astro.population` [375, 376] we adopt the radial surface density of pulsars $\rho_L(r)$ proposed by [365]:

$$\rho_L(r) = A_1 \left(\frac{r}{r_\odot}\right) \exp\left[-C\left(\frac{r - r_\odot}{r_\odot}\right)\right]. \tag{5.14}$$

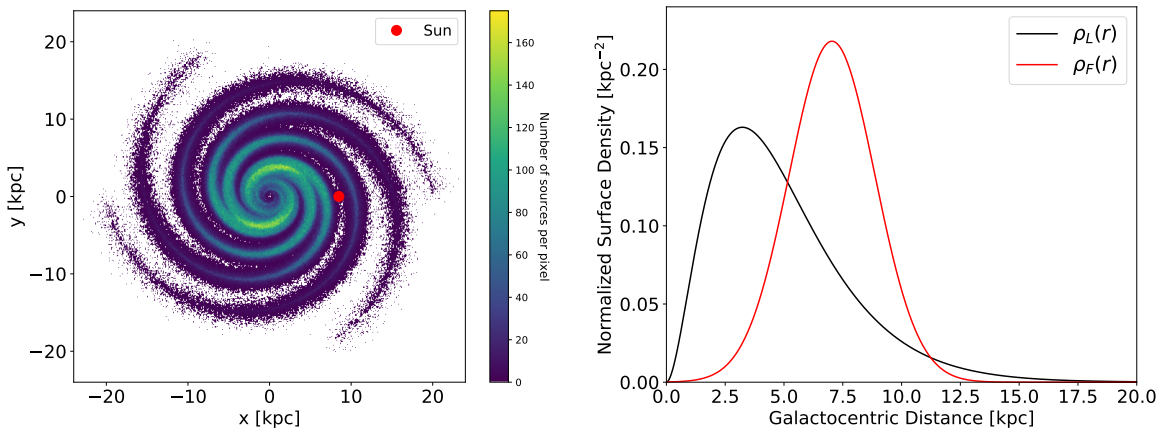

Figure 5.1: Left panel: position of pulsars in the Galactic plane (grouped in pixels of size 0.015 kpc^2) for one realization of our Galaxy obtained with $\rho_L(r)$ radial surface density [365] and the spiral-arm model of Ref. [53]. The color bar indicates the number of sources in each pixel. Right panel: the normalized radial surface densities $\rho_L(r)$ ([365], black line) and $\rho_F(r)$ ([53], red line) are reported.

As a comparison, we also consider the radial surface density $\rho_F(r)$ in [53]:

$$\rho_F(r) = A_2 \frac{1}{\sqrt{2\pi}\sigma} \exp\left(-\frac{(r-r_\odot)^2}{2\sigma^2}\right). \tag{5.15}$$

See Ref. [365, 53] for the values of the parameters. We sample the position $\mathbf{r}$ of each source combining the radial surface density with the spiral arm structure of the Milky Way of Ref. [53] (see their Table 2 for the spiral arm parameters), as implemented in `gammapy.astro.population` [375, 376]. We test only one spiral arm structure, since the most important aspect in the computation of the e^+ flux is the source density in the arms nearby the Sun, instead of the position of the arms themselves. The distance of each source is $d{=}|\mathbf{r}-\mathbf{r}_\odot|$, with $\mathbf{r}_\odot = (8.5, 0, 0)$ kpc.

In Figure 5.1 (left panel) we report the positions in the Galactic plane of the mock sources, for one configuration of our Galaxy, adopting the $\rho_L(r)$ radial surface density. Due to the fast energy-losses that affects $e^\pm$, the most relevant contribution to the e^+ flux will come from the two spiral arms that surround the Earth and that are named Sagittarius and Orion. In Figure 5.1 (right panel) we also display the $\rho_L(r)$ and $\rho_F(r)$ profiles reported in Equation 5.14 and 5.15 (normalized in order to have $\int_0^{+\infty} \rho_i(r)dr = 1$ with $i = L, F$). We note that $\rho_L(r)$ is similar to other radial distributions used in literature [379, 380], and we consider it as a good benchmark. The $\rho_F(r)$ profile effectively maximizes the effects of different radial profiles on the e^+, by setting higher pulsar densities in the two spiral arms surrounding the Earth.

5.3.2 Summary of simulation setups

We recap and label here the combinations of the different simulation setups described above and listed in Table 5.1.

- `ModA` (benchmark). Spin-down and pulsar evolution properties are taken from `CB20` [366], while the radial surface density of sources is modelled with $\rho_L(r)$ (see Equation 5.14, [365]). η and γ_e are extracted from uniform distributions, while the propagation in the Galaxy is taking into account with *Benchmark-prop* model following Ref. [325].

- `ModB` (radial distribution effect). Same as `ModA` but with the radial surface density of sources $\rho_F(r)$ instead of $\rho_L(r)$ (see Equation 5.15, [53]).

- `ModC` (spin-down properties effect). Same as `ModA`, but spin-down properties are taken from `FK06` [53].

- `ModD` (propagation effect). Same as `ModA` apart for propagation in the Galaxy, modelled as in Ref. [327] (their model *SLIM-MED*).

- `ModE` (propagation effect). Same as `ModA` apart for propagation in the Galaxy, modelled as in Chapter 4 (`Conv` $v_{0,c}$ model).

- `ModF` (kick velocity effect). Same as `ModA`, but considering only the $e^{\pm}$ emitted after the escaping of pulsars from the SNR. The birth kick velocities are sampled adopting the distribution `FK06VB` reported in Ref. [53].

5.4 Results

We describe here how we performed the fit to the data, and which are the physics results of our minimization analysis. For each simulation setup described in Section 5.3.2, we build and test 1000 simulations. All the results reported in this Section refer to the benchmark `ModA`, if not differently stated. We compute the e^+ flux at the Earth as the sum of the primary component due to PWNe emission (see Section 5.2 and Section 5.3), and a secondary component due to the fragmentation of CRs on the nuclei of the ISM, taken from Ref. [325], [327] and Chapter 4 consistently with the propagation model employed.
The secondary component enters in our fits with a free normalization factor A_S, which we generously let to vary between 0.01 and 3. This analysis was conducted prior to the stringent constraints on the production cross sections of e^+ as established in Section

3.2. The broad range considered here is justified by the fact that secondary production is significantly influenced by the diffusion coefficient associated with various sizes of the diffusive halo, denoted as L. On the other hand, in the energy range under examination (10 GeV$-$1 TeV), where energy losses dominate, the contribution from primary sources does not exhibit this pronounced dependency on the diffusion coefficient, and its sensitivity to changes in L is quite weak. Adjusting the normalization of the secondary production provides an effective means of exploring various potential values for L and, consequently, the diffusion coefficient, without the need for recalculating the primary flux, which should remain relatively unaffected by significant variations. Furthermore, since in this study we want to maintain a high level of neutrality in constraining the characteristics of the Galactic pulsar population through the AMS-02 data, we decided to adopt this extensive range of values for the parameter A_S. This choice allows us to observe which configuration reproduce better the measurements, leaving room to a wide spectrum of possibilities to be considered. We also let the total flux generated by the sum of all PWNe to be shifted by an overall normalization factor A_P. The values of A_P and A_S are obtained for each simulation with the fit procedure.
We fit AMS-02 data [131] above 10 GeV, in order to avoid strong influence from several low energy effects (see Section 1.4) and solar modulation, which is however considered following the force field approximation and leaving the Fisk potential φ free to vary between 0.1 and 1.2 GV. The comparison of our predictions with the AMS-02 e^+ data is performed by a standard χ^2 minimization procedure. We neglect the presence of correlations in the systematic errors of AMS-02 data points since the Collaboration has not provided them [131]. Moreover, we do not think the smoothness of the AMS-02 data, that is the main characteristic of the observed flux that will guide our results, would be modified significantly by such correlations.

5.4.1 Comparison to the AMS-02 positron data

The fit of the predictions for the total e^+ flux to the AMS-02 data is performed for all the 1000 simulations built for each scenario `A-B-C-D-E-F`. In Table 5.2 we report the number of simulations, out of 1000, that produce different values of $\chi^2/\text{d.o.f.} = \tilde{\chi}$ for each simulation setup.
The difference between `ModA`, `ModD` and `ModE` is relative only to the propagation and the energy losses models. With `ModD` we obtain a higher number of simulations compatible with the data: the *SLIM-MED* model produces indeed fluxes from single sources which are smoother with respect to *Benchmark-prop*, and a little bit higher at lower energies. They better accommodate the AMS-02 spectrum. In all the tested setups, the number

	$\tilde{\chi} < 2$	$\tilde{\chi} < 1.5$	$\tilde{\chi} < 1$
`ModA`	15	8	4
`ModB`	30	19	6
`ModC`	15	10	3
`ModD`	42	25	10
`ModE`	24	12	4
`ModF`	4	2	2

Table 5.2: Number of simulations (out of 1000) that produce a $\tilde{\chi}$ smaller than 2, 1.5 or 1 in the fit to AMS-02 data [131], for each simulation setup.

of mock galaxies with a $\tilde{\chi} < 1$ (2) does not exceed 1% (4%).

In Figure 5.2 we plot the e^+ flux obtained for two illustrative simulated galaxies with $\tilde{\chi} < 1$, within `ModA`. The contributions from each PWN, from the secondary emission and their sum are shown along with the AMS-02 data. The contribution from PWNe is significant for energies above $10-20$ GeV and dominant over 100 GeV and may have different features, in particular at unconstrained energies above 1 TeV, depending on the specific simulation. As we will discuss later, the number of sources that contribute to the observed spectrum is limited, from a few to $O(10)$. We notice that the secondary flux, while decreasing with energy, practically forbids the realization of sharp cut-offs in the e^+ spectrum above TeV energies. The different features of the flux from single PWNe are due to the peculiar combination of the input parameters. In particular, the peaked shape is typically associated to small γ_e and τ_0 values. After the analysis presented here, authors of [381] demonstrated how considering energy losses due to ICS as discrete and catastrophic, rather than continuous, can smooth out such features. They also state that this result reopens the possibility that only a small number of pulsars can produce the e^+ excess, which aligns with our results, as we explain below. However, the method proposed by Ref. [381] is computationally prohibitive, even for the calculation of the flux from a single source. In our opinion the adoption of the proposed treatment for energy losses may yield a slightly higher number of simulations that are compatible with the data.

All the good fits to the data provide a value for A_S around 2, except for `ModE`, with an average around 1.4 due to a higher prediction for the secondary production, that was computed based on a new evaluation of secondary e^+ reported in Chapter 4. We note that the semi-analytical propagation model used in Ref. [325] adopted in `ModA`, assume different shapes for the diffusion coefficients as a function of rigidity, for the source terms, as well as of course the production cross sections, which can be the reasons of the discrepancies. Because of this, the results obtained with `ModE` reduce the required

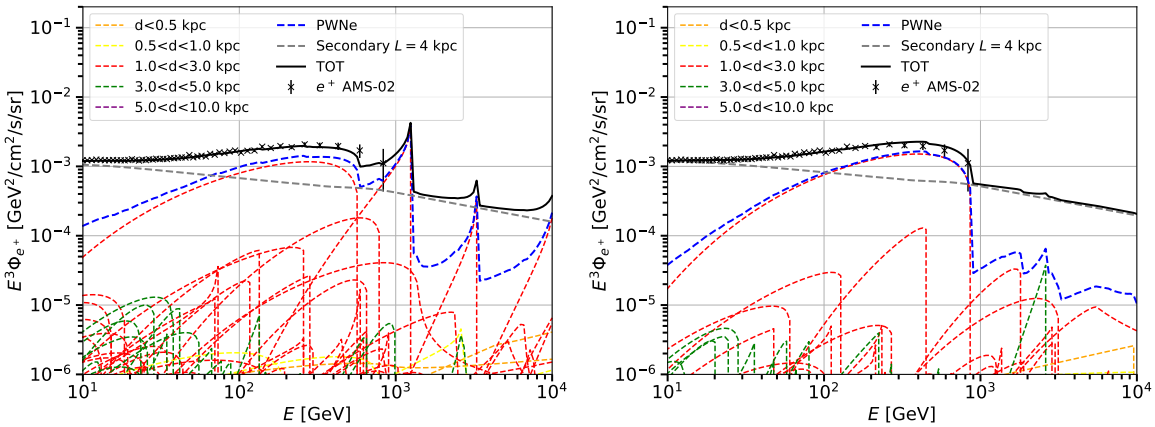

Figure 5.2: Comparison between the AMS-02 e^+ flux data [131] (black points) and the flux from secondary production (grey dashed line) and PWNe (blue dashed line) for two `ModA` realizations of the Galaxy with $\tilde{\chi} < 1$. The contributions from each source, reported with different colors depending on their distance from the Earth, are shown.

value for the normalization of secondaries, partially solving the high values obtained for the other models. As for the allowed overall normalization A_P of the PWN primary flux, we find on average values slightly smaller than one.

In order to understand the properties of the pulsar populations which fit the observations, we report in Figure 5.3 the contribution to the e^+ flux coming from pulsars grouped in different subsets of distance from the Earth (left) and age (right). In this realization, the dominant contribution comes from the ring between 1 and 3 kpc. This result is the interplay between the presence of a spiral arm (see Figure 5.1), which enhances the number of sources, and the typical propagation length of high-energetic e^+, affected by severe energy losses. Despite the smaller effect from radiative cooling, the flux from sources within 1 kpc is lower due to the paucity of sources.

The division in age rings shows the scaling of the maximum energy $E_{\rm max}$ with the age of sources. In the Thomson approximation energy losses would provide $E_{\rm max} \propto 1/t$, inferred from $dE/dt \propto -E^2$. However, in the Klein-Nishina regime we observe a more complex behaviour. Pulsars older than 10^6 kyr do not contribute significantly to the e^+ flux above 10 GeV, while the highest contribution around TeV energies come from sources younger than 500 kyr. We have checked that sources younger than 20 kyr do not produce sizeable effects on our analysis, and the energy range in which they would produce a relevant flux is well above AMS-02 data. In order to inspect the effects of different simulated Galactic populations, we plot in Figure 5.4 the total e^+ flux for all the pulsar realizations within `ModA`, and having $\tilde{\chi}$<1.5 on AMS-02 data. For energies lower than 200 GeV, differences among the realizations are indistinguishable. The data in this energy range are very constraining. Instead,

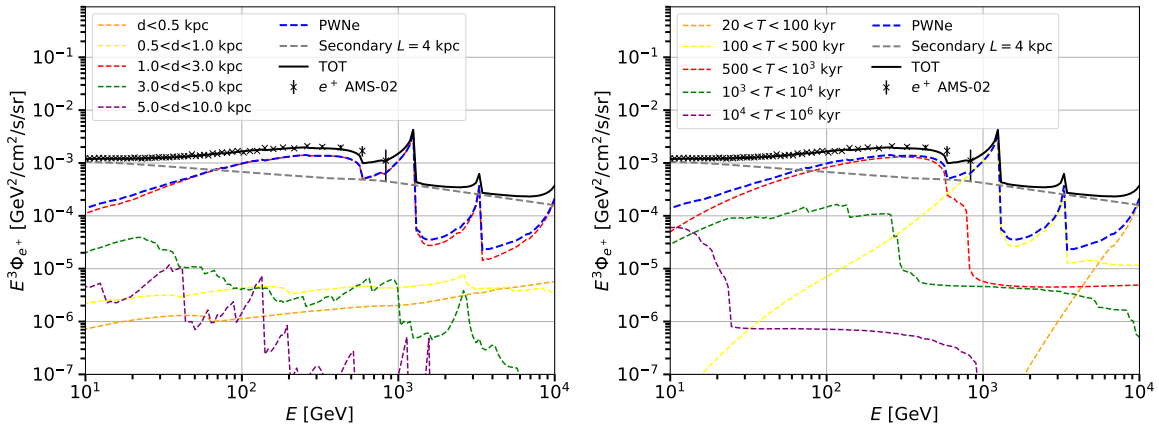

Figure 5.3: Effect of distance and age of pulsars in a specific mock galaxy within setup `ModA`. Left (right) panel reports the contribution to the e^+ flux for different distance (age) subsets. The dashed grey line reports the secondary flux, while the solid line corresponds to the total flux. AMS-02 data are from Ref. [131] (black points).

above around 300 GeV the peculiarities of each galaxy show up, thanks to the larger relative errors in the data. Above 1 TeV the predictions are unconstrained by data. Nevertheless, all the simulations predict globally decreasing fluxes, as expected by energy losses and continuous $e^{\pm}$ injection.

Concerning the other simulation setups, we do not find significant differences between `ModA` and `ModC`, namely between `CB20` and `FK06` pulsar evolution models. For both cases on average the dominant contribution from PWNe comes from the $1-3$ kpc distance ring. On the other hand, `ModB` gives a higher number of simulations that are compatible with the data. As shown in Figure 5.1 (right panel), the $\rho_F(r)$ radial distribution predicts a higher number of sources with respect to $\rho_L(r)$ in the spiral arms close to the Earth. Therefore, within `ModB` there is a higher probability to simulate sources close to the Earth with characteristics compatible with the AMS-02 data. However, the number of simulations with $\tilde{\chi} < 1.5$ is $< 2\%$ for both `ModA` and `ModB`. Except for the mean value of A_S, no significant difference is detected between `ModA` and `ModE`.

`ModF` differs from all the other cases due to the different computation of the fraction of e^+ produced by sources that actually contribute to the e^+ data (see Section 5.2.1). We consider the ISM density $n_0 = 3$ cm^{-3} in the computation of t_{BS} in order to set ourselves in the same scenario of [207], see Equation 5.9. We find that, by fixing the maximum PWN efficiency of conversion of W_0 in e^+ to 50%, only 4 simulations fit the data with $\tilde{\chi} < 2$ and all of them are dominated by a single powerful source, with $A_P \sim 5$, at the edge of the prior. We note that the renormalization factor A_P is related to η, so that the actual efficiency of the single source i is $A_P \times \eta_i$. Since this setup considers only the e^+ emitted after the escape of the pulsar from the SNR, the fit to

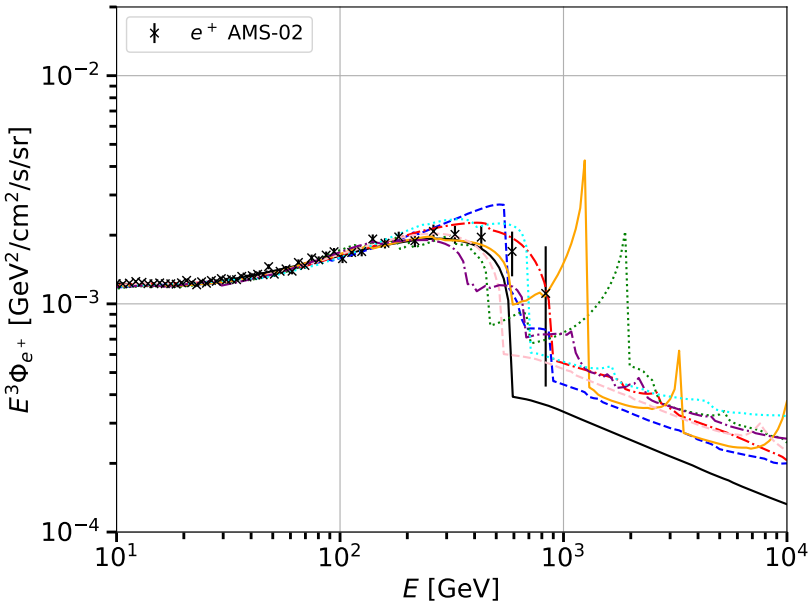

Figure 5.4: Total (secondary plus PWNe) e^+ flux obtained from all the 8 simulations within `ModA` with $\tilde{\chi} < 1.5$, along with AMS-02 data [131] (black points).

the data selects the galaxies with sources that still have a great rotational energy that can be converted into e^+ at the exit time. Instead, if we do not put any upper limit for the parameter A_P, i.e. to the efficiency, the number of simulations with $\tilde{\chi} < 2$ increases to about one hundred. These unphysical values for the PWN efficiency could be partially reduced by increasing the pulsar birth rate and so the number of pulsars in the simulations, or considering a different distribution of pulsar properties at birth which systematically predicts more energetic sources. For more information about this scenario refer to [207].

5.4.2 Mean number of PWNe dominating the positron flux

We inspect in this Section the average number of sources which contribute the most to the e^+ flux and thus can shape the AMS-02 data. We adopt two complementary criteria to estimate the number of sources that are responsible for the most significant contribution of the PWNe e^+ emission:

1. *AMS-02 errors*: we count all the sources that produce a flux higher than the experimental flux error in at least one energy bin above 10 GeV.

2. *Total flux 1%*: we count the sources that produce the integral of $\Phi_{e^\pm}(E)$ between 10 and 1000 GeV higher than 1% of the total integrated e^+ flux measured by AMS-02.

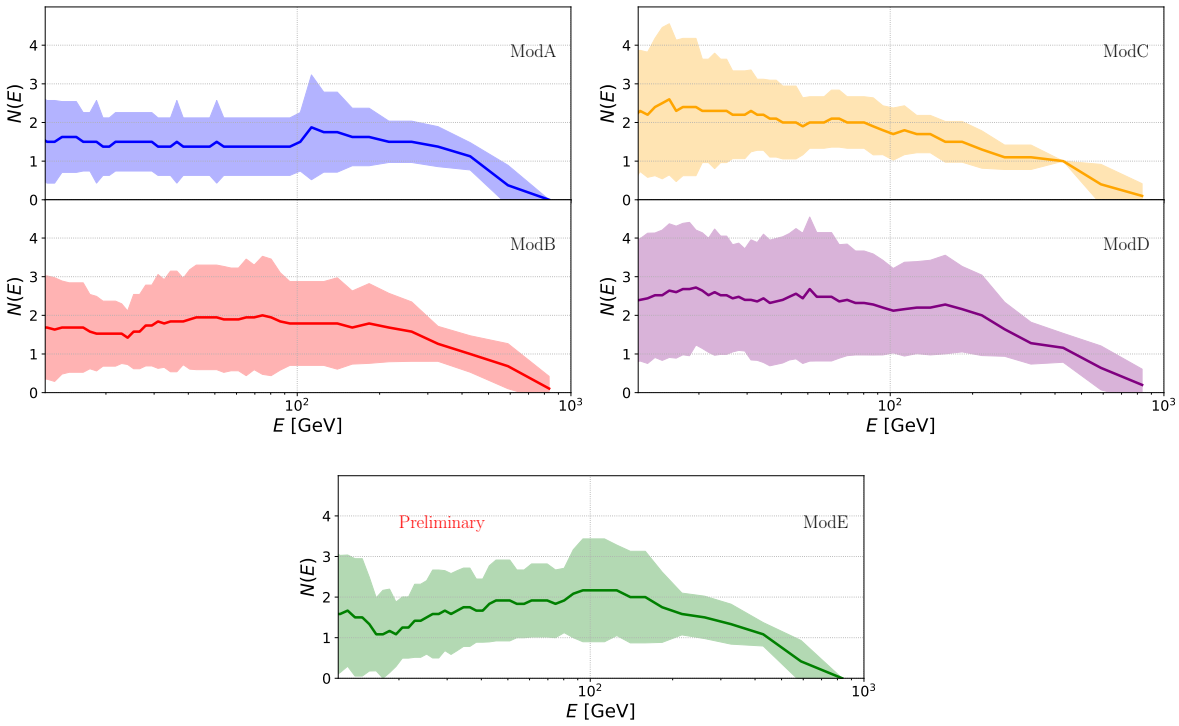

Figure 5.5: Mean number of PWNe that satisfy the *AMS-02 errors* criterion in the single energy bin of AMS-02 data [131]. We also show the 68% containment band for simulations with $\tilde{\chi} < 1.5$ (see the main text for further details).

In Figure 5.5 we report the average number of PWNe with the standard deviation (68% containment band) that contribute in the different energy bins of AMS-02, for configurations with $\tilde{\chi} < 1.5$, adopting the *AMS-02 errors* criterion. On average, $2-3$ sources shine with a flux at least at the level of AMS-02 e^+ data errors. We also find a decreasing number of dominant sources with increasing energy for all the setup reported. This result is partially induced by the larger experimental errors at high energy, which raise the threshold for the minimum flux that a PWN has to produce in order to satisfy the *AMS-02 errors* criterion. Moreover, being the age simulated in a uniform interval, the number of young sources responsible for the highest energy fluxes is smaller than for old pulsars, whose e^+ have suffered greater radiative cooling. Overall, it indicates that only a few sources with a large flux are present in the simulations that produce a good fit to the data.

In Table 5.3 we report the average number of sources that satisfy the criteria listed above, for all the simulated galaxies which provide a good fit to AMS-02 data ($\tilde{\chi} < 1.5$). We obtain small numbers of sources that satisfy the criteria, typically around 3, irrespective of the simulation scheme. Scenarios with a large number of sources explaining the CR e^+ data are disfavored. This result is due to the fact that AMS-

	AMS-02 errors	Total flux 1%
ModA	1.3/2.9/3.3	1.0/1.8/2.2
ModB	3.5	1.9
ModC	3.9	3.0
ModD	5.4	3.5
ModE	3.8	1.9
ModF	1.0	1.0

Table 5.3: Average numbers of sources that satisfy the *AMS-02 errors* and *Total flux 1%* criteria, for all the galaxies within each simulation setup, with $\tilde{\chi} < 1.5$. For ModA, results are provided also for $\tilde{\chi} < 1$ (left) and $\tilde{\chi} < 2$ (right).

02 measures a smooth flux, therefore several PWNe contributing at different energies would create wiggles in the total flux which are not detected. Instead, a few sources generating a flux that covers a wide range of energies produce a smooth contribution compatible with the data.

A slightly higher number of sources with respect to ModA satisfies the criteria for ModD. The change of propagation setup from ModA to ModD, produces a larger number of simulations that are compatible with the data, given the flux smoothing due to the alternative propagation setup. Dissecting results within ModA, we find that the mean number of sources decreases with decreasing $\tilde{\chi}$, consistently with the requirement of a smooth trend of e^+ flux. In all the other simulation setups, except for ModF, we confirm the same trend. The ModF results have already been discussed in Section 5.4.1. Summarizing, the two selection criteria *AMS-02 errors* and *Total flux 1%*, whereas based on different quantitative assumptions, provide in practice very similar results. This result is complementary also to earlier analysis [353] adopting a different strategy and working on PAMELA, *Fermi*-LAT and ATIC/PPB-BETS [382, 383] data. There, a single or a few energetic pulsars are required to explain the measurements, and scenarios composed by multiple pulsars are found to be disfavored based on age and distance criteria, and by the data themselves.

5.4.3 Characteristics of PWNe dominating the positron flux

In this Section we scrutinize the physical properties of the simulated sources selected by the fit to be compatible with the AMS-02 data. For each Galactic realization of ModA with $\tilde{\chi} < 1.5$, we report in Figure 5.6 (left panel) the distance, age and maximum $E^3\Phi_{e^+}(E)$ of the PWNe satisfying the *AMS-02 errors* criterion. The data require 1 or 2 sources with high maximum $E^3\Phi_{e^\pm}(E)$, with ages between 400 kyr and 2000 kyr and

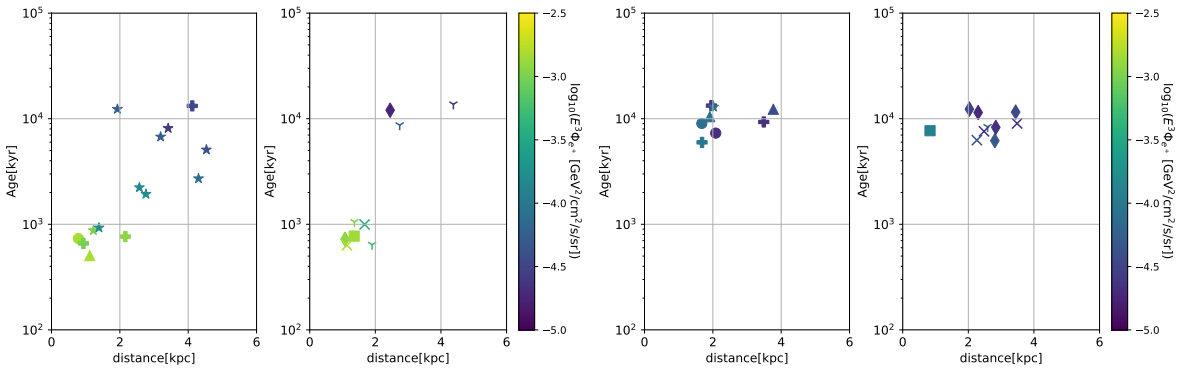

Figure 5.6: Distance, age and maximum $E^3\Phi_{e^+}(E)$ of the PWNe satisfying the *AMS-02 errors* criterion for `ModA` simulations with $\tilde{\chi} < 1.5$ (left panel) and with the worst $\tilde{\chi}$ (right panel). In each panel, sources belonging to the same mock galaxy are reported with the same symbol, subdivided in two separate plots for better readability. The color scale is common to all panels, and depicts the $\log_{10}$ of the maximum e^+ flux at the Earth in the AMS-02 data energy range.

distances to the Earth less than 3 kpc. These sources produce fluxes peaked between 100 GeV and 500 GeV, allowing a good explanation to the data. Fluxes from farther PWNe contribute less to the data. Sources with small maximum $E^3\Phi_{e^\pm}(E)$ and with ages between 2000 kyr and 10^4 kyr also satisfy the criterion, with flux peaks below 100 GeV where the secondaries are still the dominant component. We do not find any particular difference between all the simulation setups, except for `ModD` and `ModF`. As already noticed, since the *SLIM-MED* propagation implemented in `ModD` produces smoother fluxes, we find also some realizations with few more sources contributing with a bright flux to the e^+ data.

In Figure 5.6 (right panel) we report the distances, age and maximum $E^3\Phi_{e^\pm}(E)$ values of the dominant PWNe for the mock galaxies with the worst χ^2. These cases give best-fit to the data with the maximum values allowed by the priors for A_S and the lowest values of A_P. Moreover, there are not sources which satisfy the *AMS-02 errors* criterion with an age between 400 kyr and 2000 kyr. In these galaxies, the trend of $E^3\Phi_{e^\pm}(E)$ at high energies remains constant or decreases, and does not contribute sufficiently to the data above 50 GeV. To compensate this effect, the fit procedure demands the highest value of A_S.

The efficiencies obtained multiplying the simulated η values associated to a single source with the A_P obtained from the best fit of the corresponding galaxy with $\tilde{\chi} < 1.5$, have a value between 0.01 and 0.1, confirming the goodness of the η interval initially chosen.

In order to check that the characteristics of these dominant pulsars are consistent with observations, we compute $\dot{E}$ from W_0 (see Section 5.2.1), finding values quite

common in nature. The ATNF catalog [378] lists about 60 sources with $\dot{E}$ values higher than the maximum values obtained from our mock dominanting sources namely $\dot{E} \sim 10^{36}$ erg s^{-1}. We built our simulations starting from P_0 and B distributions calibrated on observations. In the end, we obtain results which are consistent with these measurements.

We also outline that all the sources that satisfy the *AMS-02 errors* criterion have values of $\gamma_e > 1.7$, for all the simulation setups. Lower values of γ_e can produce peaked features incompatible with the smoothness of the AMS-02 data, an issue that could be solved with the work by authors of [381] as discusses in 5.4.1, that could re-open to the possibility of having $\gamma_e < 1.7$. The adoption of a broken power-law injection spectrum $Q(E,t)$ (see Section 5.2.1) would probably limit the presence of peaked features at high energy, thanks to the soft spectral index above the break energy. We expect to find a slightly higher number of simulations compatible with the data, together with a slightly higher number of sources satisfying the *AMS-02 errors* criterion, producing negligible changes of our results.

5.5 Discussion and summary

In this Section we discuss our results in the context of recent literature on secondary CR e^+, and we outline their broader implications. The high-precision AMS-02 e^+ data are here used to constrain the main properties of the Galactic pulsar population and of the PWN acceleration needed to explain the observed CR flux. To this aim, we simulate a large number of Galactic pulsar populations, calibrated on ATNF catalog observations.

Independently of the simulation scenario, one of the major findings of this analysis is that the vast majority of the galaxy realizations produces several wiggles in the total contribution and therefore they do not fit well the data. In all the tested setups, the number of mock galaxies with a $\tilde{\chi} < 1$ (2) does not exceed 1% (4%). The different features of the flux from single PWNs are caused by the peculiar combination of input parameters, especially small values of γ_e and τ_0, and can be partially smoothed out with the energy loss treatment proposed by Ref. [381]. With this method we expect to find a slightly higher number of simulations compatible with the data, that would not change our conclusions.

The galaxy realizations that fit properly the AMS-02 e^+ data have tipically $2-3$ sources that produce a e^+ yield at the level of the data errors, with ages between 400 kyr and 2000 kyr and distances to the Earth less than 3 kpc. These sources produce fluxes

peaked between 100 GeV and 300 GeV, where AMS-02 data are the most constraining. The major finding of this work is that the data can be explained only by a galactic pulsars population with a small number of dominant sources with the characteristics explained above. Finally, we do not find any particular distribution for the pulsar efficiencies. In most cases they have a value between 0.01 and 0.1 consistently with what found in previous papers [324, 238].

In Ref. [361], $e^{\pm}$ fluxes are computed from simulations of different combinations of pulsar spin-down properties, injection spectrum and propagation schemes. They consider sources younger than 10 Myr, relying on observations of pulsars with ages of order $10^5 - 10^7$ years. They constrain the space of pulsar and propagation models using the e^+ fraction and $e^+ + e^-$ data. Our simulations, while being more numerous, rely on distribution of parameters simulated according to complete pulsar population models. Ref. [361] finds average values of η in the range around $0.1 - 10\%$, in agreement with our results for `ModA-B-C-D-E`.

Authors of [207] adopt the bow-shock scenario explained in Section 5.2.1 and tested in our `ModF`, and analyze only a single pulsar population model. They build mock galaxies sampling the P_0 value for each source from a gaussian distribution with $P_{0,mean} = 0.10$ s and $P_{0,std} = 0.05$ s obtained in Ref. [384], a work based on young and energetic sources, producing on average pulsars more powerful with respect to our mock catalogs. They adopt a higher pulsar birth rate (3/century), fix $\log_{10}(B) = 12.65\ \log_{10}(\mathrm{G})$, and consider a diffusion setup that implies higher values of $D(E)$, corresponding to larger propagation scale lengths λ. Ref. [207] finds that the number of contributing sources to the e^+ flux is much larger ($\sim 10^3$ at 1 TeV) than in this work and in previous works [350, 364, 374] at all energies, due to the larger diffusion coefficient. We add that this result is probably also induced by the bow shock scenario, the spin-down model and the different selection criteria adopted. With respect to their work we focus more on the characteristics that a pulsar realization has in order to fit the data. They find $\eta = 8.5\%$, that rises to 42% for $P_{0,mean} = 0.30$ s and $P_{0,std} = 0.15$ s, which is compatible with our `ModF`. However, more specific comparisons are difficult to perform, given the very different simulation setup between Ref. [207] and this analysis.

In this Chapter we have shown the power of the AMS-02 CR e^+ data in constraining properties of PWNe supposed to be sources of $e^{\pm}$, in a measure to explain the flux data. Also for leptons an era has started for charged CRs to teach about the Galaxy, in addition to the invaluable electromagnetic signals and the nuclear component. In fact, the analysis of AMS-02 data implies the combination of several phenomena, from particle production and acceleration in sources to Galactic propagation. The spectra of particles emitted by sources are significantly changed when they reach the Earth

with respect to their characteristics at injection. In the next Chapter, we will focus on pulsar halos, as introduced in Section 2.4. These halos are a direct product of particles accelerated and emitted in a region around the source, with characteristics similar to the original ones and not with energies heavely changed as for particles detected at the Earth. With the combination of AMS-02 data, cross sections, and pulsar halos, so physics at extremely different scales, a comprehensive understanding of the e^+ data will likely be achieved in the next few years.

Chapter 6

Pulsar gamma-ray halos

In the previous Chapter 5, we estimated the contribution to the e^+ excess coming from a mock population of galactic pulsars. To perform the analysis, it is necessary to propagate particles on Galactic scales, modeling the contribution at the Earth coming from sources far in space and time. The data on γ-ray halos around pulsars can provide invaluable indirect information about acceleration, injection in the ISM and propagation of $e^{\pm}$, which are responsible for this γ-ray emission, in a region close to the source. This Chapter is based on Ref. [2].

6.1 Introduction

The detection of extended (few degrees across the sky) very-high-energy γ-ray halos reported by the HAWC Collaboration around the Geminga and Monogem pulsars [233] and by the LHAASO experiment around the pulsar PSR J0622+3749 [242] led to the conclusion that the CR diffusion is inhibited within few tens of pc from the pulsar, and consequently the energy dependent CR diffusion coefficient, $D(E)$, should be smaller, by at least two orders of magnitudes, than the *nominal* value used in conventional models of propagation of Galactic CRs [233] (see Section 2.4). Even if the suppression of the diffusion coefficient around pulsars has become a popular hypothesis [235, 236, 237, 238, 239, 240], so far no convincing theoretical explanation of this effect has been proposed (see Section 2.4.3).

In this Chapter, we attempt to explain the observed TeV halos without invoking the suppression of the diffusion coefficient, showing that the characteristics of such γ-ray halos can be explained by properly accounting for the transition between two propagation regimes, the ballistic and the diffusive propagation. We will focus on the cases of Geminga and Monogem (HAWC data).

6.2 Gamma-ray emission from electrons and positrons

We here describe the models we employed for the flux of photons emitted from ICS and synchrotron radiation. We define the ICS power of photons of energy E_γ produced by $e^\pm$ of energy E as in [143, 206]:

$$\mathcal{P}^{IC}(E, E_\gamma) = \frac{3\sigma_T c\, m_e^2 c^4}{4E^2} \int_{\frac{m_e c^2}{4E}}^1 dq \frac{d\mathcal{N}}{d\epsilon}(\epsilon(q)) \times \tag{6.1}$$
$$\times \left(1 - \frac{m_e^2 c^4}{4qE^2(1-\tilde{\epsilon})}\right) \left[2q \log q + q + 1 - 2q^2 + \frac{\tilde{\epsilon}(1-q)}{2-2\tilde{\epsilon}}\right],$$

where ϵ is the ISRF photon energy, σ_T is the Thomson cross section, $\frac{d\mathcal{N}}{d\epsilon}(\epsilon(q))$ is the energy spectrum of the ISRF, and:

$$q = \frac{\tilde{\epsilon}}{\Gamma_\epsilon(1-\tilde{\epsilon})} \ , \ \Gamma_\epsilon = \frac{4\epsilon E}{m_e^2 c^4} \ , \ \tilde{\epsilon} = \frac{E_\gamma}{E}\,. \tag{6.2}$$

The flux of synchrotron photons has the same expression as in Equation 6.14, where the synchrotron power $\mathcal{P}^{\rm Sync}(E, E_\gamma)$ is now given by [385]:

$$\mathcal{P}^{\rm Sync} = \frac{dN_{\rm Sync}}{dE_\gamma dt}\,. \tag{6.3}$$

The quantity defined in Equation 6.3 is connected to the energy emitted by one lepton per unit frequency and unit time, $\frac{dE_{\rm sync}}{d\nu dt}$, as:

$$\frac{dN_{\rm Sync}}{dE_\gamma dt} = \frac{1}{hE_\gamma}\frac{dE_{\rm sync}}{d\nu dt} \tag{6.4}$$

since $N_{\rm sync} E_\gamma = E_{\rm Sync}$. To obtain the emissivity function in a random magnetic field one should average out the standard synchrotron formula [143] over the directions of the magnetic field. For $e^\pm$ with arbitrary pitch angle, the emitted energy per unit frequency and time is thus given by (see Ref. [385]):

$$\frac{dE_{\rm sync}}{d\nu dt} = \frac{\sqrt{3}e^3 B}{m_e c^2} G(x), \tag{6.5}$$

where e and m_e are the electron charge and mass, B is the magnetic field and c is the speed of light. The function $G(x)$ is an analytical approximation for the dimensionless synchrotron integral as defined in Ref. [385], where $x = \nu/\nu_c$, $\nu = E_\gamma/h$ and:

$$\nu_c = \nu_c(E) = \frac{3eBE^2}{4\pi m_e^3 c^5}\,. \tag{6.6}$$

6.3 Ballistic vs diffusive propagation

Previous studies of the HAWC data have been performed under the assumption of diffusive CR transport at any time after the injection of $e^{\pm}$. However, the propagation of leptons deviates from such a simple picture. At the first stage, determined by the timescale $\tau_c = 3D(E)/c^2$ after injection, leptons with energy E propagate ballistically. Then, as time passes, the multiple deflections experienced in the turbulent circumstellar magnetic field lead to the isotropization of the particle directions, which means that the propagation proceeds in the diffusive regime.

The formal application of the diffusion theory to timescales smaller than τ_c faces the so-called superluminal propagation problem [386, 387, 388, 389]. This can be seen by comparing the diffusion, $r_{\rm diff}$, and ballistic, $r_{\rm ball}$, distances travelled over a time $t = \alpha\tau_c$: $r_{\rm diff} \sim \sqrt{D\alpha\tau_c} \sim \sqrt{\alpha}\tau_c c$ and $r_{\rm ball} = \alpha\tau_c c$, respectively. For $t \lesssim \tau_c$ ($\alpha < 1$), $r_{\rm diff} > r_{\rm ball}$ and the propagation speed in the diffusive regime would exceed the speed of light. A fully relativistic extension of the diffusion equation, which would solve this problem, has not been found yet (see e.g., [390, 388] for a discussion). Therefore, it is necessary to adopt approximate solutions, in which the ballistic and diffusive regimes are used in the appropriate limits and the two solutions are somehow sewed together (see e.g, [386, 391] and Equation 24 of [389]).

The CR transport is characterized by three regimes depending on the time t after the injection: ballistic (for $t \ll \tau_c$), diffusive (for $t > \tau_c$) and a transition between the two, that we call quasi-ballistic. The transition is governed by the energy-dependent mean free path $\lambda_c(E)$, which, for relativistic particles, is linked to the energy-dependent (as inferred both from theory and from the Galactic CR transport phenomenology [117, 392, 336]) isotropic diffusion coefficient through $D(E) = \lambda_c(E)\, c/3$ (see e.g., [117, 393]). The time and spatial scales for the isotropization are given by $\lambda_c(E)$ and $\tau_c = \lambda_c/c$ respectively (see e.g [388, 389, 394]). In the case of a continuous source, such as pulsars, this also results in the fact that the CR spatial distribution at a distance from the source smaller than λ_c, is dominated by particles injected within the last τ_c [389]. Particles emitted at an instant earlier than τ_c, with respect to the current time, have been isotropized and thus can be treated in the diffusive approximation, while particles injected within the last τ_c should be treated in the quasi-ballistic regime.

The γ rays detected by HAWC at energies $5-50$ TeV are mostly produced through ICS predominantly by $e^{\pm}$ of energy between $20-200$ TeV (see Figure 2 of [244]). Assuming that at these energies the standard diffusion coefficient is $D \gtrsim 10^{29} - 10^{30}\,{\rm cm}^2/{\rm s}$ [117, 392, 336], we find that $\lambda_c \gtrsim 3 - 30\,{\rm pc}$. Given that the spatial extension measured for the γ-ray halo around Geminga and Monogem is ~ 10 pc [233], the correct treatment

of the transition from ballistic to diffusive propagation is critical for the interpretation of γ-ray data. This is probably the case also for the *Fermi*-LAT data analysed by [238]. Indeed, such data refer to $e^{\pm}$ of energy $E \sim 100 - 1000$ GeV, which correspond to $\lambda_c \gtrsim 3 - 10$ pc. However, here we focus on multi-TeV energies.
We assume isotropic diffusion, which typically can be applied, as a good approximation, to different astrophysical environments (see e.g., [117, 395, 393] for a discussion). In particular, this approximation has been much used in the modelling of CR propagation around pulsars [233, 235, 236, 237, 238, 239, 240]. Note, however, that the applicability of this approach often depends on poorly constrained parameters such as the coherence length of the background magnetic field and its level of turbulence [396, 397, 393, 253, 398], and ultimately on the unknown time and space dependent configurations of the field lines in the source region (see e.g [397, 399, 394] and references therein).

6.4 Transition between ballistic and diffusive propagation

We treat the diffusion coefficient as an energy-dependent parameter and, in the energy range considered here, as a pure power-law:

$$D(E) \approx D_0 E_{\rm GeV}^{\delta}\, {\rm cm}^2/{\rm s}, \tag{6.7}$$

where $E_{\rm GeV}$ is the particle energy in GeV, $D_0 \sim 1 - 4 \times 10^{28} {\rm cm}^2/{\rm s}$ at 1 GeV and $\delta \sim 0.3 - 0.6$, with $\delta = 1/3$ corresponding to a Kolmogorov-type turbulence and $\delta = 1/2$ to a Kraichnan-type turbulence [117]. Notice that what matters in the present analysis is the CR diffusion coefficient in the energy range $20 - 200$ TeV. For the given value of the diffusion coefficient, the mean free path λ_c reads:

$$\lambda_c(E_{\rm GeV}) \approx 0.3\, D_{0,28} E_{\rm GeV}^{\delta}\, {\rm pc}, \tag{6.8}$$

where $D_{0,28}$ is the diffusion coefficient at 1 GeV in units of $10^{28}\, {\rm cm}^2/{\rm s}$.
Unless otherwise stated, we assume that $\delta = 0.5$ which is compatible with recent analysis of CR data (see e.g., [336, 325]) and with the results of simulations for diffusive propagation [400]. Others analysis have assumed a value of 1/3 (see e.g. , [233, 239, 238, 236] and Section 4.5). We will explain later on how the results are modified with $\delta = 1/3$. The mean free path increases with the particle energy and with the overall normalization D_0. For example, at 100 GeV (10 TeV) it is 3 (30) pc for $D_0 = 10^{28}$ cm^2/s and 0.03 (0.3) pc for $D_0 = 10^{26}$ cm^2/s. As a consequence, the quasi-ballistic

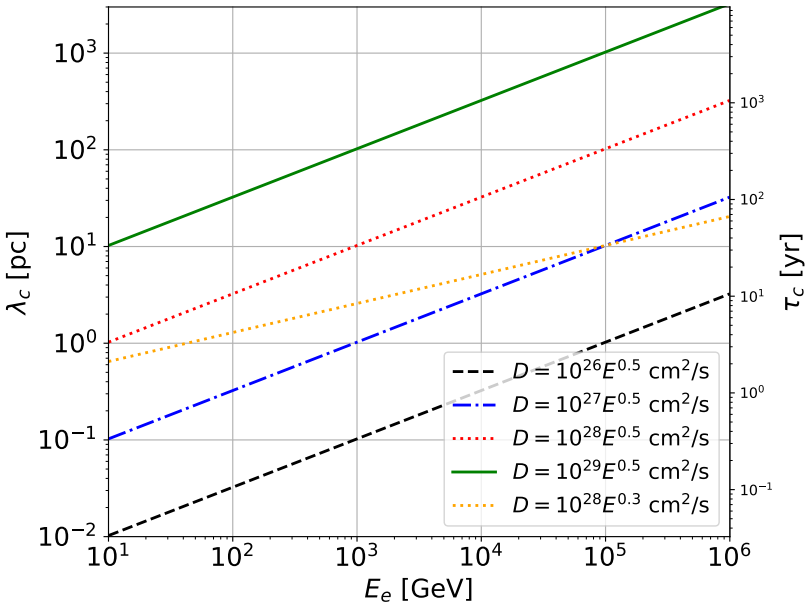

Figure 6.1: Mean free path, λ_c, and scattering time-scale τ_c, as a function of the particle energy. The curves refer to different values of the normalization of the diffusion coefficient, D_0, and of the slope, assumed as $\delta = 0.5$ or 0.3 as marked.

propagation is relevant up to larger distances from the source for increasing particle energy and larger D_0. This can be seen in Figure 6.1, where λ_c and τ_c are shown as a function of the particle energy, for several values of D_0 and for $\delta = 0.5$ and 0.3. We assume that a pulsar of age T turns on at $t = 0$ and injects leptons following the time dependent spin down luminosity $L(t)$ in Equation 5.2, taking $\tau_0 = 12$ kyr as in Refs. [233, 239, 238, 236].

In the diffusive regime (particles injected at times $t_0 \leq T - \tau_c$), the $e^{\pm}$ density, $f_{\rm diff}$, at a distance r from the source of age T, taking into account diffusion and energy losses and under the assumption of continuous injection (see, e.g. [238]), is given by:

$$f_{\rm diff}(r, E) = \int_0^{T-\tau_c} dt_0 \frac{Q(E_0) L(t_0)}{\pi^{3/2} \lambda^3(E, E_0)} \frac{b(E_0)}{b(E)} e^{-\frac{r^2}{\lambda^2(E, E_0)}}. \tag{6.9}$$

The ISFR is taken from Ref. [204], while for the synchrotron radiation losses is assumed a Galactic magnetic field of $3\,\mu$G. Particles emitted from the source at time t_0 with energy E_0 cool down to energy E during the time $T - t_0$. Our conclusions do not change if we use a different model for the ISRF, as in Ref. [205], or if we vary the strength of the Galactic magnetic field around $3\,\mu$G. λ is the propagation length due to diffusion and energy losses defined in Equation A.6. The injection spectrum is taken as in Equation 5.1 with index $\gamma_e = 1.5$ and a cut-off at an energy of $E_c = 150$

TeV. We fix the cut-off energy to this value because a softening of the spectrum is needed to fit well the HAWC spectrum of Geminga in previous analyses [233, 238] and the LHAASO source PSR J0622+3749 [242]. The spectral shape for the $e^{\pm}$ injection spectrum is compatible with multiwavelenght observations of PWNe even if the values of the parameters are not well constrained [367]. The injection spectrum is normalized as in Equation 5.3.

In the ballistic regime (particles injected at times $T - \tau_c < t_0 \leq T$), the $e^{\pm}$ density, f_{ball}, is given by [386, 389]:

$$f_{ball}(r, E) = \int_{T-\tau_c}^{T} \frac{Q(E)L(T)}{4\pi c^3 (T - t_0)^2} \delta\left((T - t_0) - \frac{r}{c}\right) dt_0 = \tag{6.10}$$
$$= \frac{Q(E)L(T)}{4\pi c r^2} H(\tau_c\, c - r),$$

where $H(\tau_c\, c - r)$ is the Heaviside function, which is zero for $r > \tau_c\, c$. Since the typical spin-down time-scale τ_0 (few kyrs) is much larger than τ_c (at most few tens yrs) we assume that the luminosity is constant and equal to $L(T)$. We also neglect energy losses since for energies of about 10 TeV and $D_0 \sim 10^{28}$ cm^2/s, $\tau_c \sim 100$ years and thus much shorter than the energy loss time. In order to have a smooth transition between the two regimes, we substitute the term $H(\tau_c\, c - r)$ in Equation 6.10 with $\exp\left[-(r/(2\lambda_c))^2\right]$. We find that our results are similar by choosing other smoothing functions, such as $\exp\left[-r/(2\lambda_c)\right]$. The total $e^{\pm}$ density is given by $f_e(r, E) = f_{\rm ball}(r, E) + f_{\rm diff}(r, E)$.

Given the relativistic nature of the ICS, γ rays are mainly emitted along the direction of the momentum of the parent CR. When the CR distribution is isotropic (diffusive regime), at any location around the source there will be CRs traveling in each direction, and the size of the γ-ray halo reflects the size of the $e^{\pm}$ halo. Instead, in the purely ballistic regime the CR angular distribution is strictly anisotropic, which would lead to a point γ-ray source, given by the γ rays produced by $e^{\pm}$ that point towards us [401, 385, 389], no matter the extension of the $e^{\pm}$ halo. In the quasi-ballistic regime the γ-ray halo size is intermediate between the two cases. The angular distribution of particles in the transition from the ballistic to the diffusive regime can be calculated in the small-angle diffusion approximation with the following distribution [389]:

$$M(\mu) = \frac{1}{Z(x)} \exp\left(-\frac{3(1-\mu)}{x}\right), \tag{6.11}$$

where $Z(x) = \frac{x}{3}\left(1 - \exp(-6/x)\right)$, $x(E) = rc/D(E) = 3\,r/\lambda_c$, $\mu = (l\cos(\theta) - s)/r$ and $r(s, \theta) = \sqrt{l^2 + s^2 - 2\,l\,s\,\cos\theta}$. Here s is the distance along the l.o.s., θ the angle

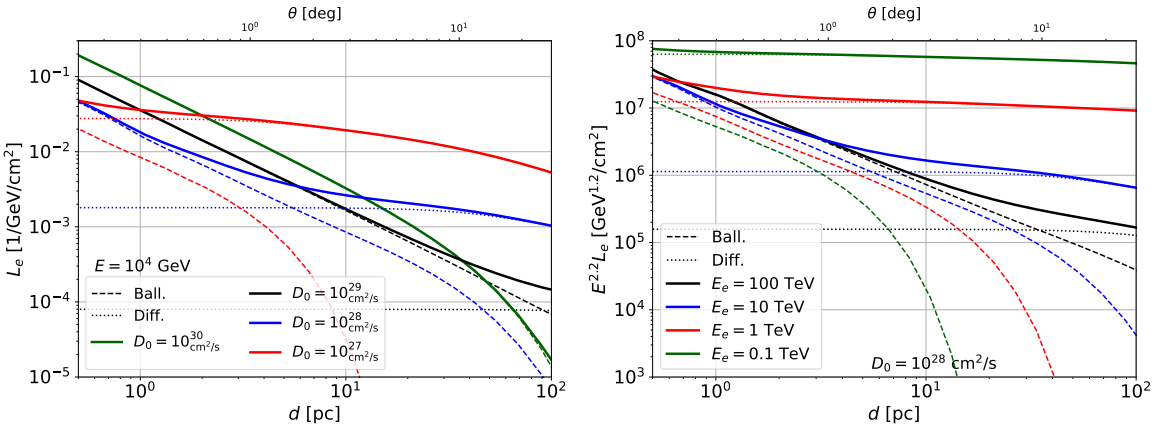

Figure 6.2: Left panel: $e^{\pm}$ density of the Geminga pulsar integrated along the l.o.s. as a function of the projected distance form the source d at 10 TeV and for different values of D_0, from $10^{27}\,\mathrm{cm}^2/\mathrm{s}$ to $10^{30}\,\mathrm{cm}^2/\mathrm{s}$. Right panel: same as left panel but at different energies from 100 GeV to 100 TeV for $D_0 = 10^{28}$ cm^2/s. The dashed lines correspond to the quasi-ballistic regime contribution, the dotted line to the diffusive contribution and the continuous lines to the total.

between the source and the l.o.s., l the distance from the source and μ the cosine of the angle between the direction of the l.o.s. and radial direction. The total particle distribution function is then given by:

$$F_e(E, s, \theta) = 2 f_e(E, r(s, \theta)) M(\mu(s, \theta)). \tag{6.12}$$

$M(\mu)$ is normalized as $\int_{-1}^{1} M(\mu) d\mu = 1$. In the limit $r >> \lambda_c$, i.e. for distances from the source much larger than the mean free path, $M(\mu)$ reduces to 1/2 (the particles pitch angle is uniformly distributed between -1 and 1 around the radial direction) and the total distribution function reduces to the diffusive (isotropic) particle density. For $r < \lambda_c$, $M(\mu)$ encompasses the small angle approximation for the particle propagation and the anisotropic angular distribution of particles in the quasi-ballistic regime.

In order to show the contribution of the ballistic and diffusive regime to the γ-ray emission we integrate the $e^{\pm}$ distribution function F_e along s [402]:

$$L_e(E, \theta) = \int_0^{\infty} ds F_e(E, s, \theta). \tag{6.13}$$

$L_e(E, \theta)$ reflects the spatial profile of the γ-ray emission at a given $e^{\pm}$ energy as a function of the projected distance from the source $d = l \tan\theta$.

In general, the photon flux emitted for the ICS or synchrotron mechanism by a source, at an energy E_γ and solid angle $\Delta\Omega$, can be written as [143, 225]:

$$\phi^{\rm IC,Sync}(E_\gamma, \Delta\Omega) = \frac{1}{4\pi}\int_{\Delta\Omega} d\Omega \int_{m_e c^2}^{\infty} dE L_e(E,\theta)\mathcal{P}^{\rm IC,Sync}(E, E_\gamma)\,, \tag{6.14}$$

where $\mathcal{P}^{\rm IC,Sync}(E, E_\gamma)$ is the power of photons emitted by a single $e^\pm$ for ICS or synchrotron emissions, as detailed in Section 6.2. The solid angle $\Delta\Omega$ is parametrized using θ.

We perform the calculation of $L_e(E,\theta)$ for the Geminga pulsar using the age $T = 342$ kyr, the distance $l = 0.19$ kpc and the current spin down luminosity 3.25×10^{34} erg/s [403]. Instead, for the Monogem pulsar we choose $T = 111$ kyr, $l = 0.288$ kpc and $\dot{E} = 3.8 \cdot 10^{34}$ erg/s using the results of the ATNF catalog [378]. The pulsars characteristics are also reported in Table 6.1. Finally, we fix the efficiency η for the conversion of spin-down pulsar luminosity into $e^\pm$ to 100%. In the top panel of Figure 6.2 we fix $E = 10$ TeV and change D_0 in the range $10^{27} - 10^{30}\,{\rm cm}^2/{\rm s}$. In the bottom panel we fix D_0 to $10^{28}\,{\rm cm}^2/{\rm s}$ and change the energy from $0.1 - 100$ TeV. We show the results only for $r > 0.5$ pc because the bow shock has a similar size (see, e.g., [232]) and so for smaller distances our model might not apply.

All the figures share a general trend. Up to distances $\approx \lambda_c(E)/3$ from the pulsar, the most important contribution to L_e comes from $e^\pm$ injected most recently, within the last τ_c, that move quasi-ballistically. This gives a spatial profile of $L_e(E,\theta)$ a bit steeper than $\propto 1/r$, expected as due to the angular distribution $M(\mu)$ (see Equation 6.11) in the quasi-ballistic regime [389]. At $d \gtrsim \lambda_c(E)/3$ the main contribution to L_e is due to particles injected at $t_0 < T - \tau_c$, which move diffusively and give a rather flat L_e profile, at least up to a distance $d \approx \lambda \sim \sqrt{4\,D(E)\,t_{\rm loss}(E)}$, where $t_{\rm loss}$ is the time scale for energy losses. Indeed, at distances larger than λ the exponential cut-off term $\exp(-r^2/\lambda^2)$ in the diffusive solution (see Equation 6.9) becomes more relevant and L_e decreases with r [374].

In the top panel of Figure 6.2 we see that for $D_0 = 10^{27}\,{\rm cm}^2/{\rm s}$ the ballistic-diffusion transition would happen so close to the pulsar, for $r < 0.05$ pc and $\theta < 0.1°$, that the γ-ray morphology observed by HAWC would be solely determined by the diffusive propagation regime. Instead, for $D_0 = 10^{28} - 10^{29}\,{\rm cm}^2/{\rm s}$, $\lambda_c > 10$ pc and the spatial extension of the γ-ray halo is mainly determined by the quasi-ballistic propagation regime, that dominates, for the $D_0 = 10^{28}\,{\rm cm}^2/{\rm s}$ case, within an angle $\theta \sim 3° - 4°$. We also show that for much larger diffusion coefficient values, i.e. $D_0 \sim 10^{29}$ ${\rm cm}^2/{\rm s}$, the quasi-ballistic model exhibits a cut-off for distances $d > 20$ pc from the pulsar. Indeed,

	$\dot{E}$ [erg/s]	T [kyr]	l [kpc]	τ_0 [kyr]	n
Geminga	3.25×10^{34}	342	0.19	12.0	3
Monogem	3.8×10^{34}	111	0.288	12.0	3
Injection Spectrum	spectral index			E_c	
	1.5			150 TeV	

Table 6.1: Characteristics of Geminga, Monogem and injection spectrum parameters: $\dot{E}$ is the current spin-down luminosity, T is the age, l the distance from Earth, τ_0 the assumed spin-down timescale and n the braking index, E_c the cut-off energy.

for such large values of D_0, $e^{\pm}$ are moving almost ballistically for hundreds of pc and thus the γ-ray source would look as point-like. In the bottom panel of Figure 6.2 we show that for $D_0 = 10^{28}\,\mathrm{cm}^2/\mathrm{s}$ and 100 TeV (10 TeV) the transition happens at a distance from the pulsar of ~ 20 (5) pc and $\theta \sim 5^\circ$ (1°).

As a final remark, we notice that, at a given D_0, changing δ from 0.5 to 0.3 implies λ_c smaller at multi-TeV energies, as shown in Figure 6.1. This would translate in a ballistic-diffusion transition happening at distances closer to the pulsar.

6.5 Fit to the HAWC data for Geminga and Monogem

Here we perform a fit to the HAWC data for the surface brightness of Geminga and Monogem by using the model that includes both the diffusive and ballistic contribution as reported in the previous section. The surface brightness is obtained from Equation 6.14 without integrating over the solid angle. We take the value of the diffusion coefficient D_0 and the $e^{\pm}$ conversion efficiency of the pulsar as free parameters. The efficiency η is calculated integrating the pulsar source term above 0.1 GeV as in Ref. [239, 238]. We also test variations of our benchmark model for Geminga by running the analysis with a distance of 0.25 kpc [404], and trying other two values for the Galactic magnetic field B, of 2 to 4 μG[1]. We do not test any variation for the model applied to Monogem because the data are much less precise than the ones for Geminga and the best fit for the diffusion coefficient is much more uncertain.

[1]The magnetic field is the most relevant quantity for calculating the $e^{\pm}$ energy losses since at energies larger than 10 TeV are dominated by Synchrotron radiation.

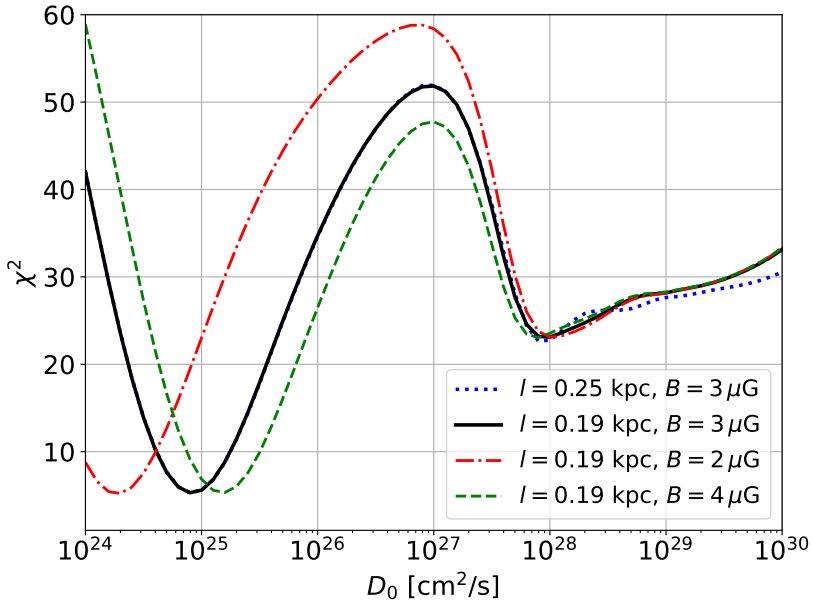

Figure 6.3: Fit to the HAWC data for Geminga: χ^2 as a function of the value of the diffusion coefficient at 1 GeV, D_0. We report the results obtained for two different distances of the Geminga pulsar and for different magnetic field values B.

The best-fit diffusion coefficients

We show the profile of the χ^2 as a function of D_0 in Figure 6.3 for Geminga. The χ^2 has a first minimum at about $D_0 \sim 0.2-2\times10^{25}$ cm^2/s ($D(100\,\mathrm{TeV}) \sim 0.6-6.4\times10^{27}$ cm^2/s) with a best-fit χ^2 of about 5. The best-fit value of D_0 decreases with smaller values of B, compensating the smaller energy loss rate. These values of D_0 are at least three orders of magnitude smaller than the results obtained by fitting CR data (see Chapter 4). For larger diffusion coefficients the χ^2 increases and then decreases again, giving a second minimum at about $D_0 \sim 0.7 - 2 \times 10^{28}$ cm^2/s ($D(100\,\mathrm{TeV}) \sim 2.2 - 6.4 \times 10^{30}$ cm^2/s) with a best-fit χ^2 of about 22. This second minimum corresponds to a scenario where the effects of the transition between ballistic and diffusive regimes cannot be ignored, with the quasi-ballistic propagation dominating at distances smaller than a few tens of pc from the source. For larger values of D_0 the χ^2 grows slowly because in the quasi-ballistic regime the radial profile is not much influenced by the specific value of D_0. On the other hand, the χ^2 distribution for Monogem presents a similar behaviour but with much less pronounced variations. There is still a first minimum at about $2 - 3 \times 10^{25}$ cm^2/s and a second minimum at about $4 - 8 \times 10^{27}$ cm^2/s.

Remarkably, the best-fit values we obtain for the quasi-ballistic scenario in the analysis of the two sources is close to the values found by fitting CR data (see Chapter 4). The goodness of the fit for the ballistic case with $\chi^2 \sim 22$ for Geminga and ~ 9

for Monogem tells us that this second minimum gives a satisfactory fit to the data, as the first minimum associated with a suppressed diffusion coefficient. Moreover, such χ^2 values for the quasi-ballistic regime are probably overestimated. Indeed, if we consider Geminga (but similar considerations apply also to Monogem) the χ^2 is mainly dominated by the first data point at $\approx 0.32°$, which corresponds to a distance from the source of of $1.1-1.4$ pc, depending on the distance of Geminga from us ($190-250$ pc). In fact, if we perform the fit without the first point we obtain for $D_0 = 10^{28}$ cm^2/s a $\chi^2 = 6$, which is much smaller than the value of 22 we obtain with the entire dataset. At such small distances two effects are relevant. First of all the actual size of the bow shock (see Section 1.3.2), which is not precisely known, but may be a sizable fraction of a pc [232]. Obviously our model is not supposed to work within the bow-shock, but only after particles have escaped. Increasing the bow-shock size from 0.3 pc, as we assume, to 1 pc would have the consequence of flattening our predictions in the first data point. Second, given the rather sharp profile predicted in the quasi-ballistic regime, the convolution with the point-spread-function (PSF) of the experiment ($\approx 0.5°$ [405]) is very important, because it would flatten our predicted radial profile close to the source, making it more compatible to the first data point. In the purely diffusive model the radial profile is already rather flat close to the source and the convolution with the PSF is not that important. However, it is not possible to properly consider such effect without the analysis tools of the HAWC collaboration. Thus, also taking into account these two caveats, both a suppressed diffusion and a typical diffusion scenario give a satisfactory fit to the Geminga and Monogem γ-ray data. Furthermore, if a typical Galactic diffusion coefficient can account for the data, there is no need to invoke a suppression of diffusion that is difficult to explain theoretically.

When we use a value for the slope of the diffusion coefficient of $\delta = 1/3$ we find that the goodness of fit is similar to the case with $\delta = 0.5$ and the best-fit value for D_0 changes as expected when taking into account the flatter energy dependence of the diffusion coefficient compared to the case with $\delta = 0.5$. We get $D_0 \sim 5 \times 10^{25}$ cm^2/s ($D(100\,\mathrm{TeV}) \sim 2.3 \times 10^{27}\,\mathrm{cm}^2/\mathrm{s}$) for the diffusive propagation and 5×10^{28} cm^2/s ($D(100\,\mathrm{TeV}) \sim 2.3 \times 10^{30}\,\mathrm{cm}^2/\mathrm{s}$) for the ballistic scenario.

The pulsar efficiency

The best-fit efficiency obtained for Geminga is between $3-5\%$ in the low diffusion coefficient scenario and $180-200\%$ for the ballistic one, testing different strengths for B and the two values of the source distance. In our benchmark case with $B = 3\ \mu$G the

efficiency for the diffusive and quasi-ballistic cases are $(3.8 \pm 0.4)\%$ and $(190 \pm 20)\%$, respectively. Instead, for Monogem the efficiency in the pure diffusion scenario is about $2 - 6\%$ while in the ballistic case is about $60 - 100\%$. The former value is consistent with some previous results [238], if D_0 is properly rescaled assuming the different value of δ used.

The different efficiency value obtained for the purely diffusive and ballistic-diffusive cases is due naively to the fact that in the first case particles are trapped in the halo by the small diffusion coefficient and can emit photons, while in the ballistic case they are immediately free to travel far from the source, not contributing to the γ-ray halo. This implies, looking at Figure 6.2 (if we assume the same luminosity), that the purely diffusive case produces a flatter L_e at small distances from the source, while in the quasi-ballistic regime $L_e \sim 1/r$ is steeper at the same distances (see Figure 6.2). As a consequence L_e is much larger for the diffusive case at the angles measured by HAWC ($\theta > 0.5°$) and so the efficiency must be smaller than the value obtained for the quasi ballistic case.

The spectral shape of the $e^{\pm}$ injected from PWNe is not well known, and the best-fit value of the efficiency can change for different spectral parameters. In particular changing the slope of the injection spectrum to $\gamma_e = 1.0$ the efficiency for Geminga in the quasi ballistic case becomes 140%. Also the energy range of $e^{\pm}$ injected by pulsars is not precisely known. A lower limit for the efficiency can be found by assuming that the pulsar injects $e^{\pm}$ only at energies of interest for the HAWC data. In particular, γ rays between $5 - 50$ TeV are produced mostly by $e^{\pm}$ between $20 - 200$ TeV. Assuming this range for the energy we find an efficiency of about 90%. There are other effects that might change the value of the efficiency. For example, the way of treating mathematically the transition between ballistic and diffusive regimes (see Ref. [389] for a discussion) and the form of the function $M(\mu)$ can lead to slightly different best-fit values for the diffusion coefficient (which affects the required efficiency). Moreover, the value of τ_0, as well as the pulsar spin-down luminosity $\dot{E}$ and its distance are not perfectly known. Given the uncertainty of all the above cited parameters the efficiency obtained to fit the HAWC data is not incompatible with the pulsar energetics.

It is also important to remark that, similarly to previous analyses of pulsar halos, we are assuming that particles escape isotropically from the source and undergo isotropic diffusion. Such setup is the one that tends to maximize the required efficiency, since particles are spread spherically. However this description may break down within a few pc from the source, where the magnetic flux tube that encompasses the source should be taken into account. The resulting propagation topology may then be different from a isotropic diffusion, with a progressive transition from 1D anisotropic to a 3D isotropic

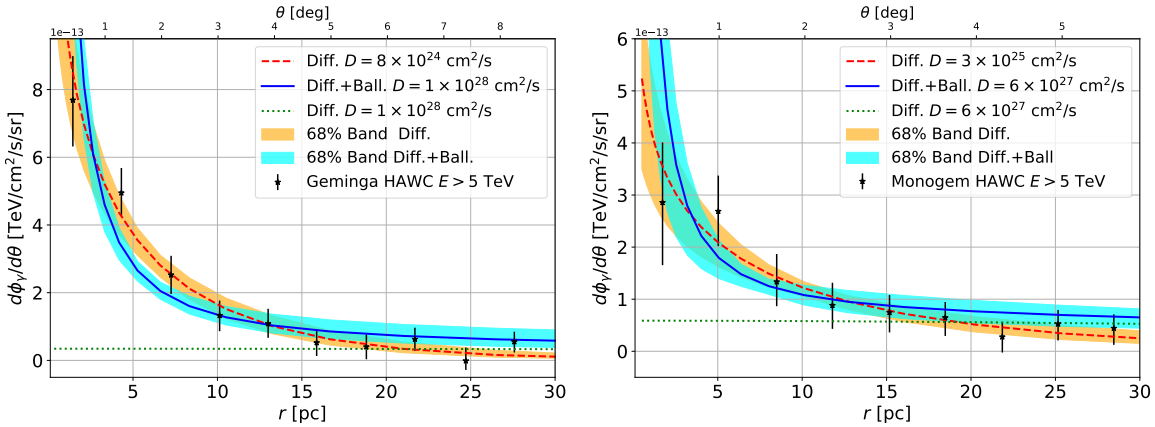

Figure 6.4: Fit to the HAWC data for Geminga (left panel) and Monogem (right panel) in the diffusive regime (red dotted line) and in the combined diffusive and ballistic model (blue solid line and cyan band). We show here the case where the distance of the Geminga and Monogem pulsars are 0.19 and 0.288 kpc, respectively.

propagation with the distance from the source (see e.g., [397]). In this case the volume occupied by the particles would be smaller, which reduces the required efficiency.

A reduction of the required efficiency compared to the isotropic setup could be obtained if relativistic $e^{\pm}$ are emitted at the pulsar's wind termination shocks in collimated jets. In this case there would be an enhancement of the observed luminosity with respect to the intrinsic one due to the beaming effect, similar to what happens for AGN. This effect, if the beams are emitted close to the direction of the l.o.s. that points to the source, can enhance the luminosity by a factor from a few to a factor of tens (see e.g., [406]).

Such a high efficiency agrees well with the PWN paradigm in which a major fraction of the spin-down luminosity of the pulsar is transferred to multi-TeV $e^{\pm}$ through production of the cold ultrarelativistic $e^{\pm}$ wind [407, 408] and less than 10% is transferred to gravitational waves [409] and protons [410]. In particular, in the case of the Crab Nebula, η is very close to 50%. Considering all the uncertainties discussed in this Section and that high efficiencies are indeed expected in pulsars, our model appears to be compatible with current data.

The surface brightness

In Figure 6.4 we show the spatial distribution of the γ-ray flux for our best-fit model to the HAWC surface brightness data, both in the case of the diffusive-only (relevant for small values of the diffusion coefficient) and of the complete model, i.e. diffusive plus ballistic. When the transition from ballistic to diffusive regime is properly taken into

account, a good fit to the data can be achieved without invoking a very small diffusion coefficient. In fact for $D_0 \gtrsim 8 \times 10^{27}\mathrm{cm}^2/\mathrm{s}$ the ballistic regime provides a surface brightness with a shape that goes as $\approx 1/r$ that fits well the data. Instead, when the ballistic-diffusion transition is ignored and the diffusive regime is applied even for very recent emission, one is forced to invoke a small diffusion coefficient to explain the spatial profile. This can be seen in Figure 6.4, where the green dotted curves show the γ-ray surface brightness that one would get if pure diffusion is applied with a typical Galactic diffusion coefficient. Without the inclusion of the ballistic-diffusion transition, one would inevitably be lead to the conclusion that a typical Galactic diffusion coefficient cannot reproduce the data.

In the case of D_0 of the order of $\sim 10^{25}$ cm^2/s, the exponential term $\exp(-r^2/\lambda^2)$ that appears in the diffusive solution (see Equation 6.9) starts to be relevant for distances $r \gtrsim \lambda \sim \sqrt{4\,D\,t_{\rm loss}}$ [374], allows to fit the spatial profile. The γ rays observed at energies $5-50$ TeV are produced by $e^{\pm}$ of energies between $20-200$ TeV. For these leptons and for $D_0 \sim 10^{25}\mathrm{cm}^2/\mathrm{s}$ the scale at which the exponential factor becomes relevant is thus $r >$ a few pc, that is exactly the scale at which the γ-ray data decreases with the distance from the source. This also explains why the best-fit D_0 decreases with smaller values of B. In fact, an increase of the loss time has to be compensated with a decreased D_0 in order to get the same spatial extension. This illustrates how the estimation of D_0 is sensitive to the chosen parameters in the low-D_0 scenario, a problem which is much less prominent in the scenario proposed here.

Authors of Ref. [411] applied the model here presented to the halo detected by LHAASO around PSR J0622+3749 [242], finding a worse fit to the γ-ray surface brightness with the ballistic model with respect to the purely diffusive scenario. It is difficult to directly compare their result with ours since they adopt another mathematical treatment based on the Jüttner propagator [388] and a slope for the diffusion coefficient of $\delta = 1/3$.

6.6 Discussion and summary

In this Chapter we demonstrated for the first time that assuming a standard diffusion coefficient, $e^{\pm}$ injected by pulsars, in the nearby of these sources, travel in the quasi-ballistic regime up to distances from the source of the order of 30 pc at multi-TeV energies. When the transition between the quasi-ballistic and diffusive regime is taken into account, it is possible to fit the HAWC data for Geminga and Monogem with typical values of the diffusion coefficient used to fit CR data [336, 325], without invoking

a suppression. The currently available data for these sources do not allow to reliably discriminate between the two scenarios because they are particularly different within 0.5° from the source, where the effect of the instrument PSF and the assumed size of the bow shock is very relevant. The future detection of halos around middle-age pulsars with $T > 50$ kyrs, i.e. pulsars not confined in the parent SNR (see Section 1.3.2), and with a distance of $1 - 5$ kpc, would provide us important hint on which scenario takes place between the quasi-ballistic or the pure-diffusive.

For such pulsars a small diffusion coefficient $D_0 \sim 10^{25}$ cm^2/s would inevitably lead to a very small angular size, while for values of the diffusion coefficient similar to the Galactic average $D_0 \sim 10^{28}$ cm^2/s, the overall extension is expected to be much larger, as due to the diffusive part of the full transport solution. Therefore, in case of an inhibited diffusion these sources should be detected by HAWC and LHAASO as very compact while with the Galactic average diffusion they would look like as a bright spot, associate to the quasi-ballistic part, surrounded by an extended faint emission due to the diffusive part.

The primary goal of this Chapter is not to claim that the ballistic model is the only valid interpretation. Rather, we tried to underline that without considering this particular regime, which has been the case in previous analyses, a bias is introduced. This bias can exclude an interpretation that doesn't require a suppressed diffusion coefficient. In the coming years, more data and detections are expected from experiments such as LHAASO and CTA. Pulsar halos will provide crucial insights into how $e^{\pm}$ particles are generated, released, and on their propagation in the region around the source. When combined with AMS-02 data and cross section from collider experiments, this will enable a comprehensive understanding of the origin of these particles. Additional information from kinetic plasma simulations concerning how these particles are accelerated in PWN in the near future will be able to complete the overall picture.

Chapter 7

Particle acceleration at quasi-perpendicular shocks

The connection between various physical scales is a recurring theme in this thesis, and kinetic plasma simulations embody this aspect. To comprehend particle acceleration in astrophysical objects and so on macroscopic scales (tens of pc), it is necessary to consider the small-scale plasma physics (hundreds of km) to correctly model the magnetic turbulence required for the acceleration processes. This Chapter is based on Ref. [6].

7.1 Collisionless shocks: kinetic simulations

Understanding the conditions conducive to particle acceleration at collisionless, non-relativistic shocks is important for the comprehension of the origin of CRs and for understanding the phenomenology of heliospheric shocks [412, 413], novae [414, 415], SNRs [186, 416], winds and lobes of active galaxies [417, 418], and galaxy clusters [419]. Energization at shocks proceeds mainly via DSA (see [65, 66, 68, 67] and Section 1.3.1), with the maximum attainable energy determined by the rate of scattering and hence on the level of magnetic perturbations [420, 421, 422] in the accelerator environment. The study of physical processes occurring in these astrophysical objects must be conducted within the framework of magnetized space plasmas, and there exist various methods to perform these analysis.

The macroscopic description is provided by the MHD approach, that could be not sufficient for a complete treatment of the problems. Indeed, the MHD approach is a continuous media description which does not consider the particle nature of plasma, and is essentially based on a limited number of evolution equations for local macroscopic

quantities (density, velocity, temperature, etc). In some situations, it is necessary to provide a more detailed description, which is related to the evolution of the full particle phase-space distribution function and contains more information on the dynamics of the plasma. This description is provided by kinetic theories that are able to model the non-linear interplay between energetic particles and the electromagnetic fields, which is very hard to tackle analytically.

In the last few decades new techniques were developed to model collisionless astrophysical plasmas, using *ab initio* PIC calculations that consist in iteratively moving particles on a grid according to the Lorentz force and self-consistently adjusting the electromagnetic fields. PIC simulations essentially solve the Vlasov equation, that describes the time evolution of the distribution function of the plasma, by sampling the phase space with individual macro-particles and considering the dynamics of both ions and e^-. These simulations are particularly useful to account for spectra that may span several order of magnitude in momentum, where standard Vlasov solvers may lose accuracy [423, 424]. An important progress in this field in recent years, regarding modeling non-relativistic shocks via first-principles calculations, was made with the first PIC simulations that showed simultaneous acceleration of both ions and e^- [425, 426, 427, 428, 429]. These simulations were only performed in 1D since it is still computationally challenging to perform simulations in higher dimensions with a PIC setup.

While for understanding e^- injection in the acceleration process at shocks full PIC simulations are needed, the general dynamics of shocks of SNRs is dominated by the accelerated ions; therefore, one may revert to the *hybrid* approach, a combination between PIC and MHD simulations. Hybrid simulations treat ions as particles, following their motion in a self-consistent manner, while e^- are considered as a massless neutralizing fluid [430] due to their significantly smaller mass. The concept here is that turbulence and instabilities produced by e^- affect significantly smaller scales compared to those relevant for ions. This contrast in scales arises from the distinct masses of these two particle species and consequently on the different Larmor radii.

With hybrid simulations we can then model the shock dynamic, ion acceleration, and plasma instabilities self-consistently without resolving the time and space scales relevant for e^-. Hybrid simulations have been extensively used for heliospheric shocks[1] (e.g., [432, 433]), and more recently even for stronger astrophysical shocks. Hybrid codes do not need to resolve the small time/length scales of the e^-, which are usually dynamically negligible, and are thus better suited than full PIC codes to simulate

[1] To give an idea, time and length scales accessible to hybrid simulations on modern supercomputers are comparable with the physical scales of the Earth's bow shock [431].

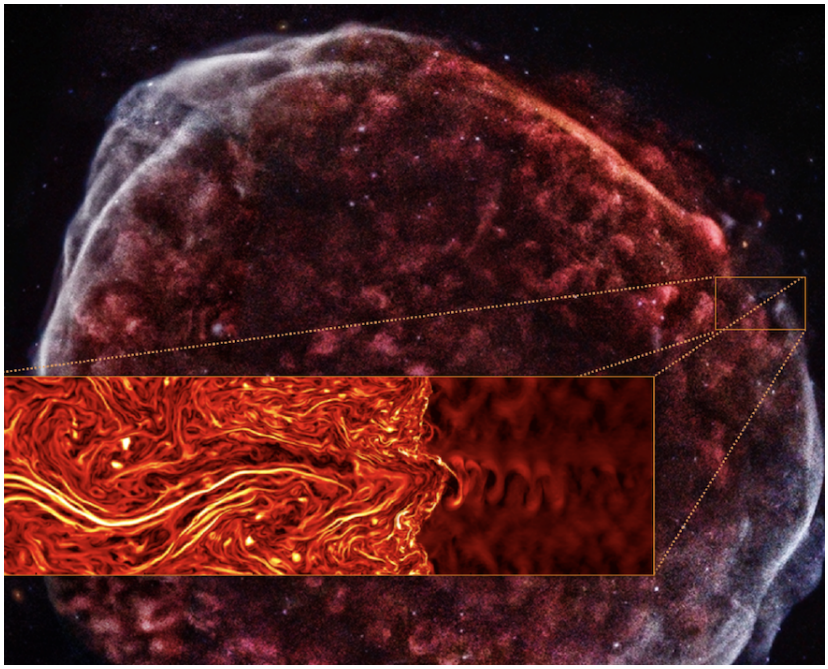

Figure 7.1: An illustrative representation of the concept underlying the usage of kinetic simulations: utilizing PIC and hybrid simulations is the equivalent of analyzing small and specific regions of astrophysical shocks. This Figure is provided with the courtesy of Prof. Damiano Caprioli.

the long-term evolution of shocks. Hybrid simulations have been used to perform a comprehensive analysis of ion acceleration at collisionless shocks as a function of the strength and topology of the pre-shock magnetic field, the nature of CR-driven instabilities, and the transport of energetic particles in the self-generated magnetic turbulence [434, 435, 436]. Moreover, they have been used to unveil the processes that lead to the injection into DSA of p [437], ions with arbitrary mass/charge ratio [438], and pre-existing CRs [439].

For scales larger than hybrid and lower than pure MHD, a promising technique is the coupling of the hybrid technique with a MHD description of the background plasma [440, 441] which is called MHD-PIC, in which only the fraction of ions that are injected in the acceleration process are tracked, neglecting all the others. In this framework, the injection into DSA must be specified by hand and the simulation is not built from a self-consistent starting point.

Utilizing PIC and hybrid simulations within 1D, 2D, or 3D setups with associated spatial coordinates is the equivalent of analyzing small and specific regions of astrophysical shocks. This approach allows us to simulate localized areas of SNR shock, for example, providing insights into the complex physics occurring on scales of hundreds of km. This

concept is visually represented in Figure 7.1.

7.2 Quasi-perpendicular non-relativistic shocks

One of the fundamental parameters that characterizes the acceleration process, the amount of turbulence and, in general, the physics of astrophysical shocks, is the inclination between the direction of motion of the shock and the orientation of the background magnetic field B_0. Full PIC simulations have captured ion and electron DSA at quasi-parallel shocks, i.e., when the angle between B_0 and the shock normal is $\vartheta_{\rm Bn} \lesssim 45°$ [425, 428, 429]. Simulations of (quasi-)perpendicular shocks ($\vartheta_{\rm Bn} \approx 90°$) have been performed in 1D [442, 443, 427], 2D [444, 445, 446, 447], and 3D [448], but evidence of particle acceleration and injection into DSA has been elusive. Also at relativistic shocks DSA is more efficient for quasi-parallel configurations [449, 84], unless the shock magnetization is sufficiently low (so for high Mach number values), which makes DSA possible also in the quasi-perpendicular configuration, though rather slow [450].

On the other hand 2D hybrid simulations have shown that thermal ions can be *spontaneously* injected into DSA at quasi-parallel shocks [451, 452, 432, 453, 435, 436, 437, 438, 439, 71, 72], but injection of ions at oblique and quasi-perpendicular shocks has been more problematic. Test-particle and Monte Carlo calculations based on a strong scattering of particles with magnetic perturbations specified by hand, seem conducive to ion injection [454, 455, 456] in the acceleration process, but no self-consistent kinetic simulation without *ad-hoc* prescription has reported the presence of energized particles. Nevertheless, hybrid simulations *augmented* with upstream magnetic fluctuations with long-wavelength and large amplitudes [457] suggest that quasi-perpendicular shocks may be efficient ion accelerators. In general, when magnetic turbulence is specified by hand in the pre-shock medium [455, 458], or when energetic seeds are added [439], which means a population of particles already energized, DSA may occur for arbitrary inclinations. In these cases the efficiency and spectra obtained are not universal but depend critically on the *ad-hoc* prescriptions adopted for the pre-existing seeds and turbulence.

It has been recognized that systems with reduced dimensionality artificially suppress particle diffusion across field lines [459, 460, 455], which likely explains why 1D/2D simulations fail to produce non-thermal tails. The question remains of whether, and under which conditions, the 3D setup can lead to *spontaneous* injection of particles into the acceleration process.

In this Chapter we use hybrid simulations to explore quasi-perpendicular shocks from

magnetized to the weakly-magnetized regime (so from low, to high Mach number regime), that characterize several astrophysical objects, from planetary bow shock (usually with low Mach numbers < 40), to SNRs and Radio SNe (with high Mach numbers > 50). We find that also for non-relativistic shocks ion acceleration is naturally unlocked if the full 3D dynamics is taken into account.

7.3 Simulation setup

Simulations are performed with the `dHybridR` code [461], here used in the non-relativistic regime [462]. We send a supersonic flow with speed v_{sh} against a reflecting wall (left boundary), which produces a shock moving from the left to the right into a background quasi-perpendicular B_0 field with $\vartheta_{\rm Bn} = 80°$ between the direction of motion of the shock and B_0.

The `dHybridR` code, like other PIC codes, employs the so-called *normalized* units. These units, derived from fundamental plasma parameters, simplify the equations of motion, making them more intuitive. Lengths and coordinates are measured in units of the ion skin depth d_i. It represents the characteristic spatial scale over which the electric field and magnetic field associated with charged ions in a plasma interact. It is defined as $d_i \equiv c/\omega_p$, where c is the light speed and $\omega_p \equiv \sqrt{4\pi ne^2/m}$ is the ion plasma frequency in cgs units, with m, e and n the ion mass, charge and number density, respectively. The ion plasma frequency represents the characteristic frequency at which charged ions in a plasma oscillate collectively in response to electric fields. Time is measured in inverse cyclotron times $\omega_c^{-1} \equiv mc/(eB_0)$, that is the time it takes for an ion to complete one full orbit or gyration around a magnetic field line. Velocities are normalized to the Alfvén speed $v_A \equiv B_0/\sqrt{4\pi mn}$ and energies to $E_{sh} \equiv mv_{sh}^2/2$. The adoption of normalized units expands the range of application for a simulation.

Table 7.1: Left: parameters for the runs in the analysis; inclination is fixed to $\vartheta_{\rm Bn} = 80°$. Right: corresponding acceleration efficiency, η, and energy spectral index, γ.

Run	M	$x[d_i]$	$\Delta t[\omega_c^{-1}]$	$\eta\ (> 10E_{sh})$	γ
A	20	5000	7.5×10^{-3}	4%	3.7
B	30	5000	4×10^{-3}	8%	3.1
C	40	5000	1.5×10^{-3}	11%	2.9
D	50	5000	1.5×10^{-3}	17%	2.7
E	100	10000	7.5×10^{-4}	30%	1.5

Different astrophysical shocks, characterized for example by diverse velocities, may have the same value of M. This depends on the Alfvén speed of the medium in which they are propagating, and so on its magnetic field strength and density. To translate normalized units into physical quantities, assumptions about the values of parameters like B_0 and n are necessary, depending on the specific problem at hand. All physical quantities are normalized to their far upstream values (e.g. B is in unit of B_0).
Simulations include the three spatial components of the particle momentum and of the electromagnetic fields. Ions are initialized with thermal velocity $v_{\rm th} = v_A$ and e^- are initially in thermal equilibrium. The hybrid model requires an explicit choice for the e^- equation of state, and are assumed to be adiabatic, i.e., the e^- pressure is related to the density as $P \propto \rho^{5/3}$. We define the Alfvénic Mach number as $M_A \equiv v_{sh}/v_A$; throughout the Chapter we indicate the shock strength simply with $M = M_A$.
We performed simulations with different M, longitudinal sizes, and time steps, as reported on the left side of Table 7.1; the transverse sizes are fixed to 50 d_i in all the cases. We use two and a half cells per d_i in each direction and 8 (4) ion particles per cell (ppc) in 3D (2D). We checked our results against convergence in particle statistics, box size, and spatial/temporal resolution: e.g., increasing the transverse sizes to 100 d_i and ppc to 16 returns energy spectra indistinguishable from those presented here. For discussions on the convergence in box size we refer to the appendix of Ref. [434, 435], for the hybrid equation of state to Ref. [71, 439], and for linear and strongly non-linear problems simulated in 2D and 3D to Ref. [461].

7.4 Results

We here discuss the results obtained with our simulation campaign, starting with the comparison of the dynamics of quasi-perpendicular shocks in 1D, 2D with **B** oriented either in plane (2Dy) or out of plane (2Dz), and 3D simulations.

Magnetic field amplification

Figure 7.2 shows the total magnetic field intensity B_{tot} for a shock with $M = 100$ and $\vartheta_{\rm Bn} = 80°$ in 2Dz, 2Dy, and a slice in the $x-y$ plane of the 3D setups; the bottom panel shows the evolution of B_{tot} for the 3D case. There is a striking difference between 2Dz and 2Dy: while in the former case the field is simply compressed at the shock, in the latter case B_{tot} overshoots and is strongly amplified downstream [445, 446, 434]; at the latest stages of the 3D simulation the field amplification extends also upstream of the shock. This is the signature of a precursor, an area with strong turbulence immediately

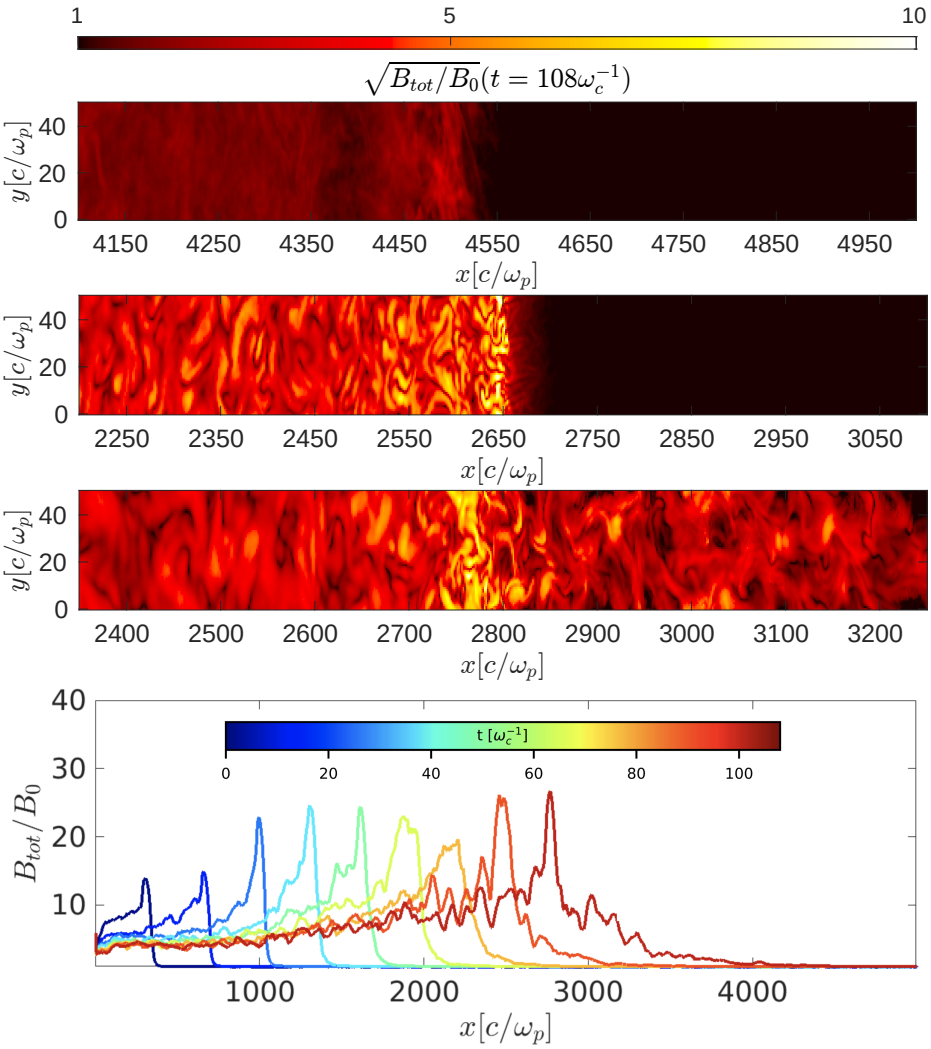

Figure 7.2: From the top: total magnetic field for the out-of-plane (2Dz), in-plane (2Dy), and 3D setups. In all cases M=100 and $t = 108\omega_c^{-1}$. Bottom panel: time evolution of B_{tot} in 3D.

in front of the shock, produced by particles that are back-streaming in the upstream. We do not engage ourselves in a full characterization through a Fourier analysis of the strongly amplified fields ($B_{tot}/B_0 \gtrsim 40$) observed for $M = 100$, though we notice that their morphology and scaling ($B_{tot}/B_0 \propto \sqrt{M}$) bear strong resemblance with those produced by the so-called ion-Weibel instability [446, 445, 447]. The Weibel-type filamentation instability arises from the interaction between shock reflected ions and upstream plasma ions. Finally, we ascribe the difference between 2Dz and 2Dy to the fact that the out-of-plane magnetic field configuration misses the Weibel instability, which changes the magnetic field amplification physics compared to the in-plane 2D simulations. Figure 7.3 displays the 3D visualisation of the magnetic field for a strong

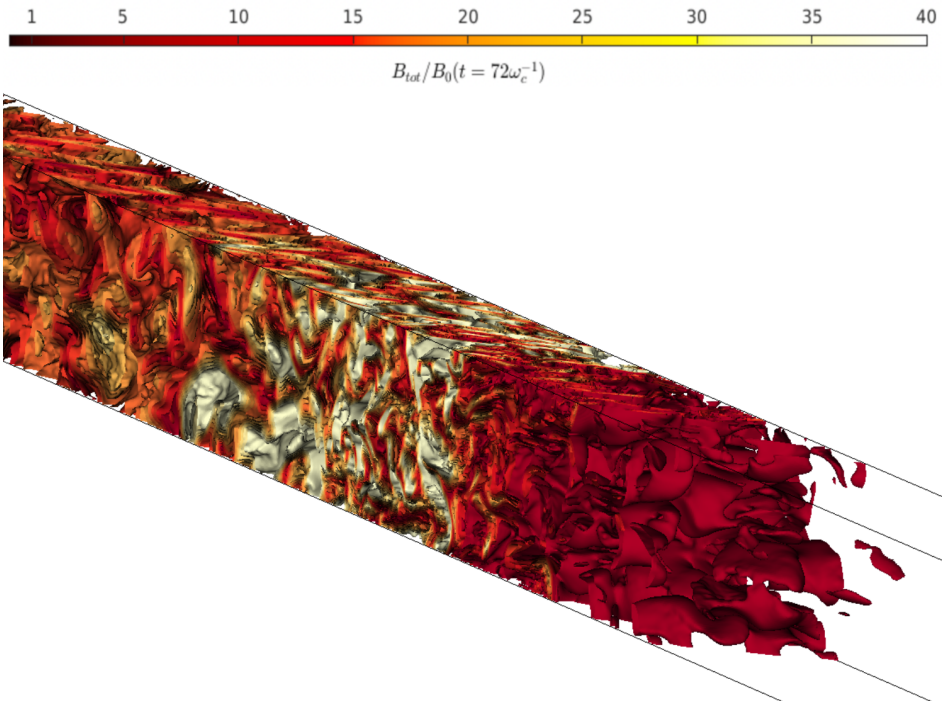

Figure 7.3: 3D visualisation of the magnetic field for $M = 100$.

shock with high $M = 100$.

Particle spectra and dependence on M

The top panel of Figure 7.4 shows the ion spectrum in the downstream region close to the shock (namely post-shock) at $t = 108\omega_c^{-1}$ for different setups: 1D and 2D exhibit only a supra-thermal bump [434] at $E = 3 - 4E_{sh}$, while 3D shows a very extended power-law tail; the dashed line corresponds to a Maxwellian distribution with temperature $\sim 80\%$ of the one expected for a purely gaseous shock that does not accelerate particles, which suggests that $\sim 20\%$ of the shock ram pressure is converted in energetic ions. This is the major result of this Chapter: we show for the first time, using self-consistent kinetic calculations, how with the 3D setup ions can be very rapidly accelerated at non-relativistic, quasi-perpendicular shocks. Note that the post-shock 2Dy magnetic turbulence, while very similar to the 3D one, is not sufficient to grant injection into the acceleration process. The evolution of the downstream ion spectrum in 3D is shown in the middle panel of Figure 7.4: from an early supra-thermal bump, similar to the 1D/2D cases, a non-thermal tail develops very quickly and extends over more than three orders of magnitude in just $\sim 100\omega_c^{-1}$.

Finally, the bottom panel of Figure 7.4 shows the spectrum for different M. Each

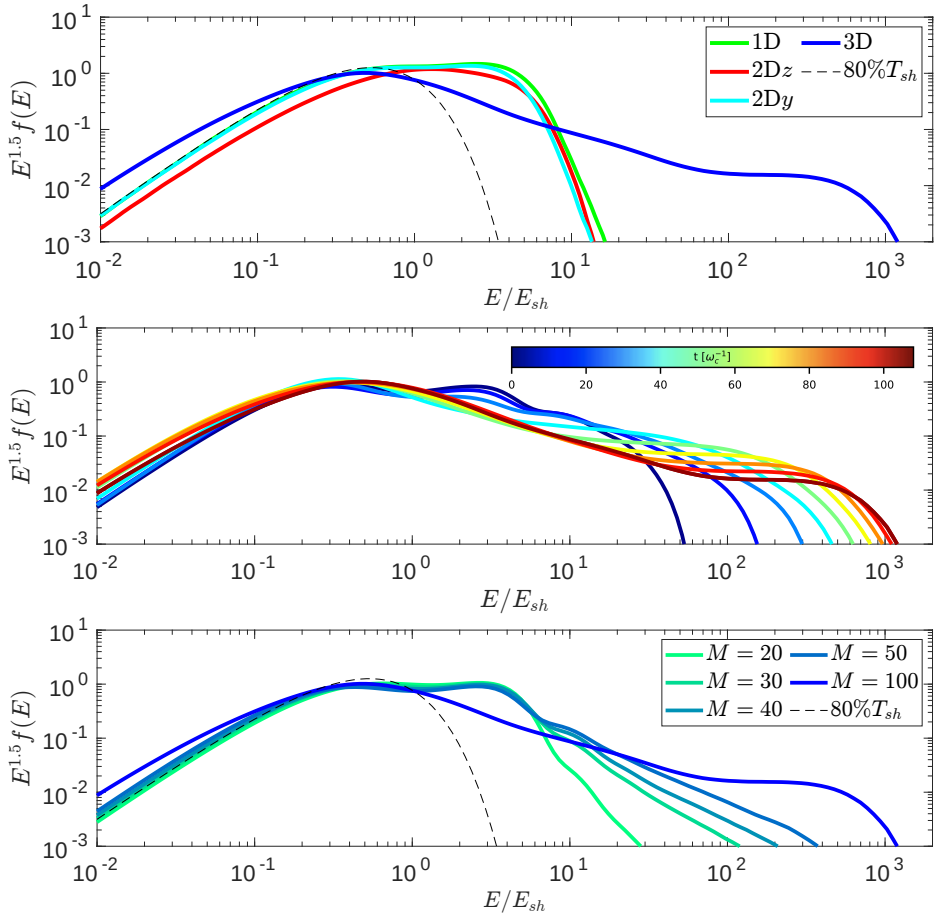

Figure 7.4: Top panel: downstream ion spectrum at $t = 108\omega_c^{-1}$ for $M = 100$ and different setups. A non-thermal tail above $10E_{sh}$ is present only in 3D, while 1D and 2D show similar truncated spectra. Middle panel: time evolution of the ion spectrum in 3D. Bottom panel: spectrum dependence on M; the dashed line indicates a Maxwellian with temperature $\sim 80\%$ of the one expected for a purely gaseous shock.

spectrum can be characterized as a power-law, $f(E) \propto E^{-\gamma}$, with an acceleration efficiency η, defined as the fraction of the post-shock energy density in ions with energy above $10E_{sh}$. The scaling of γ and η on M are reported in Table 7.1. For M=100 the spectrum tends to $E^{-1.5}$ ($\propto p^{-4}$ for non-relativistic particles), the universal spectrum expected at strong shocks; for lower values of M, non-thermal tails become steeper and less extended, almost vanishing for $M = 20$ (no tails were found for 3D simulations of $M = 6$, see [434]). The post-shock magnetic turbulence scales $\propto \sqrt{M}$, which increases the diffusion process in the downstream and the probability that ions return upstream, making the spectra harder. Overall, the acceleration efficiency increases from a few percent for $M = 20$ to $\eta \gtrsim 20\%$ for $M \gtrsim 50$, a value comparable to the efficiency of quasi-parallel shocks [434, 435, 71].

Acceleration mechanism

Let us focus now on the mechanism(s) responsible for ion acceleration. Figure 7.5 shows the $x - p_x$ (where p_x is the momentum along x) trajectory and energy gain of an ion tracked in run B. Particles gain energy through shock drift acceleration (SDA), tapping into the motional electric fields in the upstream region $\mathbf{E} \simeq -\mathbf{v}/c \times \mathbf{B}$ during their gyrations around the shock [463, 464, 465, 466]. The basic idea behind SDA is pretty much the same as DSA. The difference lies in how particles make their way back to the shock in the upstream region. At the initial stages of the process, when there aren't any magnetic perturbations in the upstream area, particles don't undergo a diffusion process. Instead, they simply gyrate around the magnetic field lines so, technically, this process can not be defined as DSA.

As pointed out in Refs. [459, 460, 455], cross-field diffusion plays a crucial role in the return of ions from downstream, and is not properly captured if not in 3D. Cross-field diffusion refers to the process in which charged particles move across the magnetic field lines. This movement can occur when particles transition from one magnetic field line to another, typically due to scattering or other physical interactions. Authors of [460] demonstrated that charged particles in an arbitrary electromagnetic field with at least one ignorable spatial coordinate remain forever tied to a magnetic-field line. Since in 2D field lines are effectively transverse sheets, ion diffusion along the shock normal is inhibited. In 3D, instead, field lines can twist and intertwine, and ions can perform cross-field diffusion, which effectively prevents them from being rapidly swept downstream. Tracking reveals that in 2D ions are advected downstream after a couple of gyrations, while in 3D they diffuse back several times, gaining energy at each SDA cycle. To some extent, this acceleration mechanism is similar to the one proposed by Ref. [467], using Monte Carlo calculations with *ad-hoc* prescription on the diffusion process; our self-consistent simulations show that the mechanism may occur only for large M and may be intrinsically limited when $\vartheta_{\rm Bn} < 90°$.

A limit on the maximum achievable energy?

Figure 7.6 shows the evolution of the maximum ion energy $E_{\rm max}$ for different M. After an initial growth $\propto t^2$, $E_{\rm max}$ saturates at an asymptotic value $E^*_{\rm max}$, which scales $\propto M$ because ions can undergo more SDA cycles.

For non-relativistic ions, the momentum gain per SDA cycle is $\Delta p/p \propto v_{sh}/v$, where v is the ion speed, which implies a constant $\Delta p \propto v_{sh}$. Since the duration of each SDA cycle is $\Delta t \approx \omega_c^{-1}$ (independent of v) and since the number of cycles $\propto t$, then $p_{\rm max} \propto \Delta p t/\omega_c^{-1} \rightarrow E_{\rm max} \propto t^2$, in good agreement with Figure 7.6. This acceleration

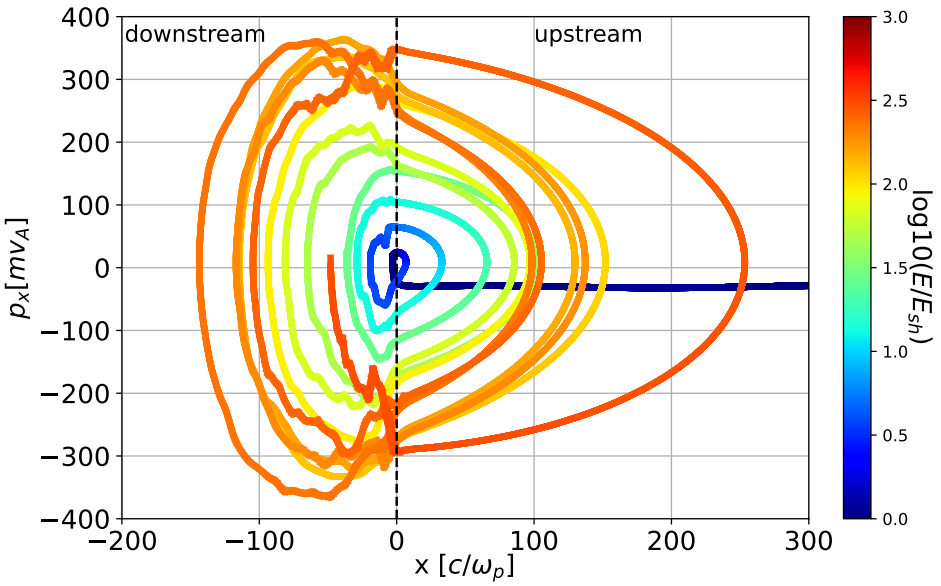

Figure 7.5: Energy gain (color code) and trajectory in the $x - p_x$ plane of a representative ion undergoing SDA in run B.

process is extremely fast [468, 469] and generally faster than DSA, since in DSA the duration of a cycle is the diffusion time $\sim p/v_{sh}\omega_c^{-1}$ [470, 436], while for SDA is the gyration time. At later times and for larger values of M, we observe a brief transition from SDA to DSA, with some sufficiently-energetic ions returning to the shock via pitch-angle diffusion rather than via ordered gyration (note the deviation from the $\propto t^2$ curve before the plateau in Figure 7.6); eventually, ions escape toward upstream infinity and non-thermal tails stall at a critical energy $E^*_{\rm max} \propto M$.

The crucial question is whether the streaming of escaping ions may trigger the NRSI instability (see Section 2.4.3) and self-support the acceleration to larger energies at later times, as at parallel shocks [435]. In the bottom panel of Figure 7.2 it is possible to see the shock precursor, that is the region immediately ahead of the shock characterized by magnetic field amplification with $B_{tot}/B_0 \gtrsim 1$, produced by ion-driven instabilities. In the $M = 100$ simulation we infer that the precursor is $\sim 1000\, d_i$ wide, comparable to the upstream diffusion length of $\lesssim E^*_{\rm max}$ ions. Further upstream, though, $\delta B \ll B_0$ and there is hardly any fluctuations at scales resonant with $E^*_{\rm max}$ ions able to scatter them back. The diffusion length for such energetic particles quickly becomes (much) larger than the box, which makes it computationally prohibitive to follow the longer-term evolution of these systems with 3D hybrid simulations.

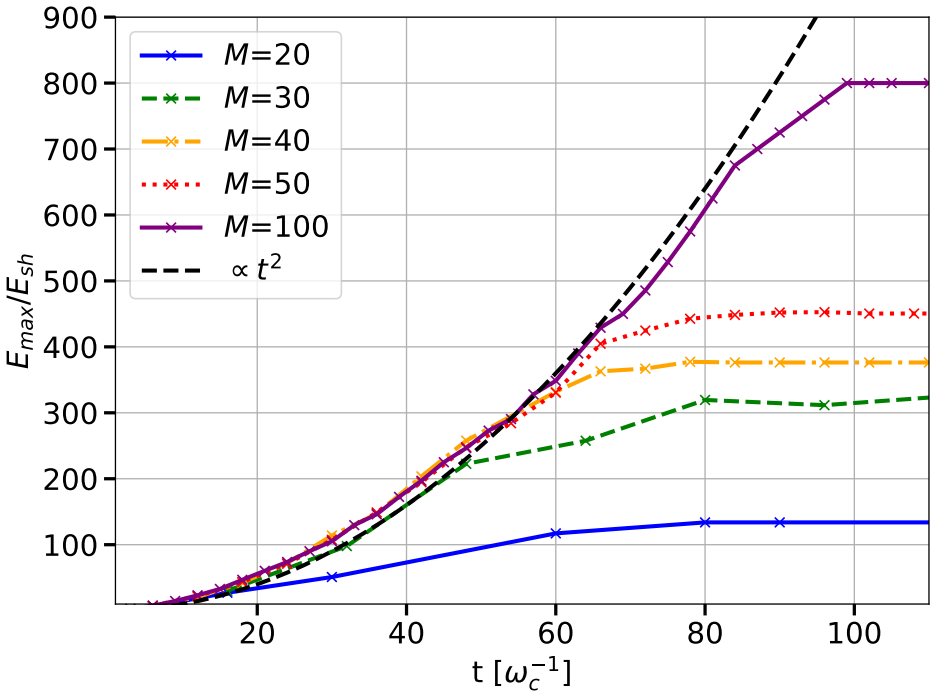

Figure 7.6: Evolution of $E_{\max}(t)$ for different M; after an initial increase $\propto t^2$ provided by SDA (black solid line), $E_{\max}(t)$ eventually reaches an asymptotic value $\propto M$.

7.5 Phenomenological implications

The results described in this analysis have several applications in space/astrophysical shocks. In the following we assume that the mechanism proposed works also for e^-, that is realistic hypothesis.

Heliospheric shocks. Magnetospheric Multiscale (MMS) spacecraft measurements at the Earth's bow shock, that is a shock wave that forms by the interaction between the magnetic field surrounding the Earth and the solar wind characterized by $M \lesssim 20$, show that quasi-parallel regions are generally more efficient than oblique ones at accelerating ions [471, 472]; yet, efficiencies $\eta \lesssim 10\%$ for $\vartheta_{\rm Bn} \gtrsim 70°$, compatible with our run at $M = 20$ (Table 7.1), and not with 2D ones which return $\eta \lesssim 1\%$ [431, 434, 471]. Another application of the very fast acceleration that we observe may be in producing relativistic e^- at foreshock disturbances at the Earth's bow shock [473], often characterized by quasi-perpendicular configurations. These disturbances are dynamic and complex regions of space that form just upstream of the bow shock as a result of the interaction between the solar wind and the Earth's magnetic field.

Supernova remnants. Particularly interesting is the case of SN 1006, a SNR which lies significantly above the Galactic plane and shows a bilateral symmetry that correlates

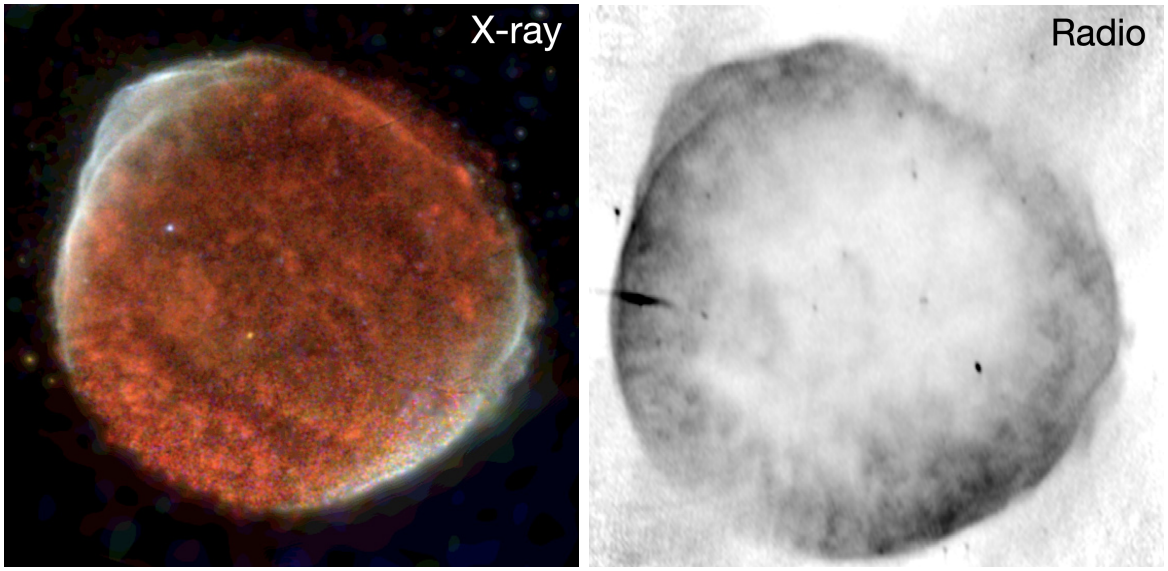

Figure 7.7: Left panel: X-ray emission from SN 1006. The areas dominated by non-thermal emission appear white. The areas dominated by the thermal emission appear red. Right panel: radio emission from SN 1006. Figures taken from Ref. [474].

with the direction of the background B_0 [474, 475]. X/γ-ray emission comes from the quasi-parallel (polar caps) regions [476, 477, 478], implying the presence of multi-TeV e^-, while radio emission is more azimuthally symmetric [474], suggesting the presence of GeV e^- also in oblique regions. The X-ray and radio emission from SN 1006 are reported in Figure 7.7.

We propose a possible interpretation of these measurements: in the quasi-parallel region, particles are accelerated up to multi-TeV energies and can produce X/γ-ray emission, as confirmed by the low polarization and strong synchrotron emission inferred in the polar caps; in quasi-perpendicular regions, based on the results of our simulations, we find a saturation of the maximum energy that particles can achieve and for SN 1006, particles may not be able to reach the necessary GeV energies for radio emission. This issue can be resolved by considering that once particles are injected into the acceleration process via SDA, as outlined here, they can subsequently reach GeV energies by undergoing DSA due to the presence of interstellar turbulence. The interstellar turbulence has the capability to produce a diffusion coefficient strong enough to scatter particles back to the shock, that can energize them up to the GeV range, as demonstrated in Ref. [479, 56]. With the proposed mechanism, we solve the problem of particle injection into the acceleration process.

Whether *multi-TeV* e^- should also be expected in quasi-perpendicular regions is an interesting question that hinges on the longer-term evolution of these systems.

Radio SNe. Finally, we consider young extra-galactic SNe, whose radio emission sug-

gests that e^- are often accelerated with a spectral index $q \simeq 3$ [480, 481]. Such steep spectra at fast shocks ($v_{sh} \approx 10^4$ km s^{-1}) are hard to reconcile with standard DSA (though see Ref. [482, 483]), but may be compatible with the results presented here, provided that $M \lesssim 50$ (see Table 7.1). A SN shock propagating in the Parker spiral of the progenitor's wind may provide both relatively-small M and quasi-perpendicular shock geometries [480]. Furthermore, a flattening of the spectrum for higher shock velocity, that could imply higher M, has also been reported [484, 480]. Scaling the asymptotic $E^*_{\rm max}$ illustrated in Figure 7.6 and considering $v_{sh} \simeq 10^4$ km s^{-1}, it is possible to infer a phenomenological equation:

$$E^*_{\rm max} \simeq 0.22\,{\rm GeV}\,\frac{M}{50}\left(\frac{v_{sh}}{10^4\,{\rm km\ s^{-1}}}\right)^2. \tag{7.1}$$

With values of $B_0 \gtrsim 3$ mG present in radio SN, particles with energies on the order of a fraction of a GeV are sufficient to emit radio waves.

7.6 Discussion and summary

We used hybrid simulations to characterize, for the first time in kinetic calculations without any *ad-hoc* prescription for particle scattering and/or injection, how ions can be very rapidly accelerated at non-relativistic, quasi-perpendicular shocks. 3D simulations are necessary to fully capture the amplification of the initial magnetic field (Figure 7.2) and the cross-field diffusion, that allows ions not to be advected away downstream after a few shock crossings. Acceleration starts via SDA, exhibiting a clear signature $E_{\rm max} \propto t^2$, then quickly transits to DSA (where $E_{\rm max} \propto t$) before reaching a limit energy $E^*_{\rm max}$, beyond which particles escape upstream.

Acceleration efficiency and spectral slope strongly depend on the shock Mach number M (Table 7.1): while for $M \lesssim 20$ efficiency is only a few percent and spectra are very steep, for $M \gtrsim 50$ it can exceed 10-20% and spectra converge to the DSA ones, as flat as p^{-4} in momentum; also the level of magnetic field amplification and the maximum energy limit increase with M. The results described in this analysis have several applications in space/astrophysical shocks, from planetary bow shocks, to SNRs.

The biggest questions that remain open are whether oblique/quasi-perpendicular shocks can efficiently drive plasma instabilities strong enough to self-sustain DSA up to energies significantly larger than $E^*_{\rm max}$, and whether the same acceleration process is viable for e^-, too. Both questions require different numerical approaches that are capable of either capturing the longer-term evolution of the system or the physics of electron

injection.

Kinetic simulations are another powerful tool for the understanding of the origin of Galactic CRs. These simulations operate within the realm of plasma turbulence scales, and allow us to model the acceleration of CRs within astrophysical environments.

Summary

The research presented in this thesis aims at contributing to unveil the mysteries of Galactic cosmic messengers, particularly focusing on Galactic CRs and γ rays. It has delved into their creation, acceleration, and propagation throughout our Galaxy, with special emphasis on $e^{\pm}$ and γ rays.

The subjects explored within this thesis encompass a wide range of scales, spanning from the infinitely small to the infinitely large. The approach employed throughout consists in combining various types of messengers to gain a deeper understanding of these cosmic emissions. Our findings have played an important role in characterizing high-energy astrophysical processes occurring within our Galaxy.

In Chapter 1, we introduced charged cosmic radiation, with a particular focus on $e^{\pm}$ components. We delved into the origins of CRs, ranging from SNRs with explanations of the diffusive shock acceleration mechanism, to PWNe as sources of $e^{\pm}$ pairs. We also considered contributions from other sources and interactions of primary CRs with the ISM. Lastly, we described the transport of accelerated CRs within the Galaxy and discussed measured $e^{\pm}$ fluxes.

Chapter 2 introduced cosmic γ-ray radiation and provided an overview of its production in astrophysical environments. We covered various components of the γ-ray sky, including steady sources within our Galaxy. To describe γ-ray emissions originating from Galactic CRs, we briefly explained the properties of the Galactic ISM and ISRF. Additionally, we introduced γ-ray halos detected around pulsars, which serve as unique tools for investigating CR propagation in specific Galactic regions.

In Part II, we presented our results. In Chapter 3, our focus was on the production cross sections of $e^{\pm}$ and γ rays in hadronic interactions. These cross sections play a crucial role in calculating the secondary $e^{\pm}$ fluxes and the Galactic diffuse emission. Ensuring the correct interpretation of contributions from primary sources relies on accurately describing the secondary production processes. The majority of secondary $e^{\pm}$ particles are generated in $p+p$ collisions and through interactions involving He, both as a target and a projectile. We established an analytical description of the Lorentz invariant cross

section of $\pi^{\pm}$ and $K^{\pm}$ and other minor channels that decay in $e^{\pm}$ in $p+p$ collisions and heavier nuclei, either by utilizing data or by referring to Monte Carlo generators. The differential cross section $d\sigma/dT_{e^{\pm}}(p+p \to e^{\pm}+X)$ was predicted within MeV to TeV energies with an uncertainty of approximately $5-7\%$, dramatically reduced with respect to the state of the art.

The diffuse Galactic emission primarily arises from the decay of π^0 produced by the inelastic scattering of nuclei CRs with the ISM. Accurate modeling of the production cross section of γ rays of hadronic origin is critical for interpreting data from the *Fermi*-LAT. We proposed a new evaluation for the production cross section of γ rays resulting from $p+p$ and heavier nuclei collisions, inferred from the limited available data on total cross sections and from the analysis of cross sections for $e^{\pm}$. Our results were complemented by a realistic and conservative estimation of the uncertainties. The total $d\sigma/dE_{\gamma}$ was estimated with an error ranging from 10% to 20% depending on E_{γ}, improving the state of the art.

In Chapter 4, we conducted a natural follow-up of the previous Chapter by calculating a new estimate of the secondary $e^{\pm}$ flux, combining the information from cross sections with improvements in Galactic propagation modelling. We performed new fits to AMS-02 CR nuclei data using GALPROP and obtained new state-of-the-art propagation models, testing different propagation scenarios with specific choices for the diffusion coefficient, the injection spectra, the convective wind and reacceleration amount. We found that propagation models with values of $L \lesssim 2$ kpc are disfavored by CR data. We show that the e^+ flux never exceeds AMS-02 data. The excess of the data with respect to secondary e^+, that depends heavily on L, is significant at energies greater than a few GeV. Contextually, we have computed the flux of secondary e^- at Earth. A further, more precise determination of the e^+ flux is only possible after a more precise determination of L.

After focusing on secondary $e^{\pm}$, in Chapter 5, we shifted our attention to the total e^+ flux, investigating the contribution from PWNe. The high-precision AMS-02 e^+ data were employed to constrain the main properties of the Galactic pulsar population and the PWN acceleration needed to explain the observed CR flux. For this purpose, a large number of Galactic pulsar populations were simulated, calibrated on ATNF catalog observations. For each mock galaxy, we computed the e^+ flux at Earth as the sum of the primary component due to PWNe emission and the secondary component. The result is fitted to AMS-02 e^+ data and the galaxy realizations that properly fit the AMS-02 e^+ data have between $2-3$ sources that dominate the flux.

In Chapter 6, we focused on pulsar γ-ray halos, which are a direct product of particles accelerated and emitted in a region around the source. The detection of these halos

in previous analyses led to the conclusion that CR diffusion is inhibited within a few tens of pc from the pulsar with respect to the rest of the Galaxy. We demonstrated that, considering that particles initially travel in the ballistic regime and taking into account the transition between the quasi-ballistic and diffusive regime, it is possible to fit the HAWC data for Geminga and Monogem pulsars with typical values of the diffusion coefficient used to fit CR data, without invoking a suppression.

In Chapter 7, we used particle-in-cell hybrid simulations to study the acceleration process at non-relativistic quasi-perpendicular shocks. We were able to characterize, for the first time in kinetic calculations without any *ad-hoc* prescription for particle scattering and/or injection, how ions can be very rapidly accelerated in this shock configuration. We discovered that 3D simulations are necessary to fully capture the amplification of the initial magnetic field and the cross-field diffusion that allows ions not to be advected away downstream after a few shock crossings. This discovery opens a new chapter in the study of quasi-perpendicular shocks in kinetic plasma simulations and can have several applications in space/astrophysical shocks, from SNRs, to radio SN and heliospheric shocks.

Exactly as for CRs, my journey into the Galaxy started from their Galactic sources, with the study of the contribution to the e^+ flux by pulsars and their associated PWNe. This marked the first project of my PhD and is reported in Chapter 5. This research highlighted how an era has begun for charged CRs, which can provide valuable information about the inner mechanisms that govern our Galaxy. This first project is interconnected with the other chapters of this thesis. In fact, to address the complex task of interpreting CRs data, an in-depth exploration of various physics topics becomes essential. This includes delving into fundamental particle physics, understanding turbulence in the interstellar medium, and studying the acceleration processes. During my PhD, I tried to explore all these aspects.

Starting from the first one, production cross sections of secondary CRs represent a point of contact between astrophysics and fundamental particle physics. This growing collaboration allowed us to precisely shape $e^{\pm}$ and γ-ray cross sections, and in the next future will help us to constrain also the fragmentation cross sections of CR nuclei, which are pivotal for understanding particle propagation in our Galaxy.

The detection of γ-ray halos around pulsars is a clear example of the multi-messenger approach, since they can provide supplementary information complementary to AMS-02 data. Understanding pulsar halos will be pivotal in shedding light on how e^+ particles are accelerated, released, and propagate in the region close to the source. The knowledge of the magnetic turbulence around these objects is of fundamental importance in their analysis. Experiments like LHAASO and the forthcoming CTA will

supply invaluable data in this direction, and this research area will be a prominent focus in astroparticle physics in the next few years. I firmly believe that by combining information derived from AMS-02 data, cross section data from collider experiments, and pulsar halos, spanning physics at vastly different scales, we will attain a comprehensive understanding of the origin of Galactic CRs, especially of $e^{\pm}$.

Another crucial aspect for interpreting CRs is understanding how these particles are accelerated in astrophysical sources, including the spectrum and maximum energy they can reach. When I initiated my PhD and consequently my first project, the understanding of the acceleration mechanism of $e^{\pm}$ in PWNe intrigued me, and I promised myself that I would eventually tackle this issue. Towards the end of my PhD journey, after being scattered on different topics in my research, exactly as a CR diffusing due to irregularities in the Galactic magnetic field, I bounced back to the starting point of what CR experiments eventually measure at the end: the investigation of particle energization. While the promise of investigating particle acceleration in PWNe remains to be fulfilled, I ventured into the realm of kinetic particle-in-cell hybrid simulations in the study of astrophysical shocks. These simulations, which require knowledge of plasma physics, constitute another powerful tool in the comprehension of cosmic radiation and are gaining increasing significance, facilitated by the availability of enhanced computational resources. They demonstrate the fundamental importance of turbulence generated at kilometer scales in understanding particle injection and acceleration at astrophysical shocks (parsec scales). The non-relativistic shocks examined in this context are just one application of the capabilities of these numerical tools. I am confident that in the coming years, they will play an even more prominent role in investigating particle acceleration processes, interstellar turbulence, and pulsar halos.

This work let me build a theoretical and technical basis for the study of cosmic messengers as a tool to understand our Universe, with a focus on our Galaxy. In the near future, further extensions of this multi-messenger approach will allow us to exploit the synergies between different high-energy astrophysical messengers, combining information from the infinitely small to the infinitely large scales. This will lead to a refinement of our description of non-thermal emissions in the Universe, opening the search for signals from exotic sources like dark matter, which requires a detailed understanding of pure astrophysical phenomena, enabling us to shed light on the origin of cosmic radiations and unveil their nature.

Bibliography

[1] L. Orusa, S. Manconi, F. Donato and M.D. Mauro, *Constraining positron emission from pulsar populations with AMS-02 data*, *Journal of Cosmology and Astroparticle Physics* **2021** (2021) 014 [2107.06300]. (Cited on pages xi and 101).

[2] S. Recchia, M. Di Mauro, F.A. Aharonian, L. Orusa, F. Donato, S. Gabici et al., *Do the Geminga, Monogem and PSR J0622+3749 γ-ray halos imply slow diffusion around pulsars?*, *Physical Review D* **104** (2021) 123017 [2106.02275]. (Cited on pages xi and 123).

[3] L. Orusa, M. Di Mauro, F. Donato and M. Korsmeier, *New determination of the production cross section for secondary positrons and electrons in the Galaxy*, *Physical Review D* **105** (2022) 123021 [2203.13143]. (Cited on pages xi, 47, 51, 53, 58, and 62).

[4] L. Orusa, M. Di Mauro, F. Donato and M. Korsmeier, *New determination of the production cross section for γ rays in the Galaxy*, *Physical Review D* **107** (2023) 083031 [2302.01943]. (Cited on pages xi, 47, and 75).

[5] M. Di Mauro, F. Donato, M. Korsmeier, S. Manconi and L. Orusa, *Novel prediction for secondary positrons and electrons in the Galaxy*, *Physical Review D* **108** (2023) 063024 [2304.01261]. (Cited on pages xi, 19, 20, 83, 90, and 94).

[6] L. Orusa and D. Caprioli, *Fast Particle Acceleration in 3D Hybrid Simulations of Quasiperpendicular Shocks*, *Physical Review Letters* **131** (2023) 095201 [2305.10511]. (Cited on pages xi and 139).

[7] S. De Coulomb, *Memoires sur l'electricite et le magnetisme*, *Mémoires de l'Académie des sciences* (1875) 612. (Cited on page 3).

[8] H. Becquerel, *Sur les radiations emises par phosphorescence*, *Comptes Rendus de l'Acad. des Sciences* **122** (1896) 420. (Cited on page 3).

[9] G.B. P. Curie, M. Curie and H. Becquerel, *Sur une nouvelle substance fortement radioactive, contenue dans la pechblende*, *Comptes Rendus de l'Acad. des Sciences* **127** (1898) 1215. (Cited on page 3).

[10] C. Wilson, *On the ionization of Atmospheric Air*, *Proceedings of The Royal Society of London* **68** (1901) 151. (Cited on page 3).

[11] T. Wulf, *Observations of the radiation of high-penetration capacity on the Eiffel Tower*, *Physikalische Zeitschrift* (1909) 152. (Cited on page 3).

[12] D. Pacini, *Sulle radiazioni penetranti*, *Rendiconti Accademia Lincei* **18** (1909) 123. (Cited on page 3).

[13] D. Pacini, *La radiazione penetrante sul mare*, *Annali dell'Ufficio centrale di meteorologia* (1910) 100. (Cited on page 3).

[14] D. Pacini, *La radiazione penetrante alla superficie ed in seno alle acque*, *Nuovo Cimento* (1912) 93. (Cited on page 3).

[15] V. Hess, *Über Beobachtungen der durchdringenden Strahlung bei sieben Freiballonfahrten*, *Physikalische Zeitschrif* **13** (1912) 1084. (Cited on page 4).

[16] J. Clay, *Penetrating radiation*, *Proceedings of the Royal Academy of Sciences Amsterdam* **30** (1927) 1115. (Cited on page 4).

[17] A.H. Compton, *Progress of Cosmic-Ray Survey*, *Physical Review* **41** (1932) 681. (Cited on page 4).

[18] L. Alvarez and A.H. Compton, *A Positively Charged Component of Cosmic Rays*, *Physical Review* **43** (1933) 835. (Cited on page 4).

[19] T.H. Johnson, *Coincidence Counter Studies of the Corpuscular Component of the Cosmic Radiation*, *Physical Review* **45** (1934) 569. (Cited on page 4).

[20] B. Rossi, *Directional Measurements on the Cosmic Rays Near the Geomagnetic Equator*, *Physical Review* **45** (1934) 212. (Cited on page 4).

[21] M. Schein, W.P. Jesse and E.O. Wollan, *The Nature of the Primary Cosmic Radiation and the Origin of the Mesotron*, *Physical Review* **59** (1941) 615. (Cited on page 4).

[22] C.L. Critchfield, E.P. Ney and S. Oleksa, *The Electrons in Cosmic Rays*, *Physical Review* **79** (1950) 402. (Cited on page 4).

[23] J.A. Earl, *Cloud-Chamber Observations of Primary Cosmic-Ray Electrons*, *Physical Review Letters* **6** (1961) 125. (Cited on page 4).

[24] V.L. Ginzburg, *Cosmic ray astrophysics (history and general review)*, *Physics-Uspekhi* **39** (1996) 155. (Cited on page 4).

[25] C. Evoli, *The Cosmic-Ray Energy Spectrum*, Oct., 2018. 10.5281/zenodo.2360277. (Cited on pages 4 and 6).

[26] K. Greisen, *End to the Cosmic-Ray Spectrum?*, *Physical Review Letters* **16** (1966) 748. (Cited on page 5).

[27] AMS collaboration, *Precision Measurement of the Helium Flux in Primary Cosmic Rays of Rigidities 1.9 GV to 3 TV with the Alpha Magnetic Spectrometer on the International Space Station*, *Physical Review Letters* **115** (2015) 211101. (Cited on pages 5 and 6).

[28] AMS collaboration, *Precision Measurement of the Proton Flux in Primary Cosmic Rays from Rigidity 1 GV to 1.8 TV with the Alpha Magnetic Spectrometer on the International Space Station*, *Physical Review Letters* **114** (2015) 171103. (Cited on pages 5 and 6).

[29] AMS collaboration, *Antiproton Flux, Antiproton-to-Proton Flux Ratio, and Properties of Elementary Particle Fluxes in Primary Cosmic Rays Measured with the Alpha Magnetic Spectrometer on the International Space Station*, *Physical Review Letters* **117** (2016) 091103. (Cited on pages 5 and 6).

[30] AMS collaboration, *Electron and Positron Fluxes in Primary Cosmic Rays Measured with the Alpha Magnetic Spectrometer on the International Space Station*, *Physical Review Letters* **113** (2014) 121102. (Cited on pages 5 and 6).

[31] AMS collaboration, *Precision Measurement of the* $(e^+ + e^-)$ *Flux in Primary Cosmic Rays from 0.5 GeV to 1 TeV with the Alpha Magnetic Spectrometer on the International Space Station*, *Physical Review Letters* **113** (2014) 221102. (Cited on pages 5 and 6).

[32] F. Fenu, *The cosmic ray energy spectrum measured using the Pierre Auger Observatory*, *Proceedings of Science* **ICRC2017** (2017) 486. (Cited on pages 5 and 6).

[33] Y. Shikaze et al., *Measurements of 0.2–20GeV/n cosmic-ray proton and helium spectra from 1997 through 2002 with the BESS spectrometer*, *Astroparticle Physics* **28** (2007) 154. (Cited on pages 5 and 6).

[34] CALET collaboration, *Extended Measurement of the Cosmic-Ray Electron and Positron Spectrum from 11 GeV to 4.8 TeV with the Calorimetric Electron Telescope on the International Space Station*, *Physical Review Letters* **120** (2018) 261102. (Cited on pages 5, 22, 23, and 101).

[35] Y.S. Yoon et al., *Cosmic-Ray Proton and Helium Spectra from the First CREAM Flight*, *The Astrophysical Journal* **728** (2011) 122. (Cited on pages 5 and 6).

[36] H.S. Ahn et al., *Energy spectra of cosmic-ray nuclei at high energies*, *The Astrophysical Journal* **707** (2009) 593. (Cited on pages 5 and 6).

[37] DAMPE collaboration, *Direct detection of a break in the teraelectronvolt cosmic-ray spectrum of electrons and positrons*, *Nature* **552** (2017) 63 [1711.10981]. (Cited on pages 5, 6, 23, and 101).

[38] M. Ackermann et al., *Fermi-LAT Observations of the Diffuse Gamma-Ray Emission: Implications for Cosmic Rays and the Interstellar Medium*, *The Astrophysical Journal* **750** (2012) 3. (Cited on pages 5, 6, 23, and 24).

[39] M. Ackermann et al., *The spectrum of isotropic diffuse gamma-ray emission between 100 MeV and 820 GeV*, *The Astrophysical Journal* **799** (2015) 86. (Cited on pages 5, 6, 29, 32, and 71).

[40] HAWC collaboration, *All-particle cosmic ray energy spectrum measured by the HAWC experiment from 10 to 500 TeV*, *Physical Review D* **96** (2017) 122001. (Cited on pages 5 and 6).

[41] H.E.S.S. collaboration, *Energy Spectrum of Cosmic-Ray Electrons at TeV Energies*, *Physical Review Letters* **101** (2008) 261104. (Cited on pages 5 and 6).

[42] M. Ahlers and F. Halzen, *Opening a new window onto the universe with IceCube*, *Progress in Particle and Nuclear Physics* **102** (2018) 73. (Cited on pages 5 and 6).

[43] R. Abbasi et al., *All-particle cosmic ray energy spectrum measured with 26 IceTop stations*, *Astroparticle Physics* **44** (2013) 40. (Cited on pages 5 and 6).

[44] T. Antoni et al., *KASCADE measurements of energy spectra for elemental groups of cosmic rays: Results and open problems*, *Astroparticle Physics* **24** (2005) 1. (Cited on pages 5 and 6).

[45] O. Adriani et al., *PAMELA Measurements of Cosmic-Ray Proton and Helium Spectra*, *Science* **332** (2011) 69. (Cited on pages 5, 6, and 23).

[46] O. Adriani et al., *PAMELA results on the cosmic-ray antiproton flux from 60 MeV to 180 GeV in kinetic energy*, *Physical Review Letters* **105** (2010) 12. (Cited on pages 5, 6, and 23).

[47] O. Adriani et al., *Cosmic-Ray Positron Energy Spectrum Measured by PAMELA*, *Physical Review Letters* **111** (2013) 081102. (Cited on pages 5, 6, and 24).

[48] M. Amenomori et al., *The all-particle spectrum of primary cosmic rays in the wide energy range from* 10^{14} *eV to* 10^{17} *eV observed with the Tibet-III air-shower array*, *The Astrophysical Journal* **678** (2008) 1165. (Cited on pages 5 and 6).

[49] O. Adriani et al. [CALET], *Energy Spectrum of Cosmic-Ray Electron and Positron from 10 GeV to 3 TeV Observed with the Calorimetric Electron Telescope on the International Space Station*, *Physical Review Letters* **119** (2017) 181101. (Cited on page 6).

[50] R. Blandford and D. Eichler, *Particle acceleration at astrophysical shocks: A theory of cosmic ray origin*, *Physics Reports* **154** (1987) 1. (Cited on page 6).

[51] D.R. Lorimer, *The Galactic Population and Birth Rate of Radio Pulsars*, *Young Neutron Stars and Their Environments* **218** (2004) 105 [astro-ph/0308501]. (Cited on pages 6 and 107).

[52] E.F. Keane and M. Kramer, *On the birthrates of Galactic neutron stars*, *Monthly Notices of the Royal Astronomical Society* **391** (2008) 2009 [0810.1512]. (Cited on pages 6 and 107).

[53] C.-A. Faucher-Giguere and V.M. Kaspi, *Birth and Evolution of Isolated Radio Pulsars*, *The Astrophysical Journal* **643** (2006) 332 [astro-ph/0512585]. (Cited on pages 6, 107, 108, 109, and 110).

[54] W. Baade and F. Zwicky, *On Super-novae*, *Proceedings of the National Academy of Science* **20** (1934) 254. (Cited on pages 7 and 8).

[55] S.E. Woosley, A. Heger and T.A. Weaver, *The evolution and explosion of massive stars*, *Review of Modern Physics* **74** (2002) 1015. (Cited on page 7).

[56] P. Blasi, *The origin of galactic cosmic rays*, *Astronomy & Astrophysics Review* **21** (2013) 70 [1311.7346]. (Cited on pages 7 and 151).

[57] R.A. Chevalier, *The interaction of supernovae with the interstellar medium*, *Annual Review of Astronomy and Astrophysics* **15** (1977) 175. (Cited on page 7).

[58] J.K. Truelove and C.F. McKee, *Evolution of Nonradiative Supernova Remnants*, *The Astrophysical Journal Supplement Series* **120** (1999) 299. (Cited on page 7).

[59] L.I. Sedov, *Similarity and Dimensional Methods in Mechanics*, *Academic Press* (1959) . (Cited on page 8).

[60] G. Ferrand, A. Decourchelle, J. Ballet, R. Teyssier and F. Fraschetti, *3D simulations of supernova remnants evolution including non-linear particle acceleration*, *Astronomy and Astrophysics* **509** (2010) L10. (Cited on page 8).

[61] B. Müller, T. Melson, A. Heger and H.-T. Janka, *Supernova simulations from a 3D progenitor model – Impact of perturbations and evolution of explosion properties*, *Monthly Notices of the Royal Astronomical Society* **472** (2017) 491. (Cited on page 8).

[62] A.M. Hillas, *Can diffusive shock acceleration in supernova remnants account for high-energy galactic cosmic rays?*, *Journal of Physics G Nuclear Physics* **31** (2005) 95. (Cited on page 8).

[63] E. Fermi, *On the origin of the cosmic radiation*, *Physical Review* **75** (1949) 1169. (Cited on pages 8 and 18).

[64] E. Fermi, *Galactic Magnetic Fields and the Origin of Cosmic Radiation*, *The Astrophysical Journal* **119** (1954) 1. (Cited on page 8).

[65] G.F. Krymskii, *A regular mechanism for the acceleration of charged particles on the front of a shock wave*, *Akademiia Nauk SSSR Doklady* **234** (1977) 1306. (Cited on pages 9 and 139).

[66] W.I. Axford, E. Leer and G. Skadron, *The acceleration of cosmic rays by shock waves*, *International Cosmic Ray Conference* **11** (1978) 132. (Cited on pages 9 and 139).

[67] R.D. Blandford and J.P. Ostriker, *Particle acceleration by astrophysical shocks*, *The Astrophysical Journal Letters* **221** (1978) L29. (Cited on pages 9 and 139).

[68] A.R. Bell, *The acceleration of cosmic rays in shock fronts. I*, *Monthly Notices of the Royal Astronomical Society* **182** (1978) 147. (Cited on pages 9, 10, 42, and 139).

[69] A.R. Bell, *The acceleration of cosmic rays in shock fronts. II*, *Monthly Notices of the Royal Astronomical Society* **182** (1978) 443. (Cited on pages 9 and 42).

[70] A. Achterberg, Y.A. Gallant, J.G. Kirk and A.W. Guthmann, *Particle acceleration by ultrarelativistic shocks: theory and simulations*, *Monthly Notices of the Royal Astronomical Society* **328** (2001) 393 [astro-ph/0107530]. (Cited on page 10).

[71] C.C. Haggerty and D. Caprioli, *Kinetic Simulations of Cosmic-Ray-modified Shocks. I. Hydrodynamics*, *The Astrophysical Journal* **905** (2020) 1 [2008.12308]. (Cited on pages 10, 142, 144, and 147).

[72] D. Caprioli, C.C. Haggerty and P. Blasi, *Kinetic Simulations of Cosmic-Ray-modified Shocks. II. Particle Spectra*, *The Astrophysical Journal* **905** (2020) 2 [2009.00007]. (Cited on pages 10 and 142).

[73] R. Bühler and R. Blandford, *The surprising Crab pulsar and its nebula: a review*, *Reports on Progress in Physics* **77** (2014) 066901. (Cited on pages 11 and 12).

[74] P. Slane, *Pulsar Wind Nebulae*, *Springer International Publishing* (2017) 2159. (Cited on pages 11 and 12).

[75] B.M. Gaensler and P.O. Slane, *The evolution and structure of pulsar wind nebulae*, *Annual Review of Astronomy and Astrophysics* **44** (2006) 17 [astro-ph/0601081]. (Cited on pages 11 and 108).

[76] A. Boulares, *The Nature of the Cosmic-Ray Electron Spectrum, and Supernova Remnant Contributions*, *The Astrophysical Journal* **342** (1989) 807. (Cited on page 11).

[77] X. Chi, K.S. Cheng and E.C.M. Young, *Pulsar Wind Origin of Cosmic Ray Positrons*, *The Astrophysical Journal Letters* **459** (1996) L83. (Cited on page 11).

[78] A.K. Harding, *Gamma-ray pulsars: Models and predictions*, *AIP Conference Proceedings* **558** (2001) 115. (Cited on page 12).

[79] G. Giacinti, A. Mitchell, R. López-Coto, V. Joshi, R. Parsons and J. Hinton, *On the TeV Halo Fraction in gamma-ray bright Pulsar Wind Nebulae*, *Astronomy & Astrophysics* **636** (2020) A113 [1907.12121]. (Cited on pages 12 and 13).

[80] P. Blasi and E. Amato, *Positrons from pulsar winds*, *Astrophysics and Space Science Proceedings* **21** (2011) 624 [1007.4745]. (Cited on page 13).

[81] L. Sironi, U. Keshet and M. Lemoine, *Relativistic Shocks: Particle Acceleration and Magnetization*, *Space Science Reviews* **191** (2015) 519 [1506.02034]. (Cited on pages 13 and 14).

[82] E.S. Weibel, *Spontaneously Growing Transverse Waves in a Plasma Due to an Anisotropic Velocity Distribution*, *Physical Review Letters* **2** (1959) 83. (Cited on page 14).

[83] M. Lemoine, *A corrugated termination shock in pulsar wind nebulae?*, *Journal of Plasma Physics* **82** (2016) 635820401 [1607.01543]. (Cited on page 14).

[84] L. Sironi and A. Spitkovsky, *Particle Acceleration in Relativistic Magnetized Collisionless Electron-Ion Shocks*, *The Astrophysical Journal* **726** (2011) 75 [1009.0024]. (Cited on pages 15 and 142).

[85] A.N. Timokhin and A.K. Harding, *On the Maximum Pair Multiplicity of Pulsar Cascades*, *The Astrophysical Journal* **871** (2019) 12 [1803.08924]. (Cited on page 15).

[86] F. Donato, D. Maurin and R. Taillet, *Beta-radioactive cosmic rays in a diffusion model: test for a local bubble?*, *Astronomy & Astrophysics* **381** (2002) 539 [astro-ph/0108079]. (Cited on pages 16 and 93).

[87] N. Weinrich, M. Boudaud, L. Derome, Y. Genolini, J. Lavalle, D. Maurin et al., *Galactic halo size in the light of recent AMS-02 data*, *Astronomy & Astrophysics* **639** (2020) A74 [2004.00441]. (Cited on pages 16, 19, 84, 87, 96, and 99).

[88] D. Maurin, E. Ferronato Bueno and L. Derome, *A simple determination of the halo size from $^{10}Be/^{9}Be$ data*, *Astronomy & Astrophysics* **667** (2022) A25 [2203.07265]. (Cited on pages 16, 19, 84, 92, 93, and 211).

[89] C. Evoli, G. Morlino, P. Blasi and R. Aloisio, *AMS-02 beryllium data and its implication for cosmic ray transport*, *Physical Review D* **101** (2020) 023013. (Cited on pages 16, 19, and 93).

[90] P. De La Torre Luque, M.N. Mazziotta, F. Loparco, F. Gargano and D. Serini, *Implications of current nuclear cross sections on secondary cosmic rays with the upcoming DRAGON2 code*, *Journal of Cosmology and Astroparticle Physics* **03** (2021) 099 [2101.01547]. (Cited on page 16).

[91] M. Korsmeier, F. Donato and M. Di Mauro, *Production cross sections of cosmic antiprotons in the light of new data from the NA61 and LHCb experiments*, *Physical Review D* **97** (2018) 103019. (Cited on pages 16, 48, 56, and 64).

[92] M. Korsmeier, F. Donato and N. Fornengo, *Prospects to verify a possible dark matter hint in cosmic antiprotons with antideuterons and antihelium*, *Physical Review D* **97** (2018) . (Cited on page 16).

[93] M. Di Mauro, F. Donato, N. Fornengo and A. Vittino, *Dark matter vs. astrophysics in the interpretation of AMS-02 electron and positron data*, *Journal of Cosmology and Astroparticle Physics* **5** (2016) 031 [1507.07001]. (Cited on pages 16 and 101).

[94] A. Cuoco, J. Heisig, L. Klamt, M. Korsmeier and M. Krämer, *Scrutinizing the evidence for dark matter in cosmic-ray antiprotons*, *Physical Review D* **99** (2019) 103014. (Cited on pages 16, 87, 89, and 210).

[95] M. Cirelli, N. Fornengo, M. Taoso and A. Vittino, *Anti-helium from dark matter annihilations*, *Journal of High Energy Physics* **2014** (2014) 009. (Cited on page 16).

[96] P. Blasi, *Origin of the Positron Excess in Cosmic Rays*, *Physical Review Letters* **103** (2009) 051104 [0903.2794]. (Cited on page 17).

[97] M. Ahlers, P. Mertsch and S. Sarkar, *Cosmic ray acceleration in supernova remnants and the FERMI/PAMELA data*, *Physical Review D* **80** (2009) 123017. (Cited on page 17).

[98] N. Tomassetti and F. Donato, *Secondary cosmic-ray nuclei from supernova remnants and constraints on the propagation parameters*, *Astronomy & Astrophysics* **544** (2012) A16 [1203.6094]. (Cited on page 17).

[99] P. Mertsch, A. Vittino and S. Sarkar, *Explaining cosmic ray antimatter with secondaries from old supernova remnants*, *Physical Review D* **104** (2021) 103029 [2012.12853]. (Cited on pages 17 and 101).

[100] P. Mertsch and S. Sarkar, *Testing astrophysical models for the PAMELA positron excess with cosmic ray nuclei*, *Physical Review Letters* **103** (2009) 081104. (Cited on page 17).

[101] C.J. Cesarsky and T. Montmerle, *Gamma-Rays from Active Regions in the Galaxy - the Possible Contribution of Stellar Winds*, *Space Science Reviews* **36** (1983) 173. (Cited on page 17).

[102] A.M. Bykov, A. Marcowith, E. Amato, M.E. Kalyashova, J.M.D. Kruijssen and E. Waxman, *High-Energy Particles and Radiation in Star-Forming Regions*, *Space Science Reviews* **216** (2020) 42 [2003.11534]. (Cited on page 17).

[103] M. Ackermann, M. Ajello, A. Allafort et al., *A Cocoon of Freshly Accelerated Cosmic Rays Detected by Fermi in the Cygnus Superbubble*, *Science* **334** (2011) 1103. (Cited on pages 17 and 34).

[104] F. Aharonian, R. Yang and E. de Oña Wilhelmi, *Massive stars as major factories of Galactic cosmic rays*, *Nature Astronomy* **3** (2019) 561 [1804.02331]. (Cited on pages 17 and 34).

[105] A.U. Abeysekara et al., *HAWC observations of the acceleration of very-high-energy cosmic rays in the Cygnus Cocoon*, *Nature Astronomy* **5** (2021) 465 [2103.06820]. (Cited on pages 17 and 34).

[106] H. E. S. S. Collaboration, A. Abramowski, F. Aharonian, F. Ait Benkhali, A.G. Akhperjanian, E.O. Angüner et al., *The exceptionally powerful TeV γ-ray emitters in the Large Magellanic Cloud*, *Science* **347** (2015) 406 [1501.06578]. (Cited on pages 17 and 34).

[107] W.R. Binns, M.E. Wiedenbeck, M. Arnould, A.C. Cummings, G.A. de Nolfo, S. Goriely et al., *OB Associations, Wolf–Rayet Stars, and the Origin of Galactic Cosmic Rays*, *Space Science Reviews* **130** (2007) 439. (Cited on page 17).

[108] Prantzos, N., *On the origin and composition of Galactic cosmic rays*, *Astronomy & Astrophysics* **538** (2012) A80. (Cited on page 17).

[109] S. Gupta, B.B. Nath, P. Sharma and D. Eichler, *Realistic modelling of wind and supernovae shocks in star clusters: addressing $^{22}Ne/^{20}Ne$ and other problems in Galactic cosmic rays*, *Monthly Notices of the Royal Astronomical Society* **493** (2020) 3159 [1910.10168]. (Cited on page 17).

[110] G. Morlino, P. Blasi, E. Peretti and P. Cristofari, *Particle acceleration in winds of star clusters*, *Monthly Notices of the Royal Astronomical Society* **504** (2021) 6096 [2102.09217]. (Cited on page 17).

[111] E.N. Parker, *Galactic Effects of the Cosmic-Ray Gas*, *Space Science Reviews* **9** (1969) 651. (Cited on page 18).

[112] V.L. Ginzburg and S.I. Syrovatskii, *The Origin of Cosmic Rays*, *Soviet Physics Uspekhi* **9** (1966) 223. (Cited on page 18).

[113] S. Chandrasekhar, *Stochastic Problems in Physics and Astronomy*, *Review of Modern Physics* **15** (1943) 1. (Cited on page 18).

[114] A.W. Strong and I.V. Moskalenko, *Propagation of Cosmic-Ray Nucleons in the Galaxy*, *The Astrophysical Journal* **509** (1998) 212. (Cited on pages 18 and 20).

[115] V.L. Ginzburg and V.S. Ptuskin, *On the origin of cosmic rays: Some problems in high-energy astrophysics*, *Review of Modern Physics* **48** (1976) 161. (Cited on pages 18 and 20).

[116] D. Maurin, F. Donato, R. Taillet and P. Salati, *Cosmic Rays below Z=30 in a diffusion model: new constraints on propagation parameters*, *The Astrophysical Journal* **555** (2001) 585. (Cited on pages 18, 91, 96, and 105).

[117] A.W. Strong, I.V. Moskalenko and V.S. Ptuskin, *Cosmic-Ray Propagation and Interactions in the Galaxy*, *Annual Review of Nuclear and Particle Science* **57** (2007) 285 [astro-ph/0701517]. (Cited on pages 18, 20, 125, and 126).

[118] I.V. Moskalenko and A.W. Strong, *Production and Propagation of Cosmic-Ray Positrons and Electrons*, *The Astrophysical Journal* **493** (1998) 694. (Cited on page 18).

[119] C. Evoli, D. Gaggero, D. Grasso and L. Maccione, *Cosmic ray nuclei, antiprotons and gamma rays in the galaxy: a new diffusion model*, *Journal of Cosmology and Astroparticle Physics* **2008** (2008) 018. (Cited on page 18).

[120] R.D. Ekers and R. Sancisi, *The radio continuum halo in NGC 4631.*, *Astronomy & Astrophysics* **54** (1977) 973. (Cited on page 18).

[121] T.A. Porter, G. Jóhannesson and I.V. Moskalenko, *The GALPROP cosmic-ray propagation and nonthermal emissions framework: Release v57*, *The Astrophysical Journal Supplement Series* **262** (2022) 30. (Cited on pages 20, 87, 88, and 98).

[122] C. Evoli, D. Gaggero, A. Vittino, G. Di Bernardo, M. Di Mauro, A. Ligorini et al., *Cosmic-ray propagation with DRAGON2: I. numerical solver and astrophysical ingredients*, *Journal of Cosmology and Astroparticle Physics* **02** (2017) 015 [1607.07886]. (Cited on page 20).

[123] C. Evoli, D. Gaggero, A. Vittino, M.D. Mauro, D. Grasso and M.N. Mazziotta, *Cosmic-ray propagation with DRAGON2: II. Nuclear interactions with the interstellar gas*, *Journal of Cosmology and Astroparticle Physics* **2018** (2018) 006. (Cited on pages 20 and 84).

[124] D. Maurin, *USINE: Semi-analytical models for Galactic cosmic-ray propagation*, *Computer Physics Communications* **247** (2020) 106942. (Cited on page 20).

[125] L. Maccione, *Low Energy Cosmic Ray Positron Fraction Explained by Charge-Sign Dependent Solar Modulation*, *Physical Review Letters* **110** (2013) 081101. (Cited on page 21).

[126] M. Boschini, S. Della Torre, M. Gervasi, G. La Vacca and P. Rancoita, *Propagation of cosmic rays in heliosphere: The HelMod model*, *Advances in Space Research* **62** (2018) 2859. (Cited on page 21).

[127] L.A. Fisk, *On the acceleration of energetic particles in the interplanetary medium*, *Journal of Geophysical Research (1896-1977)* **81** (1976) 4641. (Cited on pages 21 and 85).

[128] J.S. Perko, *Solar modulation of galactic antiprotons*, *Astronomy & Astrophysics* **184** (1987) 119. (Cited on page 21).

[129] A. Galper et al., *The PAMELA experiment: a decade of Cosmic Ray Physics in space*, *Journal of Physics Conference Series* **798** (2017) 012033. (Cited on pages 22 and 23).

[130] O. Adriani et al., *An anomalous positron abundance in cosmic rays with energies 1.5–100 GeV*, *Nature* **458** (2009) 607. (Cited on pages 23 and 25).

[131] AMS collaboration, *Towards understanding the origin of cosmic-ray positrons*, *Physical Review Letters* **122** (2019) 041102. (Cited on pages 23, 24, 25, 83, 101, 111, 112, 113, 114, 115, and 116).

[132] AMS collaboration, *Towards understanding the origin of cosmic-ray electrons*, *Physical Review Letters* **122** (2019) 101101. (Cited on pages 23, 83, and 101).

[133] AMS collaboration, *High Statistics Measurement of the Positron Fraction in Primary Cosmic Rays of 0.5–500 GeV with the Alpha Magnetic Spectrometer on the International Space Station*, *Physical Review Letters* **113** (2014) 121101. (Cited on page 23).

[134] W.B. Atwood et al., *The Large Area Telescope on the Fermi Gamma-ray Space Telescope Mission*, *The Astrophysical Journal* **697** (2009) 1071. (Cited on pages 23 and 30).

[135] The Fermi-LAT Collaboration collaboration, *Cosmic-ray electron-positron spectrum from 7 GeV to 2 TeV with the Fermi Large Area Telescope*, *Physical Review D* **95** (2017) 082007. (Cited on pages 23 and 101).

[136] HESS collaboration, *The Very-High-Energy electron spectrum observed with H.E.S.S.*, *Proceedings of Science* **ICRC2023** (2023) 261. (Cited on page 24).

[137] MAGIC collaboration, *The cosmic-ray electron energy spectrum measured with the MAGIC telescopes*, *Proceedings of Science* **ICRC2023** (2023) 323. (Cited on page 24).

[138] LHAASO collaboration, *Measurement of cosmic-ray electrons with LHAASO KM2A-WCDA synergy*, *Proceedings of Science* **ICRC2023** (2023) 315. (Cited on page 24).

[139] Grimani, C. et al., *Measurements of the absolute energy spectra of cosmic-ray positrons and electrons above 7 GeV*, *Astronomy & Astrophysics* **392** (2002) 287. (Cited on page 24).

[140] M. Boezio and othersj, *Measurements of cosmic-ray electrons and positrons by the Wizard/CAPRICE collaboration*, *Advances in Space Research* **27** (2001) 669. (Cited on page 24).

[141] AMS-01 collaboration, *Cosmic-ray positron fraction measurement from 1 to 30-GeV with AMS-01*, *Physics Letters B* **646** (2007) 145 [astro-ph/0703154]. (Cited on page 24).

[142] M.A. DuVernois et al., *Cosmic-Ray Electrons and Positrons from 1 to 100 GeV: Measurements with HEAT and Their Interpretation*, *The Astrophysical Journal* **559** (2001) 296. (Cited on page 24).

[143] G.R. Blumenthal and R.J. Gould, *Bremsstrahlung, Synchrotron Radiation, and Compton Scattering of High-Energy Electrons Traversing Dilute Gases*, *Review of Modern Physics* **42** (1970) 237. (Cited on pages 28, 124, 130, and 208).

[144] M.S. Longair, *High Energy Astrophysics* (2011). (Cited on pages 28, 29, and 207).

[145] A.D. Angelis and M. Mallamaci, *Gamma-ray astrophysics*, *The European Physical Journal Plus* **133** (2018) 324. (Cited on page 29).

[146] T.K. Gaisser, F. Halzen and T. Stanev, *Particle astrophysics with high-energy neutrinos*, *Physics Reports* **258** (1995) 173 [hep-ph/9410384]. (Cited on page 29).

[147] M. Aartsen et al., *Multimessenger observations of a flaring blazar coincident with high-energy neutrino IceCube-170922a*, *Science* **361** (2018) 147. (Cited on page 29).

[148] IceCube collaboration, *Evidence for neutrino emission from the nearby active galaxy NGC 1068*, *Science* **378** (2022) 538 [2211.09972]. (Cited on page 29).

[149] IceCube collaboration, *Observation of high-energy neutrinos from the Galactic plane*, *Science* **380** (2023) 1338. (Cited on page 29).

[150] S. Funk, *Ground- and Space-Based Gamma-Ray Astronomy*, *Annual Review of Nuclear and Particle Science* **65** (2015) 245. (Cited on pages 30 and 33).

[151] B. Degrange and G. Fontaine, *Introduction to high-energy gamma-ray astronomy*, *Comptes Rendus Physique* **16** (2015) 587. (Cited on pages 30 and 31).

[152] Fermi-LAT collaboration, *Fermi Large Area Telescope Fourth Source Catalog*, *The Astrophysical Journal. Suppl.* **247** (2020) 33 [1902.10045]. (Cited on pages 30, 32, and 33).

[153] Fermi-LAT collaboration, *Fermi Large Area Telescope Fourth Source Catalog Data Release 2*, 2005.11208. (Cited on pages 30 and 32).

[154] Fermi-LAT collaboration, *Incremental Fermi Large Area Telescope Fourth Source Catalog*, *The Astrophysical Journal Supplement Series* **260** (2022) 53 [2201.11184]. (Cited on pages 30 and 32).

[155] CALET collaboration, *Results from CALorimetric Electron Telescope (CALET) Observations of Gamma-rays on the International Space Station*, *Proceedings of Science* **ICRC2023** (2023) 708. (Cited on page 30).

[156] DAMPE collaboration, *Recent progresses on the γ-ray observations of DAMPE*, *Proceedings of Science* **ICRC2023** (2023) 670. (Cited on page 31).

[157] T.C. Weekes, M.F. Cawley, D.J. Fegan, K.G. Gibbs, A.M. Hillas, P.W. Kowk et al., *Observation of TeV Gamma Rays from the Crab Nebula Using the Atmospheric Cerenkov Imaging Technique*, *The Astrophysical Journal* **342** (1989) 379. (Cited on page 31).

[158] MAGIC collaboration, *The major upgrade of the MAGIC telescopes, Part II: A performance study using observations of the Crab Nebula*, *Astroparticle Physics* **72** (2016) 76 [1409.5594]. (Cited on page 31).

[159] J. Holder et al., *The first VERITAS telescope*, *Astroparticle Physics* **25** (2006) 391 [astro-ph/0604119]. (Cited on page 31).

[160] H.E.S.S. collaboration, *The H.E.S.S. experiment : current status and future prospects*, *Proceedings of Science* **ICRC2019** (2020) 656. (Cited on page 31).

[161] CTA Consortium collaboration, *Introducing the CTA concept*, *Astroparticle Physics* **43** (2013) 3. (Cited on page 31).

[162] HAWC collaboration, *3HWC: The Third HAWC Catalog of Very-High-Energy Gamma-ray Sources*, *The Astrophysical Journal* **905** (2020) 76 [2007.08582]. (Cited on page 31).

[163] LHAASO collaboration, *The Large High Altitude Air Shower Observatory (LHAASO) Science Book (2021 Edition)*, *Chinese Physics C* **46** (2022) 035001 [1905.02773]. (Cited on page 31).

[164] Z. Cao, F.A. Aharonian, Q. An, L.X. Axikegu, Bai, Y.X. Bai, Y.W. Bao et al., *Ultrahigh-energy photons up to 1.4 petaelectronvolts from 12 γ-ray Galactic sources*, *Nature* **594** (2021) 33. (Cited on page 31).

[165] MILAGRO collaboration, *Status of the Milagro Gamma Ray Observatory*, astro-ph/0110513. (Cited on page 31).

[166] A.W. Strong, I.V. Moskalenko and O. Reimer, *Diffuse Continuum Gamma Rays from the Galaxy*, *The Astrophysical Journal* **537** (2000) 763. (Cited on page 31).

[167] M. Fornasa and M.A. Sánchez-Conde, *The nature of the Diffuse Gamma-Ray Background*, *Physics Reports* **598** (2015) 1. (Cited on page 32).

[168] K.N. Abazajian, S. Blanchet and J.P. Harding, *Current and future constraints on dark matter from prompt and inverse-Compton photon emission in the isotropic diffuse gamma-ray background*, *Physical Review D* **85** (2012) 043509. (Cited on pages 32 and 37).

[169] T. Bringmann, F. Calore, M. Di Mauro and F. Donato, *Constraining dark matter annihilation with the isotropic γ-ray background: Updated limits and future potential*, *Physical Review D* **89** (2014) 023012. (Cited on pages 32 and 37).

[170] M. Di Mauro and F. Donato, *Composition of the Fermi-LAT isotropic gamma-ray background intensity: Emission from extragalactic point sources and dark matter annihilations*, *Physical Review D* **91** (2015) 123001. (Cited on pages 32 and 37).

[171] C. Blanco and D. Hooper, *Constraints on decaying dark matter from the isotropic gamma-ray background*, *Journal of Cosmology and Astroparticle Physics* **2019** (2019) 019. (Cited on pages 32 and 37).

[172] D.A. Kniffen, R.C. Hartman, D.J. Thompson, G.F. Bignami and C.E. Fichtel, *Gamma radiation from the Crab Nebula above 35 MeV*, *Nature* **251** (1974) 397. (Cited on page 32).

[173] T. Gold, *Rotating neutron stars as the origin of the pulsating radio sources*, *Nature* **218** (1968) 731. (Cited on page 32).

[174] Fermi-LAT collaboration, D.A. Smith et al., *The Third Fermi Large Area Telescope Catalog of Gamma-ray Pulsars*, 7, 2023. (Cited on page 32).

[175] Fermi-LAT collaboration, *The First Fermi LAT Supernova Remnant Catalog*, *The Astrophysical Journal Supplement Series* **224** (2016) 8 [1511.06778]. (Cited on page 33).

[176] T.K. Gaisser, R.J. Protheroe and T. Stanev, *Gamma-ray production in supernova remnants*, *The Astrophysical Journal* **492** (1998) 219. (Cited on page 33).

[177] H. Katagiri, L. Tibaldo, J. Ballet, F. Giordano, I.A. Grenier, T.A. Porter et al., *Fermi Large Area Telescope Observations of the Cygnus Loop Supernova Remnant*, *The Astrophysical Journal* **741** (2011) 44. (Cited on page 33).

[178] N.J. Corso, R. Diesing and D. Caprioli, *Hadronic versus leptonic origin of gamma-ray emission from supernova remnants*, *The Astrophysical Journal* **954** (2023) 1. (Cited on page 33).

[179] F. Aharonian et al., *A detailed spectral and morphological study of the gamma-ray supernova remnant RX J1713.7−3946 with HESS*, *Astronomy & Astrophysics* **449** (2006) 223. (Cited on page 33).

[180] G. Morlino, E. Amato and P. Blasi, *Gamma-ray emission from SNR RX J1713.7−3946 and the origin of galactic cosmic rays*, *Monthly Notices of the Royal Astronomical Society* **392** (2009) 240 [0810.0094]. (Cited on page 33).

[181] D.C. Ellison, D.J. Patnaude, P. Slane and J. Raymond, *Efficient Cosmic Ray Acceleration, Hydrodynamics, and Self-Consistent Thermal X-Ray Emission Applied to Supernova Remnant RX J1713.7−3946*, *The Astrophysical Journal* **712** (2010) 287 [1001.1932]. (Cited on page 33).

[182] V.N. Zirakashvili and F.A. Aharonian, *Nonthermal Radiation of Young Supernova Remnants: The Case of RX J1713.7−3946*, *The Astrophysical Journal* **708** (2010) 965 [0909.2285]. (Cited on page 33).

[183] A.A. Abdo and Fermi LAT Collaboration, *Observations of the young supernova remnant RX J1713.7−3946 with the Fermi Large Area Telescope*, *The Astrophysical Journal* **734** (2011) 28. (Cited on page 33).

[184] S.-H. Lee, P.O. Slane, D.C. Ellison, S. Nagataki and D.J. Patnaude, *A CR-hydro-NEI Model of Multi-wavelength Emission from the Vela Jr. Supernova Remnant (SNR RX J0852.0-4622)*, *The Astrophysical Journal* **767** (2013) 20. (Cited on page 33).

[185] F. Acero, M. Lemoine-Goumard, M. Renaud, J. Ballet, J.W. Hewitt, R. Rousseau et al., *Study of TeV shell supernova remnants at gamma-ray energies*, *Astronomy & Astrophysics* **580** (2015) A74. (Cited on page 33).

[186] G. Morlino and D. Caprioli, *Strong evidence for hadron acceleration in Tycho's supernova remnant*, *Astronomy & Astrophysics* **538** (2012) A81 [1105.6342]. (Cited on pages 33 and 139).

[187] M. Ackermann et al., *Detection of the characteristic pion-decay signature in supernova remnants*, *Science* **339** (2013) 807. (Cited on page 33).

[188] C.M. Urry and P. Padovani, *Unified schemes for radio-loud active galactic nuclei*, *Publications of the Astronomical Society of the Pacific* **107** (1995) 803 [astro-ph/9506063]. (Cited on page 34).

[189] P. Padovani, D.M. Alexander, R.J. Assef, B.D. Marco, P. Giommi, R.C. Hickox et al., *Active galactic nuclei: what's in a name?*, *The Astronomy and Astrophysics Review* **25** (2017) 2. (Cited on page 34).

[190] I. Tamborra, S. Ando and K. Murase, *Star-forming galaxies as the origin of diffuse high-energy backgrounds: gamma-ray and neutrino connections, and implications for starburst history*, *Journal of Cosmology and Astroparticle Physics* **2014** (2014) 043 [1404.1189]. (Cited on page 34).

[191] M. Ackermann et al., *Observations of M31 and M33 with the Fermi Large Area Telescope: A Galactic Center Excess in Andromeda?*, *The Astrophysical Journal* **836** (2017) 208. (Cited on page 34).

[192] Fermi-LAT collaboration, *Development of the Model of Galactic Interstellar Emission for Standard Point-Source Analysis of Fermi Large Area Telescope Data*, *The Astrophysical Journal Supplement Series* **223** (2016) 2 [1602.07246]. (Cited on pages 34, 71, and 80).

[193] K.M. Ferrière, *The interstellar environment of our galaxy*, *Reviews of Modern Physics* **73** (2001) 1031 [astro-ph/0106359]. (Cited on page 35).

[194] I.V. Moskalenko, A.W. Strong and O. Reimer, *Diffuse Gamma Rays*, *Springer Netherlands* (2004) 279. (Cited on pages 35 and 36).

[195] E. Churchwell, B.L. Babler, M.R. Meade, B.A. Whitney, R. Benjamin, R. Indebetouw et al., *The Spitzer/GLIMPSE Surveys: A New View of the Milky Way*, *Publications of the Astronomical Society of the Pacific* **121** (2009) 213. (Cited on page 35).

[196] P.M.W. Kalberla and J. Kerp, *The HI Distribution of the Milky Way*, *Annual Review of Astronomy and Astrophysics* **47** (2009) 27. (Cited on page 35).

[197] M.A. Kolpak, J.M. Jackson, T.M. Bania and J.M. Dickey, *The Radial Distribution of Cold Atomic Hydrogen in the Galaxy*, *The Astrophysical Journal* **578** (2002) 868. (Cited on page 35).

[198] A.D. Bolatto, M. Wolfire and A.K. Leroy, *The CO-to-h_2 conversion factor*, *Annual Review of Astronomy and Astrophysics* **51** (2013) 207. (Cited on page 35).

[199] L. Bronfman, R.S. Cohen, H. Alvarez, J. May and P. Thaddeus, *A CO Survey of the Southern Milky Way: The Mean Radial Distribution of Molecular Clouds within the Solar Circle*, *The Astrophysical Journal* **324** (1988) 248. (Cited on page 35).

[200] J.M. Dickey and F.J. Lockman, *H I in the galaxy*, *Annual Review of Astronomy and Astrophysics* **28** (1990) 215. (Cited on page 35).

[201] J.M. Cordes, J.M. Weisberg, D.A. Frail, S.R. Spangler and M. Ryan, *The galactic distribution of free electrons*, *Nature* **354** (1991) 121. (Cited on page 35).

[202] G. Jóhannesson, T.A. Porter and I.V. Moskalenko, *The Three-Dimensional Spatial Distribution of Interstellar Gas in the Milky Way: Implications for Cosmic Rays and High-Energy Gamma-Ray Emissions*, *The Astrophysical Journal* **856** (2018) 45 [1802.08646]. (Cited on pages 35, 71, and 98).

[203] T.A. Porter, G. Johannesson and I.V. Moskalenko, *High-Energy Gamma Rays from the Milky Way: Three-Dimensional Spatial Models for the Cosmic-Ray and Radiation Field Densities in the Interstellar Medium*, *The Astrophysical Journal* **846** (2017) 67 [1708.00816]. (Cited on pages 36, 71, and 98).

[204] S. Vernetto and P. Lipari, *Absorption of very high energy gamma rays in the Milky Way*, *Physical Review D* **94** (2016) 063009 [1608.01587]. (Cited on pages 36, 37, 87, 98, 106, 127, and 209).

[205] T.A. Porter, I.V. Moskalenko and A.W. Strong, *Inverse compton emission from galactic supernova remnants: Effect of the interstellar radiation field*, *The Astrophysical Journal* **648** (2006) L29. (Cited on pages 36, 37, and 127).

[206] T. Delahaye, J. Lavalle, R. Lineros, F. Donato and N. Fornengo, *Galactic electrons and positrons at the Earth: new estimate of the primary and secondary fluxes*, *Astronomy & Astrophysics* **524** (2010) A51 [1002.1910]. (Cited on pages 36, 37, 98, 105, 106, 124, and 208).

[207] C. Evoli, E. Amato, P. Blasi and R. Aloisio, *Galactic factories of cosmic-ray electrons and positrons*, *Physical Review D* **103** (2021) . (Cited on pages 36, 37, 83, 99, 101, 102, 104, 105, 114, 115, and 120).

[208] M. Di Mauro, F. Donato and S. Manconi, *Novel interpretation of the latest AMS-02 cosmic-ray electron spectrum*, *Physical Review D* **104** (2021) 083012 [2010.13825]. (Cited on pages 36, 83, and 101).

[209] M. Di Mauro, F. Calore, F. Donato, M. Ajello and L. Latronico, *Diffuse γ-ray emission from misaligned active galactic nuclei*, *The Astrophysical Journal* **780** (2014) 161 [1304.0908]. (Cited on page 37).

[210] M.D. Mauro, F. Donato, G. Lamanna, D.A. Sanchez and P.D. Serpico, *Diffuse gamma-ray emission from unresolved BL Lac objects*, *The Astrophysical Journal* **786** (2014) 129. (Cited on page 37).

[211] M. Ackermann et al., *GeV Observations of Star-forming Galaxies with Fermi LAT*, *The Astrophysical Journal* **755** (2012) 164. (Cited on page 37).

[212] F. Calore, V. De Romeri and F. Donato, *Conservative upper limits on WIMP annihilation cross section from Fermi-LAT γ rays*, *Physical Review D* **85** (2012) 023004. (Cited on page 37).

[213] G.D. Martinez, *A robust determination of Milky Way satellite properties using hierarchical mass modelling*, *Monthly Notices of the Royal Astronomical Society* **451** (2015) 2524. (Cited on page 37).

[214] M. Mateo, *Dwarf Galaxies of the Local Group*, *Annual Review of Astronomy and Astrophysics* **36** (1998) 435. (Cited on page 37).

[215] M. Lisanti, S. Mishra-Sharma, N.L. Rodd and B.R. Safdi, *Search for Dark Matter Annihilation in Galaxy Groups*, *Physical Review Letters* **120** (2018) 101101. (Cited on page 37).

[216] A. Cuoco, A. Sellerholm, J. Conrad and S. Hannestad, *Anisotropies in the diffuse gamma-ray background from dark matter with Fermi LAT: a closer look*, *Monthly Notices of the Royal Astronomical Society* **414** (2011) 2040. (Cited on page 37).

[217] T. Tröster, S. Camera, M. Fornasa, M. Regis, L. van Waerbeke, J. Harnois-Déraps et al., *Cross-correlation of weak lensing and gamma rays: implications for the nature of dark matter*, *Monthly Notices of the Royal Astronomical Society* **467** (2017) 2706. (Cited on page 37).

[218] D. Hooper and L. Goodenough, *Dark Matter Annihilation in The Galactic Center As Seen by the Fermi Gamma Ray Space Telescope*, *Physics Letters B* **697** (2011) 412 [1010.2752]. (Cited on page 37).

[219] Fermi-LAT collaboration, *The Fermi Galactic Center GeV Excess and Implications for Dark Matter*, *The Astrophysical Journal* **840** (2017) 43 [1704.03910]. (Cited on page 37).

[220] F. Calore, I. Cholis and C. Weniger, *Background model systematics for the Fermi GeV excess*, *Journal of Cosmology and Astroparticle Physics* **2015** (2015) 038. (Cited on page 37).

[221] F. Calore, I. Cholis, C. McCabe and C. Weniger, *A tale of tails: Dark matter interpretations of the Fermi GeV excess in light of background model systematics*, *Physical Review D* **91** (2015) 063003. (Cited on page 37).

[222] R. Bartels, S. Krishnamurthy and C. Weniger, *Strong Support for the Millisecond Pulsar Origin of the Galactic Center GeV Excess*, *Physical Review Letters* **116** (2016) 051102. (Cited on page 38).

[223] S.K. Lee, M. Lisanti, B.R. Safdi, T.R. Slatyer and W. Xue, *Evidence for Unresolved Gamma-Ray Point Sources in the Inner Galaxy*, *Physical Review Letters* **116** (2016) 051103. (Cited on page 38).

[224] F. Calore, M.D. Mauro, F. Donato, J.W.T. Hessels and C. Weniger, *Radio detection prospects for a bulge population of millisecond pulsars as suggested by*

Fermi LAT observations of the inner Galaxy, *The Astrophysical Journal* **827** (2016) 143. (Cited on page 38).

[225] M. Cirelli, G. Corcella, A. Hektor, G. Hütsi, M. Kadastik, P. Panci et al., *PPPC 4 DM ID: a poor particle physicist cookbook for dark matter indirect detection*, *Journal of Cosmology and Astroparticle Physics* **2011** (2011) 051. (Cited on pages 38 and 130).

[226] A.A. Abdo et al., *Fermi-LAT Observations of Two Gamma-Ray Emission Components from the Quiescent Sun*, *The Astrophysical Journal* **734** (2011) 116. (Cited on page 38).

[227] M. Ajello et al., *A Decade of Gamma-Ray Bursts Observed by Fermi-LAT: The Second GRB Catalog*, *The Astrophysical Journal* **878** (2019) 52 [1906.11403]. (Cited on page 38).

[228] G. Dobler, D.P. Finkbeiner, I. Cholis, T. Slatyer and N. Weiner, *The Fermi Haze: A Gamma-Ray Counterpart to the Microwave Haze*, *The Astrophysical Journal* **717** (2010) 825. (Cited on page 38).

[229] J. Kataoka, Y. Sofue, Y. Inoue, M. Akita, S. Nakashima and T. Totani, *X-ray and gamma-ray observations of the fermi bubbles and NPS/loop i structures*, *Galaxies* **6** (2018) 27. (Cited on page 38).

[230] A.A. Abdo et al., *Discovery of TeV Gamma-Ray Emission from the Cygnus Region of the Galaxy*, *The Astrophysical Journal* **658** (2007) L33. (Cited on page 38).

[231] H. Yuksel, M.D. Kistler and T. Stanev, *TeV Gamma Rays from Geminga and the Origin of the GeV Positron Excess*, *Physical Review Letters* **103** (2009) 051101 [0810.2784]. (Cited on page 39).

[232] P.A. Caraveo, G.F. Bignami, A. DeLuca, S. Mereghetti, A. Pellizzoni, R. Mignani et al., *Geminga's tails: A pulsar bow shock probing the interstellar medium*, *Science* **301** (2003) 1345. (Cited on pages 39, 130, and 133).

[233] HAWC collaboration, *Extended gamma-ray sources around pulsars constrain the origin of the positron flux at Earth*, *Science* **358** (2017) 911 [1711.06223]. (Cited on pages 39, 40, 41, 103, 123, 125, 126, 127, and 128).

[234] F. Aharonian et al., *Detection of extended gamma-ray emission around the Geminga pulsar with H.E.S.S.*, *Astronomy & Astrophysics* **673** (2023) A148. (Cited on page 39).

[235] D. Hooper, I. Cholis, T. Linden and K. Fang, *HAWC Observations Strongly Favor Pulsar Interpretations of the Cosmic-Ray Positron Excess*, *Physical Review D* **96** (2017) 103013 [1702.08436]. (Cited on pages 39, 41, 123, and 126).

[236] X. Tang and T. Piran, *Positron flux and γ-ray emission from Geminga pulsar and pulsar wind nebula*, *Monthly Notices of the Royal Astronomical Society* **484** (2019) 3491 [1808.02445]. (Cited on pages 39, 41, 123, 126, and 127).

[237] K. Fang, X.-J. Bi, P.-F. Yin and Q. Yuan, *Two-zone diffusion of electrons and positrons from Geminga explains the positron anomaly*, *The Astrophysical Journal* **863** (2018) 30 [1803.02640]. (Cited on pages 39, 41, 123, and 126).

[238] M. Di Mauro, S. Manconi and F. Donato, *Detection of a γ-ray halo around Geminga with the Fermi -LAT data and implications for the positron flux*, *Physical Review D* **100** (2019) 123015 [1903.05647]. (Cited on pages 39, 40, 41, 103, 105, 120, 123, 126, 127, 128, 131, and 134).

[239] M. Di Mauro, S. Manconi and F. Donato, *Evidences of low-diffusion bubbles around Galactic pulsars*, *Physical Review D* **101** (2020) 103035 [1908.03216]. (Cited on pages 39, 41, 123, 126, 127, and 131).

[240] G. Giacinti, A.M.W. Mitchell, R. López-Coto, V. Joshi, R.D. Parsons and J.A. Hinton, *Halo fraction in TeV-bright pulsar wind nebulae*, *Astronomy & Astrophysics* **636** (2020) A113 [1907.12121]. (Cited on pages 39, 41, 123, and 126).

[241] H. Fleischhack et al., *Pulsars in a Bubble? Following Electron Diffusion in the Galaxy with TeV Gamma Rays*, 1903.07647. (Cited on page 39).

[242] LHAASO collaboration, *Extended Very-High-Energy Gamma-Ray Emission Surrounding PSR J0622+3749 Observed by LHAASO-KM2A*, *Physical Review Letters* **126** (2021) 241103 [2106.09396]. (Cited on pages 39, 40, 123, 128, and 136).

[243] A. Abdo et al., *The Second Fermi Large Area Telescope Catalog of Gamma-Ray Pulsars*, *The Astrophysical Journal Supplement Series* **208** (2013) 17 [1305.4385]. (Cited on page 39).

[244] M. Di Mauro, S. Manconi, M. Negro and F. Donato, *Investigating γ-ray halos around three HAWC bright sources in Fermi-LAT data*, *Physical Review D* **104** (2021) 103002. (Cited on pages 39 and 125).

[245] F. Sheidaei, A. Djannati-Atai, H. Gast and for the Star Collaboration, *Discovery of very-high-energy gamma-ray emission from the vicinity of PSR J1831−952 with H.E.S.S*, 1110.6837. (Cited on page 40).

[246] K. Fang, S.-Q. Xi, L.-Z. Bao, X.-J. Bi and E.-S. Chen, *Features of the gamma-ray pulsar halo HESS J1831−098*, *Physical Review D* **106** (2022) 123017. (Cited on page 40).

[247] R.-Y. Liu, C. Ge, X.-N. Sun and X.-Y. Wang, *Constraining the Magnetic Field in the TeV Halo of Geminga with X-Ray Observations*, *The Astrophysical Journal* **875** (2019) 149. (Cited on page 41).

[248] A. Khokhriakova, W. Becker, G. Ponti, M. Sasaki, B. Li and R.Y. Liu, *Searching for X-Ray Counterparts of Degree Wide TeV Halos Around Middle-Aged Pulsars with SRG/eROSITA*, 2310.10454. (Cited on page 41).

[249] A. Merloni et al., *eROSITA Science Book: Mapping the Structure of the Energetic Universe*, 1209.3114. (Cited on page 41).

[250] M. Di Mauro, S. Manconi and F. Donato, *Prospects for the detection of synchrotron halos around middle-age pulsars*, *Bulletin of the AAS* **51** (2019) 183 [1903.05699]. (Cited on page 41).

[251] J. McEnery et al., *All-sky Medium Energy Gamma-ray Observatory: Exploring the Extreme Multimessenger Universe*, 1907.07558. (Cited on page 41).

[252] S.D. Hunter, L. Angelini and A. Timokhin, *AdEPT, the Advanced Energetic Pair Telescope for Medium-Energy Gamma-Ray Polarimetry*, *LPI Contributions* **2135** (2019) 5022. (Cited on page 41).

[253] R. López-Coto and G. Giacinti, *Constraining the properties of the magnetic turbulence in the Geminga region using HAWC γ-ray data*, *Monthly Notices of the Royal Astronomical Society* **479** (2018) 4526 [1712.04373]. (Cited on pages 41 and 126).

[254] R.-Y. Liu, H. Yan and H. Zhang, *Understanding the Multiwavelength Observation of Geminga's Tev Halo: The Role of Anisotropic Diffusion of*

Particles, *Physical Review Letters* **123** (2019) 221103 [1904.11536]. (Cited on pages 41 and 43).

[255] M.A. Malkov, P.H. Diamond, R.Z. Sagdeev, F.A. Aharonian and I.V. Moskalenko, *Analytic Solution for Self-regulated Collective Escape of Cosmic Rays from Their Acceleration Sites*, *The Astrophysical Journal* **768** (2013) 73 [1207.4728]. (Cited on page 41).

[256] S. Recchia, D. Galli, L. Nava, M. Padovani, S. Gabici, A. Marcowith et al., *Grammage of cosmic rays in the proximity of supernova remnants embedded in a partially ionized medium*, *Astronomy & Astrophysics* **660** (2022) A57. (Cited on pages 41 and 43).

[257] S. Recchia, P. Blasi and G. Morlino, *Cosmic ray driven Galactic winds*, *Monthly Notices of the Royal Astronomical Society* **462** (2016) 4227 [1603.06746]. (Cited on page 41).

[258] J. Skilling, *Cosmic Rays in the Galaxy: Convection or Diffusion?*, *The Astrophysical Journal* **170** (1971) 265. (Cited on page 42).

[259] C. Evoli, T. Linden and G. Morlino, *Self-generated cosmic-ray confinement in TeV halos: Implications for TeV γ -ray emission and the positron excess*, *Physical Review D* **98** (2018) 063017 [1807.09263]. (Cited on page 42).

[260] K. Fang, X.-J. Bi and P.-F. Yin, *Possible origin of the slow-diffusion region around Geminga*, *Monthly Notices of the Royal Astronomical Society* **488** (2019) 4074 [1903.06421]. (Cited on page 42).

[261] P. Mukhopadhyay and T. Linden, *Self-generated cosmic-ray turbulence can explain the morphology of TeV halos*, *Physical Review D* **105** (2022) 123008. (Cited on page 42).

[262] J. Faherty, F. Walter and Anderson, *The trigonometric parallax of the neutron star Geminga*, *Astrophysics and Space Science* **308** (2007) 225–230 [astro-ph/0504584]. (Cited on page 42).

[263] B. Schroer, O. Pezzi, D. Caprioli, C.C. Haggerty and P. Blasi, *Cosmic-ray generated bubbles around their sources*, *Monthly Notices of the Royal Astronomical Society* **512** (2022) 233 [2202.05814]. (Cited on pages 42 and 43).

[264] A.R. Bell, *Turbulent amplification of magnetic field and diffusive shock acceleration of cosmic rays*, *Monthly Notices of the Royal Astronomical Society* **353** (2004) 550. (Cited on page 42).

[265] B. Cerutti, A. Philippov, K. Parfrey and A. Spitkovsky, *Particle acceleration in axisymmetric pulsar current sheets*, *Monthly Notices of the Royal Astronomical Society* **448** (2015) 606 [1410.3757]. (Cited on page 42).

[266] S. Gupta, D. Caprioli and C.C. Haggerty, *Lepton-driven Nonresonant Streaming Instability*, *The Astrophysical Journal* **923** (2021) 208 [2106.07672]. (Cited on page 42).

[267] K. Ferriere, *Plasma turbulence in the interstellar medium*, *Plasma Physics and Controlled Fusion* **62** (2019) 014014. (Cited on page 42).

[268] J. Giacalone and J.R. Jokipii, *Magnetic Field Amplification by Shocks in Turbulent Fluids*, *The Astrophysical Journal Letters* **663** (2007) L41. (Cited on page 42).

[269] J.R. Knies, M. Sasaki and P.P. Plucinsky, *Suzaku observations of the Monogem Ring and the origin of the Gemini H α ring*, *Monthly Notices of the Royal Astronomical Society* **477** (2018) 4414. (Cited on page 43).

[270] P. Goldreich and S. Sridhar, *Toward a theory of interstellar turbulence. 2: Strong alfvenic turbulence*, *The Astrophysical Journal* **438** (1995) 763. (Cited on page 43).

[271] P.D.L.T. Luque, O. Fornieri and T. Linden, *Anisotropic diffusion cannot explain TeV halo observations*, *Physical Review D* **106** (2022) 123033. (Cited on page 43).

[272] L.C. Tan and L.K. Ng, *Parametrization of hadron inclusive cross-sections in p-p collisions extended to very low energies*, *Journal of Physics G* **9** (1983) 1289. (Cited on pages 49 and 50).

[273] S.R. Blattnig, S.R. Swaminathan, A.T. Kruger, M. Ngom and J.W. Norbury, *Parametrizations of inclusive cross-sections for pion production in proton proton collisions*, *Physical Review D* **62** (2000) 094030 [hep-ph/0010170]. (Cited on page 49).

[274] T. Kamae, N. Karlsson, T. Mizuno, T. Abe and T. Koi, *Parameterization of Gamma, e+/- and Neutrino Spectra Produced by p-p Interaction in Astronomical Environment*, *The Astrophysical Journal* **647** (2006) 692 [astro-ph/0605581]. (Cited on pages 49, 50, 67, 69, 71, and 80).

[275] T. Sjöstrand, S. Ask, J.R. Christiansen, R. Corke, N. Desai, P. Ilten et al., *An introduction to PYTHIA 8.2*, *Computer Physics Communications* **191** (2015) 159 [1410.3012]. (Cited on page 49).

[276] S.R. Kelner, F.A. Aharonian and V.V. Bugayov, *Energy spectra of gamma-rays, electrons and neutrinos produced at proton-proton interactions in the very high energy regime*, *Physical Review D* **74** (2006) 034018 [astro-ph/0606058]. (Cited on page 49).

[277] S. Koldobskiy, M. Kachelriess, A. Lskavyan, A. Neronov, S. Ostapchenko and D.V. Semikoz, *Energy spectra of secondaries in proton-proton interactions*, *Physical Review D* **104** (2021) 123027 [2110.00496]. (Cited on pages 49, 50, 67, 69, 71, 80, and 81).

[278] M. Kachelriess, I.V. Moskalenko and S.S. Ostapchenko, *New calculation of antiproton production by cosmic ray protons and nuclei*, *The Astrophysical Journal* **803** (2015) 54 [1502.04158]. (Cited on page 50).

[279] M. Kachelriess, I.V. Moskalenko and S. Ostapchenko, *AAfrag: Interpolation routines for Monte Carlo results on secondary production in proton-proton, proton-nucleus and nucleus-nucleus interactions*, *Computer Physics Communications* **245** (2019) 106846 [1904.05129]. (Cited on pages 50 and 71).

[280] P. De la Torre Luque, F. Loparco and M.N. Mazziotta, *The FLUKA cross sections for cosmic-ray leptons and uncertainties on current positron predictions*, *Journal of Cosmology and Astroparticle Physics* **10** (2023) 011 [2305.02958]. (Cited on pages 50, 67, 69, and 99).

[281] T. Delahaye, F. Donato, N. Fornengo, J. Lavalle, R. Lineros, P. Salati et al., *Galactic secondary positron flux at the Earth*, *Astronomy & Astrophysics* **501** (2009) 821 [0809.5268]. (Cited on pages 50, 63, 65, 83, 207, and 208).

[282] G.D. Badhwar, S.A. Stephens and R.L. Golden, *Analytic representation of the proton-proton and proton-nucleus cross-sections and its application to the sea-level spectrum and charge ratio of muons*, *Physical Review D* **15** (1977) 820. (Cited on page 50).

[283] NA49 collaboration, *Inclusive production of charged pions in p+p collisions at 158 GeV/c beam momentum*, *The European Physical Journal C* **45** (2005) 343–381. (Cited on pages 50, 52, 53, 54, 68, and 74).

[284] NA61/SHINE collaboration, *Measurements of $\pi^{\pm}$, $K^{\pm}$, p and $\bar{p}$ spectra in proton-proton interactions at 20, 31, 40, 80 and 158 GeV/c with the NA61/SHINE spectrometer at the CERN SPS*, *The European Physical Journal C* **77** (2017) 671 [1705.02467]. (Cited on pages 50, 52, 55, 58, 61, and 68).

[285] I. Arsene, I.G. Bearden, D. Beavis, S. Bekele, C. Besliu, B. Budick et al., *Production of Mesons and Baryons at High Rapidity and High p_T in Proton-Proton Collisions at $\sqrt{s}$=200 GeV*, *Physical Review Letters* **98** (2007) 252001. (Cited on page 50).

[286] A. Adare, S. Afanasiev, C. Aidala, N.N. Ajitanand, Y. Akiba, H. Al-Bataineh et al., *Identified charged hadron production in p+p collisions at $\sqrt{s}$=200 and 62.4 GeV*, *Physical Review C* **83** (2011) 064903. (Cited on pages 50 and 58).

[287] ALICE collaboration, *Measurement of pion, kaon and proton production in proton–proton collisions at $\sqrt{s} = 7$ TeV*, *The European Physical Journal C* **75** (2015) 226 [1504.00024]. (Cited on page 50).

[288] A. Sirunyan, A. Tumasyan, W. Adam, E. Asilar, T. Bergauer, J. Brandstetter et al., *Measurement of charged pion, kaon, and proton production in proton-proton collisions at s =13TeV*, *Physical Review D* **96** (2017) 112003. (Cited on pages 50, 52, 55, 61, and 68).

[289] A. Arbuzov, *First-order radiative corrections to polarized muon decay spectrum*, *Physics Letters B* **524** (2002) 99–106. (Cited on page 51).

[290] S. Chatrchyan, V. Khachatryan, A.M. Sirunyan, A. Tumasyan, W. Adam, E. Aguilo et al., *Study of the inclusive production of charged pions, kaons, and protons in pp collisions at $\sqrt{s} = 0.9, 2.76,$ and 7 TeV*, *The European Physical Journal C* **72** (2012) 2164. (Cited on pages 52, 55, 61, and 68).

[291] K. Aamodt et al., *Production of pions, kaons and protons in pp collisions at $\sqrt{s} = 900$ GeV with ALICE at the LHC*, *The European Physical Journal C* **71** (2011) 1655. (Cited on pages 52, 55, 61, and 68).

[292] T. Anticic, B. Baatar, J. Bartke et al., *Inclusive production of charged kaons in p+p collisions at 158 GeV/c beam momentum and a new evaluation of the*

energy dependence of kaon production up to collider energies, The European Physical Journal C **68** (2010) 1–73. (Cited on pages 52, 60, and 62).

[293] M. Antinucci, A. Bertin and P. Capiluppi, *Multiplicities of charged particles up to ISR energies*, Lettere al Nuovo Cimento **6** (1973) 121. (Cited on pages 52, 55, 61, and 68).

[294] J.W. Norbury and L.W. Townsend, *Parametrizations of inclusive cross sections for pion production in proton-proton collisions. II. Comparison to new data*, Physical Review D **75** (2007) 034001. (Cited on page 53).

[295] F. Feroz, M.P. Hobson and M. Bridges, *MultiNest: an efficient and robust Bayesian inference tool for cosmology and particle physics*, Monthly Notices of the Royal Astronomical Society **398** (2009) 1601–1614. (Cited on pages 54, 74, and 88).

[296] STAR collaboration, *Identified hadron spectra at large transverse momentum in p+p and d+Au collisions at s(NN)**(1/2) = 200-GeV*, Physics Letters B **637** (2006) 161 [nucl-ex/0601033]. (Cited on page 58).

[297] M.W. Winkler, *Cosmic ray antiprotons at high energies*, Journal of Cosmology and Astroparticle Physics **2017** (2017) 048–048. (Cited on page 58).

[298] F. Donato, M. Korsmeier and M. Di Mauro, *Prescriptions on antiproton cross section data for precise theoretical antiproton flux predictions*, Physical Review D **96** (2017) 043007 [1704.03663]. (Cited on page 58).

[299] NA61/SHINE collaboration, *K^0_S meson production in inelastic p+p interactions at 158 GeV /c beam momentum measured by NA61/SHINE at the CERN SPS*, The European Physical Journal C **82** (2022) 96 [2106.07535]. (Cited on page 61).

[300] C. Bierlich et al., *A comprehensive guide to the physics and usage of PYTHIA 8.3*, 2203.11601. (Cited on pages 62, 63, and 77).

[301] NA61/SHINE collaboration, *Production of Λ-hyperons in inelastic p+p interactions at 158* GeV/*c*, The European Physical Journal C **76** (2016) 198 [1510.03720]. (Cited on page 62).

[302] C.D. Dermer, *Binary Collision Rates of Relativistic Thermal Plasmas. II. Spectra*, The Astrophysical Journal **307** (1986) 47. (Cited on pages 63, 65, and 74).

[303] C.D. Orth and A. Buffington, *Secondary cosmic-ray $e^{\pm}$ from 1 to 100 GeV in the upper atmosphere and interstellar space, and interpretation of a recent e^{+} flux measurement*, *The Astrophysical Journal* **206** (1976) 312. (Cited on page 63).

[304] C. Alt and et al., *Inclusive production of charged pions in p+C collisions at 158 GeV/c beam momentum*, *The European Physical Journal C* **49** (2007) 897–917. (Cited on pages 63, 64, and 65).

[305] G. Barr, O. Chvala, H. Fischer, M. Kreps, M. Makariev, C. Pattison et al., *Charged pion production in p+C collisions at 158GeV/c beam momentum: Discussion*, *The European Physical Journal C* **49** (2007) 919–945. (Cited on page 64).

[306] A.M. Baldin et al., *Experimental data on inclusive cross section for cumulative production of pions, kaons, antiprotons and the quark-parton structure function of nuclei*, *JINR-E1-82-472* (1982) 28. (Cited on page 64).

[307] N. Abgrall and et al., *Measurements of $\pi^{\pm}$, $K^{\pm}$, K^{0}_{S}, Λ and proton production in proton–carbon interactions at 31 GeV/c with the NA61/SHINE spectrometer at the CERN SPS*, *The European Physical Journal C* **76** (2016) 1. (Cited on pages 65 and 66).

[308] C.D. Dermer, *Secondary production of neutral pi-mesons and the diffuse galactic gamma radiation*, *Astronomy & Astrophysics* **157** (1986) 223. (Cited on page 65).

[309] M. Korsmeier and A. Cuoco, *Testing the universality of cosmic-ray nuclei from protons to oxygen with AMS-02*, *Physical Review D* **105** (2022) 103033. (Cited on pages 66, 84, 85, 87, 88, and 89).

[310] A. Ferrari, P.R. Sala, A. Fasso and J. Ranft, *FLUKA: A multi-particle transport code (Program version 2005)*, . (Cited on page 68).

[311] R. Kissmann, F. Niederwanger, O. Reimer and A.W. Strong, *Diffuse gamma rays in 3D galactic cosmic-ray propagation models*, *AIP Conference Proceedings* **1792** (2017) 070011 [1701.07285]. (Cited on page 71).

[312] L. Tibaldo, D. Gaggero and P. Martin, *Gamma rays as probes of cosmic-ray propagation and interactions in galaxies*, *Universe* **7** (2021) 141 [2103.16423]. (Cited on page 71).

[313] A. Dundovic, C. Evoli, D. Gaggero and D. Grasso, *Simulating the Galactic multi-messenger emissions with HERMES*, *Astronomy & Astrophysics* **653** (2021) A18 [2105.13165]. (Cited on page 71).

[314] A. Widmark, M. Korsmeier and T. Linden, *Weighing the local interstellar medium using gamma rays and dust*, *Physical Review Letters* **130** (2023) 161002. (Cited on page 71).

[315] M. Bhatt, I. Sushch, M. Pohl, A. Fedynitch, S. Das, R. Brose et al., *Production of secondary particles in heavy nuclei interactions in supernova remnants*, *Astroparticle Physics* **123** (2020) 102490. (Cited on page 71).

[316] M. Mazziotta, F. Cerutti, A. Ferrari, D. Gaggero, F. Loparco and P. Sala, *Production of secondary particles and nuclei in cosmic rays collisions with the interstellar gas using the FLUKA code*, *Astroparticle Physics* **81** (2016) 21. (Cited on page 71).

[317] O. Adriani et al., *Measurements of longitudinal and transverse momentum distributions for neutral pions in the forward-rapidity region with the LHCf detector*, *Physical Review D* **94** (2016) 032007. (Cited on page 74).

[318] ALICE collaboration, *Production of π^0 and η mesons up to high transverse momentum in pp collisions at 2.76 TeV*, *The European Physical Journal C* **77** (2017) 339 [1702.00917]. (Cited on pages 74 and 78).

[319] ALICE collaboration, *π^0 and η meson production in proton-proton collisions at $\sqrt{s} = 8$ TeV*, *The European Physical Journal C* **78** (2018) 263 [1708.08745]. (Cited on page 78).

[320] PHENIX collaboration, *Cross section and double helicity asymmetry for η mesons and their comparison to neutral pion production in $p+p$ collisions at $\sqrt{s}$=200 GeV*, *Physical Review D* **83** (2011) 032001 [1009.6224]. (Cited on page 78).

[321] WA80 collaboration, *Production of eta mesons in 200-A/GeV $S + S$ and $S + Au$ reactions*, *Physics Letters B* **361** (1995) 14 [hep-ex/9507009]. (Cited on page 78).

[322] D. Hooper, P. Blasi and P.D. Serpico, *Pulsars as the sources of high energy cosmic ray positrons*, *Journal of Cosmology and Astroparticle Physics* **2009** (2009) 025 [0810.1527]. (Cited on pages 83 and 101).

[323] R. Diesing and D. Caprioli, *Nonsecondary origin of cosmic ray positrons*, *Physical Review D* **101** (2020) 103030 [2001.02240]. (Cited on page 83).

[324] M.D. Mauro, F. Donato, N. Fornengo, R. Lineros and A. Vittino, *Interpretation of AMS-02 electrons and positrons data*, *Journal of Cosmology and Astroparticle Physics* **2014** (2014) 006. (Cited on pages 83, 101, 102, and 120).

[325] M. Di Mauro and M.W. Winkler, *Multimessenger constraints on the dark matter interpretation of the Fermi-LAT Galactic Center excess*, *Physical Review D* **103** (2021) 123005. (Cited on pages 84, 99, 106, 110, 112, 126, 136, and 209).

[326] M. Korsmeier and A. Cuoco, *Implications of Lithium to Oxygen AMS-02 spectra on our understanding of cosmic-ray diffusion*, *Physical Review D* **103** (2021) 103016 [2103.09824]. (Cited on pages 84, 85, 87, 88, 89, and 93).

[327] Y. Génolini, M. Boudaud, M. Cirelli, L. Derome, J. Lavalle, D. Maurin et al., *New minimal, median, and maximal propagation models for dark matter searches with Galactic cosmic rays*, *Physical Review D* **104** (2021) 083005. (Cited on pages 84, 85, 87, 106, and 110).

[328] AMS collaboration, *The Alpha Magnetic Spectrometer (AMS) on the international space station: Part II — Results from the first seven years*, *Physics Reports* **894** (2021) 1. (Cited on pages 84 and 88).

[329] A.W. Strong and I.V. Moskalenko, *The galprop program for cosmic ray propagation: new developments*, in *26th International Cosmic Ray Conference*, 6, 1999 [astro-ph/9906228]. (Cited on page 84).

[330] A.W. Strong, I.V. Moskalenko, T.A. Porter, G. Jóhannesson, E. Orlando and S.W. Digel, *The GALPROP Cosmic-Ray Propagation Code*, 0907.0559. (Cited on page 84).

[331] N. Weinrich, Y. Génolini, M. Boudaud, L. Derome and D. Maurin, *Combined analysis of AMS-02 (Li,Be,B)/C, N/O, 3He, and 4He data*, *Astronomy & Astrophysics* **639** (2020) A131 [2002.11406]. (Cited on pages 84, 89, 92, and 99).

[332] M. Vecchi, P.I. Batista, E.F. Bueno, L. Derome, Y. Génolini and D. Maurin, *The rigidity dependence of galactic cosmic-ray fluxes and its connection with the*

diffusion coefficient, *Frontiers of Physics* **10** (2022) 858841 [2203.06479]. (Cited on page 84).

[333] D. Green, *Constraints on the distribution of supernova remnants with Galactocentric radius*, *Monthly Notices of the Royal Astronomical Society* **454** (2015) 1517 [1508.02931]. (Cited on page 85).

[334] M. Kuhlen and P. Mertsch, *Time-dependent AMS-02 electron-positron fluxes in an extended force-field model*, *Physical Review Letters* **123** (2019) 251104 [1909.01154]. (Cited on page 85).

[335] R. Kappl, *SOLARPROP: Charge-sign Dependent Solar Modulation for Everyone*, *Computer Physics Communications* **207** (2016) 386 [1511.07875]. (Cited on page 85).

[336] Y. Génolini et al., *Cosmic-ray transport from AMS-02 boron to carbon ratio data: Benchmark models and interpretation*, *Physical Review D* **99** (2019) 123028 [1904.08917]. (Cited on pages 85, 125, 126, and 136).

[337] Y. Génolini, D. Maurin, I.V. Moskalenko and M. Unger, *Current status and desired precision of the isotopic production cross sections relevant to astrophysics of cosmic rays: Li, Be, B, C, and N*, *Physical Review C* **98** (2018) 034611. (Cited on page 87).

[338] E. Orlando, *Implications on Spatial Models of Interstellar Gamma-Ray Inverse-Compton Emission from Synchrotron Emission Studies in Radio and Microwaves*, *Physical Review D* **99** (2019) 043007 [1901.08604]. (Cited on pages 87 and 98).

[339] E.C. Stone, A.C. Cummings, F.B. McDonald, B.C. Heikkila, N. Lal and W.R. Webber, *Voyager 1 Observes Low-Energy Galactic Cosmic Rays in a Region Depleted of Heliospheric Ions*, *Science* **341** (2013) 150. (Cited on page 88).

[340] V.H.M. Phan, F. Schulze, P. Mertsch, S. Recchia and S. Gabici, *Stochastic Fluctuations of Low-Energy Cosmic Rays and the Interpretation of Voyager Data*, *Physical Review Letters* **127** (2021) 141101 [2105.00311]. (Cited on page 88).

[341] A. Vittino, P. Mertsch, H. Gast and S. Schael, *Breaks in interstellar spectra of positrons and electrons derived from time-dependent AMS data*, *Physical Review D* **100** (2019) 043007 [1904.05899]. (Cited on pages 88 and 91).

[342] F. James and M. Roos, *Minuit - a system for function minimization and analysis of the parameter errors and correlations*, *Computer Physics Communications* **10** (1975) 343. (Cited on page 89).

[343] M. Boudaud, Y. Génolini, L. Derome, J. Lavalle, D. Maurin, P. Salati et al., *AMS-02 antiprotons' consistency with a secondary astrophysical origin*, *Physical Review Research* **2** (2020) 023022 [1906.07119]. (Cited on page 89).

[344] J. Heisig, M. Korsmeier and M.W. Winkler, *Dark matter or correlated errors? Systematics of the AMS-02 antiproton excess*, *Physical Review Research* **2** (2020) 043017 [2005.04237]. (Cited on page 89).

[345] NA61/SHINE collaboration, *Pilot Study on the Measurement of the Production of Boron Isotopes in C+p Reactions at 13.5A GeV/c with NA61/SHINE*, *Proceedings of Science* **ICRC2023** (2023) 075. (Cited on page 90).

[346] A. Putze, L. Derome and D. Maurin, *A Markov Chain Monte Carlo technique to sample transport and source parameters of Galactic cosmic rays: II. Results for the diffusion model combining B/C and radioactive nuclei*, *Astronomy & Astrophysics* **516** (2010) A66 [1001.0551]. (Cited on page 93).

[347] P.-X. Ma, Z.-H. Xu, Q. Yuan, X.-J. Bi, Y.-Z. Fan, I.V. Moskalenko et al., *Interpretations of the cosmic ray secondary-to-primary ratios measured by DAMPE*, *Frontiers of Physics* **18** (2023) 44301. (Cited on page 98).

[348] M.J. Boschini, S.D. Torre, M. Gervasi, D. Grandi, G. Jóhannesson, M. Kachelriess et al., *Solution of heliospheric propagation: Unveiling the local interstellar spectra of cosmic-ray species*, *The Astrophysical Journal* **840** (2017) 115. (Cited on page 99).

[349] M. Boudaud, E.F. Bueno, S. Caroff, Y. Genolini, V. Poulin, V. Poireau et al., *The pinching method for Galactic cosmic ray positrons: implications in the light of precision measurements*, *Astronomy & Astrophysics* **605** (2017) A17 [1612.03924]. (Cited on page 99).

[350] O. Fornieri, D. Gaggero and D. Grasso, *Features in cosmic-ray lepton data unveil the properties of nearby cosmic accelerators*, *Journal of Cosmology and Astroparticle Physics* **2020** (2020) 009. (Cited on pages 99, 101, 106, and 120).

[351] D. Malyshev, I. Cholis and J. Gelfand, *Pulsars versus Dark Matter Interpretation of ATIC/PAMELA*, *Physical Review D* **80** (2009) 063005 [0903.1310]. (Cited on pages 101 and 108).

[352] D. Grasso, S. Profumo, A. Strong, L. Baldini, R. Bellazzini, E. Bloom et al., *On possible interpretations of the high energy electron–positron spectrum measured by the Fermi Large Area Telescope*, *Astroparticle Physics* **32** (2009) 140–151. (Cited on page 101).

[353] N. Kawanaka, K. Ioka and M.M. Nojiri, *Is Cosmic Ray Electron Excess from Pulsars Spiky or Smooth?: Continuous and Multiple Electron/Positron Injections*, *The Astrophysical Journal* **710** (2010) 958–963. (Cited on pages 101 and 117).

[354] K. Kashiyama, K. Ioka and N. Kawanaka, *White dwarf pulsars as possible cosmic ray electron-positron factories*, *Physical Review D* **83** (2011) 023002. (Cited on page 101).

[355] S. Kisaka and N. Kawanaka, *TeV cosmic-ray electrons from millisecond pulsars*, *Monthly Notices of the Royal Astronomical Society* **421** (2012) 3543–3549. (Cited on page 101).

[356] D. Gaggero, L. Maccione, D. Grasso, G. Di Bernardo and C. Evoli, *PAMELA and AMS-02 e^+ and e^- spectra are reproduced by three-dimensional cosmic-ray modeling*, *Physical Review D* **89** (2014) 083007 [1311.5575]. (Cited on page 101).

[357] I. Cholis and D. Hooper, *Dark Matter and Pulsar Origins of the Rising Cosmic Ray Positron Fraction in Light of New Data From AMS*, *Physical Review D* **88** (2013) 023013. (Cited on page 101).

[358] M. Boudaud et al., *A new look at the cosmic ray positron fraction*, *Astronomy & Astrophysics* **575** (2015) A67 [1410.3799]. (Cited on page 101).

[359] N. Tomassetti and F. Donato, *The Connection Between the Positron Fraction Anomaly and the Spectral Features in Galactic Cosmic-Ray Hadrons*, *The Astrophysical Journal* **803** (2015) L15 [1502.06150]. (Cited on page 101).

[360] P. Lipari, *Spectral shapes of the fluxes of electrons and positrons and the average residence time of cosmic rays in the Galaxy*, *Physical Review D* **99** (2019) 043005 [1810.03195]. (Cited on page 101).

[361] I. Cholis, T. Karwal and M. Kamionkowski, *Studying the milky way pulsar population with cosmic-ray leptons*, *Physical Review D* **98** (2018) . (Cited on pages 101, 102, 108, and 120).

[362] S. Manconi, M.D. Mauro and F. Donato, *Multi-messenger constraints to the local emission of cosmic-ray electrons*, *Journal of Cosmology and Astroparticle Physics* **2019** (2019) 024–024. (Cited on page 101).

[363] S. Manconi, M. Di Mauro and F. Donato, *Dipole anisotropy in cosmic electrons and positrons: inspection on local sources*, *Journal of Cosmology and Astroparticle Physics* **01** (2017) 006 [1611.06237]. (Cited on pages 101 and 105).

[364] S. Manconi, M. Di Mauro and F. Donato, *Contribution of pulsars to cosmic-ray positrons in light of recent observation of inverse-Compton halos*, *Physical Review D* **102** (2020) 023015 [2001.09985]. (Cited on pages 102, 106, 108, and 120).

[365] D.R. Lorimer, A.J. Faulkner, A.G. Lyne, R.N. Manchester, M. Kramer, M.A. McLaughlin et al., *The Parkes Multibeam Pulsar Survey - VI. Discovery and timing of 142 pulsars and a Galactic population analysis*, *Monthly Notices of the Royal Astronomical Society* **372** (2006) 777–800. (Cited on pages 102, 107, 108, 109, and 110).

[366] A. Chakraborty and M. Bagchi, *Understanding the Galactic population of normal pulsars: A leap forward*, 2012.13243. (Cited on pages 102, 107, 108, and 110).

[367] D.F. Torres, A. Cillis, J. Martín and E. de Oña Wilhelmi, *Time-dependent modeling of TeV-detected, young pulsar wind nebulae*, *Journal of High Energy Astrophysics* **1-2** (2014) 31 [1402.5485]. (Cited on pages 103 and 128).

[368] I. Sushch and B. Hnatyk, *Modelling of the radio emission from the Vela supernova remnant*, *Astronomy & Astrophysics* **561** (2014) A139 [1312.0777]. (Cited on page 103).

[369] I. Buesching, O.C. de Jager, M.S. Potgieter and C. Venter, *A Cosmic Ray Positron Anisotropy due to Two Middle-Aged, Nearby Pulsars?*, *The Astrophysical Journal* **678** (2008) L39 [0804.0220]. (Cited on page 103).

[370] J.P. Ridley and D.R. Lorimer, *Isolated pulsar spin evolution on the diagram*, *Monthly Notices of the Royal Astronomical Society* **404** (2010) 1081–1088. (Cited on page 104).

[371] E. van der Swaluw, A. Achterberg, Y.A. Gallant, T.P. Downes and R. Keppens, *Interaction of high-velocity pulsars with supernova remnant shells*, *Astronomy & Astrophysics* **397** (2003) 913–920. (Cited on page 104).

[372] S.V. Bulanov and V.A. Dogel, *The Influence of the Energy Dependence of the Diffusion Coefficient on the Spectrum of the Electron Component of Cosmic Rays and the Radio Background Radiation of the Galaxy*, *Astrophysics and Space Science* **29** (1974) 305. (Cited on page 105).

[373] E.A. Baltz and J. Edsjö, *Positron propagation and fluxes from neutralino annihilation in the halo*, *Physical Review D* **59** (1998) 023511. (Cited on page 105).

[374] S. Recchia, S. Gabici, F. Aharonian and J. Vink, *Local fading accelerator and the origin of TeV cosmic ray electrons*, *Physical Review D* **99** (2019) 103022. (Cited on pages 106, 120, 130, and 136).

[375] C. Nigro, C. Deil, R. Zanin, T. Hassan, J. King, J.E. Ruiz et al., *Towards open and reproducible multi-instrument analysis in gamma-ray astronomy*, *Astronomy and Astrophysics* **625** (2019) A10. (Cited on pages 107, 108, and 109).

[376] CTA Consortium collaboration, *Gammapy - A prototype for the CTA science tools*, *Proceedings of Science* **ICRC2017** (2018) 766 [1709.01751]. (Cited on pages 107, 108, and 109).

[377] J. Lattimer and M. Prakash, *Neutron star observations: Prognosis for equation of state constraints*, *Physics Reports* **442** (2007) 109–165. (Cited on page 108).

[378] R.N. Manchester, G.B. Hobbs, A. Teoh and M. Hobbs, *The Australia Telescope National Facility Pulsar Catalogue*, *The Astronomical Journal* **129** (2005) 1993 [astro-ph/0412641]. (Cited on pages 108, 119, and 130).

[379] G.L. Case and D. Bhattacharya, *A New Sigma-D Relation and Its Application to the Galactic Supernova Remnant Distribution*, *The Astrophysical Journal* **504** (1998) 761–772. (Cited on page 109).

[380] I. Yusifov and I. Küçük, *Revisiting the radial distribution of pulsars in the Galaxy*, *Astronomy & Astrophysics* **422** (2004) 545–553. (Cited on page 109).

[381] I. John and T. Linden, *Pulsars do not produce sharp features in the cosmic-ray electron and positron spectra*, *Physical Review D* **107** (2023) . (Cited on pages 112 and 119).

[382] J. Chang et al., *An excess of cosmic ray electrons at energies of 300–800 GeV*, *Nature* **456** (2008) 362. (Cited on page 117).

[383] S. Torii et al., *High-energy electron observations by PPB-BETS flight in Antarctica*, 0809.0760. (Cited on page 117).

[384] K.P. Watters and R.W. Romani, *The Galactic population γ-ray pulsars*, *The Astrophysical Journal* **727** (2011) 123. (Cited on page 120).

[385] F.A. Aharonian, S.R. Kelner and A.Y. Prosekin, *Angular, spectral, and time distributions of highest energy protons and associated secondary gamma rays and neutrinos propagating through extragalactic magnetic and radiation fields*, *Physical Review D* **82** (2010) 043002 [1006.1045]. (Cited on pages 124 and 128).

[386] R. Aloisio and V.S. Berezinsky, *Anti-GZK Effect in Ultra-High-Energy Cosmic Ray Diffusive Propagation*, *The Astrophysical Journal* **625** (2005) 249 [astro-ph/0412578]. (Cited on pages 125 and 128).

[387] N. Globus, D. Allard and E. Parizot, *Propagation of high-energy cosmic rays in extragalactic turbulent magnetic fields: resulting energy spectrum and composition*, *Astronomy & Astrophysics* **479** (2008) 97 [0709.1541]. (Cited on page 125).

[388] R. Aloisio, V. Berezinsky and A. Gazizov, *The Problem of Superluminal Diffusion of Relativistic Particles and Its Phenomenological Solution*, *The Astrophysical Journal* **693** (2009) 1275 [0805.1867]. (Cited on pages 125 and 136).

[389] A.Y. Prosekin, S.R. Kelner and F.A. Aharonian, *Transition of propagation of relativistic particles from the ballistic to the diffusion regime*, *Physical Review D* **92** (2015) 083003 [1506.06594]. (Cited on pages 125, 128, 130, and 134).

[390] J. Dunkel, P. Talkner and P. Hänggi, *Relativistic diffusion processes and random walk models*, *Physical Review D* **75** (2007) 043001. (Cited on page 125).

[391] M.A. Malkov, *Exact solution of the Fokker-Planck equation for isotropic scattering*, *Physical Review D* **95** (2017) 023007 [1610.01584]. (Cited on page 125).

[392] A. Reinert and M.W. Winkler, *A Precision Search for WIMPs with Charged Cosmic Rays*, *Journal of Cosmology and Astroparticle Physics* **01** (2018) 055 [1712.00002]. (Cited on page 125).

[393] P. Subedi, W. Sonsrettee, P. Blasi, D. Ruffolo, W.H. Matthaeus, D. Montgomery et al., *Charged Particle Diffusion in Isotropic Random Magnetic Fields*, *The Astrophysical Journal* **837** (2017) 140 [1612.09507]. (Cited on pages 125 and 126).

[394] P. Mertsch, *Test particle simulations of cosmic rays*, *Astrophysics and Space Science* **365** (2020) 135 [1910.01172]. (Cited on pages 125 and 126).

[395] H. Yan and A. Lazarian, *Cosmic-Ray Propagation: Nonlinear Diffusion Parallel and Perpendicular to Mean Magnetic Field*, *The Astrophysical Journal* **673** (2008) 942 [0710.2617]. (Cited on page 126).

[396] F. Casse, M. Lemoine and G. Pelletier, *Transport of cosmic rays in chaotic magnetic fields*, *Physical Review D* **65** (2002) 023002 [astro-ph/0109223]. (Cited on page 126).

[397] L. Nava and S. Gabici, *Anisotropic cosmic ray diffusion and gamma-ray production close to supernova remnants, with an application to W28*, *Monthly Notices of the Royal Astronomical Society* **429** (2013) 1643 [1211.1668]. (Cited on pages 126 and 135).

[398] G. Giacinti and R. Lopez-Coto, *Constraining the Properties of the Interstellar Turbulence around Geminga using HAWC Measurements*, *Proceedings of Science* **ICRC2019** (2019) 685. (Cited on page 126).

[399] A. Shukurov, A.P. Snodin, A. Seta, P.J. Bushby and T.S. Wood, *Cosmic Rays in Intermittent Magnetic Fields*, *The Astrophysical Journal Letters* **839** (2017) L16 [1702.06193]. (Cited on page 126).

[400] P. Reichherzer, L. Merten, J. Dörner, J.B. Tjus, M.J. Pueschel and E.G. Zweibel, *Regimes of cosmic-ray diffusion in galactic turbulence*, *Springer Nature Applied Sciences* **4** (2021) 15. (Cited on page 126).

[401] S. Gabici and F.A. Aharonian, *Pointlike Gamma Ray Sources as Signatures of Distant Accelerators of Ultrahigh Energy Cosmic Rays*, *Physical Review Letters* **95** (2005) 251102 [astro-ph/0505462]. (Cited on page 128).

[402] V.S. Berezinskii, S.V. Bulanov, V.A. Dogiel, V.L. Ginzburg, V.S. Ptuskin and C.V. Meister, *Book-Review - Astrophysics of Cosmic-Rays*, *Astronomische Nachrichten* **312** (1991) 413. (Cited on page 129).

[403] J.M. Yao, R.N. Manchester and N. Wang, *A New Electron-density Model for Estimation of Pulsar and FRB Distances*, *The Astrophysical Journal* **835** (2017) 29 [1610.09448]. (Cited on page 130).

[404] J.M. Cordes and T. Lazio, *NE2001. 1. A New model for the galactic distribution of free electrons and its fluctuations*, astro-ph/0207156. (Cited on page 131).

[405] A.U. Abeysekara et al., *Observation of the Crab Nebula with the HAWC Gamma-Ray Observatory*, *The Astrophysical Journal* **843** (2017) 39 [1701.01778]. (Cited on page 133).

[406] L. Dondi and G. Ghisellini, *Gamma-ray-loud blazars and beaming*, *Monthly Notices of the Royal Astronomical Society* **273** (1995) 583. (Cited on page 135).

[407] M.J. Rees and J.E. Gunn, *The origin of the magnetic field and relativistic particles in the Crab Nebula*, *Monthly Notices of the Royal Astronomical Society* **167** (1974) 1. (Cited on page 135).

[408] C.F. Kennel and F.V. Coroniti, *Magnetohydrodynamic model of Crab nebula radiation.*, *The Astrophysical Journal* **283** (1984) 710. (Cited on page 135).

[409] B. Abbott et al., *Beating the Spin-Down Limit on Gravitational Wave Emission from the Crab Pulsar*, *The Astrophysical Journal Letters* **683** (2008) L45 [0805.4758]. (Cited on page 135).

[410] N. Bucciantini, J. Arons and E. Amato, *Modelling spectral evolution of pulsar wind nebulae inside supernova remnants*, *Monthly Notices of the Royal Astronomical Society* **410** (2011) 381 [1005.1831]. (Cited on page 135).

[411] L.-Z. Bao, K. Fang, X.-J. Bi and S.-H. Wang, *Slow diffusion is necessary to explain the gamma-ray pulsar halos*, *The Astrophysical Journal* **936** (2022) 183. (Cited on page 136).

[412] G.M. Mason, J.E. Mazur and J.R. Dwyer, ^{3}*He Enhancements in Large Solar Energetic Particle Events*, *The Astrophysical Journal Letters* **525** (1999) L133. (Cited on page 139).

[413] D.L. Turner et al., *Direct Multipoint Observations Capturing the Reformation of a Supercritical Fast Magnetosonic Shock*, *The Astrophysical Journal Letters* **911** (2021) L31 [2104.01123]. (Cited on page 139).

[414] B.D. Metzger, D. Caprioli, I. Vurm, A.M. Beloborodov, I. Bartos and A. Vlasov, *Novae as Tevatrons: prospects for CTA and IceCube*, *Monthly Notices of the Royal Astronomical Society* **457** (2016) 1786 [1510.07639]. (Cited on page 139).

[415] R. Diesing, B.D. Metzger, E. Aydi, L. Chomiuk, I. Vurm, S. Gupta et al., *Evidence for Multiple Shocks from the γ-Ray Emission of RS Ophiuchi*, *The Astrophysical Journal* **947** (2023) 70. (Cited on page 139).

[416] D. Caprioli, *Cosmic-ray acceleration in supernova remnants: non-linear theory revised*, *Journal of Cosmology and Astroparticle Physics* **7** (2012) 38 [1206.1360]. (Cited on page 139).

[417] C.D. Dermer, S. Razzaque, J.D. Finke and A. Atoyan, *Ultra-high-energy cosmic rays from black hole jets of radio galaxies*, *New Journal of Physics* **11** (2009) 065016. (Cited on page 139).

[418] J.H. Matthews, A.R. Bell, K.M. Blundell and A.T. Araudo, *Ultrahigh energy cosmic rays from shocks in the lobes of powerful radio galaxies*, *Monthly Notices of the Royal Astronomical Society* **482** (2019) 4303 [1810.12350]. (Cited on page 139).

[419] G. Brunetti and T.W. Jones, *Cosmic Rays in Galaxy Clusters and Their Nonthermal Emission*, *International Journal of Modern Physics D* **23** (2014) 1430007 [1401.7519]. (Cited on page 139).

[420] P.O. Lagage and C.J. Cesarsky, *Cosmic-ray shock acceleration in the presence of self-excited waves*, *Astronomy & Astrophysics* **118** (1983) 223. (Cited on page 139).

[421] P. Blasi, E. Amato and D. Caprioli, *The maximum momentum of particles accelerated at cosmic ray modified shocks*, *Monthly Notices of the Royal Astronomical Society* **375** (2007) 1471. (Cited on page 139).

[422] A.R. Bell, K.M. Schure, B. Reville and G. Giacinti, *Cosmic-ray acceleration and escape from supernova remnants*, *Monthly Notices of the Royal Astronomical Society* **431** (2013) 415 [1301.7264]. (Cited on page 139).

[423] M. Palmroth, U. Ganse, Y. Pfau-Kempf, M. Battarbee, L. Turc, T. Brito et al., *Vlasov methods in space physics and astrophysics*, *Living Reviews in Computational Astrophysics* **4** (2018) 1 [1808.05885]. (Cited on page 140).

[424] J. Juno, *A deep dive into the distribution function: Understanding phase space dynamics with continuum vlasov-maxwell simulations*, 2005.13539. (Cited on page 140).

[425] J. Park, D. Caprioli and A. Spitkovsky, *Simultaneous Acceleration of Protons and Electrons at Nonrelativistic Quasiparallel Collisionless Shocks*, *Physical Review Letters* **114** (2015) 085003 [1412.0672]. (Cited on pages 140 and 142).

[426] T.N. Kato, *Energy Loss of High-Energy Particles in Particle-in-Cell Simulation*, 1312.5507. (Cited on page 140).

[427] R. Xu, A. Spitkovsky and D. Caprioli, *Electron Acceleration in One-dimensional Nonrelativistic Quasi-perpendicular Collisionless Shocks*, *The Astrophysical Journal Letters* **897** (2020) L41 [1908.07890]. (Cited on pages 140 and 142).

[428] P. Crumley, D. Caprioli, S. Markoff and A. Spitkovsky, *Kinetic simulations of mildly relativistic shocks: Particle acceleration in high mach number shocks*, *Monthly Notices of the Royal Astronomical Society* **485** (2019) 5105 [1809.10809]. (Cited on pages 140 and 142).

[429] M. Shalaby, R. Lemmerz, T. Thomas and C. Pfrommer, *The Mechanism of Efficient Electron Acceleration at Parallel Nonrelativistic Shocks*, *The Astrophysical Journal* **932** (2022) 86 [2202.05288]. (Cited on pages 140 and 142).

[430] A.S. Lipatov, *The hybrid multiscale simulation technology: an introduction with application to astrophysical and laboratory plasmas*, *Springer Berlin* (2002) . (Cited on page 140).

[431] H. Karimabadi, V. Roytershteyn, H.X. Vu, Y.A. Omelchenko, J. Scudder, W. Daughton et al., *The link between shocks, turbulence, and magnetic reconnection in collisionless plasmas*, *Physics of Plasmas* **21** (2014) 062308. (Cited on pages 140 and 150).

[432] J. Giacalone, D. Burgess, S.J. Schwartz, D.C. Ellison and L. Bennett, *Injection and acceleration of thermal protons at quasi-parallel shocks: A hybrid*

simulation parameter survey, *Journal of Geophysical Research* **102** (1997) 19789. (Cited on pages 140 and 142).

[433] D. Burgess and M. Scholer, *Microphysics of Quasi-parallel Shocks in Collisionless Plasmas*, *Space Science Reviews* **178** (2013) 513. (Cited on page 140).

[434] D. Caprioli and A. Spitkovsky, *Simulations of Ion Acceleration at Non-relativistic Shocks: I. Acceleration Efficiency*, *The Astrophysical Journal* **783** (2014) 91 [1310.2943]. (Cited on pages 141, 144, 146, 147, and 150).

[435] D. Caprioli and A. Spitkovsky, *Simulations of Ion Acceleration at Non-relativistic Shocks: II. Magnetic Field Amplification*, *The Astrophysical Journal* **794** (2014) 46 [1401.7679]. (Cited on pages 141, 142, 144, 147, and 149).

[436] D. Caprioli and A. Spitkovsky, *Simulations of Ion Acceleration at Non-relativistic Shocks. III. Particle Diffusion*, *The Astrophysical Journal* **794** (2014) 47 [1407.2261]. (Cited on pages 141, 142, and 149).

[437] D. Caprioli, A. Pop and A. Spitkovsky, *Simulations and Theory of Ion Injection at Non-relativistic Collisionless Shocks*, *The Astrophysical Journal Letters* **798** (2015) 28 [1409.8291]. (Cited on pages 141 and 142).

[438] D. Caprioli, D.T. Yi and A. Spitkovsky, *Chemical Enhancements in Shock-Accelerated Particles: Ab initio Simulations*, *Physical Review Letters* **119** (2017) 171101 [1704.08252]. (Cited on pages 141 and 142).

[439] D. Caprioli, H. Zhang and A. Spitkovsky, *Diffusive Shock Re-Acceleration*, *Journal of Plasma Physics* (2018) [1801.01510]. (Cited on pages 141, 142, and 144).

[440] X.-N. Bai, D. Caprioli, L. Sironi and A. Spitkovsky, *Magnetohydrodynamic-PIC Method for Coupling Cosmic Rays with a Thermal Plasma: Application to Non-relativistic Shocks*, *The Astrophysical Journal* **809** (2015) 55 [1412.1087]. (Cited on page 141).

[441] A.J. van Marle, F. Casse and A. Marcowith, *On magnetic field amplification and particle acceleration near non-relativistic astrophysical shocks: particles in MHD cells simulations*, *Monthly Notices of the Royal Astronomical Society* **473** (2018) 3394 [1709.08482]. (Cited on page 141).

[442] N. Shimada and M. Hoshino, *Strong Electron Acceleration at High Mach Number Shock Waves: Simulation Study of Electron Dynamics*, *The Astrophysical Journal* **543** (2000) L67. (Cited on page 142).

[443] N. Kumar and B. Reville, *Nonthermal Particle Acceleration at Highly Oblique Nonrelativistic Shocks*, *The Astrophysical Journal Letters* **921** (2021) L14 [2110.09939]. (Cited on page 142).

[444] T. Amano and M. Hoshino, *Electron Shock Surfing Acceleration in Multidimensions: Two-Dimensional Particle-in-Cell Simulation of Collisionless Perpendicular Shock*, *The Astrophysical Journal* **690** (2009) 244 [0805.1098]. (Cited on page 142).

[445] A. Bohdan, M. Pohl, J. Niemiec, P.J. Morris, Y. Matsumoto, T. Amano et al., *Magnetic Field Amplification by the Weibel Instability at Planetary and Astrophysical Shocks with High Mach Number*, *Physical Review Letters* **126** (2021) 095101. (Cited on pages 142, 144, and 145).

[446] T.N. Kato and H. Takabe, *Nonrelativistic Collisionless Shocks in Weakly Magnetized Electron-Ion Plasmas: Two-dimensional Particle-in-cell Simulation of Perpendicular Shock*, *The Astrophysical Journal* **721** (2010) 828. (Cited on pages 142, 144, and 145).

[447] Y. Matsumoto, T. Amano, T.N. Kato and M. Hoshino, *Stochastic electron acceleration during spontaneous turbulent reconnection in a strong shock wave*, *Science* **347** (2015) 974. (Cited on pages 142 and 145).

[448] Y. Matsumoto, T. Amano, T.N. Kato and M. Hoshino, *Electron Surfing and Drift Accelerations in a Weibel-Dominated High-Mach-Number Shock*, *Physical Review Letters* **119** (2017) 105101. (Cited on page 142).

[449] L. Sironi and A. Spitkovsky, *Particle Acceleration in Relativistic Magnetized Collisionless Pair Shocks: Dependence of Shock Acceleration on Magnetic Obliquity*, *The Astrophysical Journal* **698** (2009) 1523 [0901.2578]. (Cited on page 142).

[450] L. Sironi, A. Spitkovsky and J. Arons, *The Maximum Energy of Accelerated Particles in Relativistic Collisionless Shocks*, *The Astrophysical Journal* **771** (2013) 54 [1301.5333]. (Cited on page 142).

[451] H. Kucharek and M. Scholer, *Origin of diffuse superthermal ions at quasi-parallel supercritical collisionless shocks*, *Journal of Geophysical Research* **96** (1991) 21195. (Cited on page 142).

[452] J. Giacalone, D. Burgess, S.J. Schwartz and D.C. Ellison, *Ion injection and acceleration at parallel shocks - Comparisons of self-consistent plasma simulations with existing theories*, *The Astrophysical Journal* **402** (1993) 550. (Cited on page 142).

[453] D. Burgess, E.A. Lucek, M. Scholer, S.D. Bale, M.A. Balikhin, A. Balogh et al., *Quasi-parallel Shock Structure and Processes*, *Space Science Reviews* **118** (2005) 205. (Cited on page 142).

[454] M.G. Baring, D.C. Ellison and F.C. Jones, *Monte Carlo simulations of particle acceleration at oblique shocks: Including cross-field diffusion*, *Advances in Space Research* **15** (1995) 397. (Cited on page 142).

[455] J. Giacalone and D.C. Ellison, *Three-dimensional numerical simulations of particle injection and acceleration at quasi-perpendicular shocks*, *Journal of Geophysical Research* **105** (2000) 12541. (Cited on pages 142 and 148).

[456] J. Giacalone, *The physics of particle acceleration by collisionless shocks*, *Planetary and Space Science* **51** (2003) 659. (Cited on page 142).

[457] J. Giacalone, *The efficient acceleration of thermal protons by perpendicular shocks*, *The Astrophysical Journal Letters* **628** (2005) L37. (Cited on page 142).

[458] F. Guo and J. Giacalone, *The Acceleration of Thermal Protons at Parallel Collisionless Shocks: Three-dimensional Hybrid Simulations*, *The Astrophysical Journal* **773** (2013) 158 [1303.5174]. (Cited on page 142).

[459] J.R. Jokipii, J. Kóta and J. Giacalone, *Perpendicular transport in 1- and 2-dimensional shock simulations*, *Geophysical Research Letters* **20** (1993) 1759. (Cited on pages 142 and 148).

[460] F.C. Jones, J.R. Jokipii and M.G. Baring, *Charged-Particle Motion in Electromagnetic Fields Having at Least One Ignorable Spatial Coordinate*, *The Astrophysical Journal* **509** (1998) 238 [astro-ph/9808103]. (Cited on pages 142 and 148).

[461] C.C. Haggerty and D. Caprioli, *dHybridR: A Hybrid Particle-in-cell Code Including Relativistic Ion Dynamics*, *The Astrophysical Journal* **887** (2019) 165 [1909.05255]. (Cited on pages 143 and 144).

[462] L. Gargaté, R. Bingham, R.A. Fonseca and L.O. Silva, *dHybrid: A massively parallel code for hybrid simulations of space plasmas*, *Computer Physics Communications* **176** (2007) 419 [physics/0611174]. (Cited on page 143).

[463] G. Chen and T.P. Armstrong, *Acceleration of charged particles in oblique MHD shocks*, in *International Cosmic Ray Conference*, vol. 5 of *International Cosmic Ray Conference*, pp. 1814–1819, Aug., 1975. (Cited on page 148).

[464] R.B. Decker and L. Vlahos, *Shock drift acceleration in the presence of waves*, *Journal of Geophysical Research: Space Physics* **90** (1985) 47. (Cited on page 148).

[465] L. Ball and D.B. Melrose, *Shock drift acceleration of electrons*, *Publications of the Astronomical Society* **18** (2001) 361. (Cited on page 148).

[466] Z.W. Yang, Q.M. Lu, B. Lembège and S. Wang, *Shock front nonstationarity and ion acceleration in supercritical perpendicular shocks*, *Journal of Geophysical Research: Space Physics* **114** (2009) 03111. (Cited on page 148).

[467] S.F. Kamijima, Y. Ohira and R. Yamazaki, *Fast particle acceleration at perpendicular shocks with uniform upstream magnetic field and strong downstream turbulence*, *The Astrophysical Journal* **897** (2020) 116. (Cited on page 148).

[468] J.R. Jokipii, *Rate of energy gain and maximum energy in diffusive shock acceleration*, *The Astrophysical Journal* **313** (1987) 842. (Cited on page 149).

[469] J. Giacalone, J.R. Jokipii and J. Kota, *Ion injection and acceleration at quasi-perpendicular shocks*, *Journal of Geophysical Research* **99** (1994) 19351. (Cited on page 149).

[470] L. O'C. Drury, *An introduction to the theory of diffusive shock acceleration of energetic particles in tenuous plasmas*, *Reports of Progress in Physics* **46** (1983) 973. (Cited on page 149).

[471] A. Johlander et al., *Ion Acceleration Efficiency at the Earth's Bow Shock: Observations and Simulation Results*, *The Astrophysical Journal* **914** (2021) 82. (Cited on page 150).

[472] A. Lalti, Y.V. Khotyaintsev, A.P. Dimmock, A. Johlander, D.B. Graham and V. Olshevsky, *A Database of MMS Bow Shock Crossings Compiled Using Machine Learning*, *Journal of Geophysical Research: Space Physics* **127** (2022) e2022JA030454. (Cited on page 150).

[473] L.B. Wilson III, D.G. Sibeck, D.L. Turner, A. Osmane, D. Caprioli and V. Angelopoulos, *Relativistic electrons produced by foreshock disturbances observed upstream of the Earth's bow shock*, *Physical Review Letters* **117** (2016) 215101. (Cited on page 150).

[474] R. Rothenflug, J. Ballet, G. Dubner, E. Giacani, A. Decourchelle and P. Ferrando, *Geometry of the non-thermal emission in SN 1006. Azimuthal variations of cosmic-ray acceleration*, *Astronomy & Astrophysics* **425** (2004) 121. (Cited on page 151).

[475] F. Bocchino, S. Orlando, M. Miceli and O. Petruk, *Constraints on the local interstellar magnetic field from non-thermal emission of SN1006*, *Astronomy & Astrophysics* **531** (2011) A129 [1105.2689]. (Cited on page 151).

[476] G. Cassam-Chenaï, J.P. Hughes, E.M. Reynoso, C. Badenes and D. Moffett, *Morphological Evidence for Azimuthal Variations of the Cosmic-Ray Ion Acceleration at the Blast Wave of SN 1006*, *The Astrophysical Journal* **680** (2008) 1180 [arXiv:0803.0805]. (Cited on page 151).

[477] R. Giuffrida, M. Miceli, D. Caprioli, A. Decourchelle, J. Vink, S. Orlando et al., *The supernova remnant SN 1006 as a Galactic particle accelerator*, *Nature Communications* **13** (2022) 5098 [2208.14491]. (Cited on page 151).

[478] F. Acero et al., *First detection of VHE γ-rays from SN 1006 by HESS*, *Astronomy & Astrophysics* **516** (2010) A62+ [1004.2124]. (Cited on page 151).

[479] D. Caprioli, *Cosmic-ray acceleration and propagation* , *Proceedings of Science* **ICRC2015** (2016) 008. (Cited on page 151).

[480] R.A. Chevalier and C. Fransson, *Circumstellar Emission from Type Ib and Ic Supernovae*, *The Astrophysical Journal* **651** (2006) 381 [astro-ph/0607196]. (Cited on page 152).

[481] R. Margutti and R. Chornock, *First Multimessenger Observations of a Neutron Star Merger*, *Annual Review of Astronomy and Astrophysics* **59** (2021) [2012.04810]. (Cited on page 152).

[482] A.R. Bell, K.M. Schure and B. Reville, *Cosmic ray acceleration at oblique shocks*, *Monthly Notices of the Royal Astronomical Society* **418** (2011) 1208 [1108.0582]. (Cited on page 152).

[483] R. Diesing and D. Caprioli, *Steep Cosmic-Ray Spectra with Revised Diffusive Shock Acceleration*, *The Astrophysical Journal* **922** (2021) 1 [2107.08520]. (Cited on page 152).

[484] C.-I. Bjornsson and C. Fransson, *The X-Ray and Radio Emission from SN2 002ap: The Importance of Compton Scattering*, *The Astrophysical Journal* **605** (2004) 823. (Cited on page 152).

[485] I.V. Moskalenko and A.W. Strong, *Production and propagation of cosmic ray positrons and electrons*, *The Astrophysical Journal* **493** (1998) 694 [astro-ph/9710124]. (Cited on page 207).

Appendix

A.1 Positron and electron energy losses

$e^{\pm}$ can loose energy in our Galaxy by [485]:

1. ICS off the ISRF
2. Synchrotron radiation in magnetic fields
3. Bremsstrahlung
4. Ionization of interstellar neutral matter
5. Coulomb interactions with interstellar medium

in addition to the adiabatic losses connected with the Galactic wind. In Ref. [281] a detailed study of the complete set of energy losses (including adiabatic losses) for e^+ has shown that only inverse Compton scattering and synchrotron radiation are relevant for energies higher than ~ 5 GeV. We will consider either all the energy losses or only inverse Compton scattering and synchrotron losses based on the single cases.
An effective way to write down the energy loss term as:

$$-\frac{dE}{dt} = b(E) = E_0 \frac{\epsilon^2}{\tau_E} = E_0 \left(\frac{\epsilon^2}{\tau_{sync}} + \frac{\epsilon^2}{\tau_*} + \frac{\epsilon^2}{\tau_{CMB}} + \frac{\epsilon^2}{\tau_{dust}} \right) \tag{A.1}$$

where b_0 is in units of $\mathrm{GeV}^{-1}\ \mathrm{s}^{-1}$, while $\tau_{sync}, \tau_*, \tau_{CMB}, \tau_{dust}$ are the energy-loss timescale for synchrotron emission and inverse Compton scattering on starlight photons, CMB, and interstellar dust photons respectively (see Section 2.3.2). Here $\epsilon{=}E/E_0$ where $E_0 = 1$ GeV. The Compton processes can be computed in the Thomson limit. This is a good approximation for energies of $10 - 100$ GeV. Each energy-loss timescale τ can be calculated using both the Thomson cross section σ_T and the corresponding radiation-field energy U, according to Ref. [144]:

$$\tau = \frac{E}{\frac{4}{3} c \sigma_T \gamma_e^2 U} \tag{A.2}$$

where γ is the Lorentz factor of the particle.
The Thomson approximation is valid for $\gamma_e \lesssim m_e c^2/E_\gamma$, where E_γ is the photon energy [281] and m_e is the eletron mass. The maximal $e^\pm$ energy below which it is correct to use Thomson regime is $\sim 1 \times 10^6$ GeV for interactions with CMB ($E_{ph} \simeq 2.35 \times 10^{-4}$ eV), and lower values for infrared radiation (IR) and starlight radiation (hundreds of GeV for this last one). The Thomson approximation is no longer valid for energies at Earth above a few tens of GeV, for which a full relativistic description of the term dE/dt is necessary. In this thesis we will use the fully relativistic energy losses treatment based on Ref. [143], to which we refer for more details. The complete calculation of the ICS energy losses, requires a double integration of the Klein-Nishina cross section multiplied for the ISRF energy density $n(\epsilon)$ [206]:

$$-\frac{dE}{dt} = \frac{12 c \sigma_T E}{(m_e c^2)^2} \int_0^\infty d\epsilon\, \epsilon\, n(\epsilon)\, \mathcal{J}(\Gamma), \tag{A.3}$$

where σ_T is the total Thomson cross section, $\Gamma = 4\epsilon\gamma/(m_e c^2)$ and $\mathcal{J}(\Gamma)$ is defined as

$$\mathcal{J}(\Gamma) = \int_0^1 dq\, q\, \frac{2q \log q + (1+2q)(1-q) + \frac{(\Gamma q)^2(1-q)}{2(1+\Gamma q)}}{(1+\Gamma q)^3} \tag{A.4}$$

with $q = \epsilon/(\Gamma(\gamma m c^2 - \epsilon))$.
Finally, the synchrotron emission can be expressed as an inverse Compton scattering on a black-body distribution of virtual photons from the magnetic field. The characteristic energy of the radiation field is given by the cyclotron frequency:

$$E_B = \frac{heB}{2\pi m_e} \tag{A.5}$$

where B is the value of the Galactic magnetic field. A more precise treatment of energy losses should also take into account the spatial dependence, $b(E, \mathbf{x})$, since the $e^\pm$ suffer of energy losses depending on the Galactic environment, the composition of the background light in different points of the Galaxy and the magnetic field. This space dependent approach underlines that the energy loss timescale varies according to the position in the Milky Way (from the Galactic center to the Galactic edge, for example).

The typical propagation scale for electrons and positrons

The typical propagation scale λ is a reference spatial scale useful to estimate the particle horizon, namely the typical distance which a particle with energy at source E_0 travels

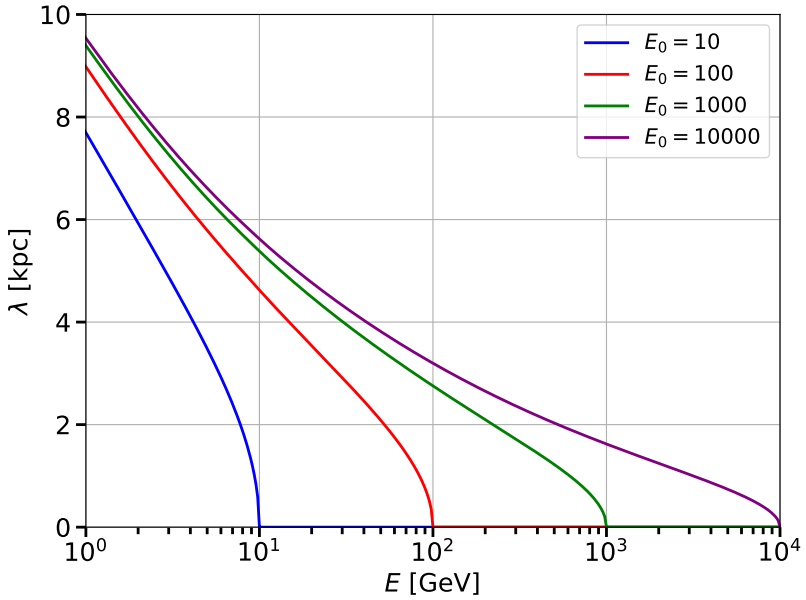

Figure A.1: Typical propagation scale λ for $e^{\pm}$ in the Milky Way as a function of their energy. Different energies at sources Es are considered. The propagation model in [325] has been assumed.

before reaching the Earth with reduced energy E. In the diffusion model, λ is defined as:

$$\lambda^2 = \lambda^2(E, E_0) \equiv 4 \int_E^{E_0} dE' \frac{D(E')}{b(E')} \tag{A.6}$$

where $D(E) = D_0 E^{\delta}$ is the diffusion coefficient as a function of energy (that can be derived from D_{xx} that is a function of rigidity). In Figure A.1 is displayed $\lambda(E, E_0)$ for different energies at source E_0, from 10 GeV (blue) to 10^4 GeV (purple). Equation A.6 has been used within the $D(E)$ taken from Ref. [325] and the ISRF of Ref. [204]. The propagation scale depends on the energy E_0, and its trend is driven by the energy losses term. Regardless of the energy at source, the horizon for electrons and positrons of energies E $\geq$ 100 GeV is limited to distances lower than 4 kpc. An electron detected at Earth with $E = 100$ GeV has propagated in the Galaxy for a typical length of $\lambda \sim 3$ kpc. At E = 1 TeV, the propagation scale is even smaller as ~ 1.5 kpc. This demonstrates that $e^{\pm}$ at E $\sim$ GeV$-$TeV probe the few kpc near the Earth, and thus are controlled by the properties of the local Galaxy.

A.2 Extended results for cosmic-ray propagation

In this Section we report an additional discussion about the results we obtain for the propagation parameters and the fit to the CR flux data.

In Figure A.2 (Figure A.3) we show the triangle plots for the propagation (primary CRs abundance and nuisance parameters of the cross sections) parameters. We display the results obtained with the models `Conv` $v_{0,c}$ with $L = 1$ and 4 kpc, and `Reacc`$_0$. For each panel we show the profiles and contours derived from the 1D and 2D marginalized posteriors.

When we use `Conv` $v_{0,c}$, almost all the parameters found for different values of L are compatible within the errors. The only exceptions are the value of D_0, which is proportional to L (as explained in Section 4.4), the convection velocity and the value of the normalization cross sections for the Be production ($A_{\rm XS} \to$ Be), see Figure 4.3. The slope we obtain for injections of protons γ_p is about $2.36 - 2.39$ while $\gamma_{\rm He}$ and $\gamma_{\rm CNO}$ are slightly softer of about -0.05 and -0.02, respectively. The diffusion coefficient for the best-fit model increases below the first rigidity break at 5 GV (δ_l has a negative slope). The second slope δ is about $0.6 - 0.7$, while above the second break, located at around 155 GV, there is an hardening of about $\delta - \delta_h = 0.3$. We find that there is a smooth transition of the diffusion coefficient between both breaks with values of the smoothing of $0.15 - 0.20$ for the low-energy and 0.5 for the high-energy break. The value we find for the slope δ is much larger than what is usually found in other references (see, e.g., [94]) because indeed we include this smoothing also for the high-rigidity break. We also note that the best-fit for $s_{D,1}$ is at the edge of the prior (see Figure A.2). Talking about the nuisance parameters for the nuclear cross sections, the value of $A_{\rm XS} \to$ Li is 1.20 and at the edge of the prior, as well as $\delta_{\rm XS} \to$ C and $\delta_{\rm XS} \to$ Li (see Figure A.3).

When we use different propagation models, i.e. the models with reacceleration, we find that leaving free different slopes for p, He and CNO CRs, the fit improves significantly. In particular, both the low and high-energy slopes of the spectra are slightly harder for He and CNO with respect to protons. The best-fit parameters and the goodness of the fits found for the model `Conv` dv/dz are basically the same of the model `Conv` $v_{0,c}$. The model labeled as `Reacc`$_0$ returns as best-fit value for v_A about 0 km/s and the diffusion coefficient for the part above 10 GV is similar to the convective cases.

The triangle plots shown in Figure A.2 show the presence of correlations of a few parameters such as D_0 and $v_{0,c}$ (see also Figure A.3). All the other parameters do not show strong correlations.

In Figure A.4 we show the ratio between the flux of secondary and primary CRs. In particular, we display the result for the ratio Be/C and B/C for the model `Conv` $v_{0,c}$

model for different values of L, and when we use the convection and reacceleration models. All the tested models, with convection or reacceleration, provide a good fit to the secondary over primary ratios when we use $L = 4$ kpc. In fact we see in the right panels that the differences between the tested models and the data are minor in the energy range of the data. The reduced χ^2 found for all the models is below 1.
Instead, some differences are seen when we test different values of L. In particular, we can see in the plots that smaller values of L are disfavored by the Be/C data for rigidities between a few GV up to tens of GV. The models with $L < 2$ kpc struggle to fit the Be/C data and B/C data at the same time. Future AMS-02 data for the Be isotopes might help to put tight constraints for the size of the diffusive halo (see, e.g., [88]).

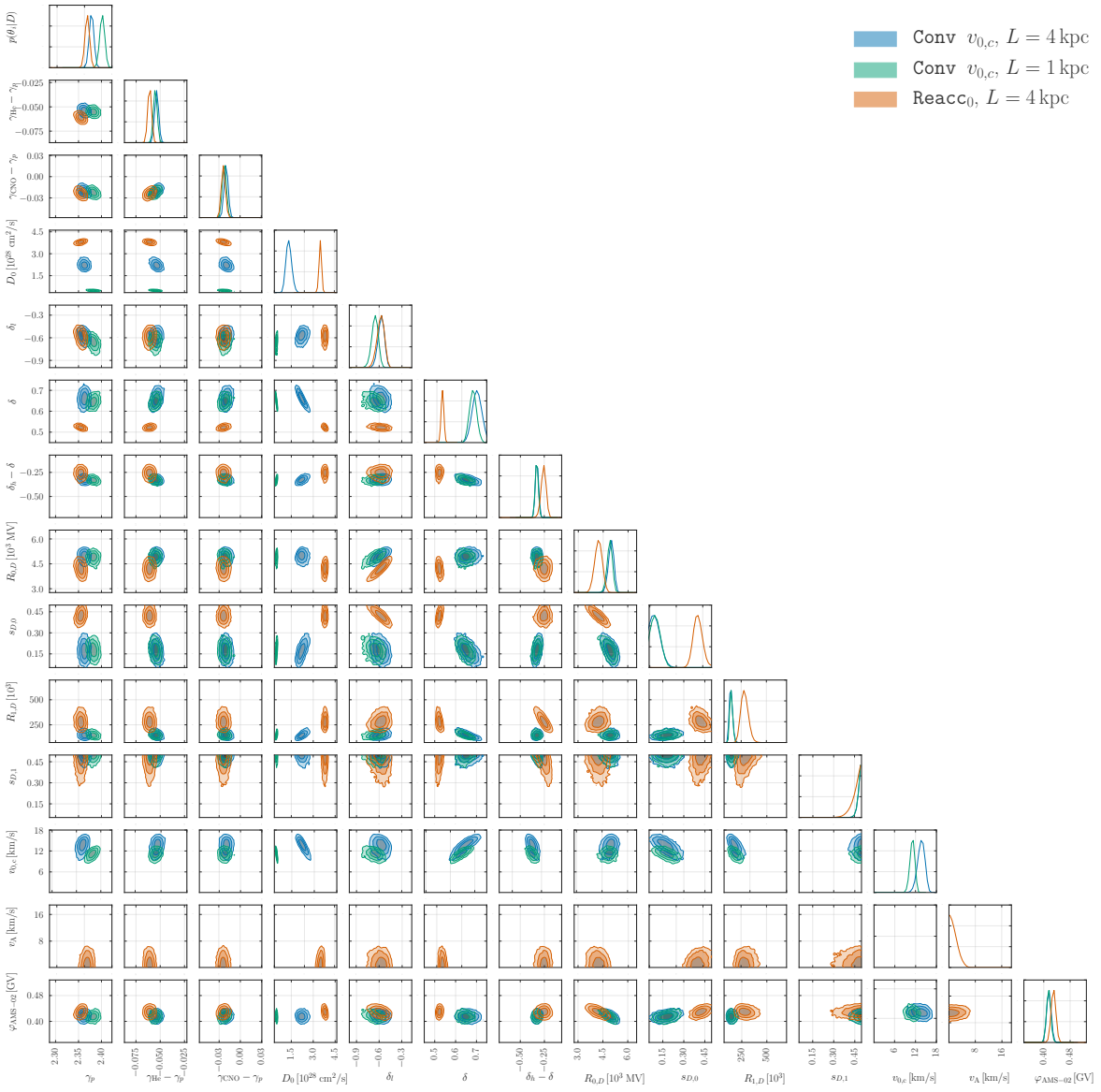

Figure A.2: Triangle plot for the propagation parameters obtained with the models `Conv` $v_{0,c}$ with $L = 1$ and 4 kpc and `Reacc`$_0$. For each panel we show the 1, 2 and 3σ contours for each combination of two parameters, while the diagonal shows the posterior distribution for each individual parameter.

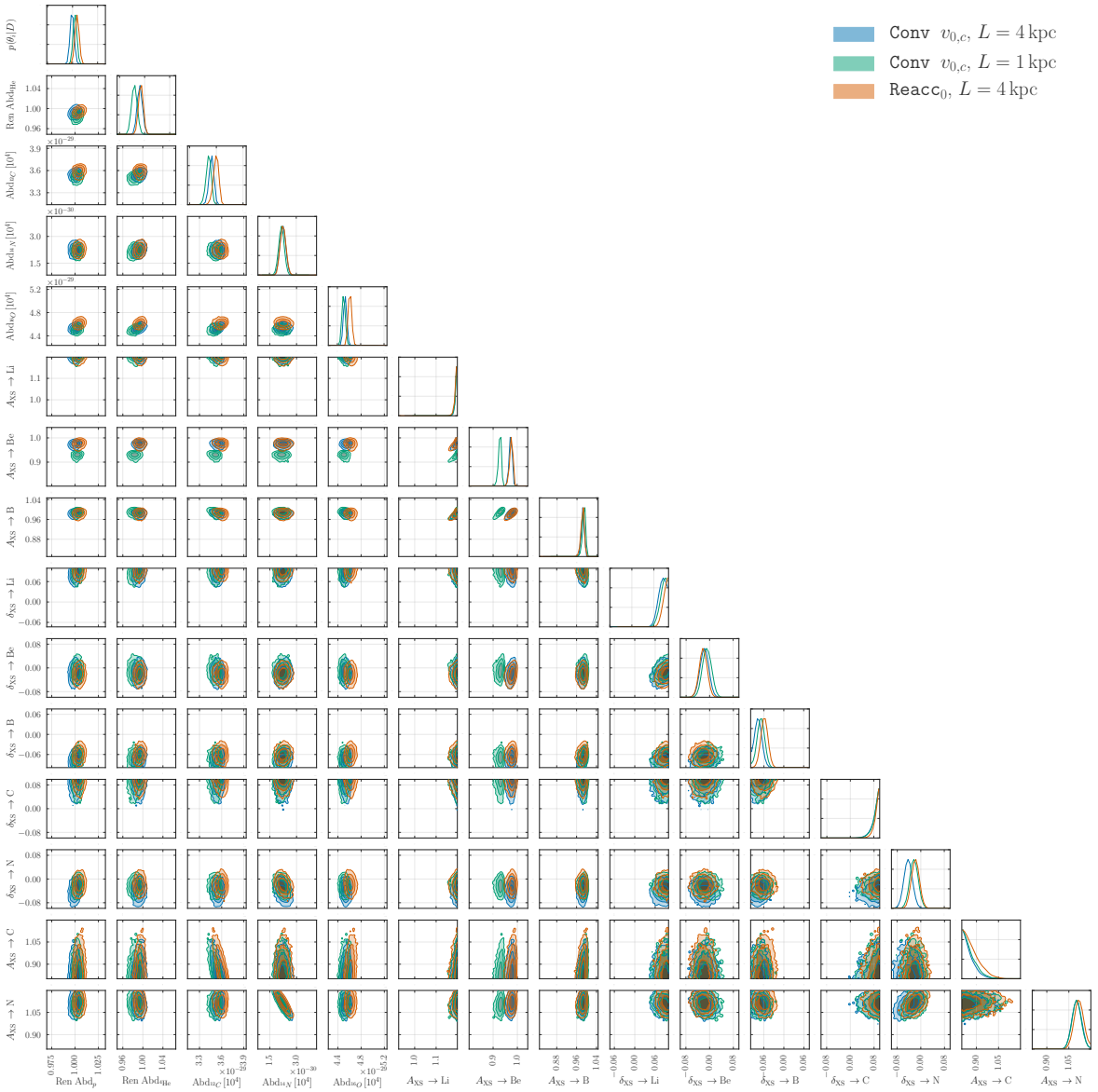

Figure A.3: Same as Figure A.2 for the abundance of primary CRs and nuisance parameters of the cross sections.

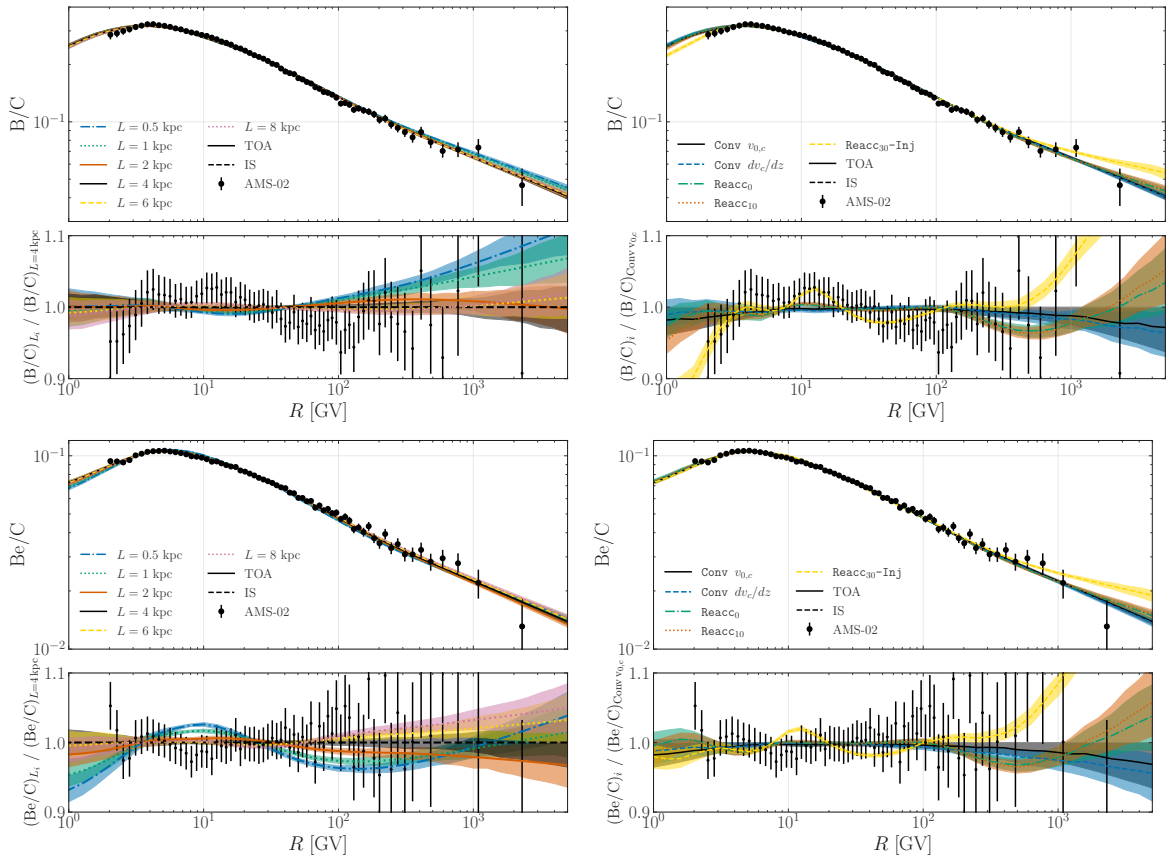

Figure A.4: Plot of the flux ratio B/C (top panel) and Be/C (bottom panel). In the left panels we show the results for the `Conv` $v_{0,c}$ model with different L, while in the right panel we report the other models tested in the paper. Below each figure we display the ratio between the different considered cases and the result obtained for `Conv` $v_{0,c}$ with $L = 4$ kpc. We also show the ratio between the data and the `Conv` $v_{0,c}$ model with $L = 4$ kpc.